Ph.D. thesis

Machine Learning and Improved Experimental Techniques for Near-field, Standoff LIBS Studies of Hazardous Materials

Submitted to the

University of Hyderabad

Towards partial fulfillment for the degree of
Doctor of Philosophy in Physics

By

Narlagiri Linga Murthy (17ACPP03)

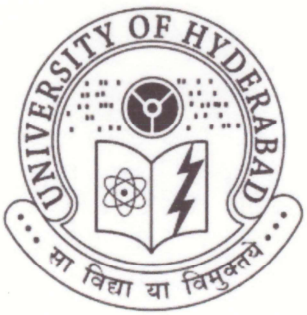

Under the guidance of

Prof. Soma Venugopal Rao

Advanced Centre of Research in High Energy Materials (ACRHEM.)
DRDO Industry Academia - Centre of Excellence (DIA-COE)
School of Physics, University of Hyderabad
Hyderabad 500046, Telangana, India.

December 2022

Dr. Soma Venugopal Rao
Professor
Tel.: +91-40 2313 8811
Fax: +91-40 2301 2800
E-mail: soma_venu@uohyd.ac.in
soma_venu@yahoo.com
somavenu@gmail.com

ACRHEM
University of Hyderabad,
Prof. C. R. Rao Road,
Gachibowli,
Hyderabad – 500 046,
Telangana, India.

Certificate

This is to certify that the thesis entitled **"Machine Learning and Improved Experimental Techniques for Near-field, Standoff LIBS Studies of Hazardous Materials"** being submitted to the University of Hyderabad by Narlagiri Linga Murthy (Reg. No. 17ACPP03), for the award of the degree of Doctor of Philosophy in Physics, is a record of *bonafide* work carried out by him under my supervision and is free of plagiarism.

The matter embodied in this report has not been submitted to any other University or Institution for the award of any degree or diploma.

S Venugopal Rao 16/12/2022

Prof. Soma Venugopal Rao
(Supervisor)

Prof. SOMA VENUGOPAL RAO
F.N.A.Sc., F.Inst.P, FRSC
ACRHEM
DRDO Industry Academic-Centre of Excellence
(DIA-COE)
University of Hyderabad
Hyderabad-500046. Telangana, INDIA.

V. Kamalakar

Director,
ACRHEM

Director
ACRHEM

16/12/22

Dean,
School of Physics

DEAN
School of Physics
University of Hyderabad
HYDERABAD - 500 046

Declaration

I hereby declare that, the thesis titled "Machine Learning and Improved Experimental Techniques for Near-field, Standoff LIBS Studies of Hazardous Materials" submitted by me under the guidance and supervision of Prof. Soma Venugopal Rao, is a bonafide research work and is free from plagiarism. I also declare that it has not been submitted previously, in part or in full to this university or any other university or institution, for the award of any degree or diploma. I hereby agree that my thesis can be deposited in shodhganga/ INFLIBNET.

A report on plagiarism statistics from the university librarian is enclosed.

Hyderabad **(Narlagiri Linga Murthy)**

Dated: 16.12.2022 **17ACPP03**

Certificate

This is to certify that the thesis entitled **"Machine Learning and Improved Experimental Techniques for Near-field, Standoff LIBS Studies of Hazardous Materials"** submitted by **Narlagiri Linga Murthy** bearing registration number **17ACPP03** in partial fulfillment of the requirements for the award of **Doctor of Philosophy in physics at ACRHEM, School of Physics, University of Hyderabad** is a bonafide work carried out by him under my supervision and guidance.

This thesis is free from plagiarism and has not been submitted previously in part or in full to this or any other University or Institution for the award of any degree or diploma.

Further, the student has the following publications before submission of the thesis for adjudication.

Review article

- L.M. Narlagiri, M.S.S. Bharati, R. Beeram, D. Banerjee, V.R. Soma, Recent trends in laser-based standoff detection of hazardous molecules, **TrAC - Trends Anal. Chem.** 153 (2022) 116645. doi:10.1016/j.trac.2022.116645

Book chapters

- Linga Murthy Narlagiri, Venugopal Rao Soma,* "Nanoparticle Enhanced LIBS for Sensing Applications," **Laser-Induced Breakdown Spectroscopy (LIBS): Concepts, Instrumentation, Data Analysis and Applications,** Eds: Dr. Vivek K. Singh, Prof. Y. Deguchi, Dr. Zhenzhen Wang, and Dr. Durgesh K. Tripathi, John Wiley & Sons, In Press, 2022.
- Linga Murthy Narlagiri, Venugopal Rao Soma,* "Recent developments in standoff laser induced breakdown spectroscopy," **Laser-Induced Breakdown Spectroscopy (LIBS): Concepts, Instrumentation, Data Analysis and Applications,** Eds: Dr. Vivek K. Singh, Prof. Y. Deguchi, Dr. Zhenzhen Wang, and Dr. Durgesh K. Tripathi, John Wiley & Sons, In Press, 2022.

Research articles

- Narlagiri, L. M., & Rao, S. V. (2020). Identification of metals and alloys using color CCD images of laser-induced breakdown emissions coupled with machine learning. **Applied Physics B,** 126, 1-8. DOI: doi:10.1007/s00340-020-07469-6
- Narlagiri, Linga Murthy, and Venugopal Rao Soma. "Improving the signal-to-noise ratio of atomic transitions in LIBS using two-dimensional correlation analysis." **OSA Continuum** 4.9 (2021): 2423-2441. doi:10.1364/OSAC.426995
- Narlagiri, Lingamurthy, and Venugopal Rao Soma. "Simultaneous quantification of Au and Ag composition from Au–Ag bi-metallic LIBS spectra combined with shallow neural network model for multi-output regression." **Applied Physics B** 127.9 (2021): 1-11. doi:10.1007/s00340-021-07681-y
- Linga Murthy Narlagiri, Chandu Byram, Sampath Kumar Satani, and Venugopal Rao Soma, "Laser beam steering automation with an Arduino-based CNC shield for standoff femtosecond filament-induced breakdown spectroscopic studies," **Appl. Opt.** 61, 4947-4955 (2022)

Venugopal Rao 16/11/2022

Prof. SOMA VENUGOPAL RAO
F.N.A.Sc., F.Inst.P, FRSC
ACRHEM
DRDO Industry Academic-Centre of Excellence
(DIA-COE)
University of Hyderabad
Hyderabad-500046. Telangana, INDIA.

Conference proceedings

- Murthy, N. L., Kalam, S. A., & Rao, S. V. (2019, December). Stand-off Femtosecond Laser Induced Breakdown Spectroscopy of Metals, Soil, Plastics and Classification Studies. In 2019 Workshop on Recent Advances in Photonics **(WRAP)** (pp. 1-3). IEEE. D.O.I:10.1109/WRAP47485.2019.9013674
- Linga Murthy N., Rao S.V. (2021) Nanoparticle Enhanced Laser Induced Breakdown Spectroscopy of Liquids. In: Singh K., Gupta A.K., Khare S., Dixit N., Pant K. (eds) **ICOL-2019**. Springer Proceedings in Physics, vol 258. Springer, Singapore. https://doi.org/10.1007/978-981-15-9259-1_105
- L. M. Narlagiri and V. R. Soma, "Plasma Temperature Evolution with Varying Compositions in an Alloy Using Laser Induced Breakdown Spectroscopy," in **Frontiers in Optics + Laser Science 2021**, C. Mazzali, T. (T.-C.) Poon, R. Averitt, and R. Kaindl, eds., Technical Digest Series (Optical Society of America, 2021), paper JW7A.29.
- Kalam, S. A., Murthy, N. L., Krishna, J. R., Srikanth, V. V. S. S., & Rao, S. V. (2016, December). Nanoparticle enhanced laser induced breakdown spectroscopy with femtosecond pulses. **In International Conference on Fibre Optics and Photonics** (pp. Th3A-89). Optical Society of America. DOI:10.1364/PHOTONICS.2016.Th3A.89.

Course No.	Course offered at	Title of the Course	Credits	Pass/Fail
PY801	ACRHEM	Research Methodology	4	Pass
PY802	School Of Physics	Advanced Quantum Mechanics	4	Pass
PY803	School Of Physics	Advanced Experimental Techniques	4	Pass
PY805	ACRHEM	Ultrafast Optical Phenomena	4	Pass

S.Venugopal Rao 16/12/2022

Supervisor,
Dr. Soma Venugopal Rao,
Professor,
ACRHEM, University of Hyderabad,
Hyderabad.

Prof. SOMA VENUGOPAL RAO
F.N.A.Sc., F.Inst.P, FRSC
ACRHEM
DRDO Industry Academic-Centre of Excellence
(DIA-COE)
University of Hyderabad
Hyderabad-500046. Telangana, INDIA.

V. Ligy Wee

Director,
ACRHEM
University of Hyderabad,
Hyderabad.

Director
ACRHEM

16/12/22

Dean,
School of Physics,
University of Hyderabad,
Hyderabad.

DEAN
School of Physics
University of Hyderabad
HYDERABAD - 500 046.

Acknowledgments

I want to express my heartfelt gratitude to my supervisor, Prof. Soma Venugopal Rao, for his invaluable guidance and support throughout my Ph.D. His strong motivation, punctuality, patience, and passion in research inspired me to work and complete this work within the time frame. I am immensely thankful to him for giving me a platform to resume my career in the research field after a gap in my academics. And I am very thankful to him by giving an opportunity to become a member in his collaborations and research projects.

I sincerely thank my doctoral committee members, Prof. A K Chaudhary and Prof. Suneel Singh for their constructive comments and suggestions. I am privileged to thank Prof.Prem Kiran, Prof. Manoj Kumar, Prof. G S Vaitheeswaran, and Dr. Sree Harsha for their support. I am pleased to thank Dr V. Kameswara Rao, Director, ACRHEM; former directors of ACRHEM; Prof.James Raju, Dean School of Physics (SoP); former deans of SoP, University of Hyderabad, for their support towards the completion of this work.

I want to thank Defence Research and Development Organization (DRDO), India for providing me the financial support (through ACRHEM) during the tenure of my Ph.D. program. It is my pleasure to express appreciation to all my seniors and present lab mates for creating productive research environment Dr. Abdul Kalam (thankful to him for introducing me to the laboratory), Dr. Chandu (thankful for his help in femtosecond laser lab), Dr. Bharathi (thankful for her support during the preparation of the thesis), Dr. Balaji, Mr. Sarang (thankful for helping me in initial standoff experiments), Dr. K Krishnakanth (thankful for his help in femtosecond lab), Dr. D. Ganesh (thankful for guiding me through thesis preparation process), Dr. J. Rajendhar (thankful for his insightful discussions on LIBS), Dr.Yelliah, Dr. Samuel Anurag (thankful for his help in SSA experiments in femtosecond pulse width measurements), Mr. Dipanjan, Ms. Reshma, Mr. Jagannath, Mr. Arun Prakash (thankful for his help in setting up experimentsin nanosecond laser lab) , Mr. Nagaraju Menchu (thankful for his support during the Ph.D. as a roommate), Mr. Naveen, Mr. Akash (thankful for fruitfull discussion in topics related to plasma), Mr. Chandan, Mr. Rajesh, Mr. Sampath Kumar and many others.

Lastly, I dedicate this thesis to my Professor Soma Venugopal Rao, my friend Abdul kalam.S, and family members for their encouragement to undertake the decision to resume my research carrier. I thank my parents N Shanker & Swarupa and my sister N. Anusha, brother N. Venkatesh and loveble younger brother N. Santosh and my girlfriend Samiksha Kapoor for their constant support

Contents

1 Introduction 1
1.1 Motivation and Introduction 1
1.2 Atomic spectroscopy 2
1.3 Laser-matter interaction and LIBS 4
1.4 Application of LIBS 5
1.5 Difference between femtosecond and nanosecond LIBS 8
1.6 Instruments and analysis used in the present thesis 10
1.6.1 Color CCD camera 10
1.6.2 Two-dimensional correlation analysis 10
1.6.3 Principal component analysis 11
1.6.4 Support vector machine 11
1.6.5 Artificial neural networks 11
1.6.6 Beam steering 12
1.6.7 Schmidt-Cassegrain telescope in standoff LIBS 13
1.6.8 Perspective on the mechanism(s) of nanoparticle enhancement LIBS 13
1.7 Thesis organization & chapter-wise details 14
1.7.1 Introduction 14
1.7.2 Experimental details 14
1.7.3 Machine learning and deep learning in LIBS 15
1.7.4 Two-dimensional correlation analysis in LIBS 15
1.7.5 Nanoparticle enhanced LIBS 16
1.7.6 Automation in the standoff FIBS studies 17
1.7.7 Conclusions and future scope 17
2 Experimental details and initial nanosecond, femtosecond LIBS studies 29
2.1 Experimental details 29
2.2 Nanosecond laser 29
2.2.1 Q-switching 29
2.2.2 Q-switching using the Pockels cell 30
2.3 Femtosecond laser and ker lens mode locking 31
2.3.1 Chirped pulse amplification 33
2.3.2 Single shot autocorrelation 35
2.4 Detectors 37
2.4.1 Non-gated spectrometers 37
2.4.2 Mechelle spectrograph equipped with ICCD 37
2.4.3 High-resolution echelle spectrometer (HRES) 38

2.4.4 Image intensifier 40
2.4.5 Schmidt-Cassegrain telescope for the standoff studies 41
2.4.6 Delays involved in acquiring LIBS spectra 42
2.5 Nanosecond laser-induced plasma temperature evolution 44
2.5.1 Experimental procedure 44
2.6 Novel femtosecond experimental configurations for fine powder samples 47
2.6.1 Experimental setup 49
2.6.2 Results and discussion 51
3 Machine learning in LIBS data analysis 59
3.1 Machine learning in the identification of metals and alloys 59
3.1.1 Introduction 59
3.1.2 Experimental details 61
3.1.3 Analysis of colour CCD images of plasma emissions 64
3.1.4 PCA of LIBS spectra and colour CCD images of plasma emissions 66
3.1.5 Results and discussion 67
3.1.6 Conclusions 68
3.2 Shallow neural network model for multi-output regression for quantification 69
3.2.1 Experimental details 72
3.2.2 Terminology in the neural network model 74
3.2.3 Model details 78
3.2.4 Results and discussion 79
3.2.5 Conclusions 84
4 Two-dimensional correlation analysis of the LIBS spectra 91
4.1 Introduction 91
4.2 Experimental procedure 93
4.3 2D correlation plots 94
4.3.1 Results and discussion 97
4.3.2 Correlation studies 100
4.3.3 Classification studies 106
4.3.4 2D correlation analysis of standoff LIBS data 108
4.4 Conclusions 110
5 Nanoparticle-enhanced LIBS 115
5.1 Introduction 115
5.1.1 Earlier reviews 116
5.1.2 Enhancement via different conditions 117
5.2 NELIBS of liquids 123
5.2.1 Results and discussion 124

5.3 NE-fs-LIBS of aluminum sheet coated with gold nanoparticle-embedded nanofibers 125
5.3.1 Introduction 125
5.3.2 Experimental procedure 126
5.3.3 Results 127
5.4 Conclusions 128
6 Standoff LIBS and automation studies 133
6.1 Literature survey of the standoff LIBS 133
6.1.1 Introduction 133
6.1.2 Experimental setup 134
6.1.3 Earlier reviews on standoff LIBS 135
6.1.4 Notable standoff LIBS studies 136
6.2 Standoff fs LIBS studies of possible interferents 142
6.2.1 Introduction 142
6.2.2 Experimental procedure 142
6.2.3 Results 142
6.2.4 Conslusions 148
6.3 Laser beam steering with arduino-based CNC shield for standoff Fs FIBS studies 148
6.3.1 Experimental setup 151
6.3.2 Automation 153
6.3.3 Results and discussions 155
6.4 Conclusions 159
7 Conclusions and future scope 167
7.1 Conclusions 167
7.2 Femtosecond LIBS for trace detection 169
7.2.1 Introduction 169
7.2.2 Experimental details 169
7.2.3 Results 171
7.2.4 Conclusions 172
7.3 Future scope 172
7.1.1 Image stabilization in standoff LIBS 172
7.1.2 Standoff double pulse LIBS 172
7.1.3 Glass fiber filter paper and nanoparticle LIBS 172
7.1.4 Grazing incidence 173
7.1.5 Single deep learning model for the quantification from LIBS spectra 173
7.1.6 Extension of the classification of the compounds based on the color CCD images to the standoff configuration 173

List of tables

Table 1.1 Summary of the differences between ns and fs LIBS. 9

Table 2.1 The parameters values of the femtosecond laser source used in the LIBS experiments 35

Table 2.2 Parameters values used in wavelength and intensity calibration of ICCD. 41

Table 2.3 Parameters of the optical fiber used for transporting the plasma emissions from the collector to the spectrometer. 41

Table 2.4 The specification of the SC telescope used for the standoff studies. 42

Table 2.5 The spectroscopic parameters taken from the NIST database used for the Boltzmann plots. 46

Table 2.6 Vibrational temperature in kelvin and peak intensities of CN (388.3 nm) and C_2 (516.5nm). 53

Table 2.7 The elemental peaks in the FIBS spectra of talcum powder were identified from the NIST database. 55

Table 3.1 LIBS spectral peaks identified from NIST database [33] 63

Table 3.2 Results of SVM on extracted features from PCA time series LIBS spectra of the samples investigated in the present study. 69

Table 3.3 Results of SVM on extracted features from PCA of colour CCD images from the plasma emission of the samples studied in the present work. 69

Table 3.4 The mean and standard deviation of the results predicted by the three different models trained with the LIBS spectral data collected at 1 μs, (1 μs and 2 μs), and (1 μs, 2 μs and 3 μs) gate delays. 82

Table 4.1 Acquisition parameters used in the time-resolved ns-LIBS experiments. 94

Table 4.2 Peaks identified from ns-LIBS spectrum of the Al target. 100

Table 4.3 Peaks identified from ns-LIBS spectrum of copper target. 101

Table 4.4 Peaks identified from ns-LIBS spectrum of the Brass target. 101

Table 4.5 Identified peaks form the ns-LIBS spectrum of Au-Ag bimetallic target. 106

Table 6.1 Peaks identified from the standoff LIBS spectrum of copper. 143

Table 6.2 Elemental peaks identified from the standoff LIBS spectrum of soil. 143

Table 6.3 Peaks identified from the fs-ST-LIBS spectrum of steel 145

Table 6.4 Peaks identified from the fs-standoff LIBS spectrum of the Al sample. 146

Table 6.5 Identified peaks form the fs-St-LIBS spectrum of PVC. 147

List of figures

Figure 1.1 Energy level diagram of a hydrogen atom with the energy levels merging towards the higher energies into a continuum. 2

Figure 1.2 The transition between two energy levels with the emission in red and absorption in blue between two energy levels 3

Figure 1.3 Critical points in the history of LIBS and its applications to diverse fields. 6

Figure 1.4 Critical points on the contributions to LIBS studies from our group. [146-148]. 7

Figure 1.5 Key points on the contributions to the LIBS from the present thesis. 8

Figure 1.6 Contrasting the evolution processes of the plasma from the ns and fs laser pulse interaction with the matter (Figure adopted from Harilal et al. [159]). 10

Figure 1.7 (a) stepper motor (b) CNC shield (c) Arduino Uno microcontroller used for the automation of the beam steering. 12

Figure 1.8 Various components of the Schmidt–Cassegrain telescope (SCT) typically used for the collection of standoff LIBS. 13

Figure 1.9 Acquisition of the LIBS spectra using a gated spectrometer for time-resolved studies. 16

Figure 2.1 The steps involved in Q-switching in the nanosecond laser. 30

Figure 2.2 The major components of the nanosecond laser combining the Pockels cell and two polarizers used for Q-switching. 30

Figure 2.3 The broad absorption range in the visible region and the broad emission in the infrared region of the Ti: sapphire crystal is helpful in pumping in with a wide range of lasers and also results in a large number of modes. [Adopted from. https://micro.magnet.fsu.edu/primer/java/lasers/tsunami/index.html]. 31

Figure 2.4 (a) The schematic of the femtosecond seed generation with pumping (Vitesse) (b) The Nd:YVO_4 based pumping the Ti:Sapphire crystal (Verdi laser) (b) The Verdi laser with Nd:YVO_4 gain medium. 32

Figure 2.5 The process of the CPA with the stretcher grating, the amplifier, and the compressor grating [Adopted from the Ph.D. thesis of Dr. Abdul kalam]. 33

Figure 2.6 The schematic of the femtosecond amplifier (Coherent, LIBRA) system with the seed pulse generator, Vitesse, and the pumping laser, Evolution, and the regenerative amplifier with the stretcher the amplifier compartments [https://www.coherent.com/resources/ preinstallation/libra-series/Libra_Preinstallation_Manual.pdf]. 34
Figure 2.7 The single shot autocorrelation of the two pulses and the schematic of the coherent SSA. The beam splitter splits the beam, and the beam traveled different paths before overlapping in the doubling crystal. 35
Figure 2.8 The second harmonic generation with the delay and the second harmonic signal at the zero delays with the calculated FWHM of 93 fs (as the roundtrips, propogation length and the dispersive elements effects the pulsewidht). Blue, scattered points are the experimental data, while the solid red line is the fit. 36
Figure 2.9 The photodiode signal of the 1 kHz femtosecond pulse train was measured using an oscilloscope. 36
Figure 2.10 Major components of the CCD-based non-gated spectrometers from the entrance to the CCD detector and the grating and mirrors [Adopted from Avantes]. 37
Figure 2.11 The echelle (blazed) grating is used in the ICCD operates at higher order for better resolution. 38
Figure 2.12 The schematic of the cross dispersion of the light, from grating and prism combination, incident on the 2D sensor [Adopted from https://www2.keck.hawaii.edu/inst/hires/]. 39
Figure 2.13 The working method of the 2D CCD sensors after the photons are converted to charge and transport. 39
Figure 2.14 The intensifier with a photocathode, microchannel plate, and phosphor screen. 40
Figure 2.15 (a) The laser pulse widh measured using photodiode in orange and (b) the signal from pockels cell in blue (b) ICCD trigger monitor in the oscilloscope shows the ICCD gate opening time of ~1 µs. 43
Figure 2.16 The time delay between the pulse from the SDG and the ICCD trigger monitor is 50 ns and the time delay between the photo diode response and the ICCD trigger monitor is ~20 ns because of propagation delay. 43
Figure 2.17 The schematic of the nanosecond laser-induced breakdown spectroscopy experiment. 44

Figure 2.18 The time-resolved ns-LIBS spectra of the bimetallic targets (a) Au20-Ag80, (b) Au30-Ag70, (c) Au50-Ag50, (d) Au70-Ag30 with identified peaks from the NIST database.....45

Figure 2.19 (a) Boltzmann plot of the Au30-Ag70 composition with the ns LIBS taken at 1μs and the evolution of plasma electron temperature for the compositions (b) Au30-Ag70 (c) Au50-Ag50 (d) Au80-Ag20. 46

Figure 2.20 (a)The experimental setup used for the filamentation mowing of traces of fine graphite powder on the Brass, (b) substrate moving tangentially to the filamentation with the ,(c) sample on the Brass plate on the optical bench, (d) the collection optics at ~45° to the horizontal Brass plate and the red arrow shows the incident laser direction. 50

Figure 2.21 The grazing incidence FIBS spectra of sparse fine graphite powder with molecular emissions of the CN violet bands, C_2 swan band enlarged in the inset. 51

Figure 2.22 The standard deviation (in red) and mean (in blue) of the (a) CN band and (b) C_2 band in the grazing incidence FIBS spectra were calculated from the 14 spectra. Mean of CN peak was 21090.05 with standard deviation of 6578.48 for peak at 388.34 nm. Mean of C_2 was 8895.05 with standard deviation of 2651.24 for peak at 516.52 nm. 52

Figure 2.23 The fitting of the computed spectra (fit in blue) with the experimental spectra (in red) for the temperature estimation form (a) CN band and (b) C_2 band. The temperature of 6536K for CN and FEHM was 0.15 nm, and the temperature of C_2 was 5436 K and FWHM of 0.25 nm. 53

Figure 2.24 Grazing incidence FIBS spectrum of the commercially available talcum powder (Ponds) with the major peaks of calcium, magnesium, sodium, and potassium identified. 54

Figure 2.25 The elemental peaks of singly ionized (a) calcium, (b) sodium, (c) potassium, (d) magnesium were identified from the FIBS spectrum of commercially available talcum powder (Ponds). 54

Figure 2.26 The calcium peaks identified from the FIBS spectra of commercially available talcum powder in low quantities (a), (b), and (d) singly ionized calcium peaks, and (c) doubly ionized calcium peaks. 55

Figure 3.1 Experimental setup for femtosecond LIBS and capturing the colour CCD images. The ICCD and spectrometer combination in the green dotted box is used for LIBS studies and imaging of plasma emissions, only CCD in the blue dotted box.....61

Figure 3.2 Fs-LIBS spectra of Al, Cu, bronze, and steel. The corresponding colour regions (violet, indigio, cyan, green, yellow, orange, and red) are for comparison with the colour CCD images from the plasma emissions. 63
Figure 3.3 Colour CCD images of plasma emissions produced when the femtosecond laser pulses ablating the (a) Al, (b) bronze, (c) Cu, (d) steel targets. 65
Figure 3.4 KDE plots of blue, red, and green channels pixel values from the CCD images of plasma emissions produced form the (a) Al, (b) bronze, (c) Cu, (d) steel targets. 65
Figure 3.5 Two-dimensional KDE plots correlating the pixel values from blue-green, blue-red and red-green channels of the plasma emission images from (a) Al, (b) bronze, (c) Cu, (d) steel.....66
Figure 3.6 PCA score plots of (a) fs-LIBS spectra of the four samples. The Triangle marker corresponds to aluminium, the square marker to steel, the circle marker to copper, plus marker to bronze, and (b) the colour CCD images of plasma emissions from the same samples.....67
Figure 3.7 LIBS spectra collected at three gate delays of 1 µs, 2 µs, and 3 µs. The spectra (a) Au20-Ag80, (c) Au50-Ag50, (d) Au80-Ag20are used for training the shallow neural network model of, and the unseen spectra (b) Au30-Ag70 were used for prediction by the model.....72
Figure 3.8 Ns-LIBS spectra collected at the gate delay of 1 µs, 2 µs, and 3 µs of (a) Aluminum, (b) copper and (c) Brass are used in the model training as zero composition of Au-Ag. 73
Figure 3.9 The schematic of the model built for the quantification studies with various compositions of Au-Ag LIBS spectra used for the test and train set and evaluation set and unseen composition used for prediction. 73
Figure 3.10 The role of the activation function in the neural networks is illustrated. The activation function introduces the nonlinearity to the regression analysis. 75
Figure 3.11 The weights are randomly excluded during the forward propagation to improve the model in the dropout.....76
Figure 3.12 The effect of the small, moderate, and large step size on the learning rate in optimizing the model. 77
Figure 3.13 The weights and biases are updated in each cycle from the knowledge of the computed gradient. The model completes a cycle in one epoch.....77
Figure 3.14 Learning curves of the model during training with the validation and training sets used in the optimization. The variation in the loss and error with every epoch in the

both the sets for ns-LIBS spectra acquired a) at 1 μs and, b) at 1 μs+ 2 μs and, c) at 1 μs + 2 μs + 3 μs. and the true values vs predicted values from the spectra at d) at 1 μs and, e) at 1 μs + at 2 μs and, f) at 1 μs + at 2 μs + at 3 μs. 79

Figure 3.15 The predictions of the model on the test set spectra recorded at a) 1 μs and, b)1 μs + 2 μs and, c)1 μs + 2 μs + 3 μs. And the true values versus predicted values of the spectra at, d) 1 μs and, e) 1 μs + 2 μs and, f) 1 μs + 2 μs + 3 μs. The line is just the guide to the eye. 81

Figure 3.16 The predictions of the model on the unseen ns-LIBS spectra of Au30-Ag70 at a) 1 μs and b) 1 μs + 2 μs and, c) 1 μs + 2 μs + 3 μs. 83

Figure 4.1 The procedure of the ns-LIBS data acquired from the target samples. 93

Figure 4.2 The time-resolved ns-LIBS spectra of (a) Al, (b) Cu, (c) Brass at five collected at regular intervals of 1 μs. The 2D correlation studies on the ns-LIBS spectra of (d) aluminium and, (e) copper, (f) Brass targets, respectively. 95

Figure 4.3 The atomic peaks of the Al in the time-resolved LIBS spectra are used for the asynchronous correlation analysis. The analysis was discontinued on the other spectra. 96

Figure 4.4 a) copper peak from the ns-LIBS spectra fitted with Lorentzian before the analysis. b) fitted with a Lorentzian function after the analysis it shows the improvement in the resolution after the 2D correlation analysis. 97

Figure 4.5 2D correlation analysis performed (a) with the spectrum acquired at 1 μs (b) the spectrum at 5 μs, (c) with the reference taken as zero and (d) the average spectrum of the five time-resolved spectra as reference. 98

Figure 4.6 The peaks from the regular ns-LIBS spectrum of (a) Al target in the spectral range of 303-312 nm and the corresponding, (b) 2D correlation analysis and (c) diagonal of the 2D correlation analysis on the LIBS spectra. 99

Figure 4.7 The improved spectrum extracted from the 2D correlation analysis on LIBS spectra of (a) Al, (b) Cu, (c) Brass, (d) Au30Ag70, (e) Au50Ag50 (f) Au80Ag20 targets, respectively. 103

Figure 4.8 Time-resolved LIBS spectra of (a) Au30-Ag70, (b) Au50-Ag50, (c) Au80-Ag20 bimetallic targets at five delays with regular intervals of 1μs with identified peaks. The 2D correlation studies on ns-LIBS spectra of (d) Au30-Ag70, (e) Au50-Ag50, (f) Au80-Ag20 targets. 104

Figure 4.9 2D correlation studies on the ns-LIBS spectra of Au-Ag bimetal with three compositions and at two delays in the range (a) 240-250 nm, (b) 260-280 nm, (c) 520-550 nm at 1 μs and, (d) 240-250 nm, (e) 260-280 nm, (f) 520-550 nm at 2 μs. 105

Figure 4.10 PCA on the ns-LIBS spectra of bimetal targets and the diagonal of the 2D correlation analysis (a) PCA score plot (b) variance plot (c) cumulative explained variance on ns-LIBS spectra and (d) PCA score plot (e) variance plot (f) cumulative explained variance on the improved diagonal of the 2D spectra. A solid line is a guide to the eye. 108

Figure 4.11 The average of fs-standoff LIBS spectra of (a) PVC, (b) CN band, (c) C_2 band compared with the diagonal of the 2D correlation analysis demonstrating the improvement of five orders of magnitude (d) whole spectra (e) the CN band, and (f) C_2 band.....109

Figure 4.12 The average of fs-standoff LIBS spectra of (a) HPC, (b) CN band, (c) C_2 band compared with the diagonal of the 2D correlation analysis demonstrating the improvement of five orders of magnitude (d) whole spectra (e) the CN band, and (f) C_2 band.....110

Figure 5.1 Exhibites the enhancement by the nanomaterial (blue colored) as compared to bulk (red colored) spectral lines of (a) Ag_2O, (b) ZnO, (c) SiO, (d) Al_2O_3, (e)Fe_3O_4 and (f) TiO_2. [adopted from IOP publishing, Journal of Physics, Conference series 548 (2014), 012031] [15].....117

Figure 5.2 Images of (a) LIBS and (b) NELIBS plasma emissions from 1 µl of 1 ppm $PbCl_2$ (Au-NPs solution 0.04 mg ml^{-1}. [Adopted from Analytical Chemistry (2016) 88 (2016), 5251-5257] [19].....119

Figure 5.3 The enhancement in the spectral intensities of Zn I peak at 481 nm and the corresponding dotted line with NPs [Adopted from Spectrochimica Acta Part B 116 (2016) 8–15] [20].....120

Figure 5.4 the enhancements obtained for a) Ti II 311.76 nm and b) Ti I 319.99 nm at two different delay times [Adopted from Spectrochimica Acta Part B, 179 (2021) 106105, 0584-8547] [21]. 121

Figure 5.5 Enhancement factors of different shaped NPs on the (a) aluminum, (b) zinc, and (c) silicon after adding silver chloride nanospheres, nanocubes, and nanowires. [Adopted from J. Anal. At. Spectrom., 35 (2020) 2982–2989] [24].....122

Figure 5.6 The comparison of LIBS and BS-NELIBS of three different quality brands of canned tuna from the normalized intensities of CN molecular bands [Adopted from Spectrochimica Acta Part B 149 (2018) 112–117] [31].....123

Figure 5.7 Fs-LIBS spectrum of acetonitrile in water with dominant CN violet band around 388 nm. 124

Figure 5.8 The CN violet band in the fs-LIBS spectra of Acetonitrile in water at (a) 1:1 ratio. (b) 1:2 ratios with and without addition of NPs. (c) 1:4 ratios with and without NPs 125
Figure 5.9 TEM images of PVA nanofibers loaded with colloidal Au NPs (a) 50 nm, (b) 20 nm magnification. 126
Figure 5.10 Al atomic (a),(b) and molecular peaks (c),(d) from the fs-LIBS with and without NPs. Regular LIBS spectra in red and NE-LIBS spectra in blue with the mean and standard deviation of 25 spectra each. 127
Figure 6.1 The experimental schematic of the fs-ST-LIBS with the target placed at beam 6 m. A combination of convex and concave lenses used for focusing. The emissions are acquired at 5 meters from the sample using SC telescope. 135
Figure 6.2 Algorithm developed by López-Moreno et al. [13] for the classification of explosive residues in standoff mode from the various elemental and molecular intensity ratios of the LIBS peaks. 137
Figure 6.3 Intensities from atomic peaks of significant elements in geological rocks observed in near-field LIBS (a) and standoff configuration (b) [Adopted from Kalam et al. [17]]. 138
Figure 6.4 (a) Fluctuation in the diameters of focused laser pulses as a function of the distant. Inset shows the prints from laser pulses on heat-sensitive paper at corresponding distances; (b) variation in the intensity with range; (c) relative standard deviation in the emission signal. [Adopted from Gaona et al. [21]. 139
Figure 6.5 Variation in the SBR with the number of shots for (a) atomic U I, (b) molecular UO for the remote collection from 2, 5, and 10 m, (c) for a single shot, (d) for 100 shots at 10 m. [Adopted from Finney et al. [24]]. 141
Figure 6.6 The fs-ST-LIBS spectra from (a) Al, (b) Cu, (c) HPC, (d) steel, (e) soil in pellet form, (f) PVC. 144
Figure 6.7 The aluminum oxide band from the fs-ST-LIBS spectrum with major peaks identified. 146
Figure 6.8 The molecular bands from the fs-ST-LIBS spectrum of the PVC (h) CN violet band and, (i) C_2 swan band from the PVC traget. 147
Figure 6.9 Classification of the fs-St-LIBS spectrum of Cu, Al, steel, PVC, HPC and soil using PCA. Each data point in the plot corresponds to a LIBS spectrum and pluse marker is used for copper, circle for Al, triangle for steel, star for PVC, square of HPC, and arrow for soil. 148

Figure 6.10 Fs-ST-FIBS setup with SCT. Inset: The actual laboratory setup with a telescope, Maya CCD spectrometer, Arduino microcontroller, two kinematic mirror mounts, variable iris, and target highlighted in the red box at 5 m distance, filamentation in the lab. 152
Figure 6.11 Optical microscope images of craters formed from the fs-filamentation interaction with (a) Cu (diameter of ~320 μm), (b) Brass (diameter of ~280 μm), (c) Al (diameter of ~260 μm) for one second (i.e., 1000 number of pulses). 153
Figure 6.12 The components used for the automation (a) Arduino Uno microcontroller, CNC shield V3, and the A4988 stepper motor drivers (b) the two kinematic mirrors coupled to the stepper motors fixed to the optical table. 154
Figure 6.13 Fs-ST-FIBS spectra of (a) Al wherein Al atomic and AlO molecular bands were identified, (b) Cu (c) Brass. Fifty spectra from each target filtered out using the highest intensity. 156
Figure 6.14 The fs-ST-FIBS spectra of three plastic samples (a) PVC, (b) CPVC with background noise, (c) UPVC. All the spectra contain the C_2 swan bands, calcium lines are identified in UPVC spectra. 157
Figure 6.15 The fs-ST-FIBS spectra of Au-Ag bimetal alloy of three compositions (a) Ag30-Au70, (b) Ag50-Au50, (b) Ag70-Au30. Fifty spectra for three compositions were filtered out using the intensity of Ag I peak at 546.55 nm. 158
Figure 6.16 Precision of the automated standoff beam steering is demonstrated from the (a) raster scan (box shape) on steel, plastic, and Brass plates and a spiral scan (circle shape) on steel and Brass with in 1cm × 1cm area on the target placed at 5 meters standoff distance, (b) Classification of three compositions of Au-Ag alloy from the fs-ST-FIBS spectra using PCA. 159
Figure 7.1 Experimental setup used for recording the femtosecond LIBS of traces on filter paper. The filter paper ablated with femtosecond laser pulses in the inset during the raster scan. 170
Figure 7.2 (a) CN band and (b) C_2 band for the filter paper, picric acid (PA) on filter paper, DNT on filter paper, and AN on a filter paper. 171
Figure 7.3 The principal component analysis on the Fs-LIBS spectra of picric acid (PA) on filter paper in blue plus symbols, plane filter paper (FP) in green triangles, DNT on filter paper (DN) in orange circles, and ammonium nitrate on filter paper (AN) in red stars. 171

1 Introduction

1.1 Motivation and Introduction

Laser-based spectroscopy techniques are advancing rapidly in the detection of hazardous compounds such as explosives with the development of new intense and tunable lasers, gated and intensified detectors, and the availability of a standard spectroscopic database of explosives, biomolecules, and several other hazardous chemical compounds. Detecting dangerous materials, especially explosives, is challenging and essential for homeland security. The aftermath of an explosion leaves the scene with traces mixed with soil and other interferents. Developing the methods to analyze these traces is highly demanding as it could help understand the materials used and will be helpful for securely tackling the situations in future encounters. Also, probing suspicious materials from standoff distances and near fields is equally crucial for security purposes. The laser-based spectroscopic techniques are advantageous for precisely investigating the surfaces at desired locations by focusing the laser beam and delivering the required power at longer distances. The directionality of the lasers for providing the required intensities at the desired location is hugely beneficial in standoff spectroscopic studies. Various laser-based techniques engaged in explosive detection, either destructively or non-destructively, are (a) laser-induced fluorescence [1–6], (b) Raman spectroscopy [7–10], (c) infrared spectroscopy and imaging [11], (d) laser-induced breakdown spectroscopy (LIBS) [12], (e) terahertz (THz) imaging and spectroscopy (f) photoacoustic spectroscopy, with their advantages and disadvantages, should be judiciously selected based on the requirement. They all have a common advantage of being able to perform standoff measurements. Based on the wavelength of the laser sources used and the underlying fundamental principles, the intensity of the source, the technique can be either destructive or non-destructive. Some techniques are extremely sensitive, while some are advantageous in probing the sample from standoff distances. For example, Raman spectroscopy offers better sensitivity for both solid and liquid samples non-destructively. THz radiation is non-ionizing and considered ideal when probing for hidden objects under clothes and in non-metallic containers. Infrared radiation helps interrogate the suspicious and hazardous compounds and rapid imaging of traces on surfaces from standoff distances, from the vibrational spectra, with earlier recorded/reported databases of chemical and dangerous biological compounds and explosives.

In the LIBS technique, the intense pulsed lasers are focused on the sample to vaporize it and for the formation of plasma at later stages. The recombination in the cooling plasma emits radiation with characteristic elemental signatures simultaneously. LIBS offers a few advantages over other optical emission spectroscopy techniques; this technique detects almost every element in the periodic table. With a couple of initial cleaning with laser pulses, the sample is ready to probe, i.e., it requires significantly less sample preparation. It is a rapid technique for data acquisition, and combined with computation tools, real-time analysis is possible. Tuned lasers are not required, as in the case of other techniques where the laser incident wavelength is matched with the specific transitions of the sample. Pulsed lasers of a few tens of mJ energy per pulse are enough for this technique to interrogate any sample. Rapid elemental mapping with high spatial resolution and good depth profile studies. The experimental setup is simple compared to the other techniques. Easily coupled with other laser-based spectroscopy techniques like Raman and infrared to acquire complementary information from the sample, which is helpful for better identification [13]. LIBS can be extended to standoff studies when intense pulsed lasers (fs) are employed. A few of the disadvantages are (a) collecting only the information regarding atomic species (not a signature spectrum) in investigating the compounds, (b) and unavoidable matrix effects, (c) self-absorption (d) self-reversal.

1.2 Atomic spectroscopy

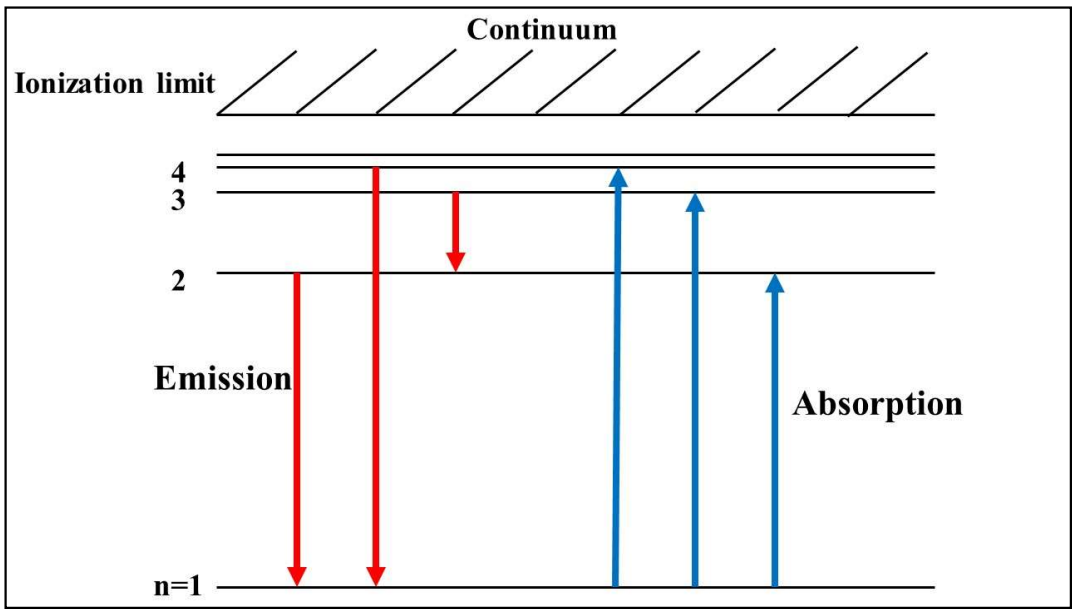

Figure 1.1 Energy level diagram of a hydrogen atom with the energy levels merging towards the higher energies into a continuum [14].

Figure 1.1 shows the energy level diagram of the hydrogen atom with the difference between the energy levels reducing and merging into a continuum of levels with increasing energy. The radiation is emitted and absorbed in discrete packets of energies equal to the energy difference between the two levels. The frequency of the spectral line resulting from a transition between the two levels is given by $h\nu_{12} = E_2 - E_1$. Figure 1.2 shows the dependency of the absorption and emission between two energy levels, E_2 and E_1, populated with N_2 and N_1, and the radiation density ρ, respectively. In LIBS, the intense pulse focused on the sample results in the absorption of multiple photons

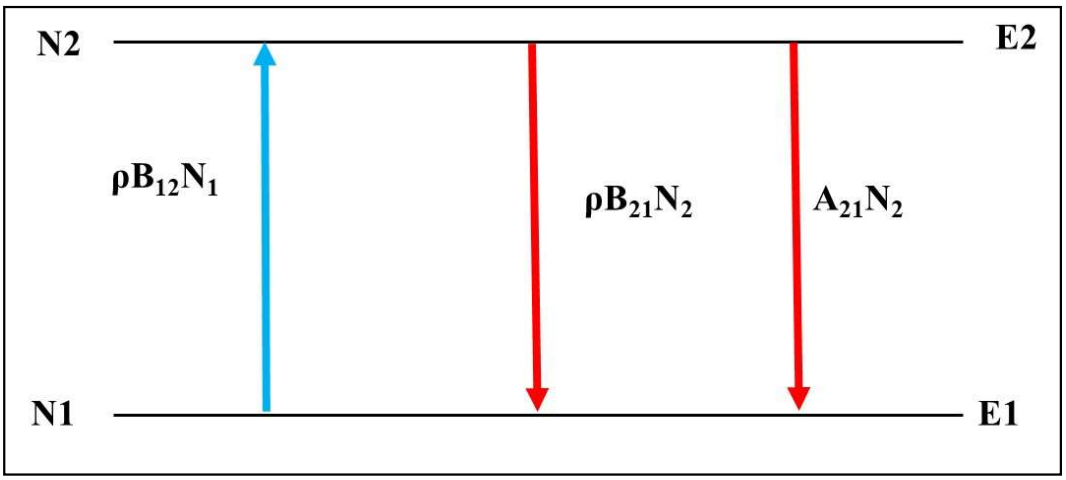

Figure 1.2 The transition between two energy levels with the emission in red and absorption in blue between two energy levels [14].

Figure 1.2 shows the three possible transitions between the two levels are stimulated absorption (in blue), spontaneous emissions (in red), and spontaneous absorption (in red).

- The spontaneous emissions per second, per cm^3, depends on the population in the E_2 level and the transition probability per second A_{21} from level E_2 to E_1 and is equal to $A_{21}N_2$
- The stimulated emission and absorption also depend on the number of photons available or the radiation density ρ.
- The probability of stimulated absorption per second per cm^3 equals $\rho B_{12}N_1$ $sec^{-1}cm^{-3}$.
- The probability of stimulated emission per second per cm^3 is equal to $\rho B_{21}N_2$ $sec^{-1}cm^{-3}$.

A_{21} is Einstein's coefficient for spontaneous emission, B_{21} for stimulated emission, and B_{12} for stimulated absorption. These are characteristics of the atom which can be determined from the wave function of two states.

From the dipole approximation, the transitions between the two states must satisfy the selection rules for angular momentum quantum number J and spin-orbit coupling L. Transitions that are prohibited in the dipole approximation may appear faintly. The line strength of a transition depends on the transition probability and the plasma system. When the plasma is thick, the light is re-absorbed before leaving the plasma resulting in self-absorption. The temperature difference in the outer and inner cores leads to self-reversal. In the ideal case, the free atom radiates with the intensity in the Lorentzian profile spread over a frequency range. The thermal energy contributes to the random motion of the atom, and the radiating atom moving in different random directions results in Doppler broadening with intensity in the Gaussian profile over a frequency range. The atoms in plasma also experience electric fields of moving electrons and ions, resulting in two kinds of broadening in the spectral line a) broadened by quadratic Stark effect results in an asymmetric spectral line as its center shifts to longer wavelengths, b) linear Stark effect gives rise to symmetrically broadened line shapes [14].

1.3 Laser-matter interaction and LIBS

The electric fields in the pulsed lasers [corresponding peak intensities in the range of a few tens of GW/cm^2] are sufficient to break down the sample when focused. Typically, 10^8–10^{10} W/cm^2 is required to produce laser-induced plasmas. The threshold power densities for ablation depend on the material and the laser pulse width of typically sub-picoseconds, as shown in equation 1.1.

$$PD_{max} = \rho L_v \sqrt{\frac{k}{\tau}} \left(\frac{\mathrm{W}}{cm^2}\right) \ldots\ldots\ldots\ldots\ldots\ldots\ldots\ldots\ldots\ldots\ldots\ldots\ldots\ldots (1.1)$$

PD_{max} is the required power density for ablation, where ρ is the density and L_v is the latent heat of vaporization, k is the thermal diffusion of the material, and τ is the laser pulse width [15]. The sample absorbs the laser pulse energy through the inverse bremsstrahlung process. The sample in the focal region passes through a series of phases. Finally, it forms plasma because of rapid ionization from the absorbed energy at the focal point, and the absorption may differ depending on the input laser pulse duration. The intense electric

fields of the focused laser pulses displace the electrons from the atoms on the sample surface within a few picoseconds, and ejected electrons transfer energy to the lattice by collisions heating the sample and vaporizing the sample at the focal point resulting in the formation of plasma. The excitation of specific energy levels in different atoms is multifaceted, and the aspects such as thermodynamic equilibrium and interplay with other molecules and atoms, ions in the plasma determine it. The plasma formed is reheated towards the end and cools after the pulse duration. The energy is transferred to the medium by radiation, conduction, and shock wave expanding into the medium. The decelerating electrons in the cooling plasma emit continuum radiation resulting from the bremsstrahlung process. The free electrons recombine with the ions resulting in ionization peaks and atomic peaks, radiation specific to the elements, and molecular peaks when the ions in the plasma recombine with the atoms in the atmosphere and other ions in the plasma. In the case of nanosecond LIBS, the plasma decays throughout one to several microseconds. In the case of femtosecond LIBS, it decays in an interval of 100 ns to one microsecond and depends on the laser energy deposited. The time scales are different when working at other pressures and shorter in a vacuum than in an open atmosphere.

The ultrashort pulses provide better ablation efficiency and a lower threshold when compared to the nanosecond and picosecond pulses. While the electron density is independent of the laser pulse duration, earlier reports suggest a slight increase in the plasma electron temperature. The ablation thresholds were smaller for the fs pulses, and they showed better efficiency in material ablation with extraordinary precision and minimal damage. The cost of the fs lasers makes it less appealing for LIBS, even though they offer better spatial resolution in imaging. And divergence-free propagation and self-focusing (filamentation) of the fs pulses was useful for standoff studies and better detection limits (LOD) with the fs lasers. The gated and intensified detectors with appropriate gate delays and gate widths optimal to laser pulse duration are efficient for LIBS studies compared to the conventional non-gated linear array detector spectrometers. However, one can choose different detectors based on the application envisaged.

1.4 Application of LIBS

Several advantages of LIBS made it famous, and have found applications in different fields, including the classification of archeological, teeth, and geological samples for identifying the place of origin and in planetary exploration. Additionally, it is used

extensively in classifying biological and pharmaceutical samples. The technique is also expansively used in the detection of explosives in traces both in the near field and standoff distances desirable for homeland security. Based on the requirement in various fields in science, technology, art, archeology, and industry, the LIBS technique mutated into wide varieties with required changes for specific needs. Double pulse [16–23] and magnetic confinement LIBS result in a better signal-to-noise ratio(SNR). Double pulse LIBS enhanced the signal for a better LOD and SNR in the near field and standoff distance. Standoff LIBS is convenient in probing hazardous samples and samples inaccessible and in hostile conditions [17, 26-71], and it makes the LIBS more appealing for real-time applications. Among the different lasers used in the standoff studies, fs pulses have an additional advantage of filamentation phenomenon by which the laser pulses, while propagation, and tend to focus instead of diverging as in the case of longer pulses. The filamentation is beneficial in the standoff studies of various compounds [72–93]. Nanoparticle-enhanced LIBS (NE-LIBS) utilizes nanoparticles for enhancing the LIBS signal and, in turn, the limit of detection (LOD). The use of nanoparticles improves the coupling of the laser pulse energy to the sample by local field enhancement and the formation of multiple hotspots at the focal spot.

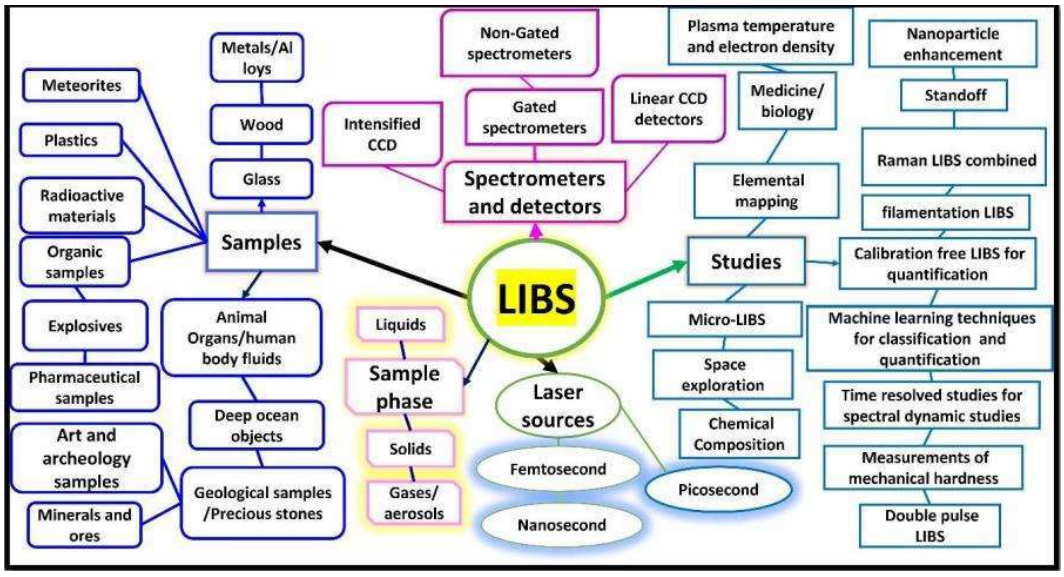

Figure 1.3 Critical points in the history of LIBS and its applications to diverse fields.

The enhancement in the emission signal up to 1-2 orders of magnitude by employing NPs on the surface is helpful in the microdroplet analysis and the study of samples in traces [94–131]. The advantage of rapid, simultaneous multi-elemental data acquisition in LIBS with enormous data attracts innovative data analysis techniques from deep learning algorithms. Achieved the classification of different compounds and the quantification of the elements effortlessly using this algorithm [132–145]. Figure 1.3 summarizes the key points of the earlier studies and the kinds of laser sources, samples, and detectors predominantly used in LIBS studies. Figure 1.4 summarizes a few significant achievements and the earlier reported LIBS studies published by our group.

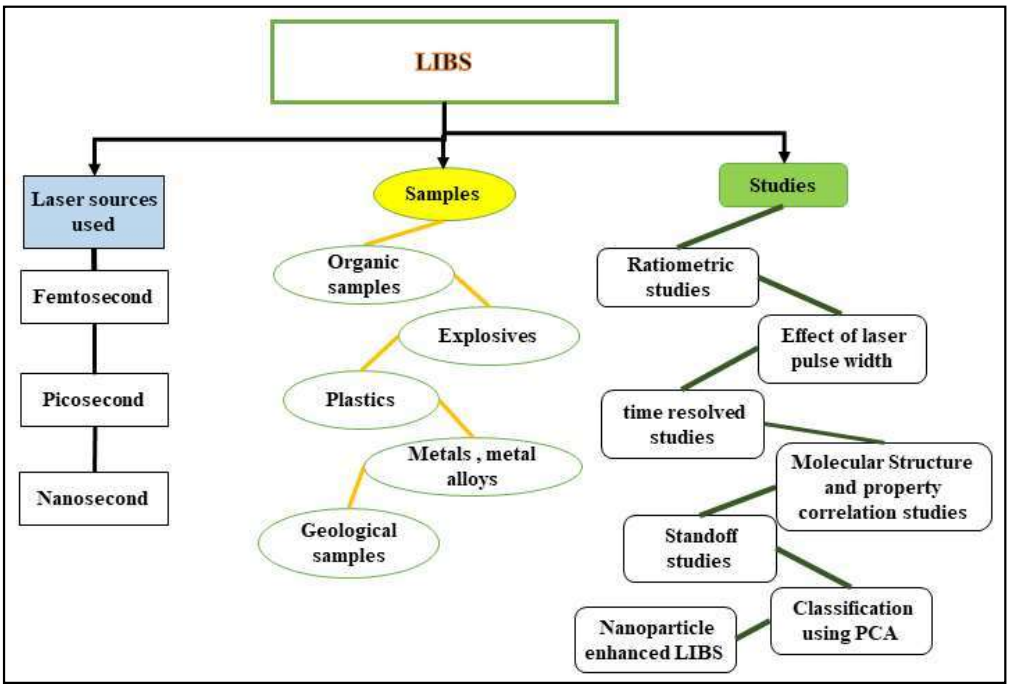

Figure 1.4 Critical points on the contributions to LIBS studies from our group. [146-148].

Earlier studies have been reported extensively on the LIBS of the explosives on RDX, HMX, NTO, AN, AP, and novel nitropyrazoles/pyrazoles [12]. The group advanced in discriminating explosives and organic compounds with ratiometric analysis [149,150]. They detailed time-resolved studies of the organic compounds [151]. They investigated the effect of the pulse width [152] and the surrounding environment of air, nitrogen, and argon on the LIBS of various explosives [153] and the correlation between the LIBS spectra and detonation parameters of the novel explosive molecules and their structure [154-156] in the near field configuration. The group carried out standoff studies in the discrimination of explosives (achieved an enhancement in the LIBS signal by introducing

the nanoparticles), and other standoff studies were revised [157,158], metal alloys, and geological samples. Further, they used principal component analysis (PCA) for better discrimination of the target samples from the low SNR standoff LIBS signal.

In continuation of the earlier achieved milestone in our group, we made advances in analyzing standoff LIBS signals in building machine-learning models to quantify the alloy samples. Significant achievements in handling the sparse powder samples and nanoparticle-enhanced LIBS. We further made valuable developments in standoff instrumentation. Figure 1.5 summarizes the present thesis's considerable contribution to LIBS studies.

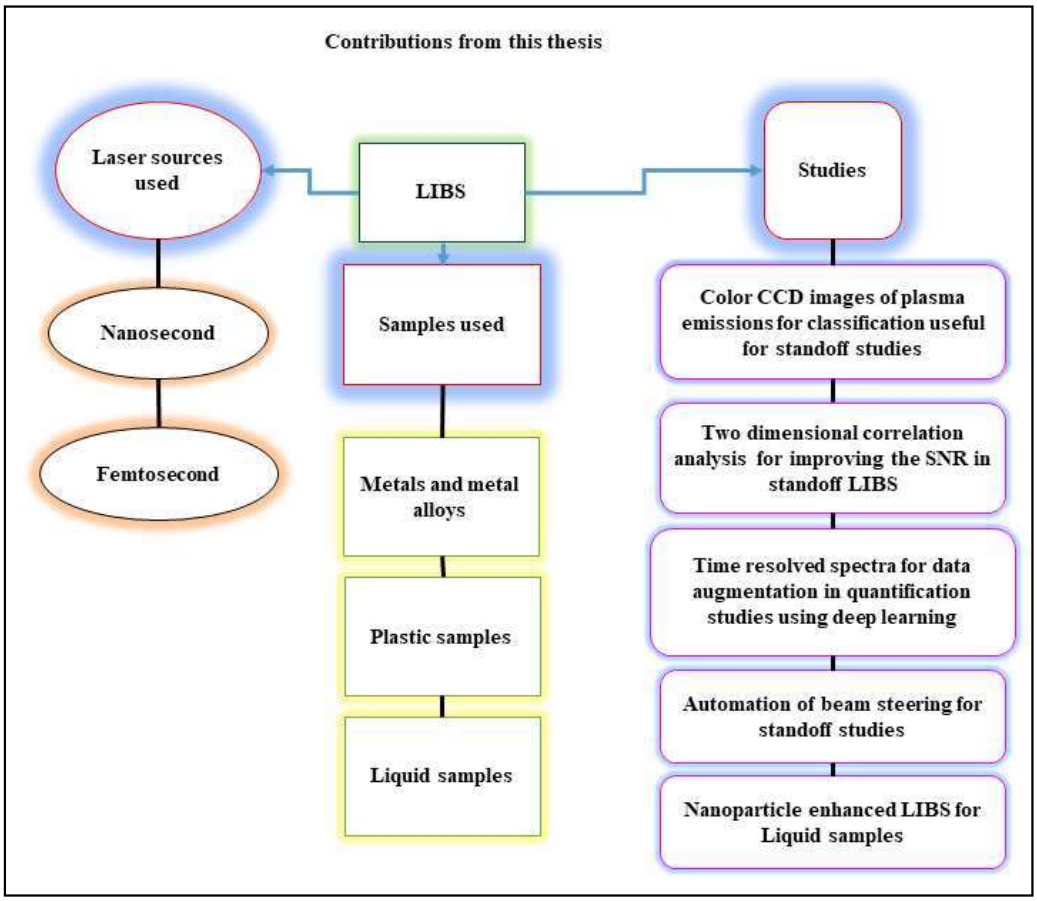

Figure 1.5 Key points on the contributions to the LIBS from the present thesis.

1.5 Difference between femtosecond and nanosecond LIBS

The alteration in the mechanisms because of the difference in the peak powers and the pulse width of the laser sources influences the LIBS studies differently with two different plasma formation pathways involved. Table 1.1 summarizes the main features and the differences between ns and fs LIBS studies. It is evident that fs LIBS or filament LIBS is

advantageous compared to ns LIBS in terms of (a) energy delivery at the desired location, (b) propagation of the pulses over long distances, (c) molecular emissions assisting in superior identification, and classification (d) better LIBS signals in the case of fs LIBS.

Table 1.1 Summary of the differences between ns and fs LIBS.

Sl. No.	Nanosecond LIBS	Femtosecond LIBS
1	Generally, they are cost-efficient and portable	Costly (compared to ns lasers) and bulk/ portable systems are available
2	Loss of beam quality as the laser propagates in the atmosphere over long distances.	Loss of beam quality is negligible in the propagation of long distances (even a few kilometers).
3	Continuum emissions dominate during the initial time delays.	Continuum emissions are negligible at any time delay.
4	The excitation of the atom is not reproducible, resulting in lower precision and sensitivity in LIBS studies.	The excitation of atoms is reproducible, resulting in sensitive and precise LIBS studies.
5	The beam diffraction occurs, and the atmospheric effect is dominant during propagation.	Atmospheric effects are low as the self-focusing phenomenon occurs.
6	Variation in the shot-to-shot pulse energies results in fluctuation in LIBS spectra.	The clamping in filamentation irradiance stabilizes the shot-to-shot variation in filamentation LIBS spectra.
7	The Rayleigh range is limited in the ns case, which requires fine adjustments in the focusing distance.	The filamentation, usually a few cm long, needs fewer fine adjustments during standoff studies.
8	Atomic and ionic emissions are dominant in the nanosecond LIBS spectra.	Molecular emissions are also dominant, along with atomic and ionic emissions in the fs LIBS spectra.
9	Beam expanders and focusing optics are required for standoff studies for required irradiance at longer distances and become impracticable in some cases.	The filamentation provides necessary irradiance even at long distances with no focusing optics.

The difference in the laser matter interaction, time scales involved and the plasma evolution process in ns and fs ablation are depicted in figure 1.6, adopted from the work of Harilal et al. [159].

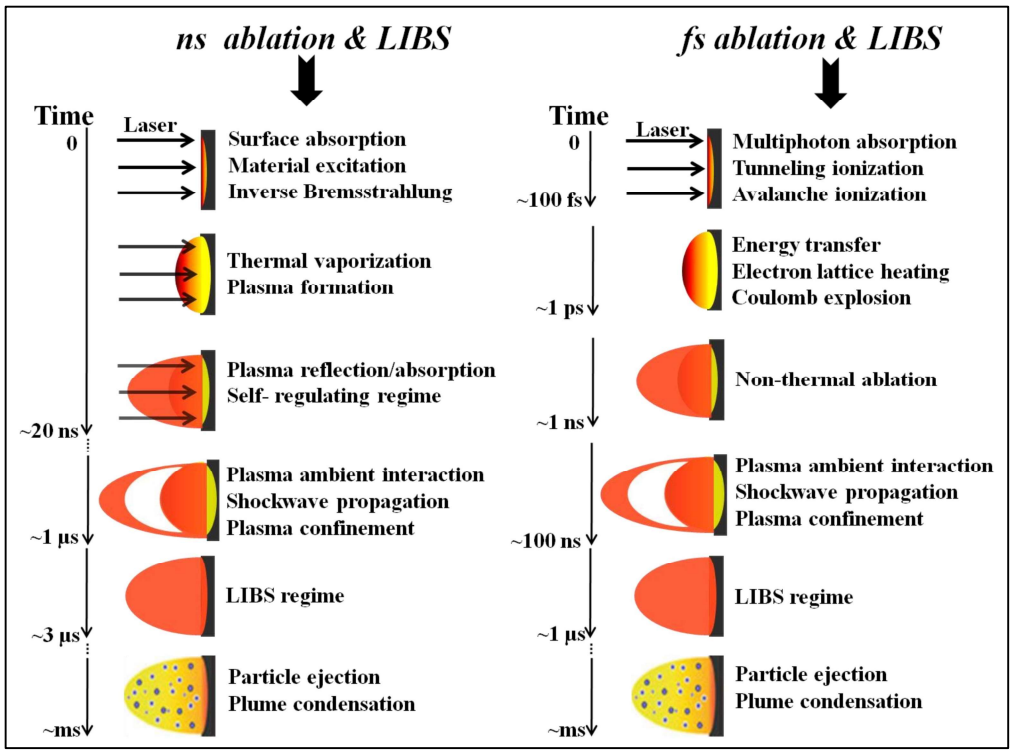

Figure 1.6 Contrasting the evolution processes of the plasma from the ns and fs laser pulse interaction with the matter (figure adopted from Harilal et al. [159]).

1.6 Instruments and analysis used in the present thesis

1.6.1 Color CCD camera

The common color CCD cameras have Bayer's filters with red, blue, and green channels mosaic, with different sensitivities. The camera records the video at 30 frames per second, and each frame has three channels red, blue, and green. The color images of the plasma emissions from different target vary slightly. The low-resolution spectra, like images from different samples, are used to identify different samples when combined with machine learning algorithms.

1.6.2 Two-dimensional correlation analysis

The system's response is recorded when a systematic perturbation is applied, and the corresponding spectra are used for the two-dimensional correlation analysis. The electron temperature, the number density decay with time, and the corresponding time-resolved spectra could be used for the two-dimensional correlation analysis. It has both synchronous (which is symmetrical) and asynchronous (asymmetrical) spectra. It helps understand the cross-correlations between different spectral modes and the autocorrelations of the same modes. It is also useful in improving the signal-to-noise ratio (SNR) and the resolution of

the peaks. The NMR, IR, and Raman spectra recorded with systematic perturbations on the system are analyzed using this analysis [160-163].

1.6.3 Principal component analysis

Principal component analysis (PCA) is an easy and popular technique for dimensionality reduction. It uses the eigen vectors and eigen values of the covariance matrix. The directions are orthogonal to each other, in which the data's maximum variance is considered. The PCA is extensively used in conjunction with the LIBS for the classification of materials in various applications like identification of explosives [38, 60,158], plastics sorting [62], soil analysis [142], alloy discrimination [40,161,162], etc., the usage of the PCA in LIBS were reviewed explained elaborately [163]. PCA reduces the dimensionality of a given dataset, which at first has many variables and features. Dimensionality reduction is achieved by orthogonally transforming a data set into a new coordinate system. Scores are assigned to the new variables. The PCs are the axes along which there is the most data fluctuation.

1.6.4 Support vector machine

Support vector machine (SVM) is a supervised machine learning technique that can be used to solve classification or regression issues. Each sample is represented as a point in the n-dimensional space where n is the total number of features in each sample. The next step is classification, which is done by locating the hyper-plane that effectively separates the two classes. Simply put, support vectors are the coordinates of a single observation. The SVM classifier is a frontier that best distinguishes between the two classes (hyper-plane/line) [132].

1.6.5 Artificial neural networks

A non-parametric supervised learning approach known as an artificial neural network (ANN) is used in predictions and pattern recognition applications like weather forecasting, fraud detection, image identification, etc. An input layer, hidden layers, optimizers, activation function, backpropagation, and loss are all used. It functions similarly to the information processing compared to the biological nervous system. It creates a nonlinear mathematical model to establish significant correlations between the input and output variables. The development and operation of a neural network depend on a vast number of interconnected neurons, which make up the ANN architecture. Weight (the strength of the

interneuron connections) and bias serves as synapse in ANN. Each synapse links the first unit of one layer to the second unit of a different layer. It learns during the learning phase by adjusting the interneuron connection strengths (weights) based on the knowledge. One hidden layer of an ANN is sufficient for approximating any complex nonlinear function, and it is established in the real-time measurements of soil samples on-site [166]. The forward propagation strategy of the algorithm starts with random values for the weights and bias in the first iteration. The output that the ANN has predicted is then matched to the actual input, and the resulting error is used in a back-propagation approach to change the bias and weights for the subsequent repetition. This process repeats until the error converges to a smallest value. ANNs are used in LIBS for the self-absorption correction of the peaks [167] and extensively in quantification studies [168-170].

1.6.6 Beam steering

Arduino Uno microcontroller with the CNC shield and NEMA 17 stepper motors have found application in 3D printing wood carving and wood burning and cutting fields. This, combined with the kinematic mirror mounts coupled to stepper motors, are useful in precise and rapid beam steering. Kinematic mirror mounts are equipped with two differential adjuster screws with a resolution of move 25-micron per revolution resulting in a high precision adjustment in the alignment of the beam. The actual images of the stepper motor, CNC shield, and Arduino Uno are presented in figure 1.7.

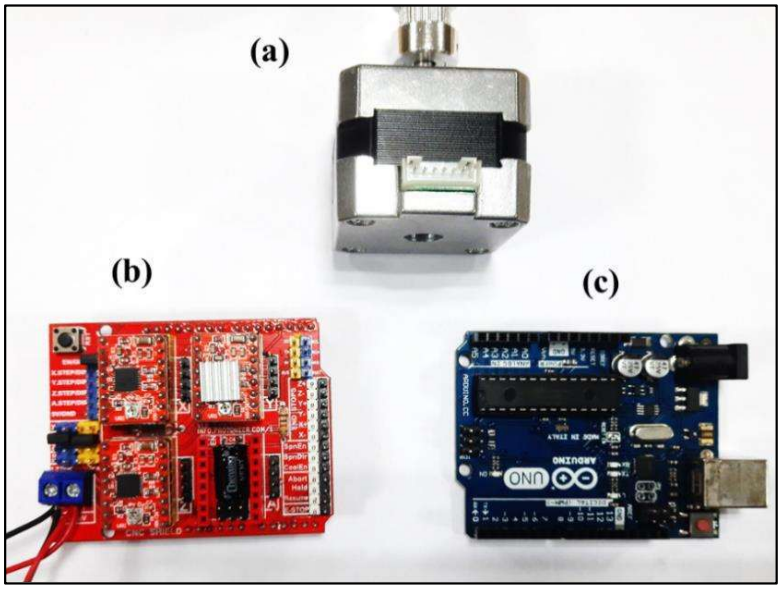

Figure 1.7 (a) stepper motor (b) CNC shield (c) Arduino Uno microcontroller used for the automation of the beam steering (photograph of the components used).

1.6.7 Schmidt-Cassegrain telescope in standoff LIBS

In a standoff LIBS uses additional optics to focus the laser on the sample at a distance and collect the distant plasma emissions. For the collection, the Schmidt-Cassegrain telescope (SCT) is typically employed. The Schmidt-Cassegrain is the combination of a spherical primary mirror, a secondary mirror, and a Schmidt corrector plate, an aspheric lens used to correct the spherical aberration caused by the spherical primary mirror. The rays that enter the optical system travel three times the length of the optical tube. This design is incredibly compact, has large-diameter optics, relatively small tube lengths, and a mobility option. The SCT's schematic is depicted in figure 1.8.

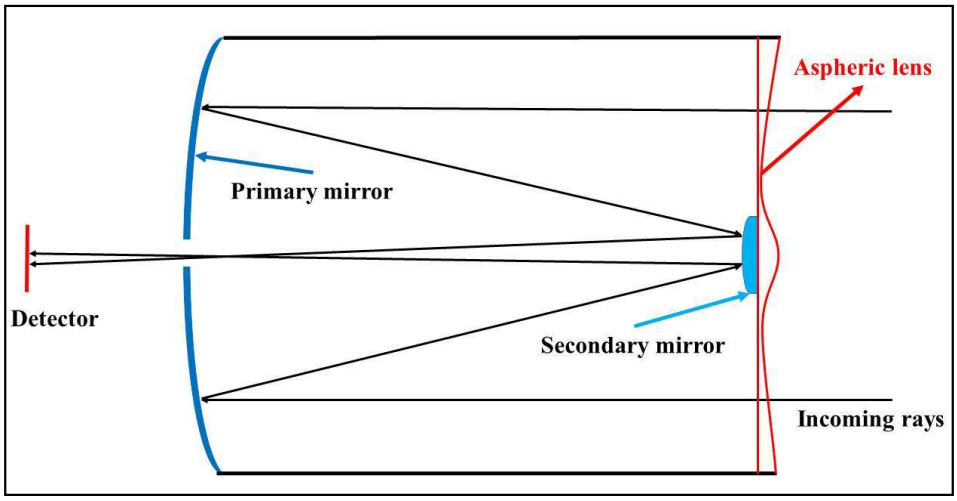

Figure 1.8 Various components of the Schmidt–Cassegrain telescope (SCT) typically used for the collection of standoff LIBS. [https://en.wikipedia.org/wiki/File:Schmidt-Cassegrain-Telescope.png]

1.6.8 Perspective on the mechanism(s) of nanoparticle enhancement LIBS

The threshold power density for breakdown of solid targets (silicon, titanium, copper, iron, teflon, Brass, and steel, as well as bronze) with Ag nanoparticles (NPs) on the surface was observed to be lesser than those without NPs [128]. Using a pulsed laser, Sherbini et al. [126] investigated the differences between bulk and ZnO nanomaterial in the Zn I spectral lines from the optical emissions in LIBS. The Zn I spectral lines depicted a significant improvement, but the H_α line showed signs of deterioration. By observing that the same factor does not enhance all the peaks, it is concluded that the relative atomic density influence the enhancement. Plasma temperature, electron density, and relative ground state population as a function of time were considered in the studies [126]. The improvement of the NELIBS signal was addressed by De Giacomo et al. [107] using surface plasmon

resonance and the Keldysh parameter (g), which distinguished between multiphoton ionization and field emission. The stylus profilometer was used to study the craters. The lack of difference between the craters in LIBS and NELIBS suggests that the ablated mass was not the cause of the enhancement. With this finding, it is concluded that the improvement is due to the additional energy delivered to the ejected mass. These investigations appear to be quite illuminating for comprehending the NELIBS [126]. The EF was described by Werner et al. [110], including a single NP evaporating when heated above its melting temperature, an ejected electron, and NPs exploding and shrinking in size. Quantum chemistry variation methods are used to comprehend the mechanism underlying the enhancement. This model was used to investigate enhancement, which relies on NPs size, concentration, and dispersion, using templates of NPs linear, one-dimensional, and two-dimensional chains [172]. From the time-resolved studies, Giacomo et al. confirmed a temporal delay in the emission of NPs compared to the substrate.

1.7 Thesis organization & chapter-wise details

1.7.1 Introduction

The chapter 1 briefs on various laser-based techniques used to detect hazardous compounds. Discussed the fundamental aspects of the laser-matter interaction and the phenomenon which leads to the plasma and emissions from the recombination of free electrons and ions in the plasma laying path for LIBS. The overview of the laser-induced breakdown spectroscopy and variations in the LIBS technique. On the advances in the LIBS technique and the machine learning algorithms used in the data analysis in the LIBS technique.

1.7.2 Experimental details

The chapter 2 discusses the components of the LIBS experiment.

1. Ti: sapphire amplified femtosecond pulsed laser and Nd: YAG^{3+} based nanosecond pulsed laser sources used to generate microplasma.
2. It uses the translation stages and motion controllers for sample displacement.
3. Optical components were revised, like lenses, optical fibers, and telescopes used for standoff studies. These focus on the laser pulses and collect plasma emissions from the ablated target.
4. The gated and non-gated detection systems, such as spectrographs and other detectors

5. Computers control the detector's gate delay and width and store the spectrum after acquisition.
6. Further, used nanosecond LIBS spectra of Au-Ag alloy with varying compositions to estimate the plasma temperature. We utilized Boltzmann plots for this study. Further discussed is a novel femtosecond experimental configuration in detecting powdered sparse samples.

- **L. M. Narlagiri** and V. R. Soma, "Plasma Temperature Evolution with Varying Compositions in an Alloy Using Laser Induced Breakdown Spectroscopy," in *Frontiers in Optics + Laser Science 2021*, C. Mazzali, T. (T.-C.) Poon, R. Averitt, and R. Kaindl, eds., Technical Digest Series (Optical Society of America, 2021), paper JW7A.29.

1.7.3 Machine learning and deep learning in LIBS

Chapter 3 discussed using machine learning algorithms in LIBS for classification and quantification studies. The usage of the principal component analysis (PCA), support vector machine, and artificial neural network in the analysis of LIBS data are in this chapter. The performance of the simple non-gated spectrometers could be improved using machine learning algorithms in both classification and quantification studies. We discuss a novel experimental method that utilizes the color (from charge-coupled device popularly known as CCD) images of the laser-induced plasma emissions along with the PCA and SVM algorithms in the classification of metals and alloys were detailed. It discusses the use of time-resolved spectra to develop the deep learning model. The model is used to quantify Au and Ag in bimetallic alloys simultaneously.

- **Narlagiri, L. M**., & Rao, S. V. (2020). Identification of metals and alloys using color CCD images of laser-induced breakdown emissions coupled with machine learning. *Applied Physics B*, *126*, 1-8. doi.org:10.1007/s00340-020-07469-6
- **Narlagiri, Lingamurthy**, and Venugopal Rao Soma "Simultaneous quantification of Au and Ag composition from Au–Ag bi-metallic LIBS spectra combined with shallow neural network model for multi-output regression." *Applied Physics B* 127.9 (2021): 1-11. doi:10.1007/s00340-021-07681-y

1.7.4 Two-dimensional correlation analysis in LIBS

In chapter 4, the application of the two-dimensional (2D) correlation analysis to the LIBS data is briefed. The SNR of the standoff LIBS spectra is poor as compared to the nearfield studies, and it reduces with the increasing standoff distances. We demonstrate the improvement in the SNR of the LIBS spectra from the time-resolved spectra of metals like aluminum, copper, and Brass and the spatially resolved standoff LIBS spectra. We used time-resolved spectra of aluminum for autocorrelation. And varying compositions of the Au-Ag spectra for the cross-correlation studies of LIBS peaks, respectively. Discussed this

analysis's advantage in classifying different compositions of Au-Ag alloy and improving the SNR of the standoff LIBS data. Figure 1.9 shows the gated acquisition of the LIBS spectra.

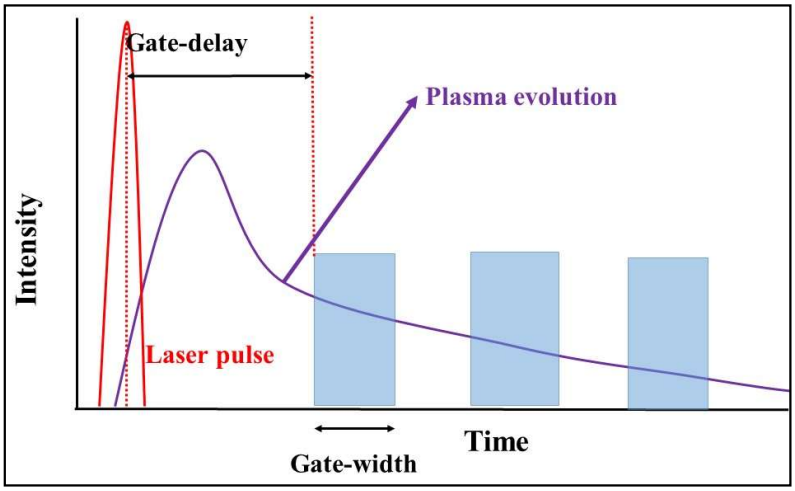

Figure 1.9 Acquisition of the LIBS spectra using a gated spectrometer for time-resolved studies.

- **Narlagiri, Linga Murthy**, and Venugopal Rao Soma. "Improving the signal-to-noise ratio of atomic transitions in LIBS using two-dimensional correlation analysis." *OSA Continuum* 4.9 (2021): 2423-2441. doi:10.1364/OSAC.426995

1.7.5 Nanoparticle enhanced LIBS

Chapter 5 discusses that LIBS signal can be improved using the nanoparticles on the sample and could be particularly useful in detecting traces, demonstrating the improvement in the limit of detection (LOD). In this chapter, we briefly described the enhancement mechanism using nanoparticles in LIBS studies and its importance in detecting samples in traces. We also present the femtosecond NE-LIBS studies of acetonitrile in water. The enhancement in the CN violet band in the LIBS spectra of solution with and without nanoparticles. We demonstrated the enhancement in the aluminum atomic peaks and AlO molecular peaks in the fs-LIBS spectra of an aluminum sheet coated with the nanofibers embedded with the gold nanoparticle.

- **Linga Murthy N.,** Rao S.V. (2021) Nanoparticle Enhanced Laser Induced Breakdown Spectroscopy of Liquids. In: Singh K., Gupta A.K., Khare S., Dixit N., Pant K. (eds) ICOL-2019. Springer Proceedings in Physics, vol 258. Springer, Singapore. https://doi.org/10.1007/978-981-15-9259-1_105
- Kalam, S. A., **Murthy, N. L**., Krishna, J. R., Srikanth, V. V. S. S., & Rao, S. V. (2016, December). Nanoparticle enhanced laser-induced breakdown spectroscopy with femtosecond pulses. In *International Conference on Fibre Optics and Photonics* (pp. Th3A-89).Optical Society of America. doi:10.1364/photonics.2016.th3a.89

- **Linga Murthy Narlagiri,** Venugopal Rao Soma, "Nanoparticle Enhanced LIBS for Sensing Applications," Laser-Induced Breakdown Spectroscopy (LIBS): Concepts, Instrumentation, Data Analysis and Applications, Eds: Dr. Vivek K. Singh, Prof. Y. Deguchi, Dr. Zhenzhen Wang, and Dr. Durgesh K. Tripathi, John Wiley & Sons, In Press, 2022.

1.7.6 Automation in the standoff FIBS studies

Chapter 6 discusses the femtosecond standoff filamentation-induced breakdown spectroscopy (fs-ST-FIBS) of possible interferents in fs ST-LIBS like plastic, soil, and metal samples and their classification studies using PCA. Earlier standoff studies used a translational stage for displacing the sample. To get a new spot for better interaction and good SNR, which is impossible in real-life scenarios, we present a rapid beam steering with a good precision technique for real-life situations. In detail, we discussed the novel instrumentation procedure for the fast and precise beam steering using the readily available and easy-to-handle Arduino and CNC shield and the universal G-code sender (UGS). Further, we discussed the importance of rapid beam steering when working with kHz femtosecond pulses. The instrumentation steered the beam to acquire better FIBS spectra of plastic samples, metals, and metal alloys to classify Au-Ag spectra.

- **Murthy, N. L.,** Kalam, S. A., & Rao, S. V. (2019, December). Stand-off Femtosecond Laser-Induced Breakdown Spectroscopy of Metals, Soil, Plastics and Classification Studies. In 2019 Workshop on Recent Advances in Photonics **(WRAP) (pp. 1-3). IEEE.** doi:10.1109/WRAP47485.2019.9013674
- **L.M. Narlagiri**, C. Byram, S.K. Satani, V.R. Soma, Laser beam steering automation with an Arduino-based C.N.C. shield for standoff femtosecond filament-induced breakdown spectroscopic studies, Appl. Opt. 61 (2022) 4947–4955. doi:10.1364/AO.453824.
- **Linga Murthy Narlagiri,** Venugopal Rao Soma,* "Recent developments in standoff laser-induced breakdown spectroscopy," Laser-Induced Breakdown Spectroscopy (LIBS): Concepts, Instrumentation, Data Analysis and Applications, Eds: Dr. Vivek K. Singh, Prof. Y. Deguchi, Dr. Zhenzhen Wang, and Dr. Durgesh K. Tripathi, John Wiley & Sons, In Press, 2022.

1.7.7 Conclusions and future scope

The chapter 7 summarizes the progress achieved during the Ph.D. The chapter also discusses the improvements required in the LIBS experimental setup. And the analysis of the LIBS data, along with the instrumentation innovations, is necessary for standoff studies in the trace detection of hazardous compounds. We anticipate that the conclusions drawn from the results and difficulties faced in our studies will help detect explosives in the real-world scenarios presented.

References

[1] P.J. Skrodzki, M. Burger, L.A. Finney, F. Poineau, S.M. Balasekaran, J. Nees, K.R. Czerwinski, I. Jovanovic, Standoff Detection of Uranyl Fluoride Using Ultrafast Laser Filamentation-Induced Fluorescence, 2019 Conf. Lasers Electro-Optics, CLEO 2019 - Proc. (2019) 4–5. doi:10.23919/CLEO.2019.8750441.

[2] A.T. Taylor, E.P.C. Lai, Current state of laser-induced fluorescence spectroscopy for designing biochemical sensors, Chemosensors. 9 (2021). doi:10.3390/chemosensors9100275.

[3] M. Kraus, F. Gebert, A. Walter, C. Pargmann, F. Duschek, Online discrimination of chemical substances using standoff laser-induced fluorescence signals, J. Chemom. 34 (2020) 1–10. doi:10.1002/cem.3121.

[4] L. Gupta, R.C. Sharma, A.K. Razdan, A.K. Maini, Laser induced fluorescence of biochemical for UV LIDAR application, J. Fluoresc. 24 (2014) 709–711. doi:10.1007/s10895-013-1341-4.

[5] S. Kumar, A. Parmar, R.C. Sharma, Remote Sensing of Biochemicals in Aerosol Form Using Fluorescence Sensor for Defence and Security, IEEE Sens. J. 19 (2019) 11129–11133. doi:10.1109/JSEN.2019.2933847.

[6] S. Buteau, Spectral Laser Induced Fluorescence for standoff detection and classification of aerosolized biological threats, in: OSA Opt. Sensors Sens. Congr. 2021 (AIS, FTS, HISE, SENSORS, ES), Optical Society of America, 2021: p. SM2C.1. doi:10.1364/SENSORS.2021.SM2C.1.

[7] D. Diaz, D.W. Hahn, Raman spectroscopy for detection of ammonium nitrate as an explosive precursor used in improvised explosive devices, Spectrochim. Acta - Part A Mol. Biomol. Spectrosc. 233 (2020) 118204. doi:10.1016/j.saa.2020.118204.

[8] A. Hakonen, P.O. Andersson, M. Stenbæk Schmidt, T. Rindzevicius, M. Käll, Explosive and chemical threat detection by surface-enhanced Raman scattering: A review, Anal. Chim. Acta. 893 (2015) 1–13. doi:10.1016/j.aca.2015.04.010.

[9] D.S. Moore, R.J. Scharff, Portable Raman explosives detection, Anal. Bioanal. Chem. 393 (2009) 1571–1578. doi:10.1007/s00216-008-2499-5.

[10] R. Gillibert, J.Q. Huang, Y. Zhang, W.L. Fu, M. Lamy de la Chapelle, Explosive detection by Surface Enhanced Raman Scattering, TrAC - Trends Anal. Chem. 105 (2018) 166–172. doi:10.1016/j.trac.2018.03.018.

[11] M. López-López, C. García-Ruiz, Infrared and Raman spectroscopy techniques applied to identification of explosives, TrAC - Trends Anal. Chem. 54 (2014) 36–44. doi:10.1016/j.trac.2013.10.011.

[12] S. Sunku, M.K. Gundawar, A.K. Myakalwar, P.P. Kiran, S.P. Tewari, S.V. Rao, Femtosecond and nanosecond laser induced breakdown spectroscopic studies of NTO, HMX, and RDX, Spectrochim. Acta - Part B At. Spectrosc. 79–80 (2013) 31–38. doi:10.1016/j.sab.2012.11.002.

[13] V. Lazic, A. Palucci, L. De Dominicis, M. Nuvoli, M. Pistilli, I. Menicucci, F. Colao, S. Almaviva, Integrated laser sensor (ILS) for remote surface analysis: Application for detecting explosives in fingerprints, Sensors (Switzerland). 19 (2019). doi:10.3390/s19194269.

[14] J.P. Singh and S.N. Thakur, eds. *Laser-induced breakdown spectroscopy,* Elsevier, 2020.

[15] D.A. Cremers, L.J.Radziemski, Handbook of laser-induced breakdown spectroscopy. John Wiley & Sons; 2013 May 13.

[16] Y. Wang, A. Chen, S. Li, L. Sui, D. Liu, D. Tian, Y. Jiang, M. Jin, Enhancement of laser-induced Fe plasma spectroscopy with dual-wavelength femtosecond double-pulse, J. Anal. At. Spectrom. 31 (2016) 497–505. doi:10.1039/C5JA00420A.

[17] L. Qi, L. Sun, Y. Xin, Z. Cong, Y. Li, H. Yu, Application of stand-off double-pulse laser-induced breakdown spectroscopy in elemental analysis of magnesium alloy, Plasma Sci. Technol. 17 (2015) 676–681. doi:10.1088/1009-0630/17/8/11.

[18] V.I. Babushok, F.C. DeLucia Jr, J.L. Gottfried, C.A. Munson, A.W. Miziolek, Double pulse laser ablation and plasma: Laser induced breakdown spectroscopy signal enhancement, Spectrochim. Acta Part B At. Spectrosc. 61 (2006) 999–1014. Doi:10.1016/j.sab.2006.09.003

[19] A. Elhassan, G. Cristoforetti, S. Legnaioli, LIBS calibration curves and determination of limits of detection (LOD) in single and double pulse configuration for quantitative LIBS analysis of bronzes, Int. Conf. Conserv. Strateg. Sav. Indoor Met. Collect. (2007) 72–77.

[20] F. Poggialini, B. Campanella, S. Legnaioli, S. Pagnotta, V. Palleschi, Investigating double pulse nanoparticle enhanced laser induced breakdown spectroscopy, Spectrochim. Acta - Part B At. Spectrosc. 167 (2020) 105845. doi:10.1016/j.sab.2020.105845.

[21] I.Y. Elnasharty, F.R. Doucet, J.-F.Y. Gravel, P. Bouchard, M. Sabsabi, Double-pulse LIBS combining short and long nanosecond pulses in the microjoule range, J. Anal. At. Spectrom. 29 (2014) 1660–1666. doi:10.1039/C4JA00099D.

[22] J.L. Gottfried, F.C. De Lucia, C.A. Munson, A.W. Miziolek, Double-pulse standoff laser-induced breakdown spectroscopy for versatile hazardous materials detection, Spectrochim. Acta - Part B At. Spectrosc. 62 (2007) 1405–1411. doi:10.1016/j.sab.2007.10.039.

[23] T. Somekawa, M. Otsuka, Y. Maeda, M. Fujita, Signal enhancement in femtosecond laser induced breakdown spectroscopy with a double-pulse configuration composed of two polarizers, Jpn. J. Appl. Phys. 55 (2016) 32–34. doi:10.7567/JJAP.55.058002.

[24] W. Li, X. Li, X. Li, Z. Hao, Y. Lu, X. Zeng, A review of remote laser-induced breakdown spectroscopy, Appl. Spectrosc. Rev. 55 (2020) 1–25. doi:10.1080/05704928.2018.1472102.

[25] F.J. Fortes, J.J. Laserna, The development of fieldable laser-induced breakdown spectrometer: No limits on the horizon, Spectrochim. Acta - Part B At. Spectrosc. 65 (2010) 975–990. doi:10.1016/j.sab.2010.11.009.

[26] M.M. Tamboli, U. V. K., P. Devangad, M.S. K. M., S. C., ST-LIBS for heavy element detection in complex matrices, Fifth Int. Conf. Opt. Photonics Eng. 10449 (2017) 104492T. doi:10.1117/12.2270895.

[27] J. Laserna, P. Lucena, A. Ferrero, A. Doña, R. González, Standoff LIBS sensor technology. fieldable, remotely operated platforms for detection of explosive residues, Predict. Detect. Improv. Explos. Devices. (2007) 11–18.

[28] I. Gaona, P. Lucena, J. Moros, F.J. Fortes, S. Guirado, J. Serrano, J.J. Laserna, Evaluating the use of standoff LIBS in architectural heritage: Surveying the Cathedral of Málaga, J. Anal. At. Spectrom. 28 (2013) 810–820. doi:10.1039/c3ja50069a.

[29] S. Abdul Kalam, S. V. Balaji Manasa Rao, M. Jayananda, S. Venugopal Rao, Standoff femtosecond filament-induced breakdown spectroscopy for classification of geological materials, J. Anal. At. Spectrom. 35 (2020) 3007–3020. doi:10.1039/d0ja00355g.

[30] C.S.C. Yang, F. Jin, S. Trivedi, E. Brown, U. Hömmerich, L. Nemes, A.C. Samuels, In situ chemical analysis of geology samples by a rapid simultaneous ultraviolet/visible/near-infrared (UVN) + longwave-infrared laser induced breakdown spectroscopy detection system at standoff distance, Opt. Express. 27 (2019) 19596. doi:10.1364/oe.27.019596.

[31] M. Wang, Q. Wang, M. Zhu, L. Sun, X. Peng, L. Liu, J. Qu, Applying stand-off LIBS to paleoclimatic research: A case study on geochemical content of carbonate rocks, 2015 Optoelectron. Glob. Conf. OGC 2015. (2015) 2–4. doi:10.1109/OGC.2015.7336854.

[32] W.T. Li, X.Y. Yang, X. Li, S.S. Tang, J.M. Li, R.X. Yi, P. Yang, Z.Q. Hao, L.B. Guo, X.Y. Li, X.Y. Zeng, Y.F. Lu, A portable multi-collector system based on an artificial optical compound eye for stand-off laser-induced breakdown spectroscopy, J. Anal. At. Spectrom. 32 (2017) 1975–1979. doi:10.1039/c7ja00173h.

[33] R.C. Wiens, S.K. Sharma, J. Thompson, A. Misra, P.G. Lucey, Joint analyses by laser-induced breakdown spectroscopy (LIBS) and Raman spectroscopy at stand-off distances, Spectrochim. Acta - Part A Mol. Biomol. Spectrosc. 61 (2005) 2324–2334. doi:10.1016/j.saa.2005.02.031.

[34] J.J. Choi, S.J. Choi, J.J. Yoh, Standoff Detection of Geological Samples of Metal, Rock, and Soil at Low Pressures Using Laser-Induced Breakdown Spectroscopy, Appl. Spectrosc. 70 (2016) 1411–1419. doi:10.1177/0003702816664858.

[35] L.P. Maguire, S. Szilagyi, R.E. Scholten, High performance laser shutter using a hard disk drive voice-coll actuator, Rev. Sci. Instrum. 75 (2004) 3077–3079. doi:10.1063/1.1786331.

[36] L.A. Álvarez-Trujillo, V. Lazic, J. Moros, J. Javier Laserna, Standoff monitoring of aqueous aerosols using nanosecond laser-induced breakdown spectroscopy: droplet size and matrix effects, Appl. Opt. 56 (2017) 3773. doi:10.1364/ao.56.003773.

[37] H. Sattar, H. Ran, W. Ding, M. Imran, M. Amir, H. Ding, An approach of stand-off measuring hardness of tungsten heavy alloys using LIBS, Appl. Phys. B Lasers Opt. 126 (2020) 1–11. doi:10.1007/s00340-019-7355-0.

[38] C. López-Moreno, S. Palanco, J.J. Laserna, F. DeLucia, A.W. Miziolek, J. Rose, R.A. Walters, A.I. Whitehouse, Test of a stand-off laser-induced breakdown spectroscopy sensor for the detection of explosive residues on solid surfaces, J. Anal. At. Spectrom. 21 (2006) 55–60. doi:10.1039/b508055j.

[39] R. Junjuri, A. Prakash Gummadi, M. Kumar Gundawar, Single-shot compact spectrometer based standoff LIBS configuration for explosive detection using artificial neural networks, Optik (Stuttg). 204 (2020). doi:10.1016/j.ijleo.2019.163946.

[40] I. Gaona, J. Moros, J.J. Laserna, New insights into the potential factors affecting the emission spectra variability in standoff LIBS, J. Anal. At. Spectrom. 28 (2013) 1750–1759. doi:10.1039/c3ja50181g.
[41] A.K. Shaik, Ajmathulla, V.R. Soma, Discrimination of bimetallic alloy targets using femtosecond filament-induced breakdown spectroscopy in standoff mode, Opt. Lett. 43 (2018) 3465. doi:10.1364/ol.43.003465.
[42] A. Ferrero, J.J. Laserna, A theoretical study of atmospheric propagation of laser and return light for stand-off laser induced breakdown spectroscopy purposes, Spectrochim. Acta - Part B At. Spectrosc. 63 (2008) 305–311. doi:10.1016/j.sab.2007.11.020.
[43] F.J. Fortes, S. Guirado, A. Metzinger, J.J. Laserna, A study of underwater stand-off laser-induced breakdown spectroscopy for chemical analysis of objects in the deep ocean, J. Anal. At. Spectrom. 30 (2015) 1050–1056. doi:10.1039/C4JA00489B.
[44] V. Sathiesh Kumar, N.J. Vasa, R. Sarathi, Remote surface pollutant measurement by adopting a variable stand-off distance based laser induced spectroscopy technique, J. Phys. D. Appl. Phys. 48 (2015) 435504. doi:10.1088/0022-3727/48/43/435504.
[45] B. Sallé, D.A. Cremers, S. Maurice, R.C. Wiens, P. Fichet, Evaluation of a compact spectrograph for in-situ and stand-off Laser-Induced Breakdown Spectroscopy analyses of geological samples on Mars missions, Spectrochim. Acta - Part B At. Spectrosc. 60 (2005) 805–815. doi:10.1016/j.sab.2005.05.007.
[46] M. Burger, P. Polynkin, I. Jovanovic, Filament-induced breakdown spectroscopy with structured beams, Opt. Express. 28 (2020) 36812. doi:10.1364/oe.412480.
[47] Y. Gong, D. Choi, B.Y. Han, J. Yoo, S.H. Han, Y. Lee, Remote quantitative analysis of cerium through a shielding window by stand-off laser-induced breakdown spectroscopy, J. Nucl. Mater. 453 (2014) 8–15. doi:10.1016/j.jnucmat.2014.06.022.
[48] L.M. Cabalín, T. Delgado, J. Ruiz, D. Mier, J.J. Laserna, Stand-off laser-induced breakdown spectroscopy for steel-grade intermix detection in sequence casting operations. At-line monitoring of temporal evolution versus predicted mathematical model, Spectrochim. Acta - Part B At. Spectrosc. 146 (2018) 93–100. doi:10.1016/j.sab.2018.05.001.
[49] W.T. Li, Y.N. Zhu, X. Li, Z.Q. Hao, L.B. Guo, X.Y. Li, X.Y. Zeng, Y.F. Lu, In situ classification of rocks using stand-off laser-induced breakdown spectroscopy with a compact spectrometer, J. Anal. At. Spectrom. 33 (2018) 461–467. doi:10.1039/c8ja00001h.
[50] G. Vítková, K. Novotný, L. Prokeš, A. Hrdlička, J. Kaiser, J. Novotný, R. Malina, D. Prochazka, Fast identification of biominerals by means of stand-off laser-induced breakdown spectroscopy using linear discriminant analysis and artificial neural networks, Spectrochim. Acta - Part B At. Spectrosc. 73 (2012) 1–6. doi:10.1016/j.sab.2012.05.010.
[51] C.G. Brown, R. Bernath, M. Fisher, M.C. Richardson, M. Sigman, R.A. Walters, A. Miziolek, H. Bereket, L.E. Johnson, Remote femtosecond laser induced breakdown spectroscopy (LIBS) in a standoff detection regime, Enabling Technol. Des. Nonlethal Weapons. 6219 (2006) 62190B. doi:10.1117/12.663821.
[52] S.S. Harilal, J. Yeak, B.E. Brumfield, M.C. Phillips, Consequences of femtosecond laser filament generation conditions in standoff laser induced breakdown spectroscopy, Opt. Express. 24 (2016) 17941. doi:10.1364/oe.24.017941.
[53] C. López-Moreno, S. Palanco, J.J. Laserna, Calibration transfer method for the quantitative analysis of high-temperature materials with stand-off laser-induced breakdown spectroscopy, J. Anal. At. Spectrom. 20 (2005) 1275–1279. doi:10.1039/b508528d.
[54] C. López-Moreno, S. Palanco, J.J. Laserna, Stand-off analysis of moving targets using laser-induced breakdown spectroscopy, J. Anal. At. Spectrom. 22 (2007) 84–87. doi:10.1039/b609705g.
[55] J.L. Gottfried, F.C. De Lucia, C.A. Munson, A.W. Miziolek, Standoff detection of chemical and biological threats using laser-induced breakdown spectroscopy, Appl. Spectrosc. 62 (2008) 353–363. doi:10.1366/000370208784046759.
[56] I. Gaona, J. Serrano, J. Moros, J.J. Laserna, Range-adaptive standoff recognition of explosive fingerprints on solid surfaces using a supervised learning method and laser-induced breakdown spectroscopy, Anal. Chem. 86 (2014) 5045–5052. doi:10.1021/ac500694j.
[57] X.-T. Lu, S.-Y. Zhao, X. Gao, K.-M. Guo, J.-Q. Lin, Effect of the distance between focusing lens and target surface on quantitative analysis of Mn element in aluminum alloys by using filament-induced breakdown spectroscopy, Chinese Phys. B. 29 (2020) 124209.
[58] M.M. Tamboli, V.K. Unnikrishnan, R. Nayak, P. Devangad, K.M. Muhammed Shameem, V.B. Kartha, C. Santhosh, Development of a stand-off laser induced breakdown spectroscopy (ST-LIBS) system for the analysis of complex matrices, J. Instrum. 11 (2016). doi:10.1088/1748-0221/11/08/P08021.

[59] D. Girón, T. Delgado, J. Ruiz, L.M. Cabalín, J.J. Laserna, In-situ monitoring and characterization of airborne solid particles in the hostile environment of a steel industry using stand-off LIBS, Meas. J. Int. Meas. Confed. 115 (2018) 1–10. doi:10.1016/j.measurement.2017.09.046.

[60] A.K. Shaik, N.R. Epuru, H. Syed, C. Byram, V.R. Soma, Femtosecond laser induced breakdown spectroscopy based standoff detection of explosives and discrimination using principal component analysis, Opt. Express. 26 (2018) 8069. doi:10.1364/oe.26.008069.

[61] P.D. Barnett, N. Lamsal, S.M. Angel, Standoff Laser-Induced Breakdown Spectroscopy (LIBS) Using a Miniature Wide Field of View Spatial Heterodyne Spectrometer with Sub-Microsteradian Collection Optics, Appl. Spectrosc. 71 (2017) 583–590. doi:10.1177/0003702816687569.

[62] N.L. Murthy, S.A. Salam, S.V. Rao, Stand-off Femtosecond Laser Induced Breakdown Spectroscopy of Metals, Soil, Plastics and Classification Studies, in: 2019 Work. Recent Adv. Photonics, 2019: pp. 1–3. DOI: 10.1109/WRAP47485.2019.9013674

[63] T. Delgado, J. Ruiz, L.M. Cabalín, J.J. Laserna, Distinction strategies based on discriminant function analysis for particular steel grades at elevated temperature using stand-off LIBS, J. Anal. At. Spectrom. 31 (2016) 2242–2252. doi:10.1039/c6ja00219f.

[64] L.A. Álvarez-Trujillo, A. Ferrero, J. Javier Laserna, Preliminary studies on stand-off laser induced breakdown spectroscopy detection of aerosols, J. Anal. At. Spectrom. 23 (2008) 885–888. doi:10.1039/b716762h.

[65] M. Dell'Aglio, M. López-Claros, J.J. Laserna, S. Longo, A. De Giacomo, Stand-off laser induced breakdown spectroscopy on meteorites: calibration-free approach, Spectrochim. Acta - Part B At. Spectrosc. 147 (2018) 87–92. doi:10.1016/j.sab.2018.05.024.

[66] B. Sallé, J.L. Lacour, E. Vors, P. Fichet, S. Maurice, D.A. Cremers, R.C. Wiens, Laser-induced breakdown spectroscopy for Mars surface analysis: Capabilities at stand-off distances and detection of chlorine and sulfur elements, Spectrochim. Acta - Part B At. Spectrosc. 59 (2004) 1413–1422. doi:10.1016/j.sab.2004.06.006.

[67] M. Burger, P.J. Skrodzki, L.A. Finney, J. Nees, I. Jovanovic, Remote detection of uranium using self-focusing intense femtosecond laser pulses, Remote Sens. 12 (2020) 1–12. doi:10.3390/RS12081281.

[68] L.A. Finney, P.J. Skrodzki, M. Burger, J. Nees, S.S. Harilal, I. Jovanovic, Single-shot, multi-signature remote detection of uranium by filament-induced breakdown spectroscopy, Opt. Lett. 44 (2019) 2783. doi:10.1364/ol.44.002783.

[69] T. Delgado, L. García-Gómez, L.M. Cabalín, J.J. Laserna, Detectability and discrimination of biomarker organic precursors in a low pressure CO2atmosphere by LIBS, J. Anal. At. Spectrom. 35 (2020) 1947–1955. doi:10.1039/d0ja00167h.

[70] I. Gaona, J. Serrano, J. Moros, J.J. Laserna, Evaluation of laser-induced breakdown spectroscopy analysis potential for addressing radiological threats from a distance, Spectrochim. Acta - Part B At. Spectrosc. 96 (2014) 12–20. doi:10.1016/j.sab.2014.04.003.

[71] X.-T. Lu, S.-Y. Zhao, X. Gao, K.-M. Guo, J.-Q. Lin, Effect of the distance between focusing lens and target surface on quantitative analysis of Mn element in aluminum alloys by using filament-induced breakdown spectroscopy, Chinese Phys. B. 29 (2020) 124209. doi:10.1088/1674-1056/abb3ef.

[72] K. Lim, Laser Filamentation - Beyond Self-focusing and Plasma Defocusing, (2014) 2004–2019. Theses and Dissertations, 2004-2019. 4856. https://stars.library.ucf.edu/etd/4856

[73] S.S. Harilal, J. Yeak, M.C. Phillips, Plasma temperature clamping in filamentation laser induced breakdown spectroscopy, Opt. Express. 23 (2015) 27113. doi:10.1364/oe.23.027113.

[74] J. Kasparian, J.-P. Wolf, Physics and applications of atmospheric nonlinear optics and filamentation, Opt. Express. 16 (2008) 466. doi:10.1364/oe.16.000466.

[75] H.L. Xu, S.L. Chin, Femtosecond laser filamentation for atmospheric sensing, Sensors. 11 (2011) 32–53. doi:10.3390/s110100032.

[76] S. Zhao, M.S. Afgan, H. Zhu, X. Gao, Femtosecond laser filamentation-induced breakdown spectroscopy combined with chemometrics methods for soil heavy metal analysis, Optik (Stuttg). 251 (2022) 168444. doi:10.1016/j.ijleo.2021.168444.

[77] K. Stelmaszczyk, P. Rohwetter, G. Méjean, J. Yu, E. Salmon, J. Kasparian, R. Ackermann, J.P. Wolf, L. Wöste, Long-distance remote laser-induced breakdown spectroscopy using filamentation in air, Appl. Phys. Lett. 85 (2004) 3977–3979. doi:10.1063/1.1812843.

[78] S.L. Chin, W. Liu, F. Théberge, Q. Luo, S.A. Hosseini, V.P. Kandidov, O.G. Kosareva, N. Aközbek, A. Becker, H. Schroeder, Some fundamental concepts of femtosecond laser filamentation, Springer Ser. Chem. Phys. 89 (2008) 243–264. doi:10.1007/978-3-540-73794-0_12.

[79] H.L. Xu, W. Liu, S.L. Chin, Remote time-resolved filament-induced breakdown spectroscopy of biological materials, Opt. Lett. 31 (2006) 1540. doi:10.1364/ol.31.001540.

[80] P.J. Skrodzki, M. Burger, I. Jovanovic, Transition of Femtosecond-Filament-Solid Interactions from Single to Multiple Filament Regime, Sci. Rep. 7 (2017) 1–8. doi:10.1038/s41598-017-13188-4.
[81] M.S. K M, M. P, R. Das, P. Bhardwaj, V. Nimma, S. Soumyashree, R.K. Kushawaha, Molecular emission dynamics from a femtosecond filament induced plasma plume, J. Opt. (2022). doi:10.1088/2040-8986/ac528a.
[82] H.L. Xu, J. Bernhardt, P. Mathieu, G. Roy, S.L. Chin, Understanding the advantage of remote femtosecond laser-induced breakdown spectroscopy of metallic targets, J. Appl. Phys. 101 (2007). doi:10.1063/1.2437580.
[83] W. Liu, S. Petit, A. Becker, N. Aközbek, C.M. Bowden, S.L. Chin, Intensity clamping of a femtosecond laser pulse in condensed matter, Opt. Commun. 202 (2002) 189–197. doi:10.1016/S0030-4018(01)01698-4.
[84] V.P. Kandidov, O.G. Kosareva, I.S. Golubtsov, W. Liu, A. Becker, N. Akozbek, C.M. Bowden, S.L. Chin, Self-transformation of a powerful femtosecond laser pulse into a white-light laser pulse in bulk optical media (or supercontinuum generation), Appl. Phys. B Lasers Opt. 77 (2003) 149–165. doi:10.1007/s00340-003-1214-7.
[85] S. Tzortzakis, D. Anglos, D. Gray, Ultraviolet laser filaments for remote laser-induced breakdown spectroscopy (LIBS) analysis: applications in cultural heritage monitoring, Opt. Lett. 31 (2006) 1139. doi:10.1364/ol.31.001139.
[86] H. Li, W. Chu, H. Zang, H. Xu, Y. Cheng, S.L. Chin, Critical power and clamping intensity inside a filament in a flame, Opt. Express. 24 (2016) 3424. doi:10.1364/oe.24.003424.
[87] S.L. Chin, S.A. Hosseini, W. Liu, Q. Luo, F. Théberge, N. Aközbek, A. Becker, V.P. Kandidov, O.G. Kosareva, H. Schroeder, The propagation of powerful femtosecond laser pulses in optical media: Physics, applications, and new challenges, Can. J. Phys. 83 (2005) 863–905. doi:10.1139/p05-048.
[88] R. Junjuri, S.A. Nalam, E. Manikanta, S.S. Harsha, P.P. Kiran, M.K. Gundawar, Spatio-temporal characterization of ablative Cu plasma produced by femtosecond filaments, Opt. Express. 29 (2021) 10395. doi:10.1364/oe.417842.
[89] H. Zang, D. Yao, S. Wang, Y. Fu, W. Zhang, S. Chen, H. Li, H. Xu, In situ determination of the equivalence ratio in a methane/air flow field by femtosecond filament excitation, Laser Phys. 30 (2020). doi:10.1088/1555-6611/ab6aa6.
[90] I. Dicaire, V. Jukna, C. Praz, C. Milián, L. Summerer, A. Couairon, Spaceborne laser filamentation for atmospheric remote sensing, Laser Photonics Rev. 10 (2016) 481–493. doi:10.1002/lpor.201500283.
[91] M. Weidman, Laser Filamentation Interaction with Materials for Spectroscopic Applications, (2012) 2004–2019. Electronic Theses and Dissertations. 2385. https://stars.library.ucf.edu/etd/2385
[92] H. Xie, G. Li, W. Chu, B. Zeng, J. Yao, C. Jing, Z. Li, Y. Cheng, Backward nitrogen lasing actions induced by femtosecond laser filamentation: Influence of duration of gain, New J. Phys. 17 (2015). doi:10.1088/1367-2630/17/7/073009.
[93] S.L. Chin, T.-J. Wang, C. Marceau, J. Wu, J.S. Liu, O. Kosareva, N. Panov, Y.P. Chen, J.-F. Daigle, S. Yuan, A. Azarm, W.W. Liu, T. Seideman, H.P. Zeng, M. Richardson, R. Li, Z.Z. Xu, Advances in intense femtosecond laser filamentation in air, Laser Phys. 22 (2012) 1–53. doi:10.1134/s1054660x11190054.
[94] A. De Giacomo, R. Gaudiuso, C. Koral, M. Dell'Aglio, O. De Pascale, Nanoparticle Enhanced Laser Induced Breakdown Spectroscopy: Effect of nanoparticles deposited on sample surface on laser ablation and plasma emission, Spectrochim. Acta Part B At. Spectrosc. 98 (2014) 19–27. doi:10.1016/j.sab.2014.05.010.
[95] Z.A. Abdel-Salam, V. Palleschi, M.A. Harith, Study of the feeding effect on recent and ancient bovine bones by nanoparticle-enhanced laser-induced breakdown spectroscopy and chemometrics, J. Adv. Res. 17 (2019) 65–72. doi:10.1016/j.jare.2018.12.009.
[96] X. Zhao, C. Zhao, X. Du, D. Dong, Detecting and mapping harmful chemicals in fruit and vegetables using nanoparticle-enhanced laser-induced breakdown spectroscopy, Sci. Rep. 9 (2019) 906 .doi:10.1038/s41598-018-37556-w
[97] D.J. Palásti, P. Albrycht Paweł and Janovszky, K. Paszkowska, Z. Geretovszky, G. Galbács, Nanoparticle enhanced laser induced breakdown spectroscopy of liquid samples by using modified surface-enhanced Raman scattering substrates, Spectrochim. Acta Part B At. Spectrosc. 166 (2020) 105793. Doi:10.1016/j.sab.2020.105793
[98] V. V. Kiris, N. V. Tarasenko, E.A. Nevar, M.I. Nedelko, E.A. Ershov-Pavlov, M. Kuzmanović, J. Savović, Enhancement of Analytical Signal of Laser Induced Breakdown Spectroscopy by

Deposition of Gold Nanoparticles on Analyzed Sample, J. Appl. Spectrosc. 86 (2019) 900–907. doi:10.1007/s10812-019-00913-2.

[99] M. Dell'Aglio, Z. Salajková, A. Mallardi, R. Mezzenga, L. van't Hag, N. Cioffi, G. Palazzo, A. De Giacomo, Application of gold nanoparticles embedded in the amyloids fibrils as enhancers in the laser induced breakdown spectroscopy for the metal quantification in microdroplets, Spectrochim. Acta - Part B At. Spectrosc. 155 (2019) 115-122. doi:10.1016/j.sab.2019.04.002.

[100] F. Poggialini, B. Campanella, S. Giannarelli, E. Grifoni, S. Legnaioli, G. Lorenzetti, S. Pagnotta, A. Safi, V. Palleschi, Green-synthetized silver nanoparticles for Nanoparticle-Enhanced Laser Induced Breakdown Spectroscopy (NELIBS) using a mobile instrument, Spectrochim. Acta Part B At. Spectrosc. 141 (2018) 53–58. doi:10.1016/j.sab.2018.01.005.

[101] L. Ren, X. Hao, H. Tang, Y. Sun, Spectral characteristics of laser-induced plasma under the combination of Au-nanoparticles and cavity confinement, Results Phys. 15 (2019) 102798. doi:10.1016/j.rinp.2019.102798.

[102] Z. Abdel-Salam, S.M.I. Alexeree, M.A. Harith, Utilizing biosynthesized nano-enhanced laser-induced breakdown spectroscopy for proteins estimation in canned tuna, Spectrochim. Acta - Part B At. Spectrosc. 149 (2018) 112–117. doi:10.1016/j.sab.2018.07.029.

[103] M. Abdelhamid, Y.A. Attia, M. Abdel-Harith, The significance of nano-shapes in nanoparticle-enhanced laser-induced breakdown spectroscopy, J. Anal. At. Spectrom. 35 (2020) 2982–2989. doi:10.1039/d0ja00329h.

[104] X. Liu, Q. Lin, Y. Tian, W. Liao, T. Yang, C. Qian, T. Zhang, Y. Duan, Metal-chelate induced nanoparticle aggregation enhanced laser-induced breakdown spectroscopy for ultra-sensitive detection of trace metal ions in liquid samples, J. Anal. At. Spectrom. 35 (2020) 188–197. doi:10.1039/c9ja00324j.

[105] X. Wen, Q. Lin, G. Niu, Q. Shi, Y. Duan, Emission enhancement of laser-induced breakdown spectroscopy for aqueous sample analysis based on Au nanoparticles and solid-phase substrate, Appl. Opt. 55 (2016) 6706-6712. doi:10.1364/ao.55.006706.

[106] A.M. El Sherbini, A.A. Galil, S.H. Allam, T.M. El Sherbini, Nanomaterials induced plasma spectroscopy, in: J. Phys. Conf. Ser., 2014: p. 12031.

[107] A. De Giacomo, R. Alrifai, V. Gardette, Z. Salajková, M. Dell'Aglio, Nanoparticle enhanced laser ablation and consequent effects on laser induced plasma optical emission, Spectrochim. Acta - Part B At. Spectrosc. 166 (2020) 105794. doi:10.1016/j.sab.2020.105794.

[108] A. De Giacomo, C. Koral, G. Valenza, R. Gaudiuso, M. Dellaglio, Nanoparticle Enhanced Laser-Induced Breakdown Spectroscopy for Microdrop Analysis at subppm Level, Anal. Chem. 88 (2016) 5251–5257. doi:10.1021/acs.analchem.6b00324.

[109] Y. Gimenez, B. Busser, F. Trichard, A. Kulesza, J.M. Laurent, V. Zaun, F. Lux, J.M. Benoit, G. Panczer, P. Dugourd, O. Tillement, F. Pelascini, L. Sancey, V. Motto-Ros, 3D Imaging of Nanoparticle Distribution in Biological Tissue by Laser-Induced Breakdown Spectroscopy, Sci. Rep. 6 (2016) 29936. doi:10.1038/srep29936.

[110] D. Werner, S. Hashimoto, Improved working model for interpreting the excitation wavelength- and fluence-dependent response in pulsed laser-induced size reduction of aqueous gold nanoparticles, J. Phys. Chem. C. 115 (2011) 5063–5072. doi:10.1021/jp109255g.

[111] H. Tang, X. Hao, X. Hu, Spectral characteristics of laser-induced plasma by combining Au-nanoparticles and magnetic field confinement on Cu, Optik (Stuttg). 171 (2018) 625–631. doi:10.1016/j.ijleo.2018.05.114.

[112] Z. Salajková, V. Gardette, J. Kaiser, M. Dell'Aglio, A. De Giacomo, Effect of spherical gold nanoparticles size on nanoparticle enhanced Laser Induced Breakdown Spectroscopy, Spectrochim. Acta Part B At. Spectrosc. 179 (2021) 106105. doi:10.1016/j.sab.2021.106105.

[113] C. Koral, A. De Giacomo, X. Mao, V. Zorba, R.E. Russo, Nanoparticle enhanced laser induced breakdown spectroscopy for improving the detection of molecular bands, Spectrochim. Acta Part B At. Spectrosc. 125 (2016) 11–17. Doi:10.1016/j.sab.2016.09.006

[114] N.L. Murthy, S.V. Rao, N. Linga Murthy and Soma Venugopal Rao, Nanoparticle Enhanced Laser Induced Breakdown Spectroscopy of Liquids, In: Singh, K., Gupta, A.K., Khare, S., Dixit, N., Pant, K. (eds) ICOL-2019. Springer Proceedings in Physics, vol 258. Springer, Singapore. https://doi.org/10.1007/978-981-15-9259-1_105

[115] A.A. Khedr, M.A. Sliem, M. Abdel-Harith, Gold Nanoparticle-Enhanced Laser-Induced Breakdown Spectroscopy and Three-Dimensional Contour Imaging of an Aluminum Alloy, Appl. Spectrosc. 75 (2021) 565-573. doi:10.1364/AS.75.000565.

[116] J. Liu, Z. Hou, T. Li, Y. Fu, Z. Wang, A comparative study of nanoparticle-enhanced laser-induced breakdown spectroscopy, J. Anal. At. Spectrom. 35 (2020) 2274–2281. doi:10.1039/d0ja00257g.

[117] F. Yang, L. Jiang, S. Wang, Z. Cao, L. Liu, M. Wang, Y. Lu, Emission enhancement of femtosecond laser-induced breakdown spectroscopy by combining nanoparticle and dual-pulse on crystal SiO2, Opt. Laser Technol. 93 (2017) 194-200. doi:10.1016/j.optlastec.2017.03.016.

[118] R.H. El-Saeid, Z. Abdel-Salam, S. Pagnotta, V. Palleschi, M.A. Harith, Classification of sedimentary and igneous rocks by laser induced breakdown spectroscopy and nanoparticle-enhanced laser induced breakdown spectroscopy combined with principal component analysis and graph theory, Spectrochim. Acta - Part B At. Spectrosc. 158 (2019) 105622. doi:10.1016/j.sab.2019.05.011.

[119] A.M. El Sherbini, C.G. Parigger, Wavelength dependency and threshold measurements for nanoparticle-enhanced laser-induced breakdown spectroscopy, Spectrochim. Acta - Part B At. Spectrosc. 116 (2016) 8-15. doi:10.1016/j.sab.2015.11.006.

[120] V. Motto-Ros, L. Sancey, X.C. Wang, Q.L. Ma, F. Lux, X.S. Bai, G. Panczer, O. Tillement, J. Yu, Mapping nanoparticles injected into a biological tissue using laser-induced breakdown spectroscopy, Spectrochim. Acta - Part B At. Spectrosc. 87 (2013) 168–174. doi:10.1016/j.sab.2013.05.020.

[121] L. Sládková, D. Prochazka, P. Pořízka, P. Škarková, M. Remešová, A. Hrdlička, K. Novotný, L. Čelko, J. Kaiser, Improvement of the Laser-Induced Breakdown Spectroscopy method sensitivity by the usage of combination of Ag-nanoparticles and vacuum conditions, Spectrochim. Acta - Part B At. Spectrosc. 127 (2017) 48-55. doi:10.1016/j.sab.2016.11.005.

[122] Z. Farooq, R. Ali, A. ul Ahmad, M. Yaseen, M.H.R. Mahmood, M. Fahad, M.N. Hussain, I. Rehan, M.Z. Khan, Ramiza, M.U. Farooq, M.A. Qayyum, M. Shafique, Electron number density conservation model combined with a self-absorption correction methodology for analysis of nanostructure plasma using laser-induced breakdown spectroscopy, Appl. Opt. 59 (2020) 2559. doi:10.1364/ao.379641.

[123] S. Niu, L. Zheng, A. Qayyum Khan, H. Zeng, Laser-Induced Breakdown Spectroscopic (LIBS) Analysis of Trace Heavy Metals Enriched by Al 2 O 3 Nanoparticles, Appl. Spectrosc. 73 (2019) 380–386. doi:10.1177/0003702819829509.

[124] V. Motto-Ros, L. Sancey, Q.L. Ma, F. Lux, X.S. Bai, X.C. Wang, J. Yu, G. Panczer, O. Tillement, Mapping of native inorganic elements and injected nanoparticles in a biological organ with laser-induced plasma, Appl. Phys. Lett. 101 (2012) 223702. doi:10.1063/1.4768777.

[125] D. Dong, L. Jiao, X. Du, C. Zhao, Ultrasensitive nanoparticle enhanced laser-induced breakdown spectroscopy using a super-hydrophobic substrate coupled with magnetic confinement, Chem. Commun. 53 (2017) 4546–4549. doi:10.1039/c6cc09695f.

[126] A.M. El Sherbini, A.-N.M. Aboulfotouh, F.F. Rashid, S.H. Allam, A. El Dakrouri, T.M. El Sherbini, Observed Enhancement in LIBS Signals from Nano vs. Bulk ZnO Targets: Comparative Study of Plasma Parameters, World J. Nano Sci. Eng. 02 (2012) 181–188. doi:10.4236/wjnse.2012.24024.

[127] C. Koral, M. Dell'Aglio, R. Gaudiuso, R. Alrifai, M. Torelli, A. De Giacomo, Nanoparticle-Enhanced Laser Induced Breakdown Spectroscopy for the noninvasive analysis of transparent samples and gemstones, Talanta. 182 (2018) 253–258. doi:10.1016/j.talanta.2018.02.001.

[128] A. De Giacomo, R. Gaudiuso, C. Koral, M. Dell'Aglio, O. De Pascale, M. Dell'Aglio, O. De Pascale, Nanoparticle-enhanced laser-induced breakdown spectroscopy of metallic samples, Anal. Chem. 85 (2013) 10180–10187. doi:10.1021/ac4016165.

[129] M. Wang, L. Jiang, S. Wang, Q. Guo, F. Tian, Z. Chu, J. Zhang, X. Li, Y. Lu, Multiscale Visualization of Colloidal Particle Lens Array Mediated Plasma Dynamics for Dielectric Nanoparticle Enhanced Femtosecond Laser-Induced Breakdown Spectroscopy, Anal. Chem. 91 (2019) 9952–9961. Doi:10.1021/acs.analchem.9b01686

[130] M.S.S. Bharathi, C. Byram, D. Banerjee, D. Sarma, B. Barkakaty, V.R. Soma, Gold nanoparticle nanofibres as SERS substrate for detection of methylene blue and a chemical warfare simulant (methyl salicylate), Bull. Mater. Sci. 103 (2021) 44. doi:10.1007/s12034-021-02402-9.

[131] X. Fu, G. Li, D. Dong, Improving the Detection Sensitivity for Laser-Induced Breakdown Spectroscopy: A Review, Front. Phys. 8 (2020) 1–11. doi:10.3389/fphy.2020.00068.

[132] L.M. Narla, S.V. Rao, Identification of metals and alloys using color CCD images of laser-induced breakdown emissions coupled with machine learning, Appl. Phys. B Lasers Opt. 126 (2020) 1–8. doi:10.1007/s00340-020-07469-6.

[133] P. Pořízka, A. Demidov, J. Kaiser, J. Keivanian, I. Gornushkin, U. Panne, J. Riedel, Laser-induced breakdown spectroscopy for in situ qualitative and quantitative analysis of mineral ores, Spectrochim. Acta - Part B At. Spectrosc. 101 (2014) 155–163. doi:10.1016/j.sab.2014.08.027.

[134] C.L. Goueguel, First-Order Multivariate Calibration in Laser-induced Breakdown Spectroscopy Laser-induced Breakdown Spectroscopy, (2019) 1–11. https://towardsdatascience.com/first-order-multivariate-calibration-in-laser-induced-breakdown-spectroscopy-ca5616dd5b38.

[135] M.M. Tripathi, K.E. Eseller, F.Y. Yueh, J.P. Singh, Multivariate calibration of spectra obtained by Laser Induced Breakdown Spectroscopy of plutonium oxide surrogate residues, Spectrochim. Acta - Part B At. Spectrosc. 64 (2009) 1212–1218. doi:10.1016/j.sab.2009.09.003.

[136] P. Devangad, V.K. Unnikrishnan, M.M. Tamboli, K.M.M. Shameem, R. Nayak, K.S. Choudhari, C. Santhosh, Quantification of Mn in glass matrices using laser induced breakdown spectroscopy (LIBS) combined with chemometric approaches, Anal. Methods. 8 (2016) 7177–7184. doi:10.1039/c6ay01930g.

[137] Q. Wang, G. Teng, C. Li, Y. Zhao, Z. Peng, Identification and classification of explosives using semi-supervised learning and laser-induced breakdown spectroscopy, J. Hazard. Mater. 369 (2019) 423–429. doi:10.1016/j.jhazmat.2019.02.015.

[138] V. Motto-Ros, A.S. Koujelev, G.R. Osinski, A.E. Dudelzak, Quantitative multi-elemental laser-induced breakdown spectroscopy using artificial neural networks, J. Eur. Opt. Soc. Rapid Publ. 3 (2008) 08011. doi:10.2971/jeos.2008.08011.

[139] Z. Yue, C. Sun, F. Chen, Y. Zhang, W. Xu, S. Shabbir, L. Zou, W. Lu, W. Wang, Z. Xie, L. Zhou, Y. Lu, J. Yu, Machine learning-based LIBS spectrum analysis of human blood plasma allows ovarian cancer diagnosis, Biomed. Opt. Express. 12 (2021) 2559. doi:10.1364/boe.421961.

[140] J.B. Sirven, B. Bousquet, L. Canioni, L. Sarger, Laser-induced breakdown spectroscopy of composite samples: Comparison of advanced chemometrics methods, Anal. Chem. 78 (2006) 1462–1469. doi:10.1021/ac051721p.

[141] K.M.M. Shameem, K.S. Choudhari, A. Bankapur, S.D. Kulkarni, V.K. Unnikrishnan, S.D. George, V.B. Kartha, C. Santhosh, A hybrid LIBS–Raman system combined with chemometrics: an efficient tool for plastic identification and sorting, Anal. Bioanal. Chem. 409 (2017) 3299–3308. doi:10.1007/s00216-017-0268-z.

[142] J. Vrábel, E. Képeš, L. Duponchel, V. Motto-Ros, C. Fabre, S. Connemann, F. Schreckenberg, P. Prasse, D. Riebe, R. Junjuri, M.K. Gundawar, X. Tan, P. Pořízka, J. Kaiser, Classification of challenging Laser-Induced Breakdown Spectroscopy soil sample data - EMSLIBS contest, Spectrochim. Acta - Part B At. Spectrosc. 169 (2020) 105872. doi:10.1016/j.sab.2020.105872.

[143] H. Fu, J. Jia, H. Wang, Z. Ni, F. Dong, Calibration Methods of Laser-Induced Breakdown Spectroscopy, Calibration Valid. Anal. Methods - A Sampl. Curr. Approaches. (2018). doi:10.5772/intechopen.72888.

[144] F.C. De Lucia, J.L. Gottfried, C.A. Munson, A.W. Miziolek, Multlvariate analysis of standoff laser-induced breakdown spectroscopy spectra for classification of explosive-containing residues, Appl. Opt. 47 (2008) G112-G121. doi:10.1364/AO.47.00G112.

[145] K.-Q. Yu, Y.-R. Zhao, F. Liu, Y. He, Laser-induced breakdown spectroscopy coupled with multivariate chemometrics for variety discrimination of soil, Sci. Rep. 6 (2016) 27574. Doi:10.1038/srep27574

[146] Sunku Sreedhar, "Femtosecond and Nanosecond Laser Induced Breakdown Spectroscopy Studies of Energetic Materials," Ph.D. Thesis, University of Hyderabad, 2015. http://www.acrhem.org/venu_publication.html

[147] E. Nageswara Rao, "Femtosecond and Nanosecond Laser Induced Breakdown Spectroscopic and Raman Studies of Nitroazoles," Ph.D. Thesis, University of Hyderabad, 2016. http://www.acrhem.org/venu_publication.html

[148] Abdul Kalam, "Femtosecond LIBS Studies of Energetic Molecules in the Near and Standoff Regimes," Ph.D. Thesis, University of Hyderabad, 2019. http://hdl.handle.net/10603/315645

[149] S. Sreedhar, M.K. Gundawar, S.V. Rao, Laser induced breakdown spectroscopy for classification of high energy materials using elemental intensity ratios, Def. Sci. J. 64 (2014) 332–338. doi:10.14429/dsj.64.4741.

[150] S. Sreedhar, S.V. Rao, P.P. Kiran, S.P. Tewari, G.M. Kumar, Stoichiometric analysis of ammonium nitrate and ammonium perchlorate with nanosecond laser induced breakdown spectroscopy, Chem. Biol. Radiol. Nucl. Explos. Sens. XI. 7665 (2010) 76650J. doi:10.1117/12.850014.

[151] E. Nageswara Rao, S. Sunku, S.P. Tewari, G. Manoj Kumar, S. Venugopal Rao, Investigation of molecular and elemental species dynamics in NTO, TNT, and ANTA using femtosecond LIBS technique, Chem. Biol. Radiol. Nucl. Explos. Sens. XIV. 8710 (2013) 871012. doi:10.1117/12.2015685.

[152] S. Sreedhar, M.A. Kumar, G.M. Kumar, P.P. Kiran, S.P. Tewari, S.V. Rao, Laser-induced breakdown spectroscopy of RDX and HMX with nanosecond, picosecond, and femtosecond pulses, Chem. Biol. Radiol. Nucl. Explos. Sens. XI. 7665 (2010) 76650T. doi:10.1117/12.850007.

[153] S. Sreedhar, E. Nageswara Rao, G. Manoj Kumar, S.P. Tewari, S. Venugopal Rao, Molecular formation dynamics of 5-nitro-2,4-dihydro-3H-1,2,4-triazol-3-one, 1,3,5-trinitroperhydro-1,3,5-triazine, and 2,4,6-trinitrotoluene in air, nitrogen, and argon atmospheres studied using femtosecond laser induced breakdown spectroscopy, Spectrochim. Acta - Part B At. Spectrosc. 87 (2013) 121–129. doi:10.1016/j.sab.2013.05.006.

[154] E.N. Rao, S. Sunku, S.V. Rao, Femtosecond laser-induced breakdown spectroscopy studies of nitropyrazoles: the effect of varying nitro groups, Appl. Spectrosc. 69 (2015) 1342–1354.

[155] E.N. Rao, P. Mathi, S.A. Kalam, S. Sreedhar, A.K. Singh, B.N. Jagatap, S.V. Rao, Femtosecond and nanosecond LIBS studies of nitroimidazoles: Correlation between molecular structure and LIBS data, J. Anal. At. Spectrom. 31 (2016) 737–750. doi:10.1039/c5ja00445d.

[156] S.A. Kalam, N.L. Murthy, P. Mathi, N. Kommu, A.K. Singh, S.V. Rao, Correlation of molecular, atomic emissions with detonation parameters in femtosecond and nanosecond LIBS plasma of high energy materials, J. Anal. At. Spectrom. 32 (2017) 1535–1546. doi:10.1039/c7ja00136c.

[157] S.A. Kalam, N.L. Murthy, J.R. Krishna, V. Srikanth, S.V. Rao, Nanoparticle enhanced laser induced breakdown spectroscopy with femtosecond pulses, in: Int. Conf. Fibre Opt. Photonics, 2016: pp. Th3A--89.

[158] A.K. Shaik, V.R. Soma, Standoff discrimination and trace detection of explosive molecules using femtosecond filament induced breakdown spectroscopy combined with silver nanoparticles, OSA Contin. 2 (2019) 554. doi:10.1364/osac.2.000554.

[159] Harilal, S.S., Freeman, J.R., Diwakar, P.K., Hassanein, A. (2014). Femtosecond Laser Ablation: Fundamentals and Applications. In: Musazzi, S., Perini, U. (eds) Laser-Induced Breakdown Spectroscopy. Springer Series in Optical Sciences, vol 182. Springer, Berlin, Heidelberg. Doi:10.1007/978-3-642-45085-3_6.

[160] L.M. Narlagiri, M.S.S. Bharati, R. Beeram, D. Banerjee, V.R. Soma, Recent trends in laser-based standoff detection of hazardous molecules, TrAC - Trends Anal. Chem. 153 (2022) 116645. doi:10.1016/j.trac.2022.116645.

[161] I. Noda, Generalized two-dimensional correlation method applicable to infrared, Raman, and other types of spectroscopy, Appl. Spectrosc. 47 (1993) 1329–1336. doi:10.1366/0003702934067694.

[162] I. Noda, Techniques of two-dimensional (2D) correlation spectroscopy useful in life science research, Biomed. Spectrosc. Imaging. 4 (2015) 109–127. doi:10.3233/bsi-150105.

[163] Y.M. Jung, I. Noda, New approaches to generalized two-dimensional correlation spectroscopy and its applications, Appl. Spectrosc. Rev. 41 (2006) 515–547. doi:10.1080/05704920600845868.

[164] L.M. Narlagiri, V.R. Soma, Improving the signal-to-noise ratio of atomic transitions in LIBS using two-dimensional correlation analysis, OSA Contin. 4 (2021) 2423. doi:10.1364/osac.426995.

[165] P. Pořízka, J. Klus, E. Képeš, D. Prochazka, D.W. Hahn, J. Kaiser, On the utilization of principal component analysis in laser-induced breakdown spectroscopy data analysis, a review, Spectrochim. Acta Part B At. Spectrosc. 148 (2018) 65–82. doi:https://doi.org/10.1016/j.sab.2018.05.030.

[166] J. El Haddad, M. Villot-Kadri, A. Ismaël, G. Gallou, K. Michel, D. Bruyère, V. Laperche, L. Canioni, B. Bousquet, Artificial neural network for on-site quantitative analysis of soils using laser induced breakdown spectroscopy, Spectrochim. Acta - Part B At. Spectrosc. 79–80 (2013) 51–57. doi:10.1016/j.sab.2012.11.007.

[167] F. Rezaei, P. Karimi, S.H. Tavassoli, Effect of self-absorption correction on LIBS measurements by calibration curve and artificial neural network, Appl. Phys. B Lasers Opt. 114 (2014) 591–600. doi:10.1007/s00340-013-5566-3.

[168] D. Luarte, A.K. Myakalwar, M. Velásquez, J. Álvarez, C. Sandoval, R. Fuentes, J. Yañez, D. Sbarbaro, Combining prior knowledge with input selection algorithms for quantitative analysis using neural networks in laser induced breakdown spectroscopy, Anal. Methods. 13 (2021) 1181–1190. doi:10.1039/d0ay02300k.

[169] J. El Haddad, D. Bruyère, A. Ismaël, G. Gallou, V. Laperche, K. Michel, L. Canioni, B. Bousquet, Application of a series of artificial neural networks to on-site quantitative analysis of lead into real soil samples by laser induced breakdown spectroscopy, Spectrochim. Acta - Part B At. Spectrosc. 97 (2014) 57–64. doi:10.1016/j.sab.2014.04.014.

[170] L. Narlagiri, V.R. Soma, Simultaneous quantification of Au and Ag composition from Au–Ag bi-metallic LIBS spectra combined with shallow neural network model for multi-output regression, Appl. Phys. B Lasers Opt. 127 (2021) 1–11. doi:10.1007/s00340-021-07681-y.

[171] A. De Giacomo, R. Alrifai, V. Gardette, Z. Salajková, M. Dell, Nanoparticle enhanced laser ablation and consequent e ff ects on laser induced plasma optical emission, Spectrochim. Acta Part B. 166 (2020) 105794. doi:10.1016/j.sab.2020.105794.

[172] A. De Giacomo, Z. Salajkova, M. Dell'aglio, A quantum chemistry approach based on the analogy with π-system in polymers for a rapid estimation of the resonance wavelength of nanoparticle systems, Nanomaterials. 9 (2019). doi:10.3390/nano9070929.

2 Experimental details and initial nanosecond, femtosecond LIBS studies

2.1 Experimental details

In this chapter, we introduce the procedure of Q-switching for the generation of ns laser pulses, the measurement of the laser pulse width using the photodiode, and the triggering of the ICCD spectrometer with input from the laser. The use of the nanosecond pulses for LIBS application, like estimating the gold-silver alloy plasma temperature. Also, the phenomenon of mode locking used for the generation of femtosecond pulses using the Kerr lensing method is detailed. We detailed the process of femtosecond pulse amplification. Reported the measured femtosecond pulse width from the autocorrelation technique. We have also briefed on the components of the CCD-based non-gated and ICCD-based gated spectrometers, along with the optical fiber and telescope specifications. Further, a novel experimental geometry demonstrates the fine powder sample's filamentation-induced spectroscopy (FIBS).

2.2 Nanosecond laser

Usually, Nd: YAG crystal is used in the generation of nanosecond pulses at 1064 nm in the far infrared and is frequency doubled using the KDP crystal to 532 nm in the visible region and frequency tripled 256 nm in the UV region. It utilizes the Q-switching technique in acquiring the nanosecond pulses with high intensities enough to ablate the sample when focused. We have used the commercially available nanosecond laser SpitLight 1200 (the number denotes the energy of the pulses 1200 mJ) by Innolas for the present studies. The system uses Xenon-filled flash lamps for pumping the gain medium.

2.2.1 Q-switching

A low Q-factor of a cavity signifies high losses and low photon density in the laser cavity and switching from low to high Q-factor results in high photon density in the cavity, stimulating the inversion in the lasing material. The upper-level lifetime of the Nd: YAG-based laser is 250 μsec. The time it takes before the intensity of the spontaneous emission decreases to 1/e of the initial value when the pumping field is switched off. By adding losses in the cavity, we reduce the optical feedback in the laser cavity, and the cavity feedback switches back on after a large inversion. Figure 2.1 depicts the method of Q-switching. There are usually two methods for Q-switching a) active and b) passive. In

active Q-switching, the losses are modulated using acousto-optic or electro-optic modulators and rotating mirrors. In Passive Q-switching, a saturable absorber controls the losses based on photon densities in the cavity. A saturable absorber modulates the losses to a sufficiently high level.

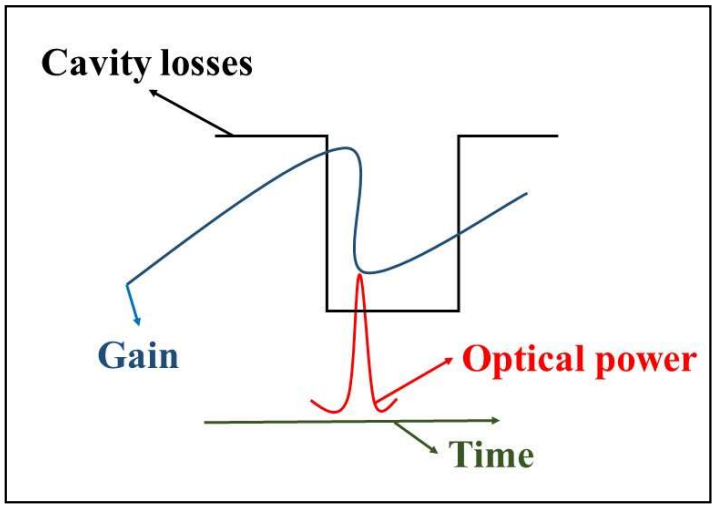

Figure 2.1 The steps involved in Q-switching in the nanosecond laser.

2.2.2 Q-switching using the Pockels cell

The Pockels cell contains of a birefringent crystal that alters the polarization of the optical beam under an electrical field's influence. The light (stimulated emission) has a definite state of polarization, and at a specific voltage, the cell acts as a quarter wave plate. The components used for Q-switching are shown in figure 2.2.

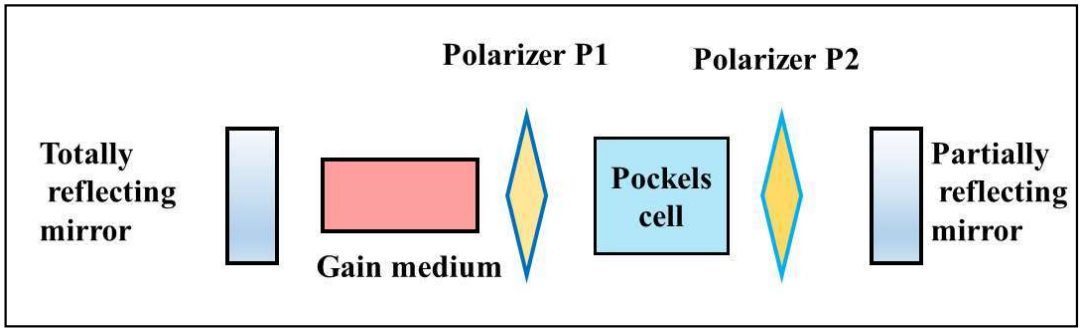

Figure 2.2 The major components of the nanosecond laser combining the Pockels cell and two polarizers used for Q-switching.

The Pockels cell voltage and the polarizer P1 are adjusted so that the plane-polarized light becomes elliptically polarized after passing through the cell. Light does not pass through

the polarizer P2 as the plane of polarization is perpendicular to the initial plane of polarization. At this stage, the cell acts as a closed shutter with no feedback into the cavity reducing the stimulated emission. After achieving the good population inversion, the electric field is switched off, the plane-polarized light passes through the cell, and the polarizer P2 is without any loss. At this stage, the cell act as an open shutter. The voltage applied to the cell determines the high Q (light stays inside the resonator) or low Q (light leaves the resonator).

2.3 Femtosecond laser and ker lens mode locking

Kerr lens mode locking in the nonlinear crystal like Ti: Sapphire with high absorption and emission bandwidth generates femtosecond pulses at 800 nm. The pulses at very low energy are amplified six orders of magnitude higher by the chirped pulse amplification (CPA). The Ti: sapphire-based amplifier (legend-HE, coherent) amplifies the fs pulses from nJ to mJ at a 1 kHz repetition rate at 800 nm central wavelength and ~ 50 fs and ~28 nm bandwidth (FWHM). Figure 2.3 shows the absorption and emission bands of the Ti: sapphire crystal.

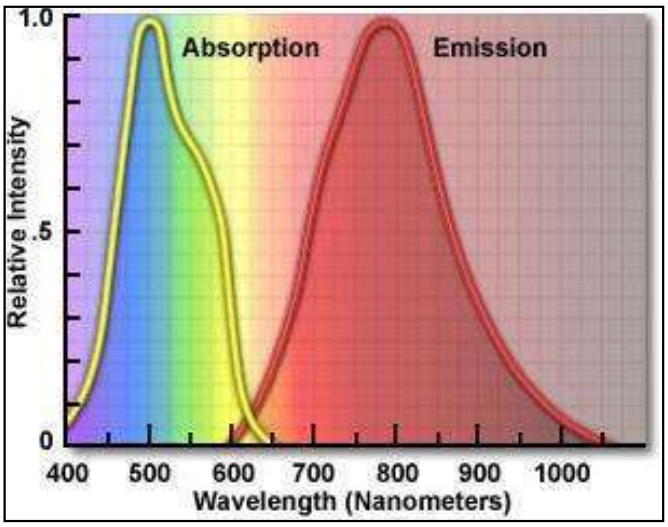

Figure 2.3 The broad absorption range in the visible region and the broad emission in the infrared region of the Ti: sapphire crystal is helpful in pumping in with a wide range of lasers and also results in a large number of modes. [Adopted from the website https://micro.magnet.fsu.edu/primer/java/lasers/tsunami/index.html].

Several longitudinal modes contribute in the lasing process. Yet, they are not necessarily in phase with one another at a cavity mirror, leading to fluctuations in the output power. These laser modes in-phase are coupled at the mirror. In that case, constructive interference occurs causing an ultrashort pulse. Modes under the gain bandwidth can lase concurrently,

giving rise to a laser bandwidth of $N\Delta\nu$. Suppose these modes are also locked together in phase. In that case, they interfere to produce a succession of intense pulses separated in time, behaving like Fourier components of a periodic function. Small fluctuations like changing the cavity length can induce mode-locking in the cavity. The atoms in the material can be distorted with large electric fields and alter the refractive index. With high-intensity lasers, this effect is called the Kerr effect**.** The refractive index is modified according to the beam's intensity distribution. As the intensity is maximum at the center and falls radially outwards, a gradient index lens is called the Kerr lens. The Kerr lens effect reduces the beam diameter when the pulses are intense or mode-locked. Kerr lens mode locking is a passive mode-locking technique. The slit at the output is placed only to allow the narrow mode-locked pulses but not the broad continuous wave. Unlike the other approaches based on transient effects within a laser cavity, mode locking is a dynamic steady-state process. Figure 2.4 (a) shows the Ti: Sapphire crystal used to generate the mode-locked femtosecond pulses and the chirped mirrors used for the compensation of the GVD. Figure 2.4 (b) shows the Nd: YVO4-based frequency-doubled laser for pumping the Ti: Sapphire.

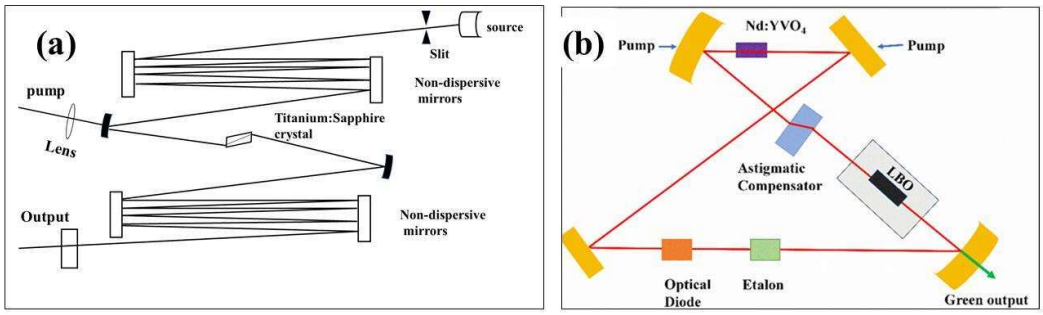

Figure 2.4 (a) The schematic of the femtosecond seed generation with pumping (Vitesse) (b) The Nd:YVO_4 based pumping the Ti:Sapphire crystal (Verdi laser) (b) The Verdi laser with Nd:YVO_4 gain medium. [Adopted from Vitesse Laser Operator's Manual https://www.coherent.com/resources]

As the number of lasing modes increases, the mode-locking and Kerr lens effect becomes persistent. Once achieved, the mode-locking persists without any initiation mechanism. The speed of light in an optical medium depends on its wavelength. As a result, the different wavelength components of the ultrashort pulses traveled at different speeds, causes temporal reshaping of the pulse, and is called group velocity dispersion. The pulse is either broadening or shortening depending on the initial condition, like the pulse chirp. As a result of negative GVD, the blue spectral components of the pulse are retarded to red, called positively chirped. The red components are retarded in the positive GVD material,

and the pulse is negatively chirped. The intensities in the ultrashort pulse are low at the leading and tailing edges and high at the center. The intensity-dependent Kerr effect modifies the refractive index of the material. As a result, the central part and leading, trailing edges move with different velocities altering the pulse shape. The frequency components are phase-shifted depending on where they occur in the pulse, generating new frequency components and introducing a positive chirp. The pulse undergoes GVD and self-phase modulation every time it traverses the cavity. Multi-layer dielectric-coated mirrors with high reflectance tackle GVD by introducing wavelength-dependent phase delays. Figure 2.4(a) is the schematic of the Vitesse laser generating the mode-locked pulses with non-dispersive mirrors (chirped mirrors) for the GVD compensation, and figure 2.4(b) is the Verdi laser pumping the Vitesse with ring cavity with Nd: YVO_4 gain medium and LBO doubling crystal. The gain medium has the highest absorption coefficient at 808 nm (easy to pump using diode lasers), performs well with shorter crystal lengths, and demonstrates a four-time larger stimulated emission cross-section than ND: YAG with strong single line emission at 1064 nm.

2.3.1 Chirped pulse amplification

The peak power of the fs pulses is high enough to initiate nonlinear processes like self-focusing in the gain medium. Further, it could damage the optics during the amplification process. Gérard Mourou and Donna Strickland devised a technique called chirped pulse amplification (CPA) to avoid such damage. The pulses passed through multiple stages for amplification.

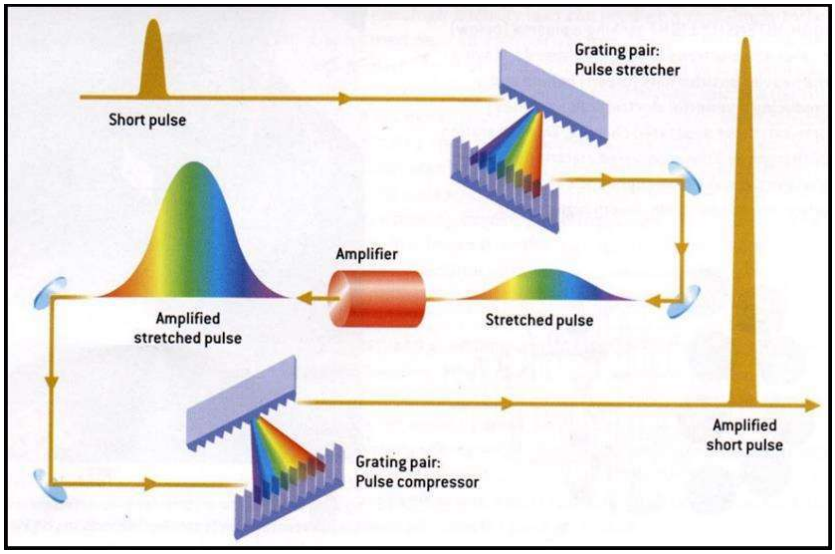

Figure 2.5 The process of the CPA with the stretcher grating, the amplifier, and the compressor grating [https://cuos.engin.umich.edu/researchgroups/hfs/facilities/chirped-pulse-amplification/].

Initially, the grating disperses the incident beam into its components resulting in the stretching of the pulses. The broadband femtosecond pulses are stretched to picosecond pulses (stretched ~10,000 times) by configuring greater path lengths for bluer frequencies than the redder components. The redder frequencies exit the stretcher first, resulting in the stretched pulse. Ti: sapphire-based regenerative amplifier uses low-energy seed laser pulses and a pumping nanosecond Nd:YLF (at second harmonic wavelength 527 nm, 20 W at 1 kHz repetition rate) to obtain high-energy efficiently. From its polarization, the pockels cell selects a single pulse from the mode-locked pulse train. The pulses are confined and amplified to appropriate energy by passing it multiple times before ejecting from the cavity. The pulse is multi-pass to amplify to a factor of 10^6 after stretcher grating. The pulses are recompressed again to femtosecond time scales after the amplification. Compression is the reverse of pulse stretching with gratings arranged for the blue frequencies to travel the shortest path to become equal with the redder frequencies. The femtosecond seed source (Vitesse) and Nd: YLF laser source pumping the regenerative amplifier (Evolution) along with the amplifier and stretcher/compressor compartments in the Libra amplifier system is shown in figure 2.6. The parameters related to the Libra femtosecond amplifier system are listed in table 2.1.

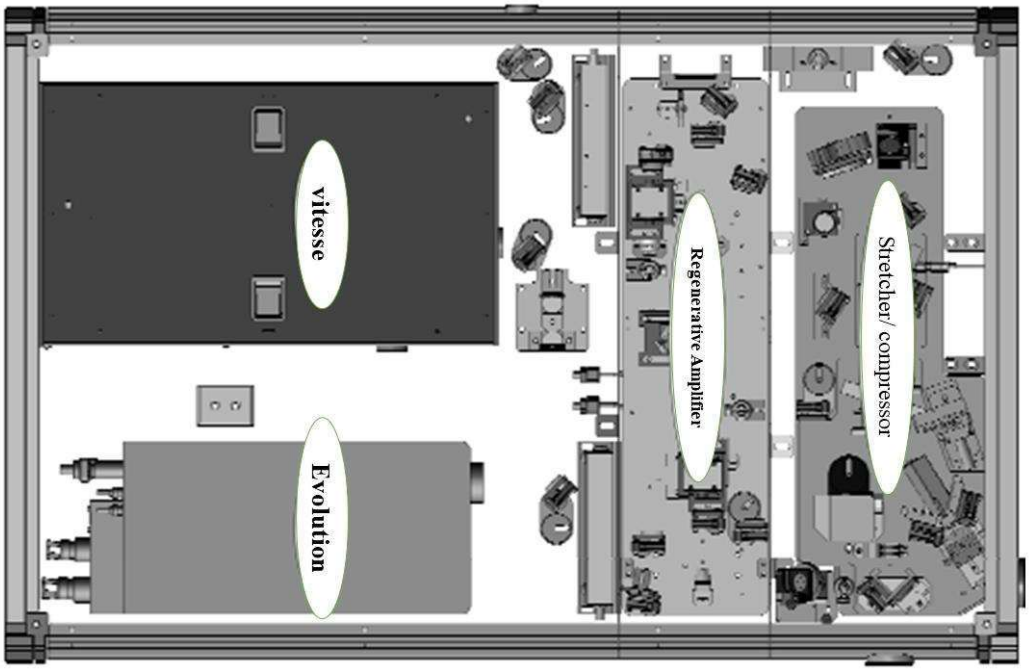

Figure 2.6 The schematic of the femtosecond amplifier (Coherent, LIBRA) system with the seed pulse generator, Vitesse, and the pumping laser, Evolution, and the regenerative amplifier with the stretcher the amplifier compartments [https://www.coherent.com/resources/ preinstallation/libra-series/Libra_Preinstallation_Manual.pdf].

Table 2.1 The parameters values of the femtosecond laser source used in the LIBS experiments

Parameters	Vitesse oscillator	Libra femtosecond amplifier
Pulse Width	~100 fs	~35 fs
Output energy	~ 6-7 nJ	~4 mJ
Repetition rate	~80 MHz	1 kHz
Beam diameter	~ 3 mm	~9 mm ($1/e^2$)
Polarization	Horizontal	Horizontal

2.3.2 Single shot autocorrelation

The Coherent single shot autocorrelator (SSA) was used for the pulse width measurements of the femtosecond pulses. In the SSA, the 800nm femtosecond laser pulses from the Ti: Sapphire-based amplifier are turned into the SSA using the input mirror M1 and are split into two beams at the BS1 beam splitter after the beam expander (includes (L1, L2). The two pulses travel different paths, as shown in figures 2.7, with a solid line and the delayed dotted line. The two beams were made to overlap non-collinearly onto the 800 nm cut KDP crystal to generate a second harmonic signal from the two pulses. BG18 bandpass filter removes the 800nm wavelength, and the SH signal was recorded in the CCD array.

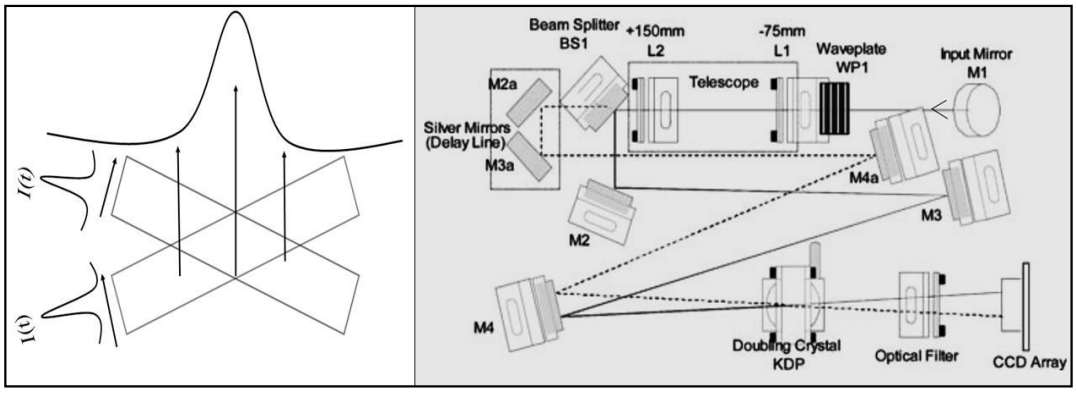

Figure 2.7 The single shot autocorrelation of the two pulses and the schematic of the coherent SSA. The beam splitter splits the beam, and the beam traveled different paths before overlapping in the doubling crystal [Adopted from Single Shot Autocorrelator Operator's Manual https://www.coherent.com/resources].

An oscilloscope was used to record the output signal from the CCD. The overlap of the two tilted wavefronts results in autocorrelation, as shown in figure 2.7. The micrometer reading is calibrated with the oscilloscope signal, and zero delays was achieved by maximizing the SH signal. The deconvolution factor of $\sqrt{2}$ was used in calculating the

pulse width from the second harmonic signal assuming the pulses are Gaussian. Figure 2.8 shows the SH signal at different delays (left) and the signal at zero delays (right). The data collected at different delays are shown in figure 2.8, and the SH signal at zero delays.

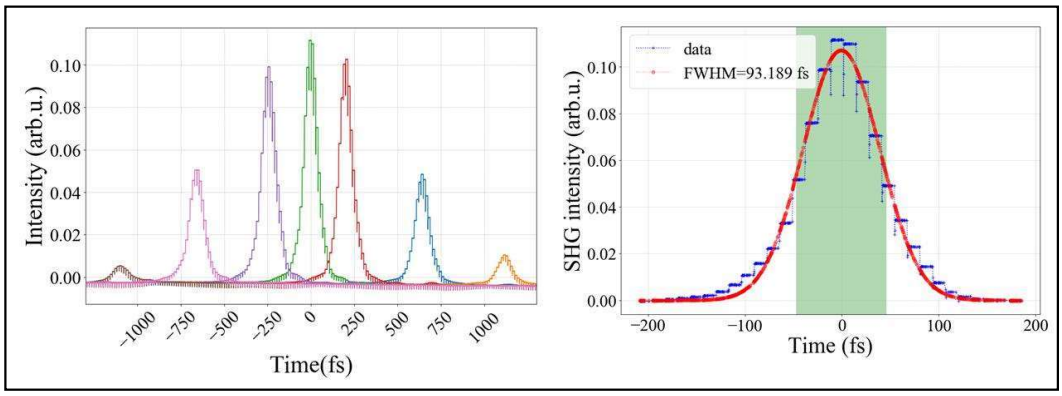

Figure 2.8 The second harmonic generation with the delay and the second harmonic signal at the zero delays with the calculated FWHM of 93 fs (as the roundtrips, propogation length and the dispersive elements effects the pulsewidht). Blue, scattered points are the experimental data, while the solid red line is the fit.

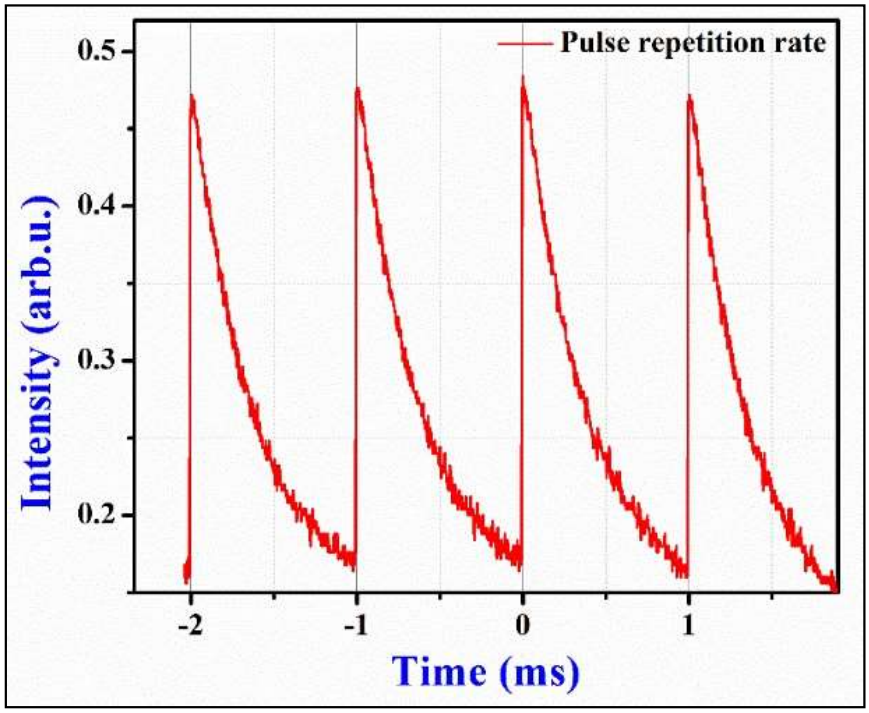

Figure 2.9 The photodiode signal of the 1 kHz femtosecond pulse train was measured using an oscilloscope.

The femtosecond amplifier output was at a 1 kHz repetition rate and was measured using the photodiode signal fed to the Tektronix oscilloscope. The signal is shown in figure 2.9.

2.4 Detectors

2.4.1 Non-gated spectrometers

The typical spectrometers use the Czerny-turner configuration for its advantages like compactness and flexibility and efficient aberration-free performance. The folded Czerny-Turner spectrograph provide a good coma correction and a flattened spectral field. Czerny-Turner optical bench is designed to reduce image aberrations with a f-number of >3, which restricts its throughput. Compared to usual multimode fibers (NA ≈ 0.22), the relatively large f/# cause a high level of random photons in the optical bench. This can be eased by unfolding the optical bench. Typical spectrometers ranging from 190 nm to 1100 nm use three filters for order sorting. Some spectrometers use thin films continuously varying the cut-on wavelength of the order sorting filter for essential signal detection. SMA-connector, 2) Collimating mirror, 3) Grating, 4) Focusing mirror, 5) Order Sorting Filter, 6) Collection lens, 7) Line scan detector. The major components of the spectrometer are shown in figure 2.10

Figure 2.10 Major components of the CCD-based non-gated spectrometers from the entrance to the CCD detector and the grating and mirrors [Adopted from https://www.avantes.com/support/theoretical-background/introduction-to-spectrometers/].

2.4.2 Mechelle spectrograph equipped with ICCD

The echelles gratings are used for cross-dispersion and prisms and are operated at higher orders, usually around 100. Figure 2.11 shows the blazed grating with all the angle measurements involved in the grating equation 2.1.

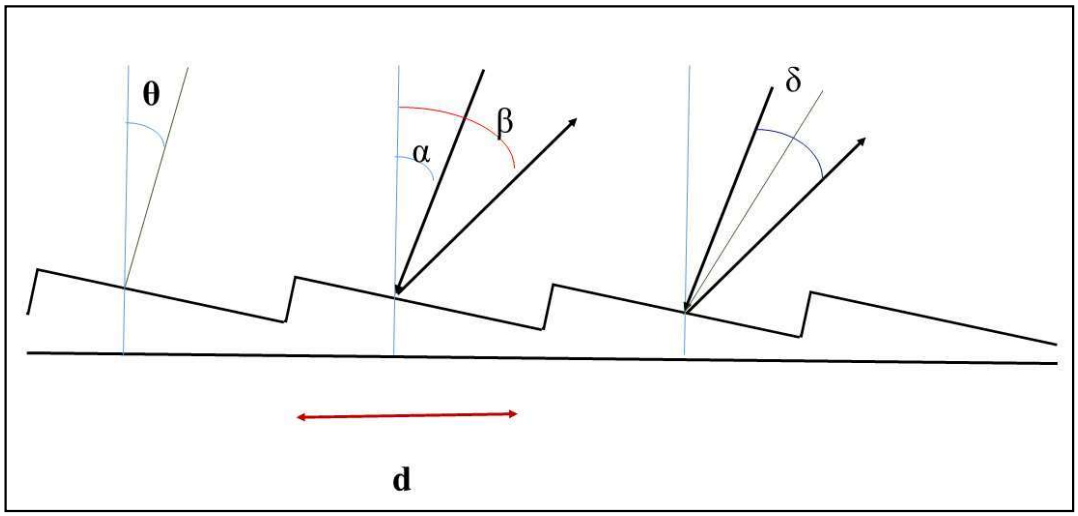

Figure 2.11 The echelle (blazed) grating is used in the ICCD operates at higher order for better resolution.

$$m\lambda = d(sin\alpha + sin\beta) \tag{2.1}$$

α = incidence angle, β= diffraction angle, d= grating constant, f= focal length, θ=blaze angle, m=diffraction order, W= width of grating, N= total number of grooves W/d. Intensity is maximum for the wavelength at which α +β= 2θ, and auto-collimation is achieved when α=β= θ. Sorting is achieved using cross dispersion from the prism (dispersion at right angles to the dispersion from grating). Prisms were chosen as the cross-dispersing elements of the spectrograph for several reasons. One is that the inter-order separation is much less dependent on wavelength than in the case of a diffraction grating. This format is suitable for array-based detectors with a square display format.

2.4.3 High-resolution echelle spectrometer (HRES)

A uniform order distribution is produced when the prism and echelle grating are combined, assisting in effectively using the CCD sensor. The combination also results in 2D dispersed light at higher order resulting in high resolution along a broad range. Figure 2.12 displays a typical schematic for high-resolution echelle spectrometers. The spectrometer's resolution is (λ/Δλ) ~ 5000, and its wavelength range is 200 nm to 920 nm. Compared to the CCD sensor, the ICCD sensor offers gating capabilities when coupled with the intensifier.

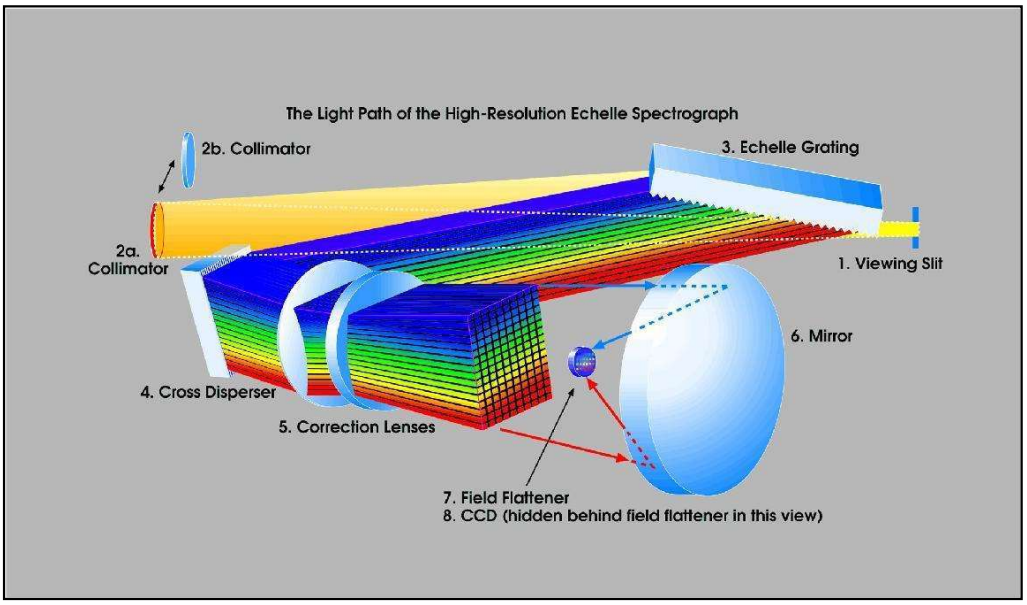

Figure 2.12 The schematic of the cross dispersion of the light, from grating and prism combination, incident on the 2D sensor [Adopted from https://www2.keck.hawaii.edu/inst/hires/].

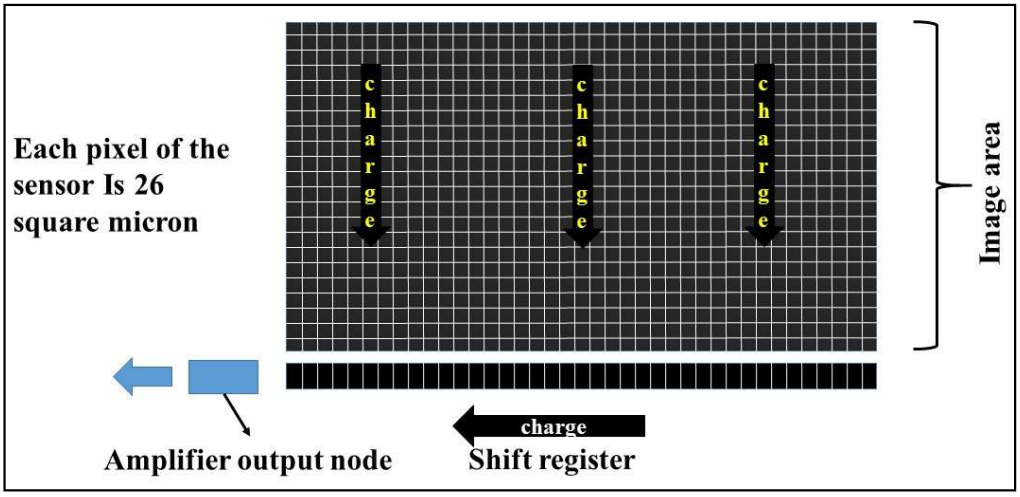

Figure 2.13 The working method of the 2D CCD sensors after the photons are converted to charge and transport.

CCD is a photo-sensors of two- dimensional on semiconductor chips based on silicon shown in figure 2.13. The light shined on the sensors produces electrons, a charge pattern corresponding to the source is formed, and the charge is transferred from the chip to the computer memory. The individual sensors are clocked to shift the charge of one row at a time to the shift register, masked from the light, using a series of vertical electrodes. The charge in the shift register is further transferred to the output node using the series of horizontal electrodes and is converted into a 16-bit binary number using analog to digital (A/D) converted.

2.4.4 Image intensifier

Photons from the light source strike the input window with a photocathode on its inner surface. The photoelectrons are emitted when photons strike the photocathode and are drawn to the microchannel plate by a high electric field. The intensifier consists of three significant components i) photocathode, ii) microchannel plate iii) phosphor screen. The intensifier can be rapidly turned on and off and used as gating for the CCD detector, as shown in figure 2.14.

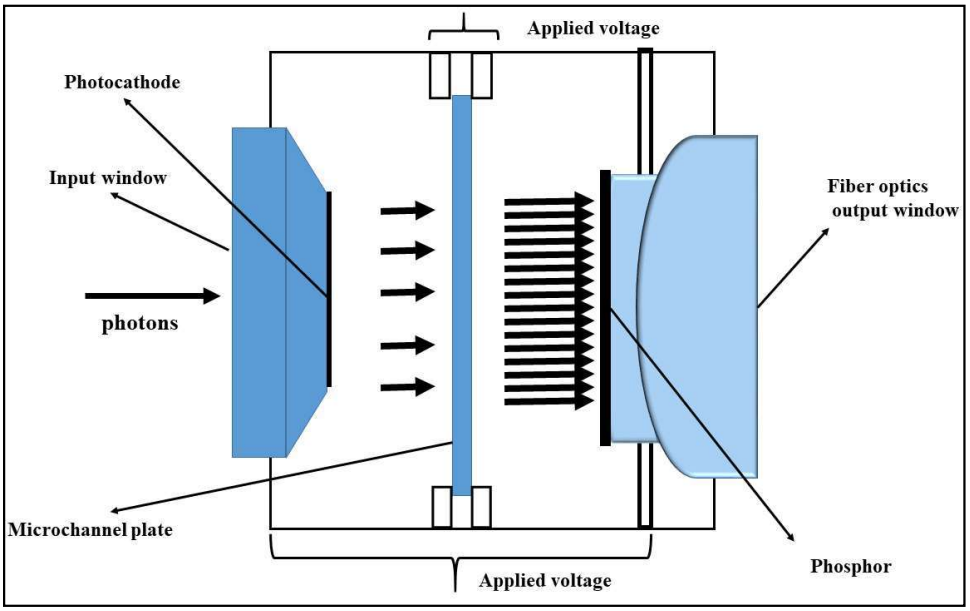

Figure 2.14 The intensifier with a photocathode, microchannel plate, and phosphor screen.

The gated LIBS experiments were performed using the Mechelle spectrograph (ME 5000; based on echelle grating) outfitted with an Andor iStar intensified charge-coupled device (ICCD). Due to their respective triggering speeds of 1 kHz and 500 Hz, Mechelle was equipped with the iStar ICCD of model number DH334T-18U-E3 for femtosecond LIBS experiments and the iStar ICCD of model number DH734-18U-03 for nanosecond LIBS experiments. The Mechelle spectrographs are ideal in field applications because of their robustness, high resolving power, and wide spectral range when coupled with CCDs or ICCD. For instance, the larger spectral resolving power of 5000 results in the resolution of 0.05 nm @ 500 nm. They provide multi-elemental analysis with a wide spectral range over ultraviolet (UV) to near-infrared (IR) region, including the visible region (200 to 900 nm), in an acquisition. Mechelle spectrographs are frequently used to study laser-induced plasmas (LIP).

Additionally, they offer minimal cross-talks between the orders. Standard mercury-argon (Hg-Ar) lamps and Deuterium-Halogen (DH-3) lamps were used for wavelength and intensity calibration, respectively. The DH-3 lamp has two sources: a deuterium lamp with a wavelength between 200 nm and 400 nm and a tungsten halogen lamp with a wavelength between 380 nm and 975 nm due to the difference in intensity between these lamps. Table 2.2 displays the acquisition parameters applied to the Hg-Ar and DH-3 lamps.

Table 2.2 Parameters values used in wavelength and intensity calibration of ICCD.

ICCD parameters	Hg-Ar lamp	DH-3 Lamp
Gate delay	0 ns	0 ns
Exposure time	0.2 S	2.5 S
Gate width	0.13 S	2.5 S
Gain (0-4000)	700	3000

Specifications of the optical fiber used for the experiments are listed in table 2.3

Table 2.3 Parameters of the optical fiber used for transporting the plasma emissions from the collector to the spectrometer.

Model number	QP400-2-SR-BX
Wavelength range(nm)	200-1100
Fiber core size (microns)	400, 600
Fiber type	UV/SR-VIS
Length (m)	2
Numerical aperture	0.22
Jacket	Stainless-steel
Buffer material	Polyimide

2.4.5 Schmidt-Cassegrain telescope for the standoff studies

The major components of the Schmidt-Cassegrain telescope (SCT) are the a) aspherical corrector plate, b) the primary mirror and c) the secondary mirror, d) the Knob to adjust the focal length, and e) the eyepiece. The total length traveled by the light inside and the aperture of the telescope decides its performance. The focal length of the telescope objective is 1500 mm, and the eyepiece focal length is 25 mm. The magnification power of the telescope, or the amount that a telescope enlarges its subject, is 60, which is its focal length divided by the eyepiece's focal length. The size of the circle of light that hits the eye when we look through the eyepiece is 7mm and is called the exit pupil of the telescope. The schematic of the SCT is shown in figure 1.8. The other relevant parameters, like the

resolving power, the light-gathering power, and the field of view, are tabulated in table 2.4.

Table 2.4 The specification of the SC telescope used for the standoff studies.

Property	Value
Objective focal length **F**	1500 mm
Eyepiece focal length **f**	25 mm
Objective aperture **D**	150 mm
Magnification **M**	60x
F ratio	F/10
Field of view	1.7^0
Resolving power	0.77 arc second
Exit pupil	2.5 mm
Approximate Limiting Magnitude of Telescope	12.9
Light-gathering power	459.18

2.4.6 Delays involved in acquiring LIBS spectra

The intensifier increases the signal's strength and is helpful for gating the acquisition in LIBS experiments. Due to increased sensitivity, image intensifiers with CCD are typically used to study extremely weak processes. In addition to serving as gate control, ICCD is useful for recording the spectrum at desired time delays synchronized to the input trigger. The gate delay, which occurs after the laser pulse, and gate width, which describes how far the emissions are recorded. Thus, LIBS spectra with (i) time-integrated and (ii) time-resolved spectra, can be recorded using ICCD. Time-resolved emissions are acquired to study the transient LIPs and comprehend various molecular and atomic pathways by observing the signal-to-background ratio. In the nanosecond LIBS, the ICCD is triggered with the help of reference TTL pulse from the Pockels cell. The TTL pulse from the Pockels cell is taken as reference T_0, and desired delays are produced using the delay generator. In this study, the DG535 digital delay generator by Stanford research systems was used. The desired initial delay, including the insertion delays by all the components like insertion delays from the digital delay generator and the ICCD itself, to the ICCD was set by monitoring the LIBS signal with minimum plasma background. The delays included in the gated LIBS experiment are measured using the oscilloscope and shown in figures 2.15 and 2.17. In figure 2.15(a) orange channel represents laser pulse of pulse width 8.6 ns FWHM. Figure 2.15(b) represents TTL pulse Pockel's cell via delay generator (DG535),

with insertion delay of ~90 ns and opening time of 840 ns. Figure 2.16(c) is the ICCD trigger monitor showing the ICCD opening time of 1 µs after the laser pulse.

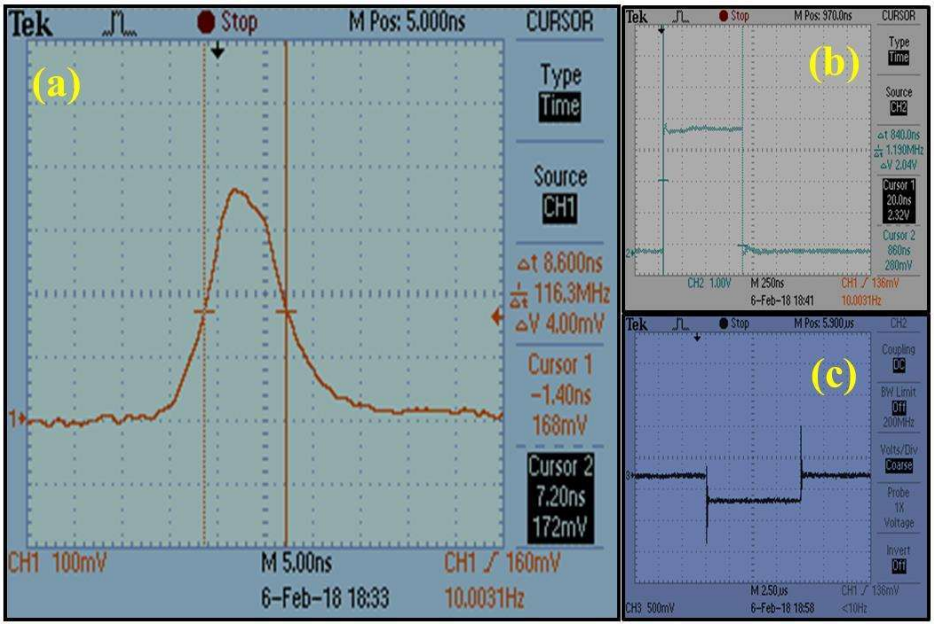

Figure 2.15 (a) The laser pulse widh measured using photodiode in orange and (b) the signal from pockels cell in blue (b) ICCD trigger monitor in the oscilloscope shows the ICCD gate opening time of ~1 µs.

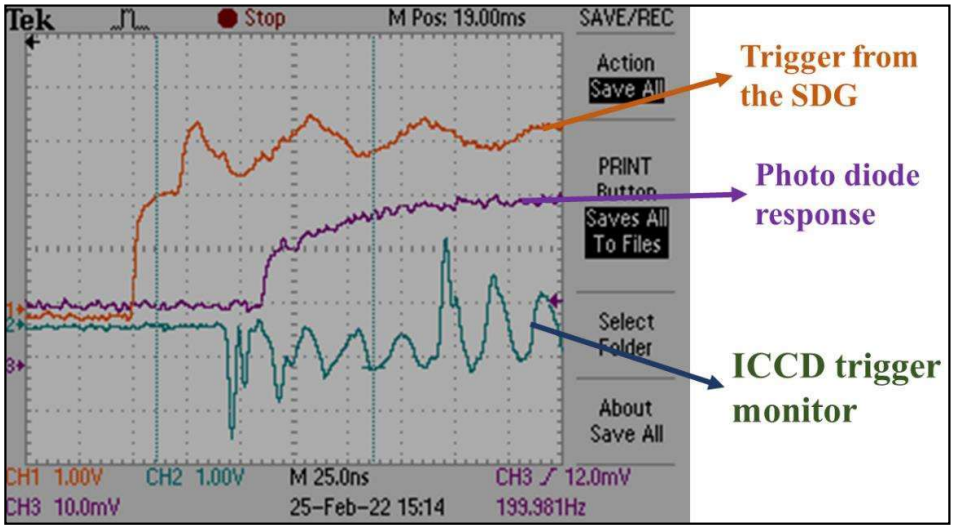

Figure 2.16 The time delay between the pulse from the SDG and the ICCD trigger monitor is 50 ns and the time delay between the photo diode response and the ICCD trigger monitor is ~20 ns because of propagation delay.

In the case of the femtosecond LIBS experiments, the TTL pulse from a synchronized delay generator (SDG) is used to trigger the ICCD. The violet color in the figure 2.16 represents the incidence of laser pulse onto the sample surface. The orange line represents

the TTL from the SDG, and the green represents ICCD gate monitoring signals. The time between the laser pulse and the ICCD gate opening are adjusted for better LIBS signal.

2.5 Nanosecond laser-induced plasma temperature evolution

The interaction of nanosecond pulses with varied compositions of Au-Ag bimetal target resulted LIBS spectra and the time-resolved spectra was acquired using ICCD. The effect of Au-Ag composition on the time evolution of plasma temperature was investigated. LIBS is used to identify and quantify elements in plasma discharges [1]. It has found application in various disciplines due to its speedy and minimal sample preparation for material classification [2] and quantification research [3]. The atomic and ionic peaks and corresponding spectroscopic parameters are used for determining the plasma temperature [4]. For quantification studies, generally, plasma temperature is employed in conjunction with electron density.

2.5.1 Experimental procedure

With a 10-cm focal length plano-convex lens made of fused-silica, ~8 ns laser pulses from a Q-switched Nd: YAG laser at 1Hz repetition rate, 532 nm were focused on Au-Ag bimetal samples. The studies used three distinct compositions (Au30-Ag70, Au50-Ag50, and Au80-Ag20). The plasma emissions produced by the intense laser pulse and sample interaction were collected using Andor made (ME-OPT-0007) collection optics and fed into the (ANDOR ISTAR ICCD and MECHELLE 5000) intensified spectrometer through a 600-micron optical cable with a 230nm to 800nm wavelength range. The spectra were obtained with a 1 µs gate delay and a 1 µs gate width. Figure 2.17 depicts the setup and figure 2.18 the substantial portion of the spectra.

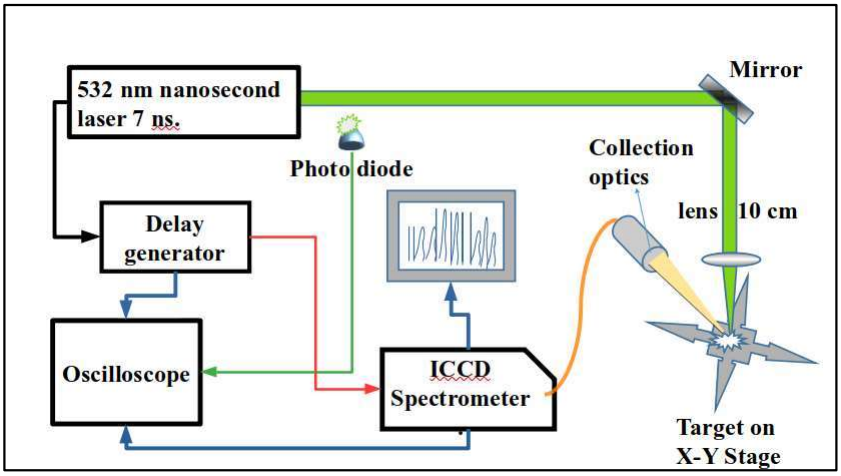

Figure 2.17 The schematic of the nanosecond laser-induced breakdown spectroscopy experiment.

After one second, the plasma is thought to be in local thermodynamic equilibrium (LTE). Using the Boltzmann distribution law, Equation 2.2 to equation 2.5 express the relationship between peak intensity (I) and wavelength, population n, transition probability (A), plasma characteristic length (L), and degeneracy (g). The equations use the symbols population (n) at a particular energy E and temperature T of a specific ionization state Z. P_z is the partition function, while K_B is the Boltzmann constant. The table contains the values used in the calculations. The following equations were used to calculate the plasma temperature, where Z denotes the element's ionization state. The peak Au intensities were employed in the analysis.

$$\frac{n_{k,Z}}{n_Z} = \frac{g_{k,Z}}{P_Z(T)} exp\left(-\frac{E_{k,Z}}{K_B T}\right) \tag{2.2}$$

$$I_Z = \frac{hc}{4\pi\lambda_{ki,Z}} \times A_{ki,Z} n_{k,z} L \tag{2.3}$$

$$I_Z = \frac{hc}{4\pi\lambda_{ki,Z}} \times A_{ki,Z} \frac{g_{k,Z} n_Z}{P_Z(T)} \times exp\left(-\frac{E_{k,Z}}{K_B T}\right) L \tag{2.4}$$

$$ln\left(\frac{I_Z \lambda_{ki,Z}}{g_{k,Z} A_{ki,Z}}\right) = -\frac{E_{k,Z}}{K_B T} + ln\left(\frac{hcLn_z}{4\pi P_z(T)}\right) \tag{2.5}$$

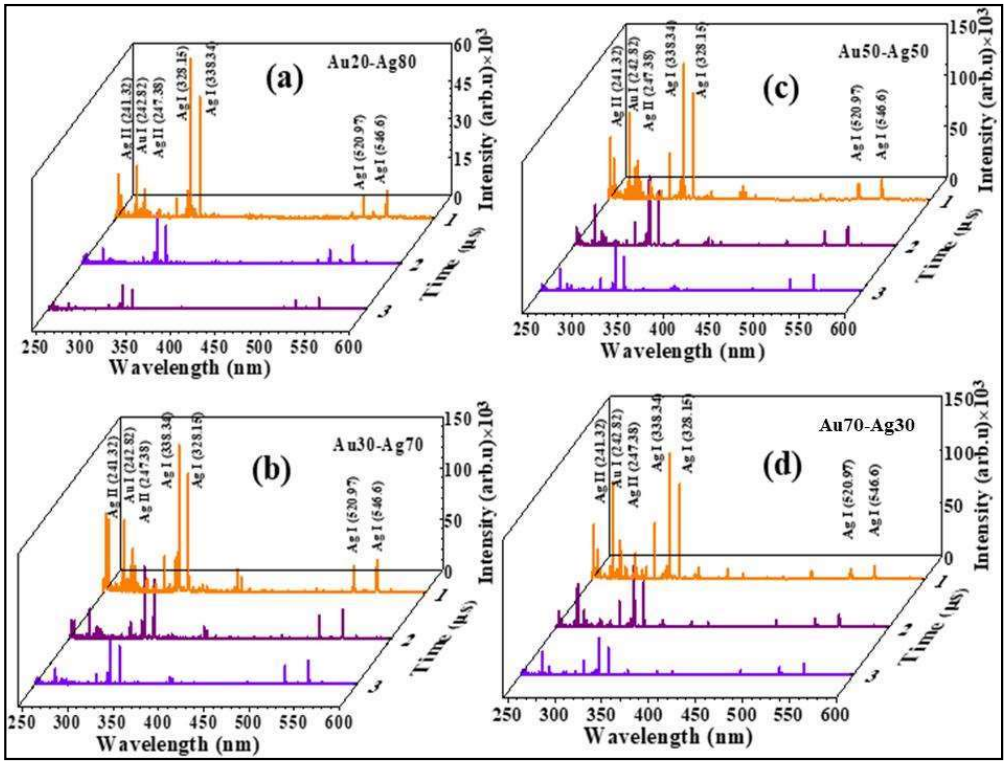

Figure 2.18 The time-resolved ns-LIBS spectra of the bimetallic targets (a) Au20-Ag80, (b) Au30-Ag70, (c) Au50-Ag50, (d) Au70-Ag30 with identified peaks from the NIST database.

Table 2.5 The spectroscopic parameters taken from the NIST database used for the Boltzmann plots.

Sl. N0.	Wavelength (nm)	A_{ki} (S^{-1}) $\times 10^5$	E_i (eV)	E_k (eV)	Degeneracy g_i	Degeneracy g_k
1	274.82	103	1.14	5.65	6	8
2	312.27	190	1.14	5.11	6	4
3	406.5	850	4.63	7.68	2	4
4	479.25	890	5.11	7.69	4	6
5	583.91	295	4.63	6.76	2	2
6	627.81	34	2.66	4.63	4	2

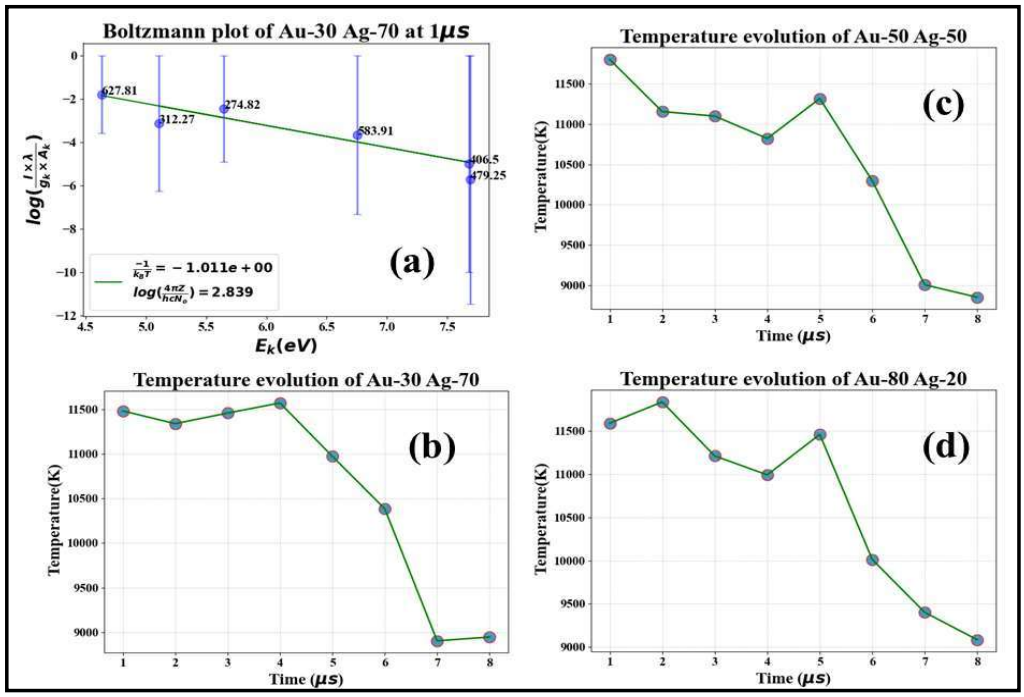

Figure 2.19 (a) Boltzmann plot of the Au30-Ag70 composition with the ns LIBS taken at 1μs and the evolution of plasma electron temperature for the compositions (b) Au30-Ag70 (c) Au50-Ag50 (d) Au80-Ag20.

For the investigation, six Au peaks were chosen from the LIBS spectra. For each composition, standard deviation of the 20 spectra was calculated, which was used for error bars and the mean for the points. The equation 1, along with the spectroscopic parameters presented in table 2.5, was utilized to estimate the temperature from Boltzmann plots between 1μs and 8μs. The plasma temperature is related to the reciprocal of the slope of

the straight line fit, and the intercept is related to the material composition. The electron plasma temperature is known to drop rapidly as t^{-2} (where t is time) within 1 μs [5]. The temperature declines consistently during the time (1 μs and 10 μs), as illustrated in figure 2.19. These investigations can be extended to investigate the relationship between composition and temperature evolution, which could aid in quantifying and comprehending laser-produced plasma characteristics.

2.6 Novel femtosecond experimental configurations for fine powder samples

A novel experimental geometry for studying sparse fine-powdered samples utilizing femtosecond filamentation-induced breakdown spectroscopy is described here (fs FIBS). The FIBS spectra were acquired after mowing fine graphite powder and commercially available talcum powder on a Brass substrate with a femtosecond filament, considerably avoiding substrate interference. The FIBS spectra revealed the production of CN and C_2 bands in graphite and calcium, magnesium, potassium, and sodium peaks. The FIBS signal fluctuation and vibrational temperature are important in plasma diagnostics of the CN and C_2 diatomic molecules. The emission spectra arising from the recombination of free electrons and ions, generating neutral atoms and short-lived molecules, from the decaying plasma created when an intense pulsed laser is focused on the sample are the basis for laser-induced breakdown spectroscopy [6, 7]. The spectra can provide quantitative and qualitative information about the elemental composition [8, 9]. Many previous studies [10,11] found molecular emissions such as CN and C_2 in the LIBS spectra of organic materials. The LIBS approach is also utilized to detect trace elements in complicated matrices such as minerals and soils [12]. LIBS without calibration is commonly used for quantitative analysis of trace materials [13, 14].

Furthermore, the LIBS signal can be amplified in the presence of nanoparticles, in the detection of substances in micro-drops [15]. The nanoparticle-enhanced LIBS (NE-LIBS) signal's molecular bands can be significantly improved [16]. In the case of femtosecond (fs) pulses, an exciting phenomenon known as filamentation occurs when narrow plasma channels interact with the sample in generating plasma, and atomic and molecular emissions are observed during recombination [17,18]. The filamentation is induced by the balancing effect of beam self-focusing caused by the nonlinear Kerr effect and self-defocusing caused by the former [19]. In a gaseous medium, the critical power, P_c, beyond

which self-focusing begins, is around a few GW. Both phenomena are affected by the intensity of the laser pulse. Equation 2.6 gives the intensity-dependent refractive index responsible for self-focusing, where n_2 is the Kerr nonlinear index coefficient.

$$n = n_o + n_2 I \tag{2.6}$$

The refractive index change due to plasma is $\Delta n_p = -\frac{\omega_p^2}{2\omega_o^2}$ (here, the central frequency of the femtosecond pulses is $\omega_{0,}$ and the plasma frequency ω_p. The relation between the electron density and plasma frequency is shown in equation 2.7. An empirical formula relates the electron density N_e to the nonlinear order of ionization 'm' and intensity I, as shown in equation 2.8.

$$\omega_p = \sqrt{\frac{e^2 N_e}{\epsilon_o m_e}} \tag{2.7}$$

$$N_e(t) \propto I^m \tag{2.8}$$

Where m_e and e are the mass of the electron and charge, ε_0 is the permittivity of free space.

The electron density escalates with intensity because of multiphoton ionization is a highly nonlinear absorption process. In the air, 'm' is around 8. Therefore, the effective refractive index can be written as shown in equation 2.9.

$$\mathrm{n} = \mathrm{n_o} + \Delta \mathrm{n_{kr}} + \Delta \mathrm{n_p} = \mathrm{n_o} + \mathrm{n_2 I} - \frac{\mathrm{e}^2}{2\varepsilon_\mathrm{o} \mathrm{m_e} \omega_\mathrm{o}^2} \beta \mathrm{I}^\mathrm{m} \tag{2.9}$$

This self-balancing effect produces a threshold in intensity (5×10^{13} W/cm^2), which results in well-established plasma temperature clamping [20]. Clamping in fs filamentation decreases shot-to-shot noise in filamentation-induced breakdown spectroscopy (FIBS) spectra and delivers the required irradiance even at greater distances without focusing optics [17]. The advantages of FIBS with loosely focused beams over lens-free FIBS are higher intensities and persistent emissions. Harilal et al. documented these in their extensive research [21, 22]. Earlier spectroscopic experiments with filamentation concentrated mostly on employing bulk targets/rocks with normal incidence geometry, such as metal and geological samples. The disadvantages of supercontinuum caused by distorted pulses on the FIBS signal and the advantages in studying rough surfaces have been described [23, 24]. Because of its spectacular self-focusing ability, the filamentation phenomenon is useful in investigating targets at vast distances [25]. Filamentation

propagation in flames reduces the clamping intensity by a factor of two [26]. Chin et al. studied [27] in detail the mechanism of filamentation and its applications. The interaction of filamentation revealed contaminants in the atmosphere, breaking down the medium along the path [28]. The filamentation LIBS has also been proven helpful in detecting radioactive elements at a distance [29]. Our group used principal component analysis on FIBS spectra acquired from standoff distances to discriminate Au-Ag bimetallic samples with varying weight percentages [30]. The FIBS was also used in explosive discrimination, and the parameters impacting the FIBS signal in standoff modes, such as fluence and collection optics, were previously described by our group [31]. Milo Burger et al. [32] discussed the effect of the starting phase of ultrashort pulses (fs pulses) on uranium FIBS spectra and other optimization parameters, such as group delay dispersions. Recently, the identification of plastics, the classification of bimetals with a small spectrometer, and the benefit of beam steering in FIBS have all been described [33]. Most LIBS applications used either the normal incidence or the oblique incidence of laser pulses on the material. LIBS investigations are typically performed on bulk samples in pellets, metallic solids, and trace components dispersed or drop cast on the substrate material. The peaks of the substrate are inescapable in sparse samples, and for the first time, we present the pure spectra of sparse samples on the Brass substrate with only the sample's molecular peaks. In addition, the vibrational temperatures of the CN and C_2 were determined using the GUI-based software, which employs the BESP-modelled spectra and the NMT algorithm for fitting. It was found that fine powder samples produce superior FIBS spectra than coarse samples. We are confident that this innovative geometry will improve the FIBS technique's capacity to record the clean spectra of finely powdered sparse samples like explosives and other sparse samples, which are the primary concerns of homeland security. The experimental configuration is possible with fs laser-produced filamentation only. This technique can be improved by using a cylindrical lens to capture spectra along the filamentation length. Furthermore, the use of nanoparticles could improve the signal in the FIBS spectra.

2.6.1 Experimental setup

Ti: sapphire-based amplified pulses (~50 fs, ~1.8 mJ, and 1 kHz repetition rate) were focused on 50 cm using a convex lens of 50 cm focal length to achieve the filamentation of the length ~3 cm. The plasma emissions were subsequently fed to gated (ANDOR make) ICCD and (Mechelle) spectrograph combination. An exposure time of 2 s gate delay of

120 ns, a gate width of 300 ns, and 5 accumulations were used for a better signal. As the sample is sparse, 2 s, 120 ns gate delay, and 500 ns gate width with single accumulation were used in the study of the signal fluctuation and temperature estimation via an optical fiber of 400 µm core diameter. The synchronized gate delay triggered the ICCD gate, and the trigger pulses were monitored using an oscilloscope. Figure 2.20(a) shows the schematic of the novel experimental setup used for the standoff femtosecond FIBS studies. The fine graphite powder of particle size ≤ 20 µm (~99.5% pure) from Sigma Aldrich (CAS No 7782-42-5) and commercially available Ponds (radiance talc) mixture of different size particles (from size ~20 µm up to ~ 150 µm) were used for the present study. The powder sample of ~20 mg was spread across 2 mm×40 mm line on the Brass plate of 40 mm × 40 mm perpendicular to the laser direction [see figures 2.20(b) and 2.20(c), 2.20(d) for the schematics]. The filament was moved tangentially to the fine graphite powder on a flat Brass plate surface.

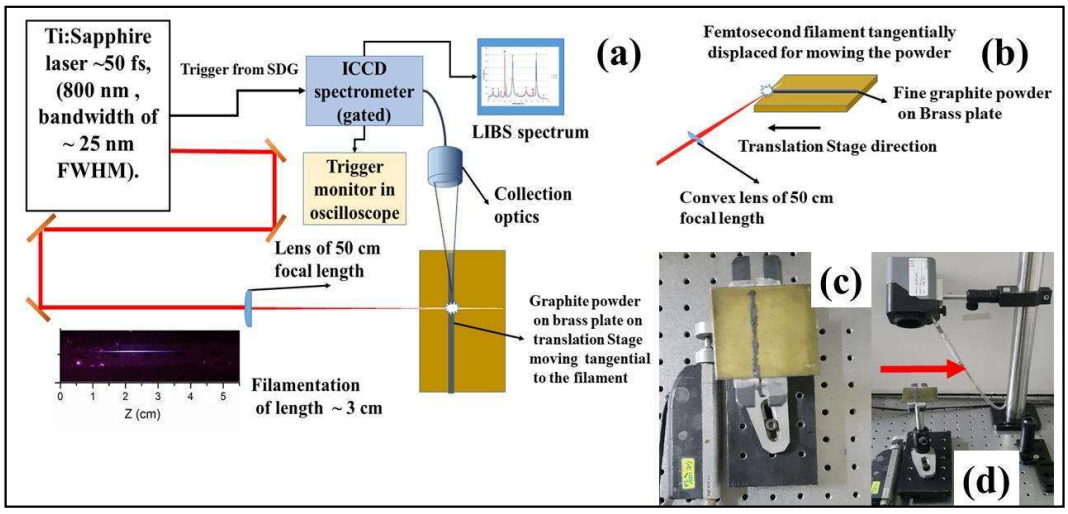

Figure 2.20 (a)The experimental setup used for the filamentation mowing of traces of fine graphite powder on the Brass, (b) substrate moving tangentially to the filamentation with the ,(c) sample on the Brass plate on the optical bench, (d) the collection optics at ~45° to the horizontal Brass plate and the red arrow shows the incident laser direction.

2.6.2 Results and discussion

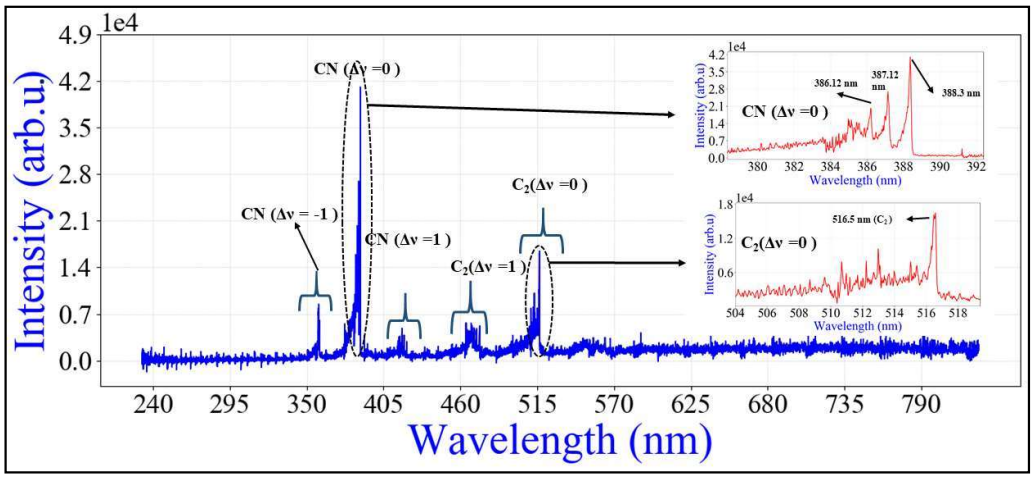

Figure 2.21 The grazing incidence FIBS spectra of sparse fine graphite powder with molecular emissions of the CN violet bands, C_2 swan band enlarged in the inset.

The sparse sample's FIBS spectra were acquired without any substantial background peaks from the substrate. Figure 2.21 depicts the CN violet and C_2 swan bands from the graphite powder FIBS spectrum. The molecular emissions dominated, and atomic peaks (often the carbon peak at 247.9 nm) normally seen in organic compound LIBS spectra were absent. Figure 2.21 depicts the molecular transitions ($B^2\Sigma^+$-$X^2\Sigma^+$) CN violet band with the intense peak of $\Delta v = 0$ at 388.3 nm, $\Delta v = 1$ at 359.04 nm, and $\Delta v = -1$ at 421.58 nm with the CN molecular emissions, C_2 molecular emissions highlighted in the inset. It is observed that the finer the powder, the better the interaction with the filament, hence a better FIBS signal. This could be related to the fine powder sample's lower ablation threshold. The fluctuation in the FIBS signal is reported to be substantial as compared to the FIBS spectra of solids and samples in pellet form. It is useful in qualitative analysis, and the employment of superior machine learning methods are essential in quantitative analysis [29]. Figure 2.22 depicts the standard deviation in the CN and C_2 bands of the 14 other graphite powder spectra.

The vibrational temperature of diatomic molecules such as CN and C_2 relevant in plasma diagnostics from molecular emissions was estimated using experimentally recorded grazing incidence FIBS spectra of fine graphite powder.

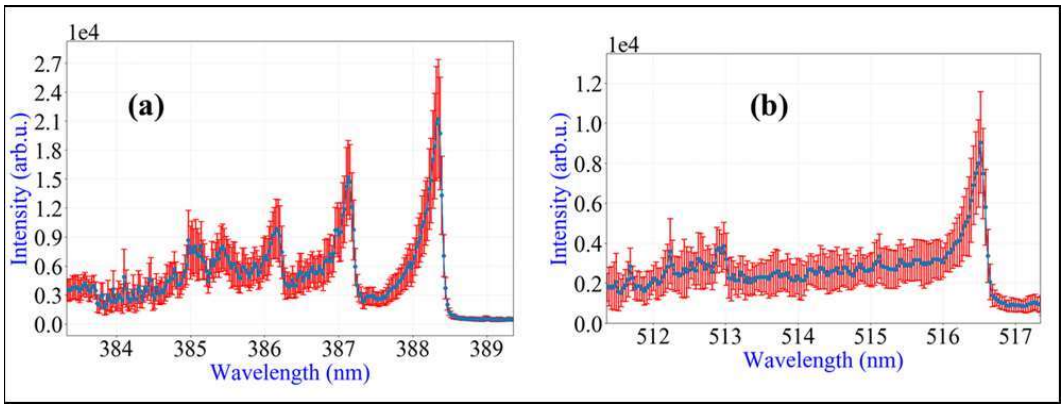

Figure 2.22 The standard deviation (in red) and mean (in blue) of the (a) CN band and (b) C_2 band in the grazing incidence FIBS spectra were calculated from the 14 spectra. Mean of CN peak was 21090.05 with standard deviation of 6578.48 for peak at 388.34 nm. Mean of C_2 was 8895.05 with standard deviation of 2651.24 for peak at 516.52 nm.

The observed spectrum is fitted to the modeled spectra from the Boltzmann equilibrium spectrum program for the CN and C_2 transitions. The Nelder-Mead algorithm was utilized to optimize the fitting of the theory spectrum with the collected experimental spectrum, assuming the local thermodynamic equilibrium described in previous reports [20, 35]. The software with the GUI given by Parigger et al. [36, 37] was employed for the current experiments. The best fit optimizes variables such as temperature and spectral line FWHM. Table 2.6 lists the temperatures of the CN and C_2 diatomic molecules that provided the best fit. Figure 2.23 depicts the optimal fit and experimental data of a single spectrum's CN and C_2 bands. As shown in table 2.6, the vibrational temperature was unaffected by fluctuations in the intensities of the CN most significant peak at 388.3 nm and the C_2 highest peak at 516.5 nm, as the temperature is dependent on the overall band strength [38]. Even though the limit of detection improved with decreasing particle size in the case of mesoporous V-SiO_2 catalysts [39], more research could aid in better understanding because the threshold fluence depends on density and thermal properties of the material other than just particle size in powder samples [7,40].

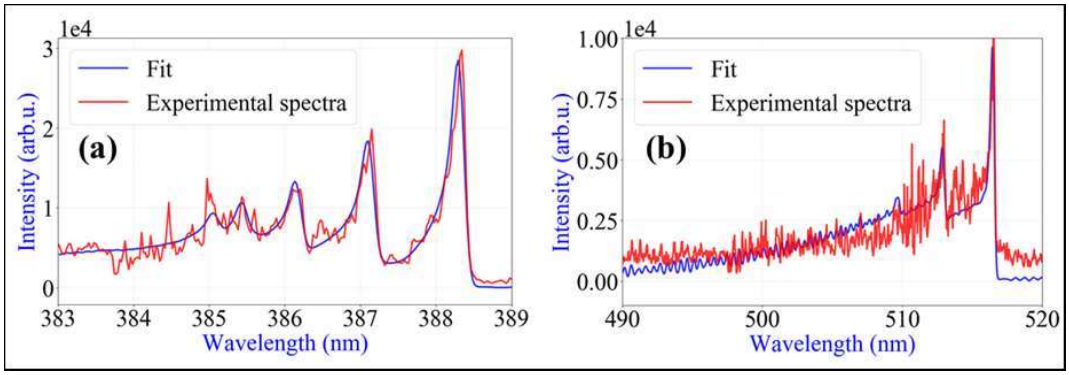

Figure 2.23 The fitting of the computed spectra (fit in blue) with the experimental spectra (in red) for the temperature estimation form (a) CN band and (b) C_2 band. The temperature of 6536K for CN and FEHM was 0.15 nm, and the temperature of C_2 was 5436 K and FWHM of 0.25 nm.

Table 2.6 Vibrational temperature in degrees kelvin and peak intensities of the CN (388.3 nm) and C_2 (516.5 nm).

CN (^{0}K)	CN peak intensity (arb. units)	C_2 (^{0}K)	C_2 peak intensity (arb. units)
6536	10128.8	5436	4971.67
6551	23175.6	6803	7954.85
6661	16917	6413	8690.26
6530	33729	6375	13845
6451	29735.7	6342	11567.7
6755	19524.5	6239	6989.81
6689	24779.7	6042	10909.4
6139	28798.2	6150	12384
6573	14920.2	6450	5769.55
5869	20237	6035	9311.04
6311	19507.6	5999	7813.34
6239	13736.7	6744	5989.55
6594	18919.5	6764	7846.85
6351	23459.7	6296	10557.9

The FIBS spectra of commercially available talcum powder (Ponds) were also recorded. The interaction was reduced compared to graphite powder and could be attributed to the granular nature of talcum powder not as fine as graphite, resulting in a less intense noisy spectrum. Figure 2.24 depicts the FIBS spectrum of talcum powder. Figure 2.25 depicts the elemental peaks of calcium, magnesium, sodium, and potassium identified from the talcum powder spectrum. Figure 2.26 depicts the calcium peaks identified from the NIST database. Table 2.7 summarizes all the identified peaks from the FIBS spectra of talcum powder.

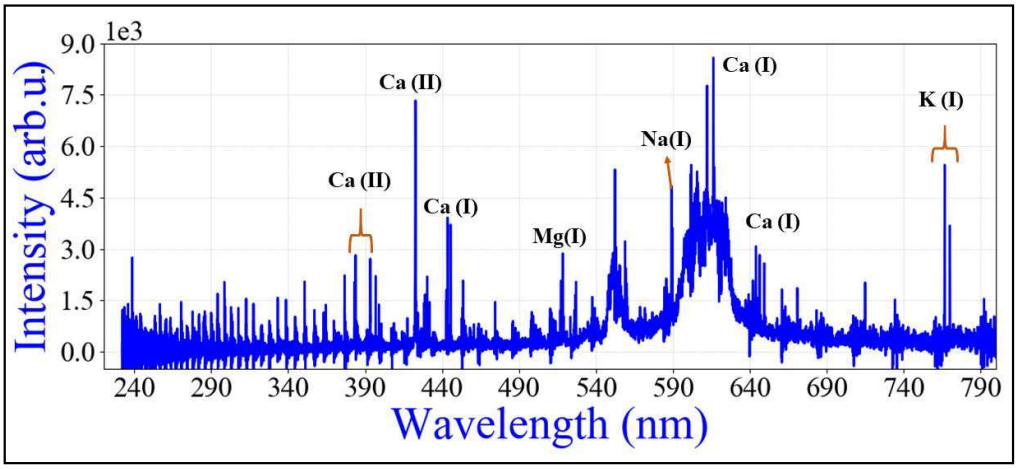

Figure 2.24 Grazing incidence FIBS spectrum of the commercially available talcum powder (Ponds) with the major peaks of calcium, magnesium, sodium, and potassium identified.

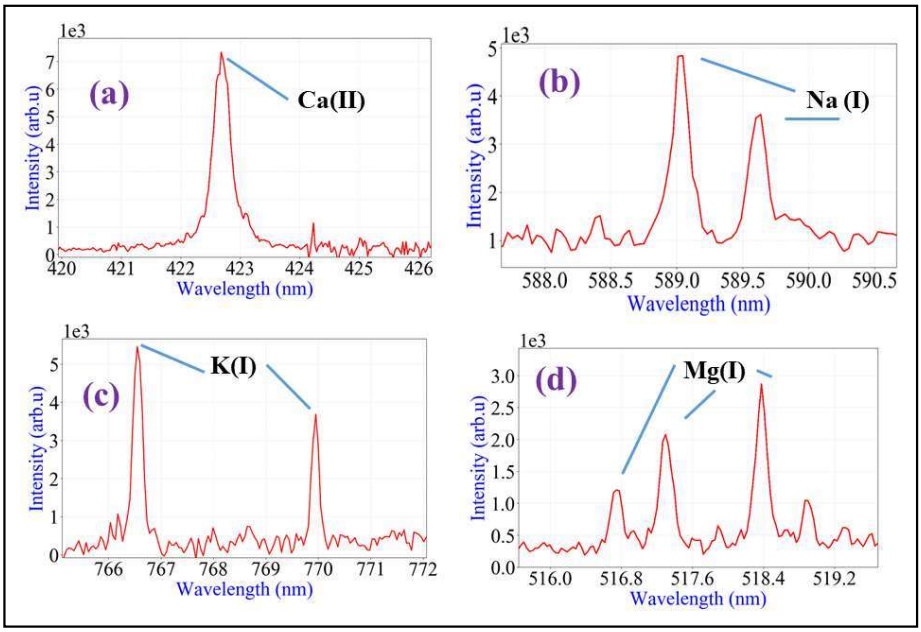

Figure 2.25 The elemental peaks of singly ionized (a) calcium, (b) sodium, (c) potassium, (d) magnesium were identified from the FIBS spectrum of commercially available talcum powder (Ponds).

Figure 2.26 shows the doubly ionized calcium peak at 422.67 nm, sodium peaks at 589.03 nm, 589.63 nm, potassium peaks at 766.56 nm, 769.93 nm, and magnesium peaks at 516.76 nm, 517.30 nm, and 518.38 nm. As shown in figure 2.26, the calcium singly ionized peaks at 428.36 nm, 428.93 nm, 430.25 nm, 442.54 nm, 612.22 nm, 616.21 nm, 643.90 nm, 644.98 nm, and doubly ionized peaks at 393.36 nm, 396.84 nm were recognized using the NIST atomic spectrum database. Compared to graphite powder, the interaction with talcum powder was modest, and the accompanying FIBS spectrum was noisy. Table 2.7 shows the identified peaks from the FIBS spectra of the talcum powder.

Table 2.7 The elemental peaks in the FIBS spectra of talcum powder were identified from the NIST database.

Elements	**Peaks from FIBS spectrum (nm)**	**Peaks identified from the NIST database (nm)**
Mg	516.73,517.29, 518.37	516.73, 517.26, 518.36
Ca	393.37,396.87,428.31,428.94, 430.27, 442.56, 443.50, 445.49, 612.24, 616.25, 643.92, 644.85, 645.52, 646.31, 649.41.	393.36, 396.84, 428.36, 428.93, 430.25, 442.54, 443.49, 445.47, 612.22, 616.21, 643.90, 644.98, 645.56, 646.25, 649.37.
K	766.56, 769.95	766.48, 769.89
Na	588.63, 589.63	588.99, 589.59

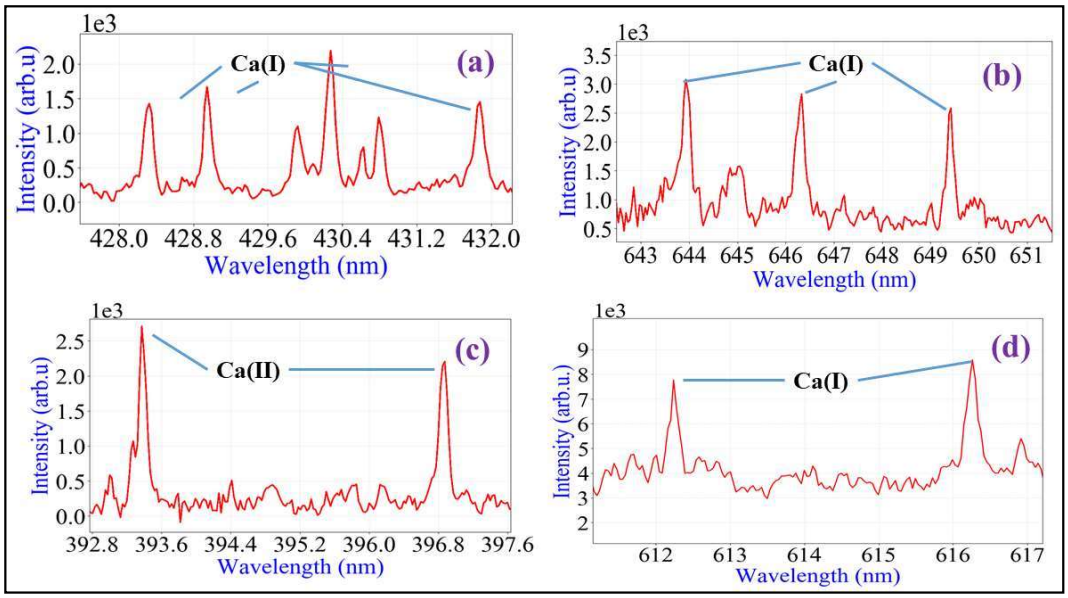

Figure 2.26 The calcium peaks identified from the FIBS spectra of commercially available talcum powder in low quantities (a), (b), and (d) singly ionized calcium peaks, and (c) doubly ionized calcium peaks.

References

[1] D. A. Cremers and L. J. Radziemski, Handbook of laser-induced breakdown spectroscopy. John Wiley & Sons; 2013 May 13.

[2] N. L. Murthy, S. A. Salam, and S. V. Rao, Stand-off Femtosecond Laser-Induced Breakdown Spectroscopy of Metals, Soil, Plastics and Classification Studies, in 2019 Workshop on Recent Advances in Photonics (WRAP) (2019), pp. 1–3. doi:10.1109/WRAP47485.2019.9013674.

[3] J. M. Gomba, C. D'Angelo, D. Bertuccelli, and G. Bertuccelli, Spectroscopic characterization of laser-induced breakdown in aluminium-lithium alloy samples for quantitative determination of traces, Spectrochim. Acta - Part B At. Spectrosc. 56, 695–705 (2001). doi:10.1016/S0584-8547(01)00208-7

[4] A. Ciucci, M. Corsi, V. Palleschi, S. Rastelli, A. Salvetti, and E. Tognoni, New procedure for quantitative elemental analysis by laser-induced plasma spectroscopy, Appl. Spectrosc. 53, 960–964 (1999). doi:10.1366/0003702991947612.

[5] S. S. Harilal, C. V Bindhu, V. P. N. Nampoori, and C. P. G. Vallabhan, Temperature in a Laser-Produced Plasma from YBa 2 Cu 3 O 7, 52, 449–455 (1998). doi:10.1007/s003400050448.

[6] J.P. Singh, S.N. Thakur, Laser-induced breakdown spectroscopy, Elsevier, 2020.

[7] D.A. Cremers, L.J. Radziemski, Handbook of laser-induced breakdown spectroscopy, John Wiley & Sons, 2013.

[8] V.K. Unnikrishnan, K. Mridul, R. Nayak, V.B. Kartha, C. Santhosh, G.P. Gupta, K. Alti, B.M. Suri, Calibration-free laser-induced breakdown spectroscopy for quantitative elemental analysis of materials, Pramana - J. Phys. 2012, 79, 299–310. doi:10.1007/s12043-012-0298-1.

[9] V. Motto-Ros, A.S. Koujelev, G.R. Osinski, A.E. Dudelzak, Quantitative multi-elemental laser-induced breakdown spectroscopy using artificial neural networks, J. Eur. Opt. Soc. Rapid Publ. 3 (2008). doi:10.2971/jeos.2008.08011.

[10] E.N. Rao, P. Mathi, S.A. Kalam, S. Sreedhar, A.K. Singh, B.N. Jagatap, S.V. Rao, Femtosecond and nanosecond LIBS studies of nitroimidazoles: Correlation between molecular structure and LIBS data, J. Anal. At. Spectrom. 31 (2016) 737–750. doi:10.1039/c5ja00445d.

[11] S.S. Harilal, J. Yeak, B.E. Brumfield, J.D. Suter, M.C. Phillips, Dynamics of molecular emission features from nanosecond, femtosecond laser and filament ablation plasmas, J. Anal. At. Spectrom. 31 (2016) 1192–1197. doi:10.1039/c6ja00036c.

[12] S.A. Kalam, N.L. Murthy, P. Mathi, N. Kommu, A.K. Singh, S.V. Rao, Correlation of molecular, atomic emissions with detonation parameters in femtosecond and nanosecond LIBS plasma of high energy materials, J. Anal. At. Spectrom. 32 (2017) 1535–1546. doi:10.1039/c7ja00136c.

[13] V.K. Unnikrishnan, R. Nayak, K. Aithal, V.B. Kartha, C. Santhosh, G.P. Gupta, B.M. Suri, analysis of trace elements in complex matrices (soil) by Laser Induced Breakdown Spectroscopy (LIBS), Anal. Methods. 5 (2013) 1294–1300. doi:10.1039/C2AY26006A.

[14] S. Pandhija, N.K. Rai, A.K. Rai, S.N. Thakur, Contaminant concentration in environmental samples using LIBS and CF-LIBS, Appl. Phys. B Lasers Opt. 98 (2010) 231–241. doi:10.1007/s00340-009-3763-x.

[15] H. Shakeel, S.U. Haq, G. Aisha, A. Nadeem, Quantitative analysis of Al-Si alloy using calibration free laser induced breakdown spectroscopy (CF-LIBS), Phys. Plasmas. 24, (2017) 063516. doi:10.1063/1.4985327.

[16] A. De Giacomo, C. Koral, G. Valenza, R. Gaudiuso, M. Dellaglio, Nanoparticle Enhanced Laser-Induced Breakdown Spectroscopy for Microdrop Analysis at subppm Level, Anal. Chem. 88 (2016) 5251–5257. doi:10.1021/acs.analchem.6b00324.

[17] C. Koral, A. De Giacomo, X. Mao, V. Zorba, R.E. Russo, Nanoparticle enhanced laser induced breakdown spectroscopy for improving the detection of molecular bands, Spectrochim. Acta Part B At. Spectrosc. 125 (2016) 11–17. doi :10.1016/j.sab.2016.09.006.

[18] M. Weidman, Laser Filamentation Interaction with Materials for Spectroscopic Applications, (2012). Electronic Theses and Dissertations. 2385. https://stars.library.ucf.edu/etd/2385

[19] K.M.Muhammed Shameem, P. Madhusudhan, R. Das, P. Bhardwaj, V. Nimma, S. Soumyashree, R.K. Kushawaha, Molecular emission dynamics from a femtosecond filament induced plasma plume, J. Opt. 24 (2022) 044015. doi:10.1088/2040-8986/ac528a.

[20] S.L. Chin, W. Liu, F. Théberge, Q. Luo, S.A. Hosseini, V.P. Kandidov, O.G. Kosareva, N. Aközbek, A. Becker, H. Schroeder, Some fundamental concepts of femtosecond laser filamentation, Springer Ser. Chem. Phys. 89 (2008) 243–264. doi:10.1007/978-3-540-73794-0_12.

[21] S.S. Harilal, J. Yeak, M.C. Phillips, Plasma temperature clamping in filamentation laser induced breakdown spectroscopy, Opt. Express. 23 (2015) 27113. doi:10.1364/oe.23.027113.

[22] S.S. Harilal, J. Yeak, B.E. Brumfield, M.C. Phillips, Consequences of femtosecond laser filament generation conditions in standoff laser induced breakdown spectroscopy, Opt. Express. 24 (2016) 17941. doi:10.1364/oe.24.017941.

[23] H.L. Xu, J. Bernhardt, P. Mathieu, G. Roy, S.L. Chin, Understanding the advantage of remote femtosecond laser-induced breakdown spectroscopy of metallic targets, J. Appl. Phys. 101 (2007) 033124. doi:10.1063/1.2437580.

[24] S. Abdul Kalam, S. V. Balaji Manasa Rao, M. Jayananda, S. Venugopal Rao, Standoff femtosecond filament-induced breakdown spectroscopy for classification of geological materials, J. Anal. At. Spectrom. 35 (2020) 3007–3020. doi:10.1039/d0ja00355g.

[25] K. Stelmaszczyk, P. Rohwetter, G. Méjean, J. Yu, E. Salmon, J. Kasparian, R. Ackermann, J.P. Wolf, L. Wöste, Long-distance remote laser-induced breakdown spectroscopy using filamentation in air, Appl. Phys. Lett. 85 (2004) 3977–3979. doi:10.1063/1.1812843.

[26] H. Li, W. Chu, H. Zang, H. Xu, Y. Cheng, S.L. Chin, Critical power and clamping intensity inside a filament in a flame, Opt. Express. 24 (2016) 3424-3431. doi:10.1364/oe.24.003424.

[27] S.L. Chin, T.-J. Wang, C. Marceau, J. Wu, J.S. Liu, O. Kosareva, N. Panov, Y.P. Chen, J.-F. Daigle, S. Yuan, A. Azarm, W.W. Liu, T. Seideman, H.P. Zeng, M. Richardson, R. Li, Z.Z. Xu, Advances in intense femtosecond laser filamentation in air, Laser Phys. 22 (2012) 1–53. doi:10.1134/s1054660x11190054.

[28] H.L. Xu, S.L. Chin, Femtosecond laser filamentation for atmospheric sensing, Sensors. 11 (2011) 32–53. doi:10.3390/s110100032.

[29] L.A. Finney, P.J. Skrodzki, M. Burger, J. Nees, S.S. Harilal, I. Jovanovic, Single-shot, multi-signature remote detection of uranium by filament-induced breakdown spectroscopy, Opt. Lett. 44 (2019) 2783-2786. doi:10.1364/ol.44.002783.

[30] AK Shaik, Ajmathulla, V.R. Soma, Discrimination of bimetallic alloy targets using femtosecond filament-induced breakdown spectroscopy in standoff mode, Opt. Lett. 43 (2018) 3465-3468. doi:10.1364/ol.43.003465.

[31] AK Shaik, N.R. Epuru, H. Syed, C. Byram, V.R. Soma, Femtosecond laser induced breakdown spectroscopy based standoff detection of explosives and discrimination using principal component analysis, Opt. Express. 26 (2018) 8069-8083 . doi:10.1364/oe.26.008069.

[32] M. Burger, P.J. Skrodzki, L.A. Finney, J. Nees, I. Jovanovic, Remote detection of uranium using self-focusing intense femtosecond laser pulses, Remote Sens. 12 (2020) 1–12. doi:10.3390/RS12081281.

[33] L.M. Narlagiri, C. Byram, S.K. Satani, V.R. Soma, Laser beam steering automation with an Arduino-based CNC shield forstandoff femtosecond filament-induced breakdown spectroscopicstudies, Appl. Opt. 61 (2022) 4947–4955. doi:10.1364/AO.453824.

[34] L. Narlagiri, V.R. Soma, Simultaneous quantification of Au and Ag composition from Au–Ag bi-metallic LIBS spectra combined with shallow neural network model for multi-output regression, Appl. Phys. B Lasers Opt. 127 (2021) 1–11. doi:10.1007/s00340-021-07681-y.

[35] R. Junjuri, S.A. Nalam, E. Manikanta, S.S. Harsha, P.P. Kiran, M.K. Gundawar, Spatio-temporal characterization of ablative Cu plasma produced by femtosecond filaments, Opt. Express. 29 (2021) 10395-10405. doi:10.1364/oe.417842.

[36] C.G. Parigger, A.C. Woods, D.M. Surmick, G. Gautam, M.J. Witte, J.O. Hornkohl, Computation of diatomic molecular spectra for selected transitions of aluminum monoxide, cyanide, diatomic carbon, and titanium monoxide, Spectrochim. Acta - Part B At. Spectrosc. 107 (2015) 132–138. doi:10.1016/j.sab.2015.02.018.

[37] M.J. Witte, Diatomic Carbon Measurements with Laser- Induced Breakdown Spectroscopy, (2015). https://trace.tennessee.edu/utk_gradthes/3423/. Last accessed on 2nd july.

[38] S.S. Harilal, R.C. Issac, C. V. Bindhu, P. Gopinath, V.P.N. Nampoori, C.P.G. Vallabhan, Time resolved study of CN band emission from plasma generated by laser irradiation of graphite, Spectrochim. Acta - Part A Mol. Biomol. Spectrosc. 53 (1997) 1527–1536. doi:10.1016/S1386-1425(97)00062-0.

[39] M. Pouzar, T. Kratochvíl, S. Kaski, J. Kaiser, P. Knotek, L. Apek, T. Ernohorský, Effect of particle size distribution in laser-induced breakdown spectroscopy analysis of mesoporous V-SiO2 catalysts, J. Anal. At. Spectrom. 26 (2011) 2281–2288. doi:10.1039/c1ja10167f.

[40] S.A. Beal, A.M. Mossell, J.L. Clausen, Matrix and Target Particle-Size Effects on LIBS Analysis of Soils, (2020). https://apps.dtic.mil/sti/citations/AD1091335

3 Machine learning in LIBS data analysis

Abstract: The method of categorizing and identifying metals and metal alloys using colour CCD (Charge coupled device) images of femtosecond (fs) laser-produced plasma emissions has been demonstrated. The machine learning method for identification was trained using the non-gated colour CCD images of the plasma emissions. The current work investigates the feasibility of identifying Steel, aluminium (Al), Copper (Cu), bronze, and other metals using CCD images. The results of the principal component analysis (PCA) was used as input to the support vector machine (SVM) for identification. Further gold (Au) and silver (Ag) compositions were simultaneously predicted using the multi-output regression model from the LIBS spectra from Au-Ag bimetallic target. To estimate the composition of one element each, the shallow neural networks model for multi-output regression uses two nodes at the output layer. The trained model was used to predict from Au30-Ag70 LIBS spectra not seen by the model and weren't a part of the training set after being evaluated on the test set. We demonstrate the usefulness of this methodology within 10% error.

3.1 Machine learning in the identification of metals and alloys

3.1.1 Introduction

Using the emissions from the recombinations from the cooling plasma produced by intense and short laser pulses focused on the sample, the constituent elements can be detected using the LIBS technique [1-2]. Explosive detection [3-4], mining [5], elemental mapping of mineral samples [6], underwater chemical analysis utilizing standoff LIBS [7], exploration of planets [8], and detecting nutrients and pollutants in edibles [9] are just a few of the many fields that benefit from LIBS. The ability to increase signal strength using techniques like double-pulse with varying wavelength LIBS [10], double-pulse LIBS with variable pulse widths [11], and nanoparticle-enhanced LIBS [12–14] is another benefit of LIBS. The automated LIBS system was used to separate recyclable metal and plastic. In complicated matrices like minerals and soils, it is also utilized for trace element analysis [15]. LIBS is a quick technique to securely test material from a distance in hazardous industrial contexts [16]. Compared to nanosecond pulses, femtosecond LIBS offers the additional benefit of intense molecular emissions [17]. LIBS was used with machine learning to identify the geological origins of precious stones like jade [18]. It was used for

real-time analysis of geological samples [19]. Even from non-gated spectrometer data with a plasma continuum background, machine learning techniques have demonstrated an increase in the classification of similar stoichiometry substances, such as pharmaceuticals [20]. Compared to regularly processed spectra, the classification accuracy of the chosen pixels from an echellogram (greyscale CCD image of plasma emissions through dispersive elements) was outstanding [21]. In the classification of plastic materials, Erwan Negre et al. used gated ICCD images of plasma plumes acquired with narrow bandwidth filters [22]. In rectifying the underwater LIBS signal fluctuations, the images of the plasma plume were employed to normalize the spectral line intensity with the plasma intensity [23]. In the present study, plasma emissions recorded using colour CCD sensor via an optical fiber rather than being imaged or directed to a spectrometer. Machine learning algorithms were utilized in the analysis of the images. Many machine-learning techniques were used to analyze the standoff data for rapid classification, identification, and accuracy. Studies comparing the remote LIBS with the standoff LIBS for standoff up to 2 m and up to 8.5 m remote detection were reported [16]. It is asserted that at a 5 m standoff distance, LDA (Linear discriminant analysis) performance exceeded PCA in classification and that LDA with two spectrometers significantly improved prediction classification accuracy [24]. It was also asserted that the LDA method addressed the disadvantage of a miniature spectrometer (Czerny-Turner) with a limited spectral range and resolution to achieve high classification accuracy. The classification performance of a single-channel spectrometer (Czerny-Turner) was nearly identical to that of an Echelle spectrometer with a broad spectral range using the research of LDA. The archaeological samples were probed using standoff LIBS at 6.2 m, and the PCA scores were used as input data. Additionally, ANN was used to predict the material properties with good accuracy. When the PCA was applied to remote LIBS spectra of high-energy materials (HEMs), the first three PCs accounted for 88% of the variation, equivalent to the results at a standoff distance of 50 cm. Coaxial double-pulse laser excitation was employed in standoff LIBS to distinguish between different steel classes [25–27]. When heated in air, an oxide layer was formed on the steel samples' surface. The chemical composition of such a layer is different from the bulk. Discriminant function analysis, usually called DFA, was selected as the statistical method for classifying the steel classes. Junjuri et al. [28] examined standoff (1-m) detection of bulk explosives (CL-20, TNT, HMX, RDX, NTO) using nanosecond laser pulses in a laboratory setting. An excellent classification was achieved using PCA and the ratiometric methods. Junjuri et al. [29] extended their standoff (6.5 m) efforts using a single shot mode

and simple CCD spectrometer, employing ANN. A better identification accuracy (98% and 94%) was achieved in terms of the data (i) among explosives, (ii) explosives, and non-explosives. By carefully selecting a suitable lens that matches the F-number of the employed spectrometer, the collection system was optimized for obtaining the best signal. The plasma plume was recorded using CCD for an effective light coupling. A 10 cm aperture lens was used to record the spectra. The lens's larger aperture resulted in the doubled intensity. LIBS technique was used at 20 m to discriminate between five different organophosphate nerve agent simulants [30]. Using a single ST-LIBS sensor in conjunction with the partial least square – discriminant analysis (PLS-DA) model for hazardous compound detection, the potential of standoff LIBS was exemplified. The machine learning algorithms are helpful in the standoff LIBS data analysis in the subsequent chapters.

3.1.2 Experimental details

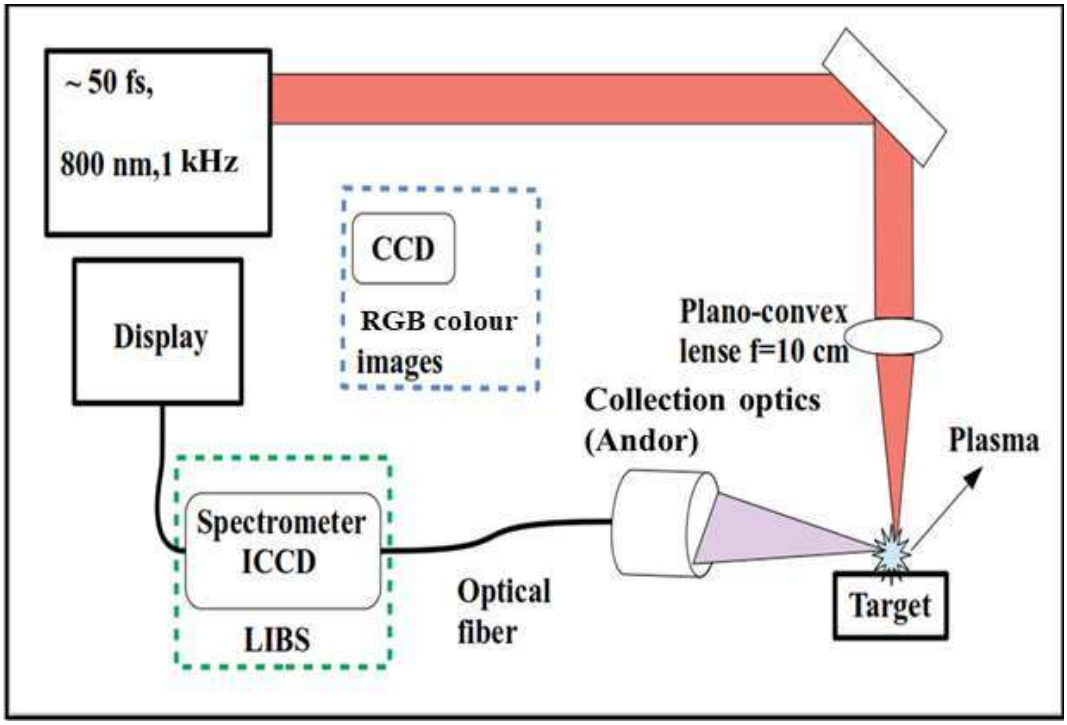

Figure 3.1 Experimental setup for femtosecond LIBS and capturing the colour CCD images. The ICCD and spectrometer combination in the green dotted box is used for LIBS studies and imaging of plasma emissions, only CCD in the blue dotted box.

The femtosecond pulses at 1.2 mJ per pulse were directed at the target sample. The gate delay and width used to record the fs LIBS spectra were 150 ns and 100 ns, respectively. The blue dotted box in figure 3.1 illustrates how the plasma emissions were collected and supplied to a colour CCD (M/s Samsung colour digital isight inside model number SHC-410PF) through an optical fiber. Twenty spectra obtained with one second exposure time were used for the PCA analysis. Locally available Al 6 series with a purity of 98%, Cu with a purity of 99% and traces of impurities, Bronze with 90% Cu, 10% zinc, stainless steel 304 with 65-70% Fe and 18% Cr, 8% Ni were used for the studies. Only Al and Steel have emissions in violet, and the ionic and atomic emissions of Al, Bronze, Cu, and steel in the ultraviolet (300 nm) (420 nm). steel, Cu, and Bronze all have peaks in the wavelength ranges of blue (470 nm) and cyan (500 nm). Although their magnitude was weak, Cu and bronze have transitions in the infrared (800 nm) range. As shown in figure 3.2, these colours are visible in the corresponding plasma emissions images. AlO, which forms in the later stages of plasma recombinations, was found in corresponding colour regions of blue, cyan, and partially green regions of the LIBS spectra[31,32]. This observation serves as inspiration for the present studies to classify the samples form the plasma emissions using coloured CCD images shown in figure 3.3. Using PCA score plots, classification and identification capabilities of the recorded fs-LIBS spectra were compared to the non-gated colour CCD images from the colour CCD sensor, which were taken at regular intervals. The observed persistent peaks are tabulated in table 3.1 below correlating with colors.

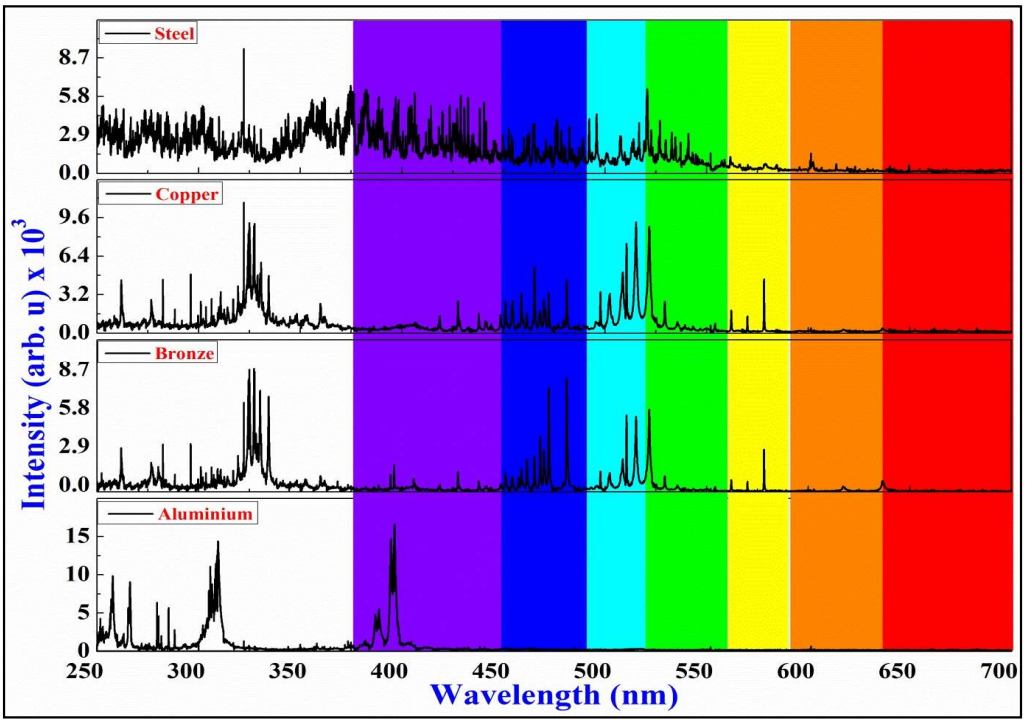

Figure 3.2 Fs-LIBS spectra of Al, Cu, bronze, and steel. The corresponding colour regions (violet, indigio, cyan, green, yellow, orange, and red) are for comparison with the colour CCD images from the plasma emissions.

Table 3.1 LIBS spectral peaks identified from NIST database [33] .

Elements	Identified Peaks (nm)
Al	394.4, 396.15, 386.61, 308.16, 308.405, 309.18, 309.52
Cu	324.75, 327.39, 465.11, 502.48, 508.83, 510.65, 515.44, 521.89, 578.29,
Zn	330.29, 334.5, 472.22, 481.1, 636.23
Pb	363.97, 368.35, 373.99, 504.78
Fe	358.11, 371.99, 373.48, 373.71, 374.55, 374.82, 374.94, 375.82, 382.04, 385.99, 388.62, 404.58, 438.35
Cr	396.46, 396.68, 398.46, 399.05, 400.2, 416.57, 425.5, 427.25, 434.54, 435.27, 416.57, 425.5, 427.25, 434.54, 435.27, 520.67, 529.93, 532.92, 541.1
Mn	3405.64, 344.13, 344.18, 346.64, 346.05, 347.64, 347.38, 349.15, 349.8, 405.86, 406.44, 406, 408.41, 408.4,460.17, 460.48, 462.73, 462.68, 471.2, 471.09, 476.72, 476.35, 478.46, 478.42, 482.47, 482.29

3.1.3 Analysis of colour CCD images of plasma emissions

Generally CCDs have three sensitive regions in 350 nm to 850 nm range. The blue, green, and red colour regions at the corresponding wavelengths each have one peak in the sensitivity curves. The Bayer filter mosaic, a selectively transmissive colour filter array (CFA) on a grid of photosensors, is the colour CCD's building block. Most cameras used to produce colour images employ single-chip digital image sensors. Green filters cover half of the square grid, while red and blue filters cover each of the remaining quadrants. As a result, it is also known as red-green-green-blue (RGGB) [34] or green-red-green-blue (GRGB) [35]. Using 600 μ optical fibre, the emissions from the plasma are directed toward the sensor.

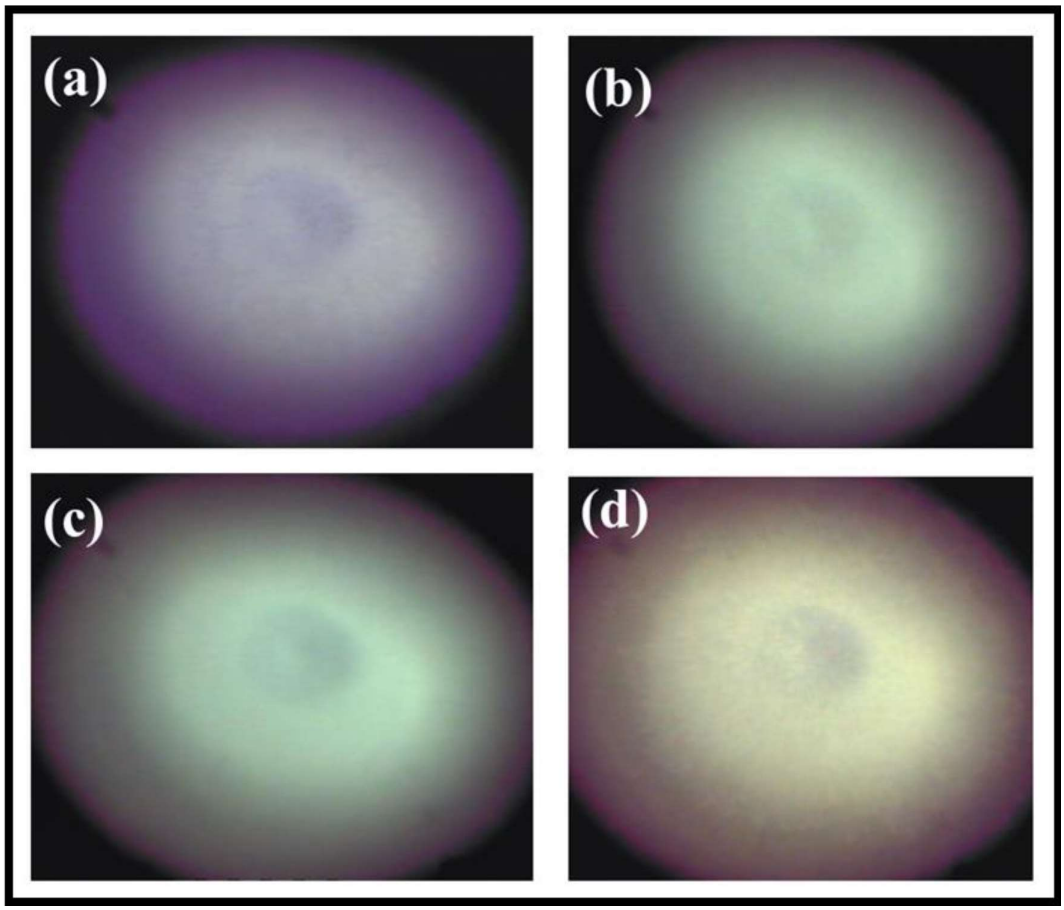

Figure 3.3 Colour CCD images of plasma emissions produced when the femtosecond laser pulses ablating the (a) Al, (b) bronze, (c) Cu, (d) steel targets. The emissions video was recorded at 29 to 30 frames per second.

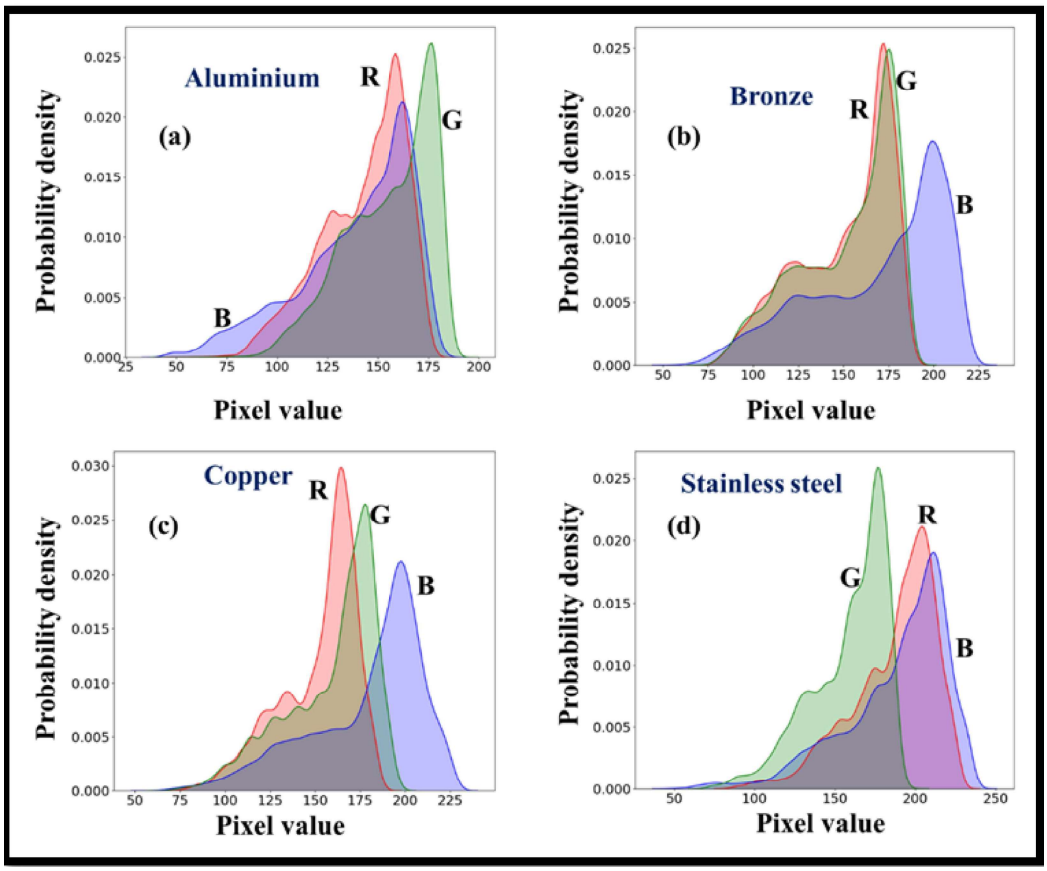

Figure 3.4 KDE plots of blue, red, and green channels pixel values from the CCD images of plasma emissions produced form the (a) Al, (b) bronze, (c) Cu, (d) steel targets.

Histograms and kernel density estimates are closely linked. However, when a kernel uses ImageJ software, the images are extracted from the video using ImageJ software [36]. As the laser operates at 1 kHz, each frame integrates light from the plasma emission of 33–34 pulses interacting with the sample. Each image consists of 500 pixels vertically and 700 pixels horizontally. Only a section of the image, which contains the circular portion and ranges in size from 50 to 300 pixels vertically and 50 to 300 pixels horizontally, was extracted. Three values represent red, blue, and green channels at each pixel. The RGB image's green channel was used for the studies. Pixel values are arranged in a 250 by 250 matrix on a single channel. The rows of this matrix were added to create an array of 250 values for the analysis. Figure 3.3 displays the colour CCD images of the plasma emissions from the four samples. Figure 3.3 represents the color image of plasma emissions from (a) Al, (b) bronze, (c) Cu, and (d) steel.

The probability density of a continuous variable is represented by a kernel density estimate (KDE). The Gaussian kernel is used for the present studies, and histograms inherit the qualities like continuity. The four samples' KDE plots for the image's blue,green and red channels are illustrated in figure 3.4, with distinguishable curves from each colour.

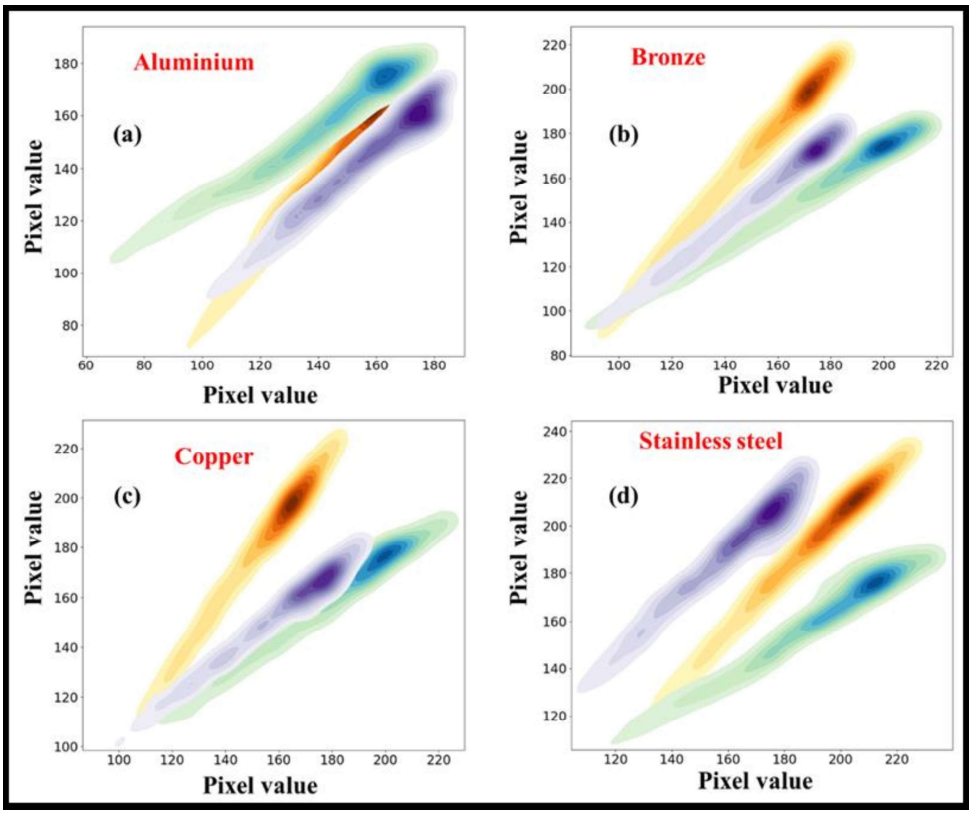

Figure 3.5 Two-dimensional KDE plots correlating the pixel values from blue-green, blue-red and red-green channels of the plasma emission images from (a) Al, (b) bronze, (c) Cu, (d) steel.

Intermediate colours like purple, brown, cyan are produced due to the intersection in the sensitivity of RGB filters. Each sample's correlation of colour pairs is investigated using 2D KDE plots. Blue-red in purple, red-green in brown, and the combined blue-green channel in cyan. Figure 3.5 illustrates the probability density on pixel values for four samples Al, bronze, Cu, and steel forming distinguishable 2D density plots for each of the combinations of RGB channels (R-B, R-G, and G-B). These associations imply that metal sample categorization and identification can be accomplished using colour CCD pictures.

3.1.4 PCA of LIBS spectra and colour CCD images of plasma emissions

Figure 3.6(a) shows the categorization of four classes of LIBS spectra, and figure 3.6(b) shows the classification using colour CCD images. The LIBS spectra are highly accurately identified by comparing LIBS spectra to colour CCD images.

3.1.5 Results and discussion

The model was created by combining supervised (SVM) and unsupervised (PCA) learning algorithms. The red, blue, and green channel pixel values make up the CCD picture matrix. The green channel of each image is transformed into a 250-value array by summing along one dimension of the matrix. The principal component analysis is utilized to reduce the dimensionality. Thus, the least useful variables can be discarded while keeping the most valuable variable; this procedure is known as feature extraction. The first three PCs achieved significant accuracy. As seen in figure 3.6, one point on the plots represents one image or one spectrum.

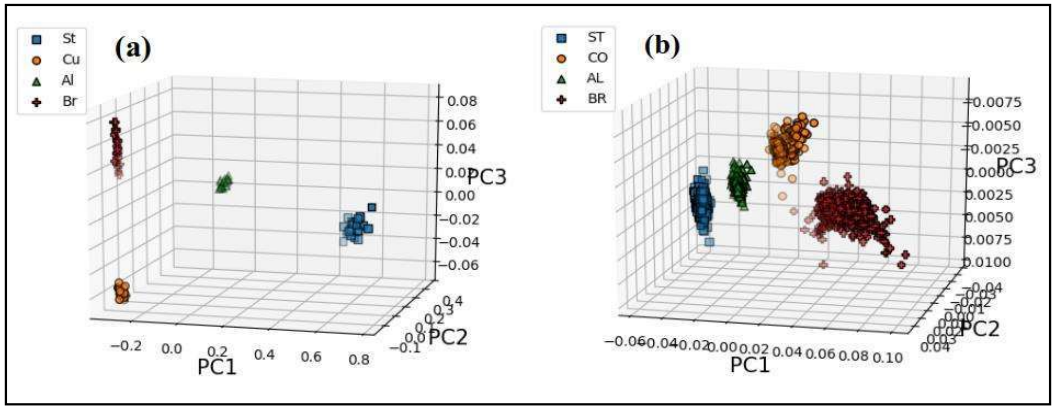

Figure 3.6 PCA score plots of (a) fs-LIBS spectra of the four samples. The Triangle marker corresponds to Al, the square marker to steel, the circle marker to copper, plus marker to bronze, and (b) the colour CCD images of plasma emissions from the same samples.

The first three PCs were fed as input to the SVM algorithm for identification. The algorithm takes a one-to-one approach for all the conceivable pairs to achieve multiclass classification. It starts with a plane that parts both classes, and the algorithm finds a plane splitting the classes with the great margin distance from the two extreme points of both classes. The margin distance (γ) and the other factors are adjusted in both cases of LIBS spectra and colour images for improved performance. The results are charted in table 3.2 and table 3.3.

- The variables that were retrieved from the PCA were divided into two groups at random, with the first half being utilized for training the algorithm. The SVM algorithm randomly assigned the remaining half of the images without labels for identification. 2190 images, in total, were used for testing. Even with little adjustments to the parameters C, gamma produced good results despite the image data being slightly imbalanced. Remarkably, the average prediction accuracy of the images from the four samples of Al, Bronze, Cu, and steel reached 100%.

- Precision is the capability of SVM not to label an occurrence positive that is negative. Each class is the ratio of true positives to the sum of true and false positives.
- The recall is the capability of SVM to find every positive occurrences. It is the ratio of true positives to the sum of true positives and false negatives.
- The F1 score is a weighted harmonic mean of precision and recall such that the best score is 1.0 and the worst is 0.0. Generally, F1 scores are lower than accuracy measures as they embed precision and recall into their computation.
- Support is the number of data points from different classes given to the trained SVM to identify.

3.1.6 Conclusions

We conclude that the colour CCD images are indispensable for the classification studies by comparing the PCA investigations on LIBS spectra and colour CCD images with the femtosecond pulses. Given that they are not time-gated, the images form as separate, extended clusters. When trained with SVM for identifying metal samples from plasma emissions, the colour CCD images provided 100% accuracy, just like LIBS. These findings demonstrate that easy class separation from plasma emissions can be accomplished even with a broad spectral resolution (in this instance, the green filter). In contrast to the 22424 data points from the LIBS spectrum, we could obtain this result with just 250 values retrieved from each image. Tables 3.2 and 3.3 present an overview of the outcomes of the prediction techniques. We believe this research has great potential for industrial applications (e.g., waste management by sorting scrap in environmental monitoring). This technique will simplify keeping track of known and pre-labelled simple classes for repetitive monitoring. The research can be expanded to include miscellaneous classes using multispectral images. For instance, difficult classes like explosives and mineral ores can be categorized and identified.

Table 3.2 Results of SVM on extracted features from PCA time series LIBS spectra of the samples investigated in the present study.

Elements	precision	recall	F1-score	support
Al	1.00	1.00	1.00	12
Bronze	1.00	1.00	1.00	10
Cu	1.00	1.00	1.00	8
Steel	1.00	1.00	1.00	7
Accuracy			1.00	37
Macro avg.	1.00	1.00	1.00	37
weighted avg.	1.00	1.00	1.00	37

Table 3.3 Results of SVM on extracted features from PCA of colour CCD images from the plasma emission of the samples studied in the present work.

Elements	precision	recall	F1-score	support
Al	1.00	1.00	1.00	604
Bronze	1.00	1.00	1.00	517
Cu	1.00	1.00	1.00	551
Steel	1.00	0.99	1.00	518
Accuracy			1.00	2190
Macro avg.	1.00	1.00	1.00	2190
weighted avg.	1.00	1.00	1.00	2190

3.2 Shallow neural network model for multi-output regression for quantification

The elemental analysis of the samples can be achieved using the atomic spectroscopy technique known as LIBS. It is based on the emission spectroscopy of the plasma formed by focusing a short laser pulse on to the sample, usually in a few nanosecond or ultrashort femtoseconds [37-39]. It is a quick method and can be modified for standoff and remote detection of target [40–44]. It has the advantage in identifying substances at lower concentrations and can also be used in conjunction with Raman spectroscopy [45]. Additionally, recent approaches, like NE-LIBS [46–49], found to improve the limit of detection by enhancing the LIBS signal. Numerous machine-learning techniques were used for categorizing and identifying the samples due to the rapid acquisition of large

amounts of data from atomic and ionic transitions in LIBS [50, 51]. LIBS data was also utilized for the quantification, which includes calibration and calibration-free techniques. For calibration-free techniques, compositions are estimated using plasma properties with the condition that the plasma composition should be representative of the material composition (stoichiometric ablation), which is reasonable when the power density on the sample surpasses 10^9 W/cm^2. Standard samples and calibration curves are required for the calibration method used for quantification. The plasma must be at local thermodynamical equilibrium, optically thin, and devoid of self-absorption [52]. The steps in the quantification process include i) determining the plasma temperature T using Boltzmann's equation, ii) determining the intensity of the peaks iii) determining the electron density n_e, iv) determining the density ratio of the sample of a particular element, v) and checking the criterion for optically thin conditions and LTE [53]. The plasma temperature must be calculated to assess the element composition of a sample. For reliable estimation using the calibration-free technique, careful spectral treatment is necessary, such as background and self-absorption correction. With correction, improved precision of an order of magnitude was reported [54]. By optimizing the temporal window of the LIBS acquisition, the CF-LIBS performance can be made even better [55]. The technique was used to quantify oxide layers in thin film [56], alloys and glasses [57], and oxide materials [58], and to monitor the composition of several elements in coral skeletons [59]. In environmental monitoring [60], monitoring the toxic compounds in the industrial waste [61], analysis of meteorite fragments [62], and elemental ratios in intermetallic nanoalloys and nano- composites [63] in the analysis of metals in waste foundry sand [64]. Several standardization techniques have been used in the calibration-free LIBS [65].

Simultaneously, regression models using machine learning techniques gradually replace the CF-LIBS in quantification investigations using the LIBS spectra. For the quantitative analysis of chromium in soil, LIBS in combination with neural networks was used [66]. An artificial neural network (ANN) was utilized to identify the primary elements in natural rocks and soil samples and quantify several elements using LIBS spectra [67]. This method builds a multivariate nonlinear function associating the LIBS spectra to the target composition. The study of the LIBS spectral dataset from the target samples with already known compositions is used to determine this function empirically. It was used in a variety of fields for the quantitative analysis of elements, including ceramics [68], soil analysis [69], the quantification of manganese in various glass matrixes [70], and the analysis of

plutonium oxide [71]. Calibration is carried out using principal component regression (PCR) and partial least-square regression to estimate Mn in glass (PLSR). In addition to calibration, the ANN is employed in the elemental analysis of solidified mineral melt samples [72] to correct self-absorption peaks in the CF-LIBS. It was found that multivariate calibration techniques can be applied in an unsupervised manner and are noise resistant. In the instance of pellets containing glass components like manganese at different weight percentages, the multivariate calibration was said to perform better than the univariate calibration [73]. The following is a list of some of the multivariate algorithms used for the calibration analysis in LIBS [74].

- Principal component regression (PCR)
- Principal covariates regression (PCovR)
- Partial least squares regression (PLSR)
- Multiple linear regression (MLR)
- Ridge regression (RR)
- ANN (Artifical Neural Network).

Unlike machine learning models, which reach saturation in accuracy at a particular data size, deep learning models' accuracy rises continuously as the size of the data increases. Additionally, many tuning parameters are available for optimizing the models. The use of time-resolved LIBS spectra as data augmentation for deep learning models is discussed here. We assess the model's performance on the unobserved composition of the one-shot multi-output regression result. The time-resolved LIBS spectra served as the training data for three shallow neural network models. The LIBS spectra obtained using nanosecond laser pulses demonstrate that the Au and Ag in the bimetallic alloy can be quantified simultaneously.

3.2.1 Experimental details

Aluminum (Al), copper (Cu), and Brass were utilized as the targets in the studies, along with four distinct alloy compositions (Au20-Ag80, Au30-Ag70, Au50-Ag50, and Au80-Ag20). Figure 2.18 illustrates the LIBS experimental technique, the plasma emissions produced by the recombination of ions and electron, were collected and directed through a 600-µ optical fiber to the intensified gated spectrometer. The spectra were recorded between 230 nm and 800 nm. For the training procedure, a total of 64 spectra from three compositions (Au20-Ag80, Au50-Ag50, and Au80-Ag20) as well as 2 spectra from each of Al, Cu, and Brass, were used. Each spectrum was collected from various targets positioned on the translation stage. Figures 3.7 and 3.8 show the LIBS spectra of the four distinct bimetal compositions and Cu, Brass, and Al in the relevant wavelength range. The details of the nanosecond laser parameter and the experimental setup are presented in chapter 2.

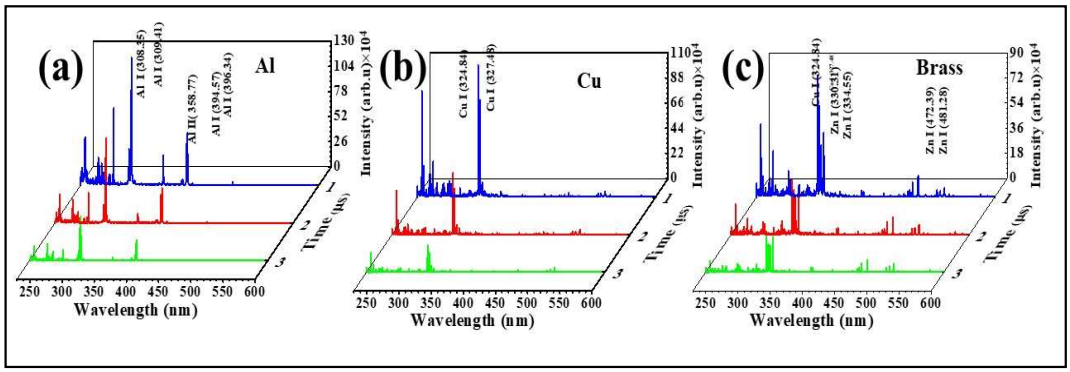

Figure 3.7 LIBS spectra collected at three gate delays of 1µs, 2 µs, and 3 µs. The spectra (a) Au20-Ag80, (c) Au50-Ag50, (d) Au80-Ag20are used for training the shallow neural network model of, and the unseen spectra (b) Au30-Ag70 were used for prediction by the model.

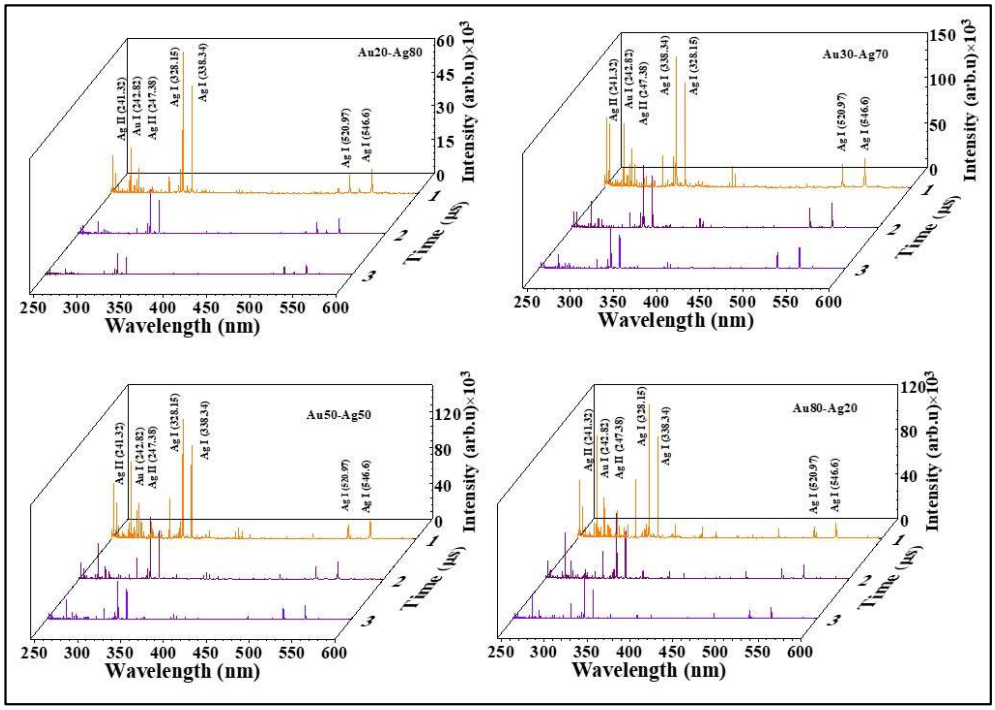

Figure 3.8 Ns-LIBS spectra collected at the gate delay of 1 µs, 2 µs, and 3 µs of (a) Aluminum, (b) copper and (c) Brass are used in the model training as zero composition of Au-Ag.

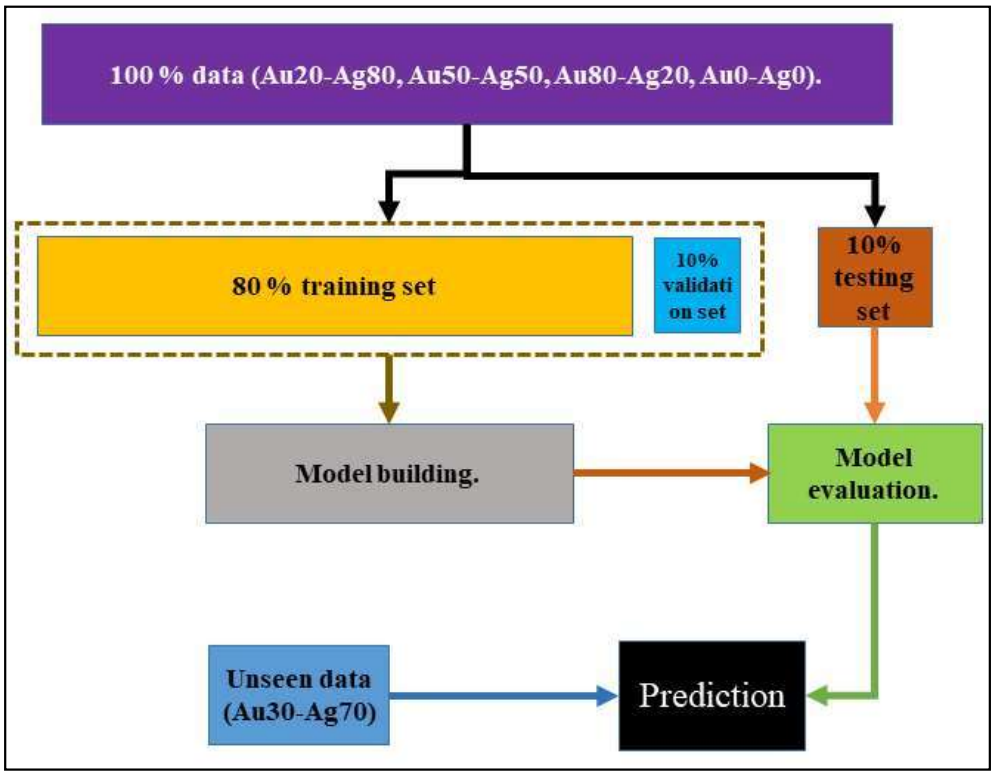

Figure 3.9 The schematic of the model built for the quantification studies with various compositions of Au-Ag LIBS spectra used for the test and train set and evaluation set, and unseen composition used for prediction.

Figure 3.9 illustrates the procedures followed in the analyses of the LIBS data. The data was divided into three sections, a) 80% for the model's training, b) 10% for its validation while being trained, c) and 10% for its evaluation post training. After evaluation, the model was used to estimate the composition from the LIBS spectra earlier not seen by the model (Au30-Ag70).

3.2.2 Terminology in the neural network model

3.2.2.1 Forward propagation

The neuron's output is determined by taking the inputs, multiplying them by the weights to produce the output, and then passing the obtained value through the activation function. Equation 3.1 clarifies the relationship between the inputs, biases, weights, and output.

$$Y^{(i)} = \sum_{j=1}^{3} x_j^{(i)} w_j + b_i = x_1^{(i)} w_1 + x_2^{(i)} w_2 + x_3^{(i)} w_3 + b_1 + b_2 + b_3 \quad (3.1)$$

Where x's are inputs, b's are bias, w's are weight, and y's are outputs.

3.2.2.2 Back propagation

The biases and weights are optimized in each iteration to enhance the model performance, and the errors are fed back through the network. The difference between the output and the anticipated is used to compute the loss. As stated in equation 3.2, the loss is used to modify the weights.

$$w_{new} = w_{old} - \eta \frac{\partial L}{\partial w_{new}} \quad (3.2)$$

Here L is the cost function, η is the learning rate, and W is the weight. The cost function contains the loss function and regularization terms, which is discussed below.

3.2.2.3 Loss function

The loss function, necessary for modifying the weights, measures the prediction error in the neural network's output. The mean absolute error (MAE), represented by equation 3.3, serves as both a measure and the loss function in the model we utilized.

$$MAE = \frac{\sum_{i=1}^{n} |y_i^p - y_i|}{n} \quad (3.3)$$

y_i = expected value

y_i^p = predicted value

n is the number of data points

3.2.2.4 Ridge and lasso regularization

Regularization discourages some coefficients (weights) in the model or causes them to shrink toward zero to prevent overfitting. L2 or Ridge regularization will prefer the significant coefficients resulting in a robust model. L2 regularizations include changing the cost function by introducing a penalty equal to the square of the coefficients' magnitude. By penalizing the model with a penalty termed L2-norm, the sum of the squared coefficients, the coefficients are reduced. The model optimization process uses the parameter λ from equation 3.4.

$$\sum_{i=1}^{n}\left(y^{i}-w_{0}-\sum_{j=1}^{p}w_{j}x_{j}^{i}\right)^{2}+\lambda\sum_{j=1}^{p}w_{j}^{2} \tag{3.4}$$

3.2.2.5 Activation function

$$Y=\text{activation function}\left(\sum(\text{weight}*\text{input})+\text{bias}\right)$$

The hidden layer's activation function was a rectified linear unit (ReLU), whereas the output layer's activation function was linear. The process is illustrated in figure 3.10.

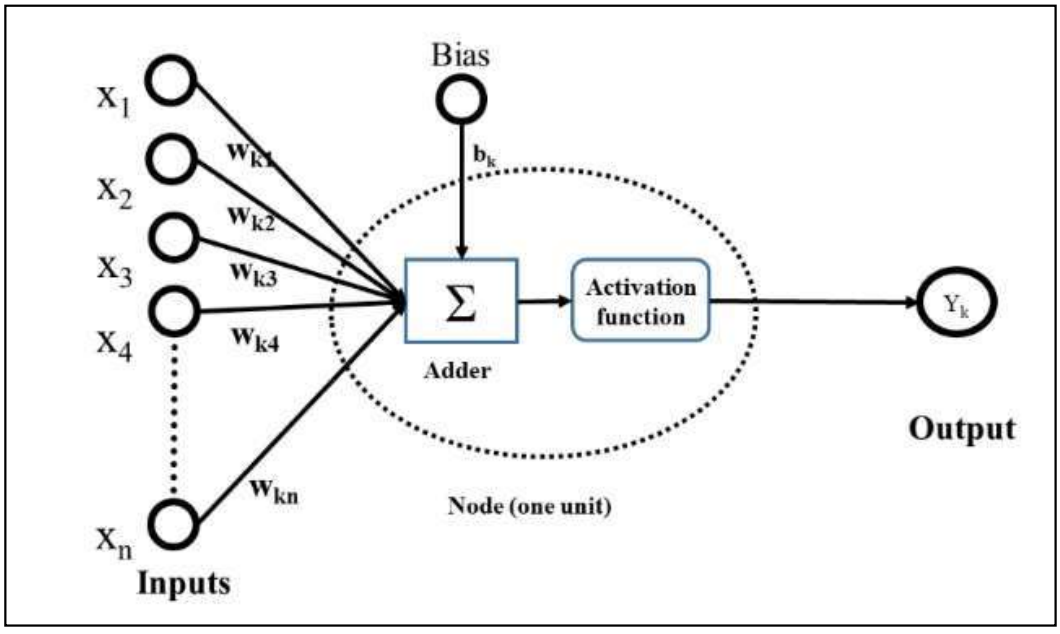

Figure 3.10 The role of the activation function in the neural networks is illustrated. The activation function introduces the nonlinearity to the regression analysis.

ReLU is a nonlinear function since it outputs zero for negative inputs and is linear for values greater than zero, as illustrated in equation 3.5.

$$f(x) = \begin{cases} x & \text{if } x > 0 \\ 0 & \text{if } x < 0 \end{cases} \quad (3.5)$$

3.2.2.6 Least absolute shrinkage and selection operator (Lasso) regularizations

Penalizing the regression model with a penalty L1-norm, the sum of the absolute coefficients reduces the regression coefficients to zero. It could mitigate some of the coefficients, which are not helping to improve the performance of the model using the λ value as indicated in equation 3.6. LAASO regularization, along with additional methods like PCA and competitive adaptive reweighted sampling (CARS) was employed for feature selection to enhance the model's performance. In improving the accuracy of the regression model utilizing LIBS data of mineral samples, shrinkage parameters can be applied [75, 76].

$$\sum_{i=1}^{n}\left(y^i - w_0 - \sum_{j=1}^{p} w_j x_j^i\right)^2 + \lambda \sum_{j=1}^{p} |w_j| \quad (3.6)$$

3.2.2.7 Dropout

Different regularizations are used in the model's generalization, and dropout is among them. The nodes are dropped probabilistically in each iteration, and the nodes to be dropped are optimized. The dropout is illustrated in figure 3.11.

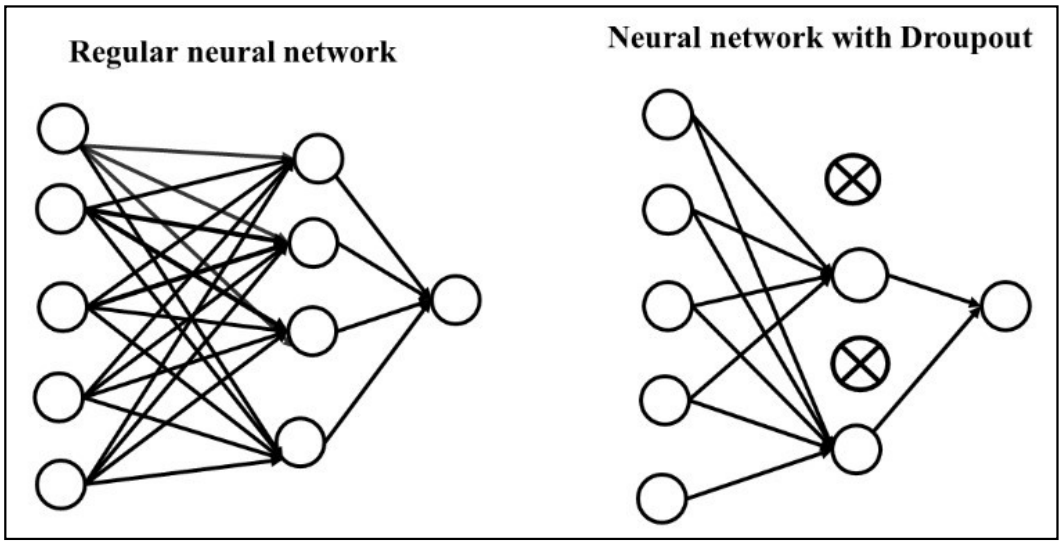

Figure 3.11 The weights are randomly excluded during the forward propagation to improve the model in the dropout.

3.2.2.8 Learning rate

The learning rate is used to optimize the step size in minimizing the loss function. It decides how fast or slows the model should reach the minimum. The effect of different step size η is shown in figure 3.12 in minimizing the function with a single parameter.

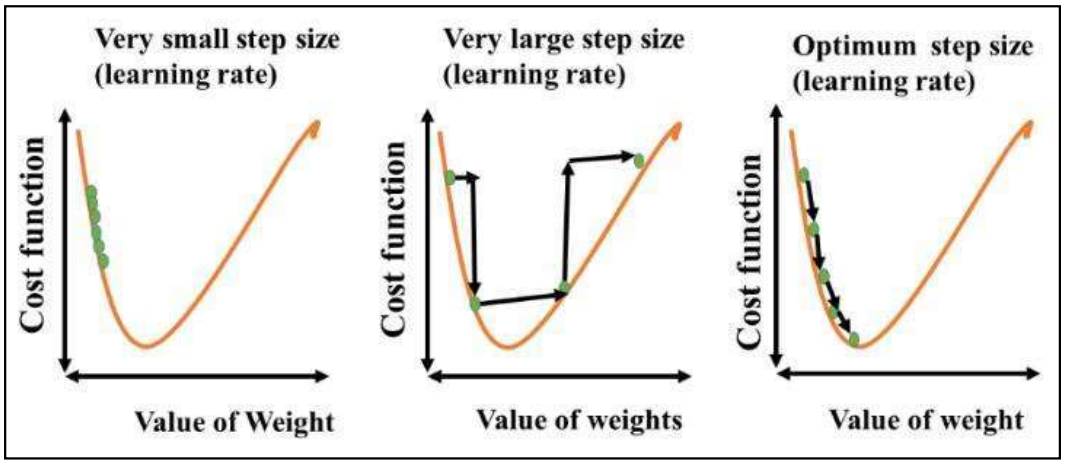

Figure 3.12 The effect of the small, moderate, and large step size on the learning rate in optimizing the model.

3.2.2.9 Epoch

It is one iteration the model goes through in which the biases and weights are adjusted to obtain the output, the process is shown in figure 3.13.

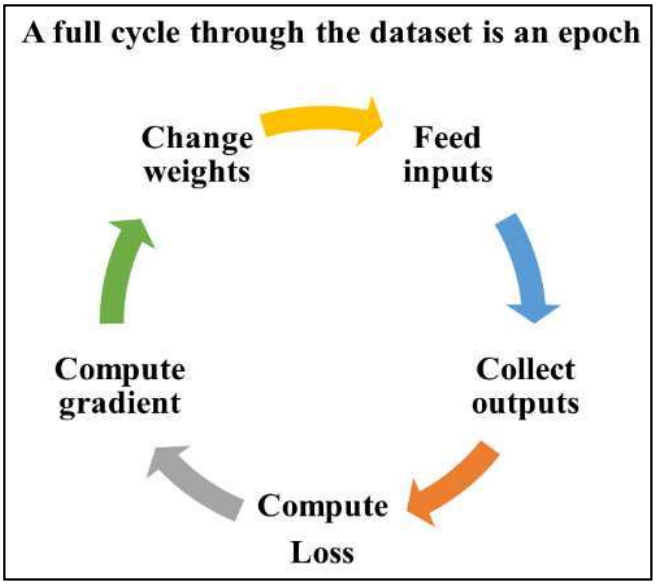

Figure 3.13 The weights and biases are updated in each cycle from the knowledge of the computed gradient. The model completes a cycle in one epoch.

3.2.2.10 Hyperparameter tuning

The initial weights, number of hidden layers, number of nodes per hidden layer, dropout parameter, L1, L2, batch size, and number of epochs, along with the learning rate, were optimized or tuned. As mentioned above, this parameter adjustment process is known as hyperparameter tuning.

3.2.3 Model details

We made an innovative effort to use LIBS spectra collected at three different gate delays to measure the compositions of Au and Ag in bimetallic samples. The model's performance was assessed by noticing the learning curves on the training and validation sets with the variation in the loss for each epoch. Underfitting is when the model has a low error on the validation data set compared to the training data set and a huge variance; on the other hand, overfitting is when the model has a small error on the training data set and a great error on the validation set. Both examples demonstrate that the model do not generalize to the new data since the relationship between the models' output and the inputs are not accurately associated, resulting in a significant inaccuracy in the output of the new dataset. The learning curves were monitored when the parameters were set to get the best variance and bias, also known as the bias-variance trade-off. ReLU was used as the activation function for the model, with 1200 nodes in the hidden layer and two nodes in the output layer having linear activation functions. The batch sizes the number of epochs and were adjusted for each dataset. RMSProp method was used to optimize the loss function's mean absolute error. Three different datasets—one with spectra collected only at 1 µs, another with spectra obtained at 1 µs and 2 µs, and a third with spectra obtained at 1 µs, 2 µs, and 3 µs—were used to generate the three models. The number of epochs (35, 40, and 30) and the batch size (12, 24, and 36) were adjusted for each model, keeping the other factors the same. Reports include the evaluation and prediction results and the learning curves for the NN three models. The training/validation errors and losses were seen to decrease with the number of epochs simultaneously, demonstrating that the model is fitting appropriately [see figures 3.14 (a), (b), and (c) for training and validation errors and figures 3.14(d), (e), and (f) for training and validation losses]. Figure 3.14 displays the complete collection of learning curves during the evaluation.

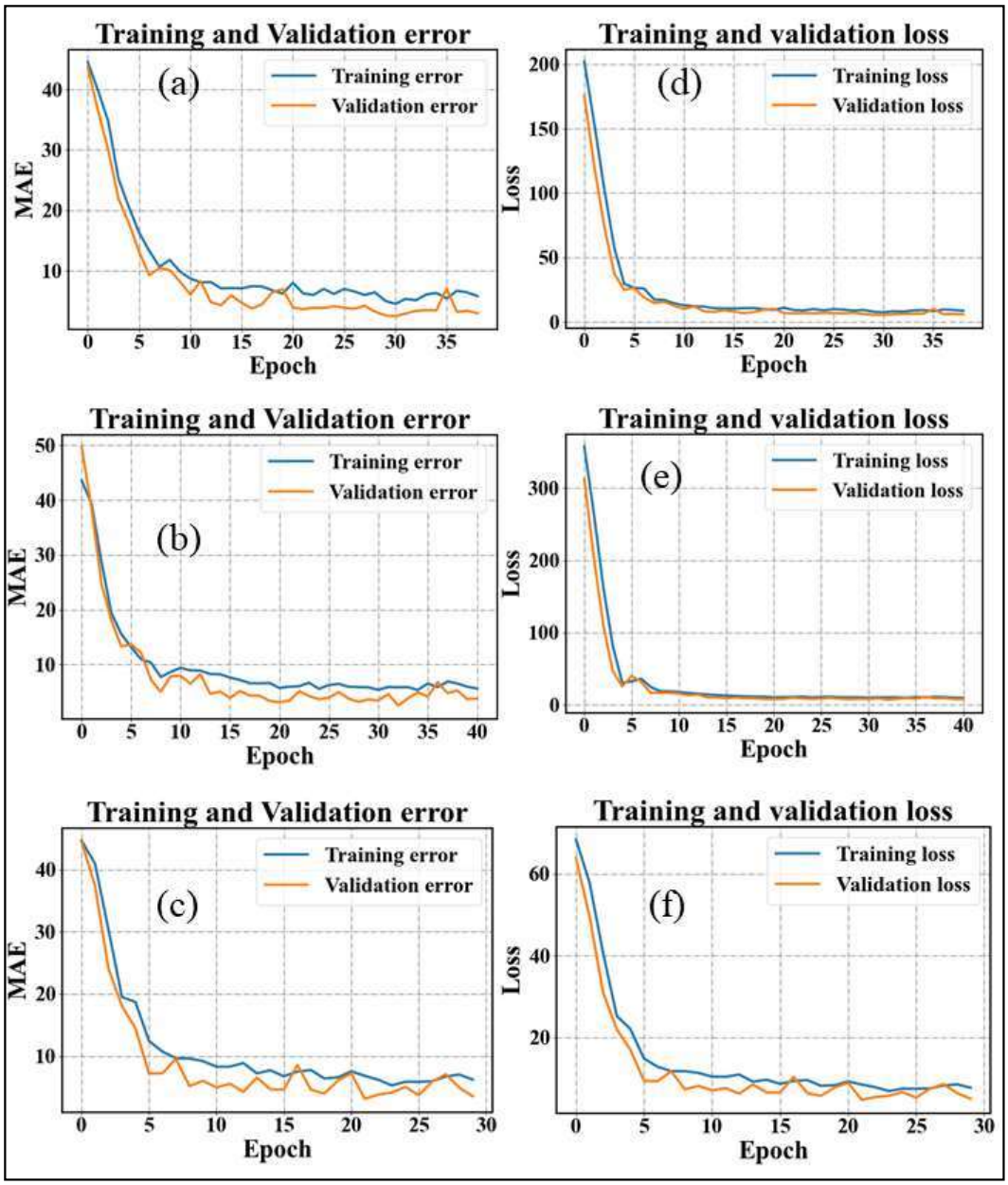

Figure 3.14 Learning curves of the model during training with the validation and training sets used in the optimization. The variation in the loss and error with every epoch in the both the sets for ns-LIBS spectra acquired a) at 1 µs and, b) at 1 µs+ 2 µs and, c) at 1 µs + 2 µs + 3 µs. and the true values vs predicted values from the spectra at d) at 1 µs and, e) at 1 µs + at 2 µs and, f) at 1 µs + at 2 µs + at 3 µs.

3.2.4 Results and discussion

The data were normalized as part of the preprocessing procedure, and the principal components from the PCA were then supplied into the neural network (NN) model's input. PCA is typically used to reduce dimensionality. To accurately estimate the proportions of the two elements in the bimetallic alloy, we have successfully created three shallow NN

models. L1, L2 regularizations were fixed to 10^{-3} each, and initial weights were set to all ones. The shallow neural networks model's learning rate, dropout, batch size, and number of epochs were optimized for enhanced performance. The percentage error in the predicted composition on the test set for each of the three models were trained using the dataset collected at the (a) 1 μs, (b) 1 μs and 2 μs, (c) 1 μs, 2 μs, and 3 μs gate delays.The figures 3.15 (d),(e), (f) represent the true values versus predicted values by the model trained using the data collected at 3.15 (d) 1 μs, (e) 1μ s and 2 μs, (f) 1 μs, 2μ s. The test set includes spectra from 2 μs and 3 μs, the percentage error for all three models is less than 10, with a few outliers in the third model. When the data set is inadequate, and time-resolved spectra are accessible, this method can be used for improving the model performance. It should be noted that even though there are few outliers, the model still holds true for prediction from the data collected at different time windows. This shows that time-resolved LIBS spectra are helpful in quantification studies. The model can be expanded to predict several elemental compositions from various alloys. Figures 3.15(a), (b), (c) shows the X-axis displays the % error in each prediction, and the Y-axis displays the number of counts at that error and figures 3.15 (d), (e), (f) the true vs predicted values of the three models.

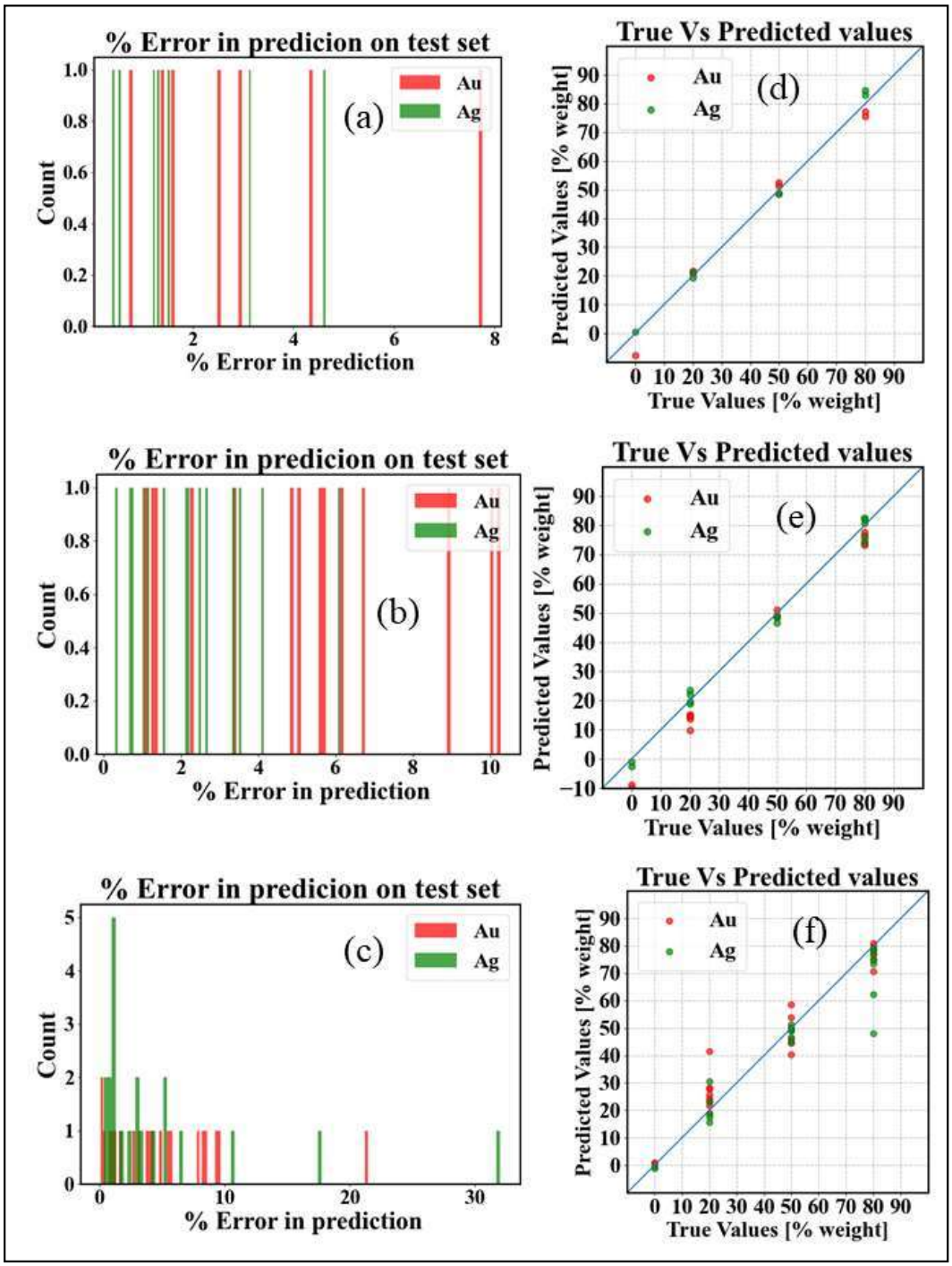

Figure 3.15 The predictions of the model on the test set spectra recorded at a) 1 µs and, b)1 µs + 2 µs and, c)1 µs + 2 µs + 3 µs. And the true values versus predicted values of the spectra at, d) 1 µs and, e) 1 µs + 2 µs and, f) 1 µs + 2 µs + 3 µs. The line is just the guide to the eye.

The results in figures 3.16 (a), (b), (c) illustrate that the number of outliers increased when more time-gated data was included, most spectrum were still accurately quantified. Data at various shorter time intervals, along with slightly altered acquisition parameters, instead

of using enormous amounts of data acquired with the same parameters, could help generalize the model. Following the model's evaluation, the LIBS spectra using three different datasets 1 µs, 2 µs, and 3 µs gate delay and previously unknown composition spectra are provided for prediction. The findings are presented in figure 3.16. The error in each bar's forecast from a single spectrum is shown. The graphs below show that, with a few outliers, most predictions are within 10% error. It was discovered that the insertion of greater delay timed spectra increased the outliers' range. The R-squared error for the model's prediction of the Ag-Au composition using training data from only the 1 µs, the 1 µs and 2 µs, and the first three µs data was 0.98, 0.96, and 0.99, respectively. In all situations, the R-squared value was greater than 0.9, although it is seen that this value decreases when more spectra are added to the model. Because the test set also includes successive time-resolved spectra, the prediction on the test set shows an increase in outliers. These results should also serve as a reminder that models can be created for composing perdition using data collected at various times. Table 3.4 below lists the mean and standard deviation for the one-shot findings on 22 separate spectra for the three models' performance on the unknown data, in this case, the composition of Au30 and Ag70.

Table 3.4 The mean and standard deviation of the results predicted by the three different models trained with the LIBS spectral data collected at 1 µs, (1 µs and 2 µs), and (1 µs, 2 µs and 3 µs) gate delays.

Time-resolved Spectra at microseconds.	**1 µs**	**1 µs**	**1 µs and 2 µs**	**1 µs, and 2 µs**	**1 µs, 2 µs & 3 µs**	**1 µs, 2 µs & 3 µs**
Element	Au	Ag	Au	Ag	Au	Ag
Predicted Mean (Wt. %)	30.73	65.55	29.78	64.39	27.77	70.79
Standard deviation (Wt. %)	1.63	1.47	1.4	1.46	1.37	1.27

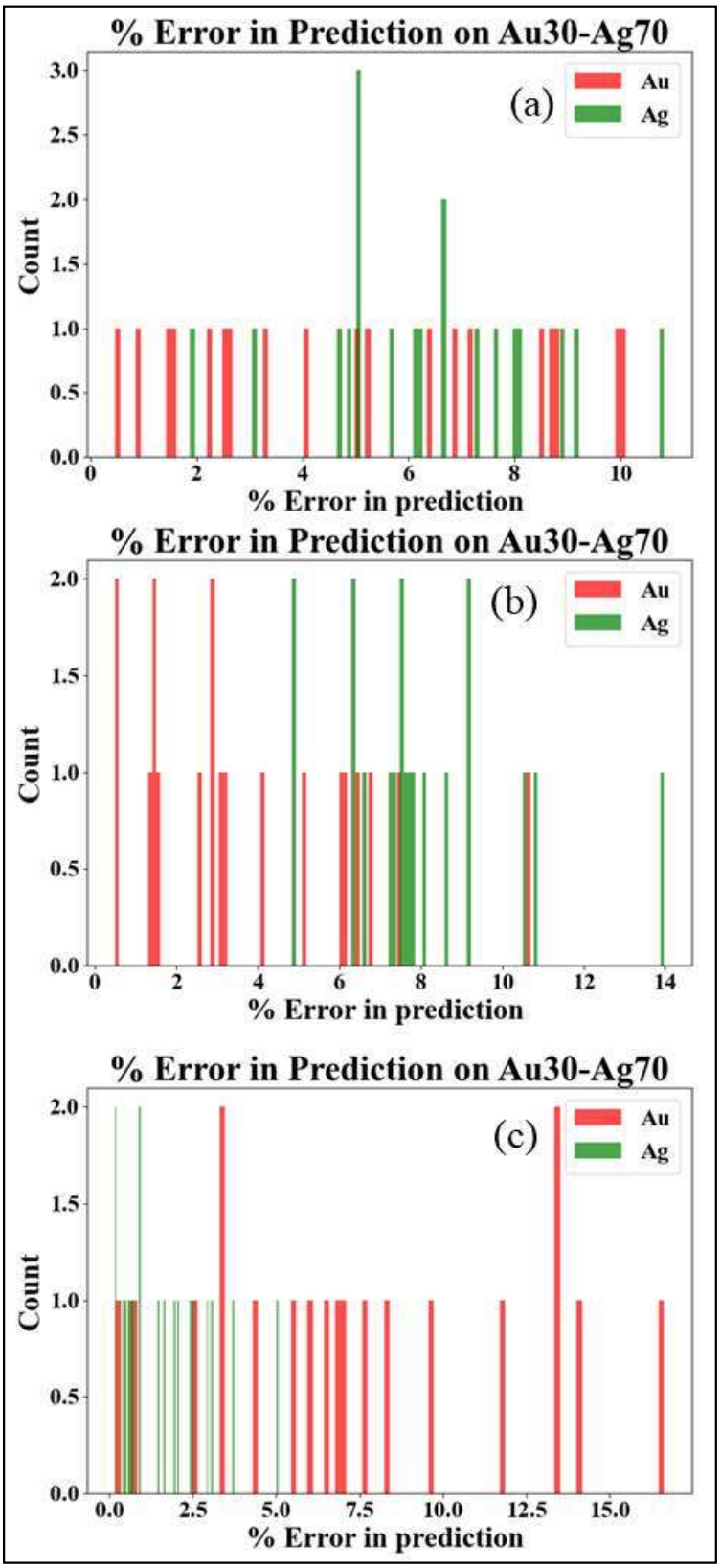

Figure 3.16 The predictions of the model on the unseen ns-LIBS spectra of Au30-Ag70 at a) 1 µs and b) 1 µs + 2 µs and, c) 1 µs + 2 µs + 3 µs.

3.2.5 Conclusions

Using the multi-output regression model, the composition of bimetallic alloy was quantified from the LIBS spectra. Each model was evaluated during training by keeping an eye on the cross-validation learning curves. The time-resolved spectra were employed for both training and testing. Composition from the previously unseen Au30-Ag70 LIBS spectra was successfully predicted by the models. The studies can be expanded to include more than two elements' composition with extra nodes in the output layer. Here, the time-resolved spectra were used to enhance the data and let the model generalize to predict from the spectra collected at three gate delays. Additionally, the standard deviations in the predicted composition of the unexplored spectra decreased from 1.63 to 1.37 and from 1.47 to 1.27. We envision a unified single model that could predict the composition from any spectrum, trained from data gathered by varying all conceivable factors.

References

[1] J.D. Winefordner, I.B. Gornushkin, T. Correll, E. Gibb, B.W. Smith, N. Omenetto, Comparing several atomic spectrometric methods to the super stars: special emphasis on laser induced breakdown spectrometry, LIBS, a future super star, J. Anal. At. Spectrom. 19 (2004) 1061–1083. doi:10.1039/B400355C.

[2] C.G. Parigger, Atomic and molecular emissions in laser-induced breakdown spectroscopy, Spectrochim. Acta Part B At. Spectrosc. 79 (2013) 4–16. doi:https://doi.org/10.1016/j.sab.2012.11.012.

[3] J.L. Gottfried, F.C. De Lucia, C.A. Munson, A.W. Miziolek, Strategies for residue explosives detection using laser-induced breakdown spectroscopy, J. Anal. At. Spectrom. 23 (2008) 205–216. doi:10.1039/b703891g.

[4] S.A. Kalam, N.L. Murthy, P. Mathi, N. Kommu, A.K. Singh, S.V. Rao, Correlation of molecular{,} atomic emissions with detonation parameters in femtosecond and nanosecond LIBS plasma of high energy materials, J. Anal. At. Spectrom. 32 (2017) 1535–1546. doi:10.1039/C7JA00136C.

[5] S. Sheta, M.S. Afgan, Z. Hou, S.-C. Yao, L. Zhang, Z. Li, Z. Wang, Coal analysis by laser-induced breakdown spectroscopy: a tutorial review, J. Anal. At. Spectrom. 34 (2019) 1047–1082. doi:10.1039/C9JA00016J.

[6] F. Trichard, S. Moncayo, D. Devismes, F. Pelascini, J. Maurelli, A. Feugier, C. Sasseville, F. Surma, V. Motto-Ros, Evaluation of a compact VUV spectrometer for elemental imaging by laser-induced breakdown spectroscopy: application to mine core characterization, J. Anal. At. Spectrom. 32 (2017) 1527–1534. doi:10.1039/C7JA00185A.

[7] F.J. Fortes, S. Guirado, A. Metzinger, J.J. Laserna, A study of underwater standoff laser-induced breakdown spectroscopy for chemical analysis of objects in the deep ocean, J. Anal. At. Spectrom. 30 (2015) 1050–1056. doi:10.1039/C4JA00489B.

[8] S. Maurice, S.M. Clegg, R.C. Wiens, O. Gasnault, W. Rapin, O. Forni, A. Cousin, V. Sautter, N. Mangold, L. Le Deit, M. Nachon, R.B. Anderson, N.L. Lanza, C. Fabre, V. Payré, J. Lasue, P.-Y. Meslin, R.J. Léveillé, B.L. Barraclough, P. Beck, S.C. Bender, G. Berger, J.C. Bridges, N.T. Bridges, G. Dromart, M.D. Dyar, R. Francis, J. Frydenvang, B. Gondet, B.L. Ehlmann, K.E. Herkenhoff, J.R. Johnson, Y. Langevin, M.B. Madsen, N. Melikechi, J.-L. Lacour, S. Le Mouélic, E. Lewin, H.E. Newsom, A.M. Ollila, P. Pinet, S. Schröder, J.-B. Sirven, R.L. Tokar, M.J. Toplis, C. d'Uston, D.T. Vaniman, A.R. Vasavada, ChemCam activities and discoveries during the nominal mission of the Mars Science Laboratory in Gale crater{,} Mars, J. Anal. At. Spectrom. 31 (2016) 863–889. doi:10.1039/C5JA00417A.

[9] G. Kim, J. Kwak, J. Choi, K. Park, Detection of nutrient elements and contamination by pesticides in spinach and rice samples using laser-induced breakdown spectroscopy (LIBS), J. Agric. Food Chem. 60 (2012) 718–724. doi:10.1021/jf203518f.

[10] Y. Wang, A. Chen, S. Li, L. Sui, D. Liu, D. Tian, Y. Jiang, M. Jin, Enhancement of laser-induced Fe plasma spectroscopy with dual-wavelength femtosecond double-pulse, J. Anal. At. Spectrom. 31 (2016) 497–505. doi:10.1039/C5JA00420A.

[11] I.Y. Elnasharty, F.R. Doucet, J.-F.Y. Gravel, P. Bouchard, M. Sabsabi, Double-pulse LIBS combining short and long nanosecond pulses in the microjoule range, J. Anal. At. Spectrom. 29 (2014) 1660–1666. doi:10.1039/C4JA00099D.

[12] A. De Giacomo, M. Dell'Aglio, R. Gaudiuso, C. Koral, G. Valenza, Perspective on the use of nanoparticles to improve LIBS analytical performance: nanoparticle enhanced laser induced breakdown spectroscopy (NELIBS), J. Anal. At. Spectrom. 31 (2016) 1566–1573. doi:10.1039/C6JA00189K.

[13] A. De Giacomo, R. Gaudiuso, C. Koral, M. Dell'Aglio, O. De Pascale, Nanoparticle Enhanced Laser Induced Breakdown Spectroscopy: Effect of nanoparticles deposited on sample surface on laser ablation and plasma emission, Spectrochim. Acta Part B At. Spectrosc. 98 (2014) 19–27. doi:10.1016/j.sab.2014.05.010.

[14] A. De Giacomo, R. Gaudiuso, C. Koral, M. Dell'Aglio, O. De Pascale, M. Dell'Aglio, O. De Pascale, Nanoparticle-enhanced laser-induced breakdown spectroscopy of metallic samples, Anal. Chem. 85 (2013) 10180–10187. doi:10.1021/ac4016165.

[15] V.K. Unnikrishnan, R. Nayak, K. Aithal, V.B. Kartha, C. Santhosh, G.P. Gupta, B.M. Suri, Analysis of trace elements in complex matrices (soil) by Laser Induced Breakdown Spectroscopy (LIBS), Anal. Methods. 5 (2013) 1294–1300. doi:10.1039/C2AY26006A.

[16] A.K. Shaik, N.R. Epuru, H. Syed, C. Byram, V.R. Soma, Femtosecond laser induced breakdown spectroscopy based standoff detection of explosives and discrimination using principal component analysis, Opt. Express. 26 (2018) 8069-8083. doi:10.1364/oe.26.008069.

[17] E.N. Rao, P. Mathi, S.A. Kalam, S. Sreedhar, A.K. Singh, B.N. Jagatap, S.V. Rao, Femtosecond and nanosecond LIBS studies of nitroimidazoles: Correlation between molecular structure and LIBS data, J. Anal. At. Spectrom. 31 (2016) 737–750. doi:10.1039/c5ja00445d.

[18] J. Yu, Z. Hou, S. Sheta, J. Dong, W. Han, T. Lu, Z. Wang, Provenance classification of nephrite jades using multivariate LIBS: a comparative study, Anal. Methods. 10 (2018) 281–289. doi:10.1039/C7AY02643A.

[19] R.S. Harmon, F.C. De Lucia, A.W. Miziolek, K.L. McNesby, R.A. Walters, P.D. French, Laser-induced breakdown spectroscopy (LIBS)--an emerging field-portable sensor technology for real-time, in-situ geochemical and environmental analysis, Geochemistry Explor. Environ. Anal. 5 (2005) 21–28. doi:10.1144/1467-7873/03-059.

[20] A.K. Myakalwar, N.C. Dingari, R.R. Dasari, I. Barman, M.K. Gundawar, Non-gated laser induced breakdown spectroscopy provides a powerful segmentation tool on concomitant treatment of characteristic and continuum emission, PLoS One. 9 (2014) e103546.

[21] J.K. Pavel Pořízka, Jakub Klus, Jan Mašek, Martin Rajnoha, David Prochazka, Pavlína Modlitbová, Jan Novotný, Radim Burget, Karel Novotný, Multivariate classification of echellograms: a new perspective in Laser-Induced Breakdown Spectroscopy analysis, Sci. Rep. 7 (2017) 3160. doi:10.1038/s41598-017-03426-0.

[22] E. Negre, V. Motto-Ros, F. Pelascini, J. Yu, Classification of plastic materials by imaging laser-induced ablation plumes, Spectrochim. Acta Part B At. Spectrosc. 122 (2016) 132–141. doi:10.1016/j.sab.2016.06.009

[23] Q. Li, Y. Tian, B. Xue, N. Li, W. Ye, Y. Lu, R. Zheng, Improvement in the analytical performance of underwater LIBS signals by exploiting the plasma image information, J. Anal. At. Spectrom. 35 (2020) 366–376. doi:10.1039/c9ja00367c.

[24] G. Vítková, K. Novotný, L. Prokeš, A. Hrdlička, J. Kaiser, J. Novotný, R. Malina, D. Prochazka, Fast identification of biominerals by means of stand-off laser-induced breakdown spectroscopy using linear discriminant analysis and artificial neural networks, Spectrochim. Acta - Part B At. Spectrosc. 73 (2012) 1–6. doi:10.1016/j.sab.2012.05.010.

[25] T. Delgado, J. Ruiz, L.M. Cabalín, J.J. Laserna, Distinction strategies based on discriminant function analysis for particular steel grades at elevated temperature using stand-off LIBS, J. Anal. At. Spectrom. 31 (2016) 2242–2252. doi:10.1039/c6ja00219f.

[26] D. Girón, T. Delgado, J. Ruiz, L.M. Cabalín, J.J. Laserna, In-situ monitoring and characterization of airborne solid particles in the hostile environment of a steel industry using stand-off LIBS, Meas. J. Int. Meas. Confed. 115 (2018) 1–10. doi:10.1016/j.measurement.2017.09.046.

[27] L.M. Cabalín, T. Delgado, J. Ruiz, D. Mier, J.J. Laserna, Stand-off laser-induced breakdown spectroscopy for steel-grade intermix detection in sequence casting operations. At-line monitoring of temporal evolution versus predicted mathematical model, Spectrochim. Acta - Part B At. Spectrosc. 146 (2018) 93–100. doi:10.1016/j.sab.2018.05.001.

[28] R. Junjuri, A.K. Myakalwar, M.K. Gundawar, Standoff detection of explosives at 1 m using laser induced breakdown spectroscopy, Def. Sci. J. 67 (2017) 623–630. doi:10.14429/dsj.67.11498.

[29] R. Junjuri, A. Prakash Gummadi, M. Kumar Gundawar, Single-shot compact spectrometer based standoff LIBS configuration for explosive detection using artificial neural networks, Optik (Stuttg). 204 (2020). doi:10.1016/j.ijleo.2019.163946.

[30] J. L. Gottfried, F.C. De Lucia, C.A. Munson, and A.W. Miziolek, Standoff Detection of Chemical and Biological Threats Using Laser-Induced Breakdown Spectroscopy, Appl. Spectrosc. 62, 353-363 (2008). doi:10.1117/2.1201506.005844.

[31] C.G. Parigger, J.O. Hornkohl, Computation of AlO $B^2\Sigma^+ \rightarrow X^2\Sigma^+$ emission spectra, Spectrochim. Acta Part A Mol. Biomol. Spectrosc. 81 (2011) 404–411. doi:10.1016/j.saa.2011.06.029.

[32] C.G. AU - Parigger, A.C. AU - Woods, M.J. AU - Witte, L.D. AU - Swafford, D.M. AU - Surmick, Measurement and Analysis of Atomic Hydrogen and Diatomic Molecular AlO, C2, CN, and TiO Spectra Following Laser-induced Optical Breakdown, JoVE. (2014) e51250. doi:doi:10.3791/51250.

[33] Kramida, A., Ralchenko, Yu., Reader, J. and NIST ASD Team (2021). NIST Atomic Spectra Database (version 5.9), [Online]. Available: https://physics.nist.gov/asd [Fri Sep 23 2022]. National Institute of Standards and Technology, Gaithersburg, MD. DOI: https://doi.org/10.18434/T4W30F

[34] M. Brown, Advanced digital photography, Media Publishing, 2004.

[35] T. Maschke, Digitale kameratechnik: technik digitaler kameras in theorie und praxis, Springer-Verlag, 2013.

[36] Schneider, C. A., Rasband, W. S., & Eliceiri, K. W. (2012). NIH Image to ImageJ: 25 years of image analysis. Nature Methods, 9(7), 671–675. doi:10.1038/nmeth.2089

[37] Cremers, David A., and Leon J. Radziemski. Handbook of laser-induced breakdown spectroscopy. John Wiley & Sons, 2013.

[38] L. Radziemski, D. Cremers, A brief history of laser-induced breakdown spectroscopy: From the concept of atoms to LIBS 2012, Spectrochim. Acta - Part B At. Spectrosc. 87 (2013) 3–10. doi:10.1016/j.sab.2013.05.013.

[39] J.P. Singh, S.N. Thakur, Laser-induced breakdown spectroscopy, Elsevier, 2020.

[40] F.J. Fortes, J.J. Laserna, The development of fieldable laser-induced breakdown spectrometer: No limits on the horizon, Spectrochim. Acta - Part B At. Spectrosc. 65 (2010) 975–990. doi:10.1016/j.sab.2010.11.009.

[41] N.L. Murthy, S. Abdul Salam, S.V. Rao, Stand-off Femtosecond Laser Induced Breakdown Spectroscopy of Metals, Soil, Plastics and Classification Studies, 2019 Work. Recent Adv. Photonics, WRAP 2019. (2019) 16–18. doi:10.1109/WRAP47485.2019.9013674.

[42] S. Abdul Kalam, S. V. Balaji Manasa Rao, M. Jayananda, S. Venugopal Rao, Standoff femtosecond filament-induced breakdown spectroscopy for classification of geological materials, J. Anal. At. Spectrom. 35 (2020) 3007–3020. doi:10.1039/d0ja00355g.

[43] I. Gaona, P. Lucena, J. Moros, F.J. Fortes, S. Guirado, J. Serrano, J.J. Laserna, Evaluating the use of standoff LIBS in architectural heritage: Surveying the Cathedral of Málaga, J. Anal. At. Spectrom. 28 (2013) 810–820. doi:10.1039/c3ja50069a.

[44] I. Gaona, J. Moros, J.J. Laserna, New insights into the potential factors affecting the emission spectra variability in standoff LIBS, J. Anal. At. Spectrom. 28 (2013) 1750–1759. doi:10.1039/c3ja50181g.

[45] R.C. Wiens, S.K. Sharma, J. Thompson, A. Misra, P.G. Lucey, Joint analyses by laser-induced breakdown spectroscopy (LIBS) and Raman spectroscopy at standoff distances, Spectrochim. Acta - Part A Mol. Biomol. Spectrosc. 61 (2005) 2324–2334. doi:10.1016/j.saa.2005.02.031.

[46] L. Sládková, D. Prochazka, P. Pořízka, P. Škarková, M. Remešová, A. Hrdlička, K. Novotný, L. Čelko, J. Kaiser, Improvement of the Laser-Induced Breakdown Spectroscopy method sensitivity by the usage of combination of Ag-nanoparticles and vacuum conditions, Spectrochim. Acta - Part B At. Spectrosc. 127 (2017) 48-55. doi:10.1016/j.sab.2016.11.005.

[47] A. De Giacomo, R. Alrifai, V. Gardette, Z. Salajková, M. Dell'Aglio, Nanoparticle enhanced laser ablation and consequent effects on laser induced plasma optical emission, Spectrochim. Acta - Part B At. Spectrosc. 166 (2020) 105794. doi:10.1016/j.sab.2020.105794.

[48] N.L. Murthy, S.V. Rao, N. Linga Murthy and Soma Venugopal Rao, Nanoparticle Enhanced Laser Induced Breakdown Spectroscopy of Liquids. In.Proc. Int. Conf. Opt. Electro-Optics, In: Singh, K., Gupta, A.K., Khare, S., Dixit, N., Pant, K. (eds) ICOL-2019. Springer Proceedings in Physics, Springer, Singapore 258 (2019) 459–462.. https://doi.org/10.1007/978-981-15-9259-1_105.

[49] M. Abdelhamid, Y.A. Attia, M. Abdel-Harith, The significance of nano-shapes in nanoparticle-enhanced laser-induced breakdown spectroscopy, J. Anal. At. Spectrom. 35 (2020) 2982–2989. doi:10.1039/d0ja00329h.

[50] Z. Yue, C. Sun, F. Chen, Y. Zhang, W. Xu, S. Shabbir, L. Zou, W. Lu, W. Wang, Z. Xie, L. Zhou, Y. Lu, J. Yu, Machine learning-based LIBS spectrum analysis of human blood plasma allows ovarian cancer diagnosis, Biomed. Opt. Express. 12 (2021) 2559. doi:10.1364/boe.421961.

[51] F. Poggialini, B. Campanella, S. Legnaioli, S. Pagnotta, S. Raneri, V. Palleschi, Improvement of the performances of a commercial hand-held laser-induced breakdown spectroscopy instrument for steel analysis using multiple artificial neural networks, Rev. Sci. Instrum. 91 (2020) 073111. doi:10.1063/5.0012669.

[52] A. Ciucci, M. Corsi, V. Palleschi, S. Rastelli, A. Salvetti, E. Tognoni, New procedure for quantitative elemental analysis by laser-induced plasma spectroscopy, Appl. Spectrosc. 53 (1999) 960–964. doi:10.1366/0003702991947612.

[53] V.K. Unnikrishnan, K. Mridul, R. Nayak, V.B. Kartha, C. Santhosh, G.P. Gupta, K. Alti, B.M. Suri, Calibration-free laser-induced breakdown spectroscopy for quantitative elemental analysis of materials, Pramana - J. Phys. 79 (2012) 299–310. doi:10.1007/s12043-012-0298-1.

[54] D. Bulajic, M. Corsi, G. Cristoforetti, S. Legnaioli, V. Palleschi, A. Salvetti, E. Tognoni, A procedure for correcting self-absorption in calibration free-laser induced breakdown spectroscopy, Spectrochim. Acta - Part B At. Spectrosc. 57 (2002) 339–353. doi:10.1016/S0584-8547(01)00398-6.

[55] E. Mal, R. Junjuri, M.K. Gundawar, A. Khare, Optimization of temporal window for application of calibration free-laser induced breakdown spectroscopy (CF-LIBS) on copper alloys in air employing a single line, J. Anal. At. Spectrom. 34 (2019) 319–330. doi:10.1039/c8ja00415c.

[56] S.A. Davari, S. Hu, R. Pamu, D. Mukherjee, Calibration-free quantitative analysis of thin-film oxide layers in semiconductors using laser induced breakdown spectroscopy (LIBS), J. Anal. At. Spectrom. 32 (2017) 1378–1387. doi:10.1039/c7ja00083a.

[57] V.S. Burakov, S.N. Raikov, Quantitative analysis of alloys and glasses by a calibration-free method using laser-induced breakdown spectroscopy, Spectrochim. Acta - Part B At. Spectrosc. 62 (2007) 217–223. doi:10.1016/j.sab.2007.03.021.

[58] S. Pandhija, A.K. Rai, In situ multielemental monitoring in coral skeleton by CF-LIBS, Appl. Phys. B Lasers Opt. 94 (2009) 545–552. doi:10.1007/s00340-008-3343-5.

[59] B. Praher, V. Palleschi, R. Viskup, J. Heitz, J.D. Pedarnig, Calibration free laser-induced breakdown spectroscopy of oxide materials, Spectrochim. Acta - Part B At. Spectrosc. 65 (2010) 671–679. doi:10.1016/j.sab.2010.03.010.

[60] S. Pandhija, N.K. Rai, A.K. Rai, S.N. Thakur, Contaminant concentration in environmental samples using LIBS and CF-LIBS, Appl. Phys. B Lasers Opt. 98 (2010) 231–241. doi:10.1007/s00340-009-3763-x.

[61] R. Kumar, A.K. Rai, D. Alamelu, S.K. Aggarwal, Monitoring of toxic elements present in sludge of industrial waste using CF-LIBS, Environ. Monit. Assess. 185 (2013) 171–180. doi:10.1007/s10661-012-2541-0.

[62] M. Hornáčková, J. Plavcan, J. Rakovsky, V. Porubcan, D. Ozdín, P. Veis, Calibration-free laser induced breakdown spectroscopy as an alternative method for found meteorite fragments analysis, EPJ Appl. Phys. 66 (2014) 1–10. doi:10.1051/epjap/2014130465.

[63] S.A. Davari, S. Hu, D. Mukherjee, Calibration-free quantitative analysis of elemental ratios in intermetallic nanoalloys and nanocomposites using Laser Induced Breakdown Spectroscopy (LIBS), Talanta. 164 (2017) 330–340. doi:10.1016/j.talanta.2016.11.031.

[64] D.M. Díaz Pace, R.E. Miguel, H.O. Di Rocco, F. Anabitarte García, L. Pardini, S. Legnaioli, G. Lorenzetti, V. Palleschi, Quantitative analysis of metals in waste foundry sands by calibration free-laser induced breakdown spectroscopy, Spectrochim. Acta - Part B At. Spectrosc. 131 (2017) 58–65. doi:10.1016/j.sab.2017.03.007.

[65] V.C. Costa, D. V. Babos, J.P. Castro, D.F. Andrade, R.R. Gamela, R.C. MacHado, M.A. Speranca, A.S. Araujo, J.A. Garcia, E.R. Pereira-Filho, Calibration strategies applied to laser-induced breakdown spectroscopy: A critical review of advances and challenges, J. Braz. Chem. Soc. 31 (2020) 2439–2451. doi:10.21577/0103-5053.20200175.

[66] J.B. Sirven, B. Bousquet, L. Canioni, L. Sarger, S. Tellier, M. Potin-Gautier, I. Le Hecho, Qualitative and quantitative investigation of chromium-polluted soils by laser-induced breakdown spectroscopy combined with neural networks analysis, Anal. Bioanal. Chem. 385 (2006) 256–262. doi:10.1007/s00216-006-0322-8.

[67] V. Motto-Ros, A.S. Koujelev, G.R. Osinski, A.E. Dudelzak, Quantitative multi-elemental laser-induced breakdown spectroscopy using artificial neural networks, J. Eur. Opt. Soc. Rapid Publ. 3 (2008) 08011. doi:10.2971/jeos.2008.08011.

[68] R. Hernández-García, M.E. Villanueva-Tagle, F. Calderón-Piñar, M.D. Durruthy-Rodríguez, F.W.B. Aquino, E.R. Pereira-Filho, M.S. Pomares-Alfonso, Quantitative analysis of Lead Zirconate Titanate (PZT) ceramics by laser-induced breakdown spectroscopy (LIBS) in combination with multivariate calibration, Microchem. J. 130 (2017) 21–26. doi:10.1016/j.microc.2016.07.024.

[69] J. Yongcheng, S. Wen, Z. Baohua, L. Dong, Quantitative Analysis of Magnesium in Soil by Laser-Induced Breakdown Spectroscopy Coupled with Nonlinear Multivariate Calibration, J. Appl. Spectrosc. 84 (2017) 731–737. doi:10.1007/s10812-017-0537-9.

[70] P. Devangad, V.K. Unnikrishnan, M.M. Tamboli, K.M.M. Shameem, R. Nayak, K.S. Choudhari, C. Santhosh, Quantification of Mn in glass matrices using laser induced breakdown spectroscopy (LIBS) combined with chemometric approaches, Anal. Methods. 8 (2016) 7177–7184. doi:10.1039/c6ay01930g.

[71] M.M. Tripathi, K.E. Eseller, F.Y. Yueh, J.P. Singh, Multivariate calibration of spectra obtained by Laser Induced Breakdown Spectroscopy of plutonium oxide surrogate residues, Spectrochim. Acta - Part B At. Spectrosc. 64 (2009) 1212–1218. doi:10.1016/j.sab.2009.09.003.

[72] S. Laville, M. Sabsabi, F.R. Doucet, Multi-elemental analysis of solidified mineral melt samples by Laser-Induced Breakdown Spectroscopy coupled with a linear multivariate calibration, Spectrochim. Acta - Part B At. Spectrosc. 62 (2007) 1557–1566. doi:10.1016/j.sab.2007.10.003.

[73] F. Rezaei, P. Karimi, S.H. Tavassoli, Effect of self-absorption correction on LIBS measurements by calibration curve and artificial neural network, Appl. Phys. B Lasers Opt. 114 (2014) 591–600. doi:10.1007/s00340-013-5566-3.

[74] C.L. Goueguel, First-Order Multivariate Calibration in Laser-induced Breakdown Spectroscopy Laser-induced Breakdown Spectroscopy, (2019) 1–11. https://towardsdatascience.com/first-order-multivariate-calibration-in-laser-induced-breakdown-spectroscopy-ca5616dd5b38.

[75] R.S. Bricklemyer, D.J. Brown, P.J. Turk, S.M. Clegg, Improved intact soil-core carbon determination applying regression shrinkage and variable selection techniques to complete spectrum laser-induced breakdown spectroscopy (LIBS), Appl. Spectrosc. 67 (2013) 1185–1199. doi:10.1366/12-06983.

[76] D. Luarte, A.K. Myakalwar, M. Velásquez, J. Álvarez, C. Sandoval, R. Fuentes, J. Yañez, D. Sbarbaro, Combining prior knowledge with input selection algorithms for quantitative analysis using neural networks in laser induced breakdown spectroscopy, Anal. Methods. 13 (2021) 1181–1190. doi:10.1039/d0ay02300k.

4 Two-dimensional correlation analysis of the LIBS spectra

Abstract: The signal-to-noise ratio (SNR) of the laser-induced breakdown spectroscopy (LIBS) data was significantly improved in this study using two-dimensional (2D) correlation analysis. Time-resolved LIBS spectra of metallic samples and LIBS spectra of Au-Ag bimetallic samples with different compositions were used for the analysis. The diagonal in the 2D synchronous spectra was used to show the SNR improvement. The peak intensities were improved, and the noise was suppressed at the same time. The correlation between LIBS peaks was visualized using 2D correlation analysis. aluminum (Al), copper (Cu), and Brass display correlation strengths in the atomic transitions, and the Au-Ag bimetallic targets with various compositions show correlation strengths in atomic and ionic transitions (Au30-Ag70, Au50-Ag50, Au80-Ag20). The principal component analysis was utilized to classify the four bimetallic target compositions using the enhanced spectra (Au20-Ag80, Au30-Ag70, Au50-Ag50, and Au80-Ag20). The study revealed that the variance of the first three components had decreased. The first three components from improved spectra could describe 95 percent of the total variation. In contrast, the normal LIBS spectra could explain only 80 percent of the total variance from PCA research.

4.1 Introduction

The spectral emissions from the cooling plasma produced when powerful short laser pulses are focused on the sample surface, are used in the laser-induced breakdown spectroscopy (LIBS) technique [1]. Ionic, atomic, and molecular transitions are the main constituents of typical LIBS spectra [2]. Additionally, the knowledge of the changing intensities in LIBS spectrum with elemental compositions combined with machine learning approaches is used for sample categorization and identification. Because of its adaptability, speed, and minimal sample preparation requirements, LIBS has found great success in a variety of fields, including the classification of bacteria [3-5], the study of ancient paintings [14], the study of fundamental plasma properties [15], planetary exploration, minerals [7], explosive detection [10, 11], archaeology [8, 9], and in the analysis of the minerals. Due to its potential advantage of combining with the Raman spectroscopy [16, 17] and its ability to function in double-pulse and standoff mode [18], this technique found a variety

of applications. It is a potent tool for the trace detection of samples due to the advantage of signal enhancement utilizing nanoparticles [19].

Along with ionic and atomic emissions, the LIBS spectra of organic materials and a few metals also show molecular emissions [20–22]. These emissions can be used to deduce the material's properties [23, 24]. Noda et al. [25] first developed 2D correlation spectroscopy (2DCOS). It was primarily utilized to interpret data from Raman, near-infrared, and nuclear magnetic resonance spectroscopy (NMR) [25–28]. It has been demonstrated that 2D spectroscopy improves the resolution of the spectrum [29]. With a slight perturbation, it is possible to study the concurrent changes or coupling between the corresponding spectral emissions. The 2D correlation spectra provide the ability to better understand the sample properties compared to conventional spectra [30]. The correlations in the atomic transitions of aluminum, Copper, Brass, and an Au-Ag bimetallic target have been shown. The LIBS data of Al, Cu, Brass, and Au-Ag bimetallic metals have been subjected to 2D correlation analysis. We used times-resolved LIBS spectra and composition-varying LIBS spectra to show the advantage of 2D correlation spectroscopy. Two-dimensional contour plots can be used to visualize the analysis. The strength of the diagonal points in the two-dimensional spectra corresponds to the peaks' self-correlation, also known as autocorrelation. It details the temporal association between a specific transition intensity and itself. The strength of the off-diagonal points reflects the peak intensity's temporal association with other peaks. Similarly, the 2D analysis of spectra with different concentrations reveals the autocorrelation and cross-correlation in the LIBS spectra. The resolution and SNR of the spectrum could be improved using this technique in addition to viewing. Our investigation shows that it is possible to enhance the SNR of the LIBS data by at least 3–4 orders of magnitude. It is important to note that the observed improvements were (a) not restricted to a small number of peaks or (b) were not random; they were seen over the whole LIBS spectrum. Additionally, we have shown that enhanced spectra can be employed to improve classification capabilities (here, we used the PCA analysis). Applications for this can be found in standoff LIBS and other techniques where the SNR is often extremely low. By altering the acquisition time and material composition, the perturbation was achieved. To the best of our knowledge, we showed this technique for the first-time utilizing nanosecond LIBS data, even though it has been well established in the analysis of NMR and IR data. Additionally, we discussed a few more potential applications in the section on conclusions.

4.2 Experimental procedure

The experimental setup for the time-resolved ns-LIBS is shown in figure 2.18 of chapter 2. An ICCD and spectrometer system received the collected LIBS signal. Due to the significant plasma emissions from both metals and bimetals, the gate delay and width were optimized for each sample. Table 4.1 lists the acquisition parameters. Each spectrum resulted from an average of 10 acquisitions obtained repeatedly from different locations. Au-Ag bimetallic targets' LIBS spectra were collected for four distinct compositions, including 20-80, 30-70, 50-50, and 80-20, respectively. The spectrometer and ICCD, activated by the delay generator's output, were connected to the gathered light through a 600 m optical fiber. Typically, 20 time-resolved kinetic spectra were obtained, averaged at each time delay, as shown in figure 4.1. The averaging was carried out to reduce, if any, matrix influence. The driving force behind this work to investigate the correlation between the transitions in the LIBS spectra was the irregular variation in the intensity of the peaks with increasing compositions. The coupling between the Au and Ag peaks for various compositions was shown at various ranges.

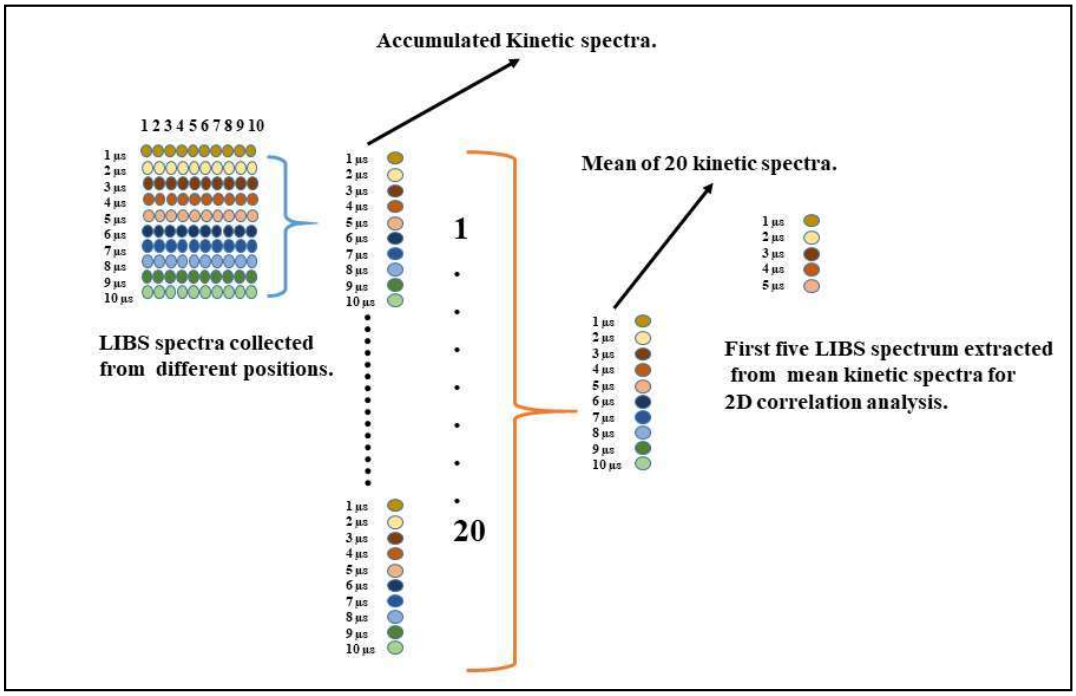

Figure 4.1 The procedure followed in the acquisition of the time-resolved ns LIBS data from various target samples.

Table 4.1 Acquisition parameters used in the time-resolved ns-LIBS experiments.

Samples	Gate delay	Gate width	Exposure time	ICCD Gain
Al, Cu, Brass	0.5 µs	0.5 µs	2 ms	100
Au-Ag Bimetals	1 µs	1 µs	2 ms	50

4.3 2D correlation plots

A set of 'm' LIBS spectra of the system under orderly disturbance resulting a change in the spectral intensity are represented by $y(\lambda_j, t_i)$. Where the discrete variable λ_j for $j = 1,2,3..n$ related to the wavelength sampled over 'n' values in the single spectrum represents. The second variable to time t_i for $i = 1,2,3...m$ represents the effect of the applied perturbation on the system sampled over m time values.

The dynamic spectrum $\tilde{y}(\lambda_j, t_i)$ in the time interval t_1 to t_m is defined in the below equation as

$$\tilde{y}(\lambda_j, t_i) = y(\lambda_j, t_i) - \bar{y}(\lambda_j) \tag{4.1}$$

Where $\tilde{y}(\lambda_j, t_i)$ is the averaged spectra used as a reference in calculating the dynamic spectra. The reference spectra can be either the first or last spectrum of the time-resolved spectra and can be set to zero [30].

The reference spectrum is set to zero in the present studies.

$$\bar{y}(\lambda_j) = \frac{1}{m}\sum_{i=1}^{m} y(\lambda_j, t_i) \tag{4.2}$$

The synchronous part $\Phi(\lambda_1, \lambda_2)$and asynchronous part $\Psi(\lambda_1, \lambda_2)$ of the correlation analysis are written as

$$\Phi(\lambda_1, \lambda_2) = \frac{1}{m-1}\sum_{j=1}^{m} \tilde{y}_j(\lambda_1) \cdot \tilde{y}_j(\lambda_2) \tag{4.3}$$

Where $\tilde{y}_j$is the spectral intensity at a point of time t_j

$$\tilde{y}_j(\lambda_i) = \tilde{y}(\lambda_i, t_j) \qquad i = 1,2$$

$$\Psi(\lambda_1, \lambda_2) = \frac{1}{m-1}\sum_{j=0}^{m} \tilde{y}_j(\lambda_1) \cdot \sum_{j=0}^{m} N_{jk} \cdot \tilde{y}_k(\lambda_2) \tag{4.4}$$

Where N_{jk} Hilbert-Noda transformation matrix

$$\begin{Bmatrix} 0 & if\ j = k \\ \frac{1}{\pi(k-j)} & otherwise \end{Bmatrix} \tag{4.5}$$

In general, the perturbations in the system are introduced by changing temperature, chemical composition, or varying magnetic or electrical field strengths. The present correlation analysis uses the time-resolved LIBS spectra of metal and bimetallic targets with different compositions as the perturbing parameters.

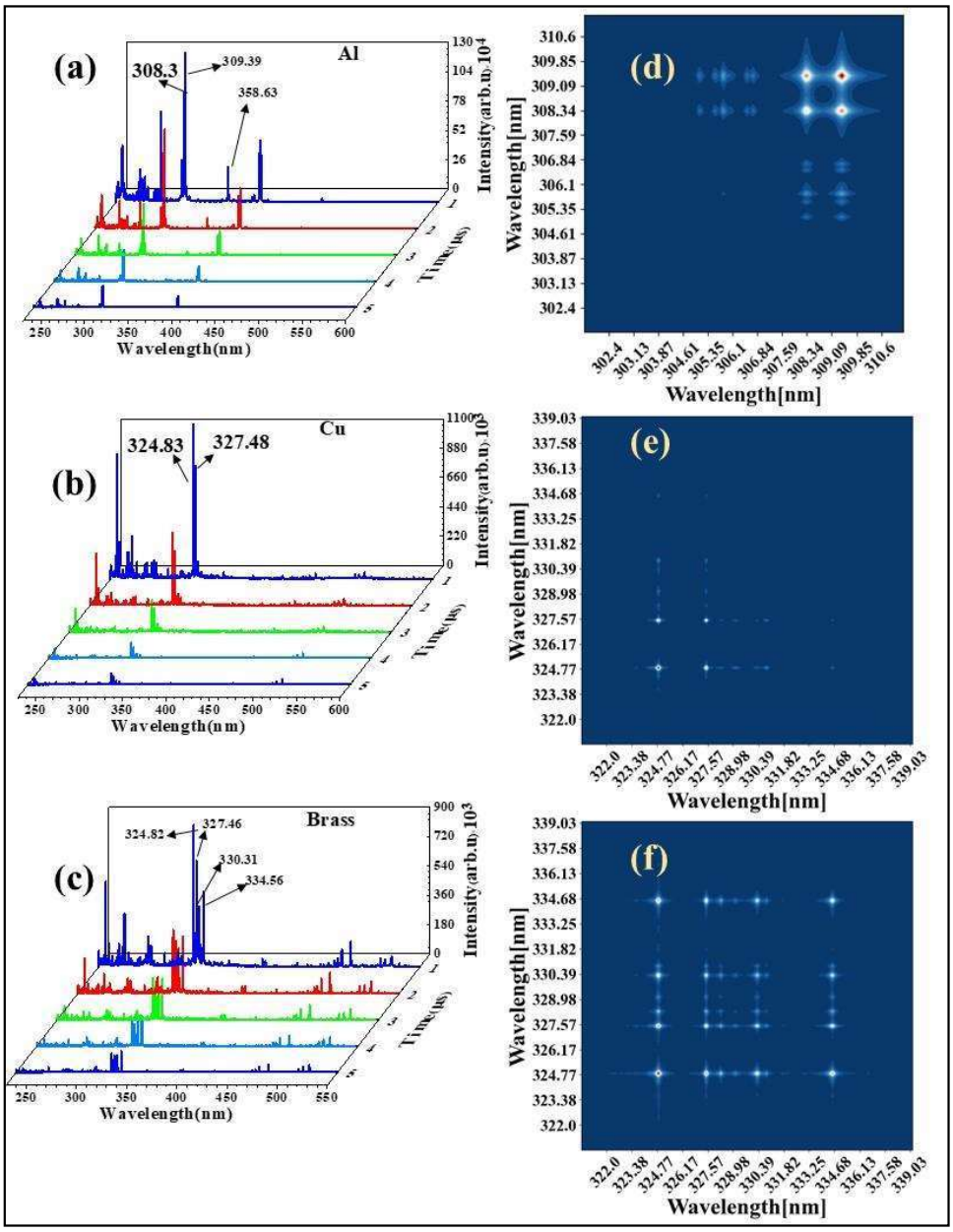

Figure 4.2 The time-resolved ns-LIBS spectra of (a) Al, (b) Cu, (c) Brass at five collected at regular intervals of 1 μs. The 2D correlation data obtained from the ns-LIBS spectra of (d) Al and, (e) Cu, (f) Brass targets, respectively.

The resulting synchronous and asynchronous 2D correlation spectra are complementary to each another. The 2D asynchronous spectra were not explored in this investigation since they did not show significant variation. Figures 4.2 (a), (b), (c) depict the time-resolved LIBS spectra of Al, Cu, and Brass at five specific times at regular intervals of one second respectively. The same data was used for the 2D correlation studies of Al, Cu, and Brass, respectively, in figure 4.2(d), figure 4.2(e), and figure 4.2(f). We have calculated the asynchronous correlation spectrum for only Al demonstrating the inconsiderable variations and not useful in SNR improvement. The asynchronous spectra of aluminum peaks is shown in figure 4.3.

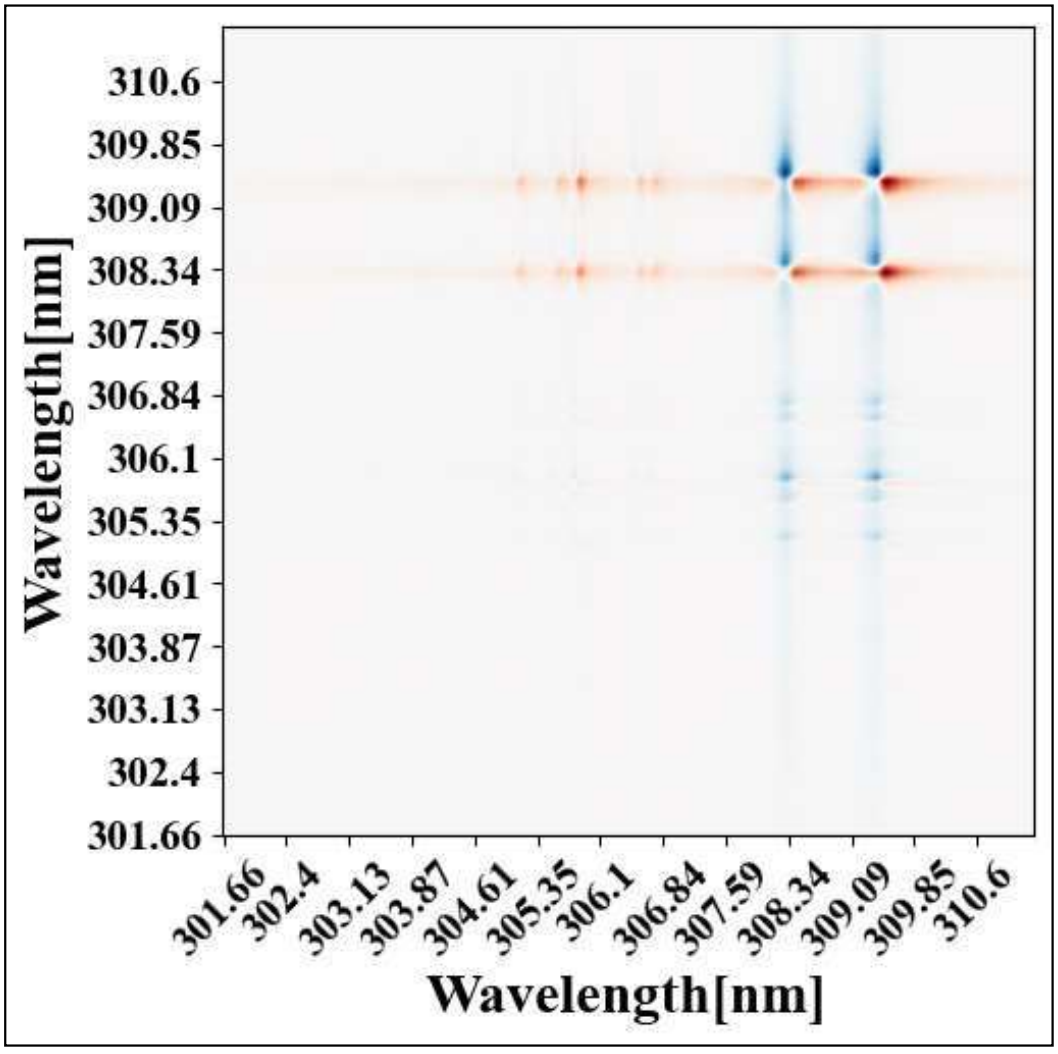

Figure 4.3 The atomic peaks of the Al in the time-resolved LIBS spectra are used for the asynchronous correlation analysis. The analysis was discontinued on the other spectra.

The copper peak at 324.82 nm fitted with a Lorentzian curve before and after the 2D correlation analysis, and the width measured before analysis was 0.153 nm and 0.09 nm.

It was observed that the FWHM of the peak is reduced, indicating an improvement in the resolution, as shown in the figure 4.4.

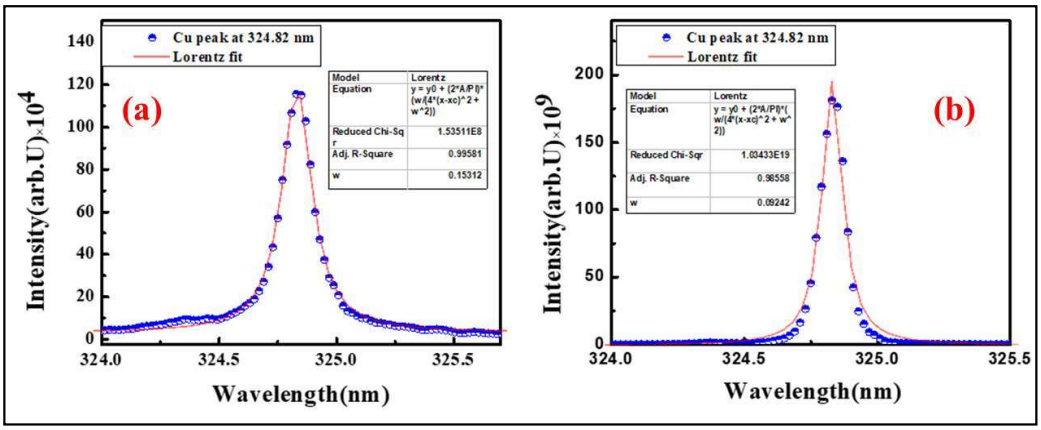

Figure 4.4 a) Cu peak from the ns-LIBS spectra fitted with Lorentzian before the analysis. b) The same data fitted with a Lorentzian function after the analysis it shows the improvement in the resolution after the 2D correlation analysis.

4.3.1 Results and discussion

The effect of reference spectra on the analysis were tested using four distinct spectra, as shown in figure 4.5(a) shows the analysis when the first spectrum collected at 1µs was used for the reference. Figure 4.5(b) shows the analysis when the final spectrum collected at 5µs was used for the reference. In contrast, figure 4.5(c) shows the analysis when zero references were used, and figure 4.5(d) shows the analysis when the average of the five spectra was used for the reference. For various reference spectra, the fluctuation in the intensity and width is seen. When the first spectrum is used as a reference, as shown in figure 4.5(a), the peaks are broad and high, and the breadth and height are decreased in the case when the final spectrum was used for reference [figure 4.5(b)] and the zero for reference spectrum [figure 4.6(c)]. When the reference spectrum utilized was an average of all the spectra, the intensities were too low [figure 4.6(d)] could be the result of the flat baseline in LIBS spectra that were acquired using the gated spectrometer, where the radiation of the plasma continuum was avoided. The 2D synchronous correlation plot's amplitude depends on the intensity of the correlated peaks in the LIBS signals and the degree to which their changes are associated. Because there is no autocorrelation in the noise, the contributions from the random noise are insignificant and are supressed in the diagonal of the 2D correlation plots.

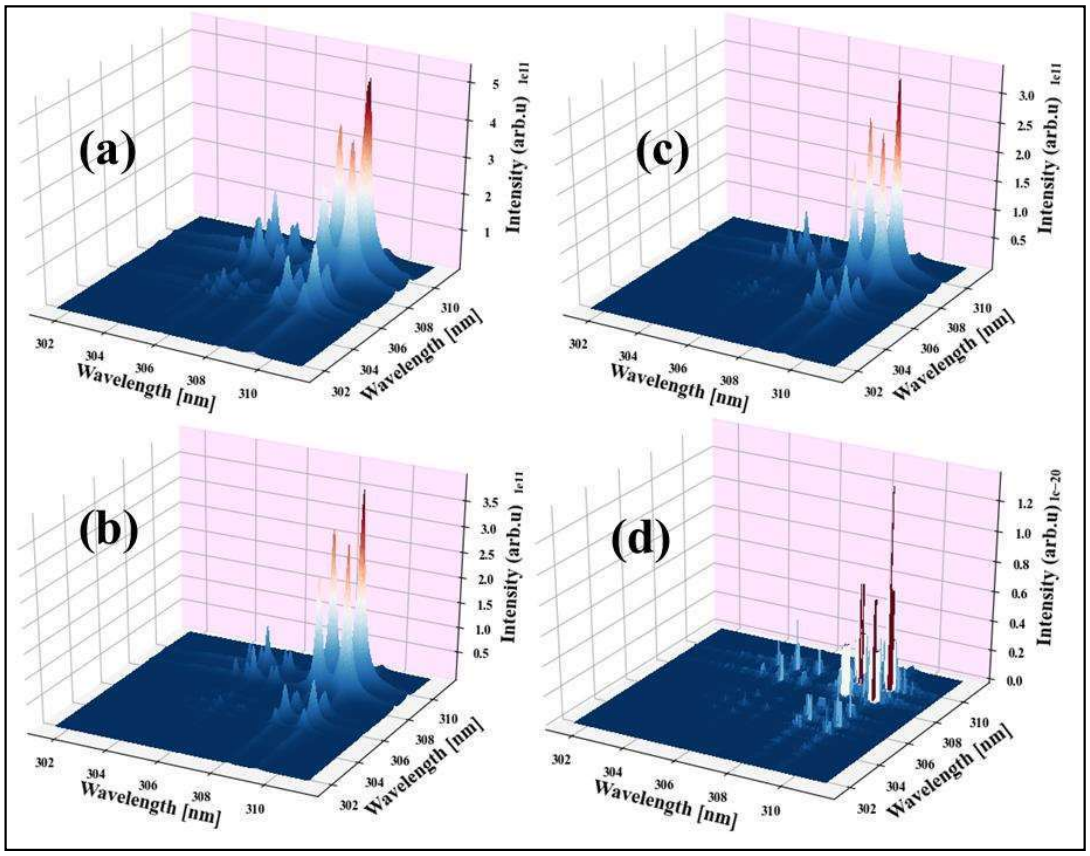

Figure 4.5 2D correlation analysis performed (a) with the spectrum acquired at 1 µs, (b) the spectrum at 5 µs, (c) with the reference taken as zero and (d) the average spectrum of the five time-resolved spectra as reference.

The LIBS spectra and the diagonal of the 2D correlation analysis were compared to substantiate the improvement in the signal, as shown in figure 4.6. Figure 4.6(a) shows the time-resolved LIBS spectra of Al in the spectral region of 303–312 nm, whereas figure 4.6(b) displays the matching 2D correlation spectra while figure 4.6(c) displays the diagonal plot of the 2D correlation analysis.

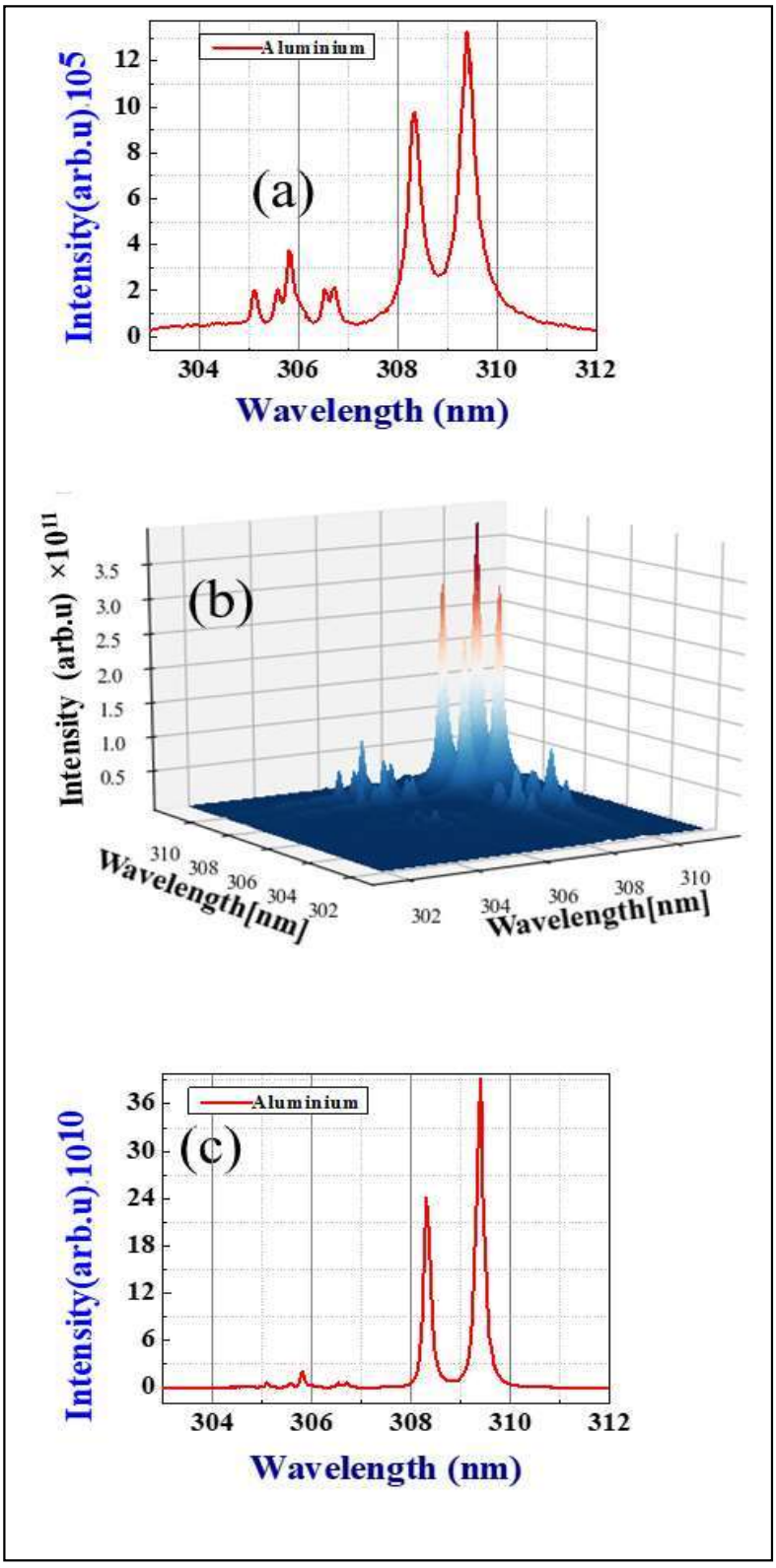

Figure 4.6 The peaks from the regular ns-LIBS spectrum of (a) Al target in the spectral range of 303-312 nm and the corresponding, (b) 2D correlation analysis, and (c) diagonal of the 2D correlation analysis on the LIBS spectra.

4.3.2 Correlation studies

The wavelength serves as the X and Y-axis, and the contour plot's color gradient is the correlation strength. The diagonal peaks, also known as auto-peaks, are the autocorrelation of the peak, while the off-diagonal peaks, also known as cross-peaks, correlate with other peaks. Python program was used to analyze the dynamic spectra and calculate the synchronous and asynchronous spectra, using the average spectra as a reference. The contour's shape pertains to how uniformly the peak broadens. Because the random noise did not correlate with the signal over time, the noise in the 2D spectra was reduced, resulting in improved signal-to-noise. The atomic peaks at 309.27 nm and 309.28 nm of Al correlate positively, as seen in figure 4.2(d), and the peak values are listed in table 4.2. The Cu peaks at 329.54 and 330.20 nm in figure 4.2(e) showed a good association, and table 4.3 lists the identified peaks. The magnitude of the cross-peaks reveals the degree of correlation. Figure 4.2(f) data of Brass demonstrates the correlation between the atomic peaks of copper at 324.75 nm and Zinc at 334.5 nm; this correlation was stronger than the Zinc peak autocorrelation. Table 4.4 lists the Brass LIBS peaks in brief. Brass and Cu exhibit comparable correlation in the 220-250 nm range and vary in the 320-340 nm range. It was discovered that the autocorrelation of the peak at 327.39 nm was weaker than the peak at 324.7 nm and the cross peak, indicating that the transition at 327.39 nm and 324.7 nm was coupled.

Table 4.2 Peaks identified from the near-field ns-LIBS spectrum of the Al target.

Sl. No.	Wavelength Observed (nm)	Element	Ionization
1	305.00	Al	I
2	305.71	Al	I
3	308.21	Al	I
4	309.27	Al	I
5	309.28	Al	I
6	358.65	Al	II
7	394.40	Al	I
8	396.15	Al	I

Table 4.3 Peaks identified from ns-LIBS spectrum of copper target.

Sl. No.	Wavelength Observed (nm)	Element	Ionization
1	296.11	Cu	I
2	324.75	Cu	I
3	327.39	Cu	I
4	329.05	Cu	I
5	330.79	Cu	I
6	333.78	Cu	I
7	465.11	Cu	I
8	510.55	Cu	I
9	515.32	Cu	I
10	521.82	Cu	I
11	529.25	Cu	I
12	578.21	Cu	I

Table 4.4 Peaks identified from ns-LIBS spectrum of the Brass target.

Sl. No.	Wavelength observed (nm)	Element	Ionization
1	324.75	Cu	I
2	327.39	Cu	I
3	32905	Cu	I
4	330.79	Cu	I
5	333.78	Cu	I
6	330.25	Zn	I
7	330.29	Zn	I
8	334.50	Zn	I
9	334.55	Zn	I
10	334.59	Zn	I
11	468.01	Zn	I
12	472.21	Zn	I
13	481.05	Zn	I

Figure 4.7 data [4.7(a) represents Al, figure 4.7(b) represents Cu, and figure 4.7(c) represents Brass] shows that the LIBS signal intensity of the atomic peaks increased by ~5 orders of magnitude. In contrast, bimetallic targets illustrated ~4 orders of magnitude improvement [figure 4.7(d) illustrates Au30-Ag70, figure 4.7(e) illustrates Au50-Ag50, and figure 4.7(f) illustrates Au80-Ag20 targets data, respectively]. It is important to note here that the SNR gains have only been seen for these specific data sets under the previously described experimental circumstances. We beleive that further LIBS data will benefit from similar changes as well. This study will be beneficial in cases where the SNR is very lowfor instance, standoff LIBS spectra of explosive compounds in the single shot mode. However, thorough studies are required to support this claim. Recently, Quaroni et al. revealed that for time-resolved infrared spectra, the signal has increased by three orders of magnitude [31]. Additionally, the peaks' widths were reduced, indicating improvement in resolution. This exemplifies how using multiple spectra taken under perturbed conditions can enhance the quality of the spectra. Exploring the use of this strategy to combat the matrix effects in LIBS would also require more research.

Brighter off-diagonal peaks indicate strong correlation between time-resolved spectra. Figures 4.8(a), 4.8(b), and 4.8(c) depict the 2D correlations analysis from the time-resolved LIBS spectra of bimetal targets for Au30-Ag70, Au50-Ag50, and Au80-Ag20, respectively. The 2D correlation analyses for the Au30-Ag70, Au50-Ag50, and Au80-Ag20 targets are illustrated in figure 4.8(d), figure 4.8(e), and figure 4.8(f), respectively, using five different gate delays with regular intervals of 1 μs. Superior correlations were seen for the Au50-Ag50 than for the other two. Additionally, it is noted that although the intensity of the off-diagonal peaks varies with the change in Ag%, the first ionized peak of Ag at 241.32 nm does not exhibit considerable variation. Ag's first ionized peak at 241.32 nanometers and Au's atomic peak at 242.7 nm exhibit a more substantial cross peak.

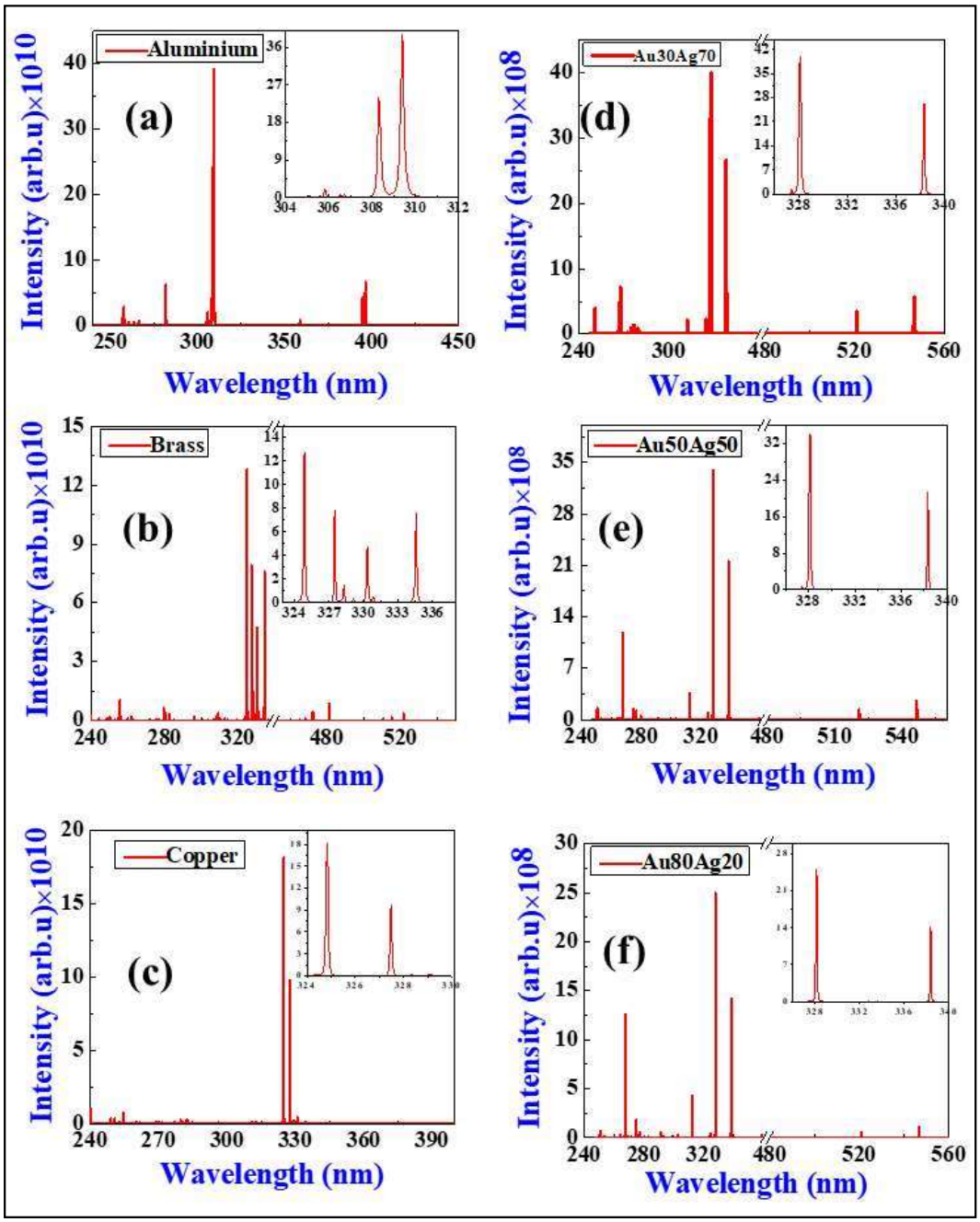

Figure 4.7 The improved spectrum extracted from the 2D correlation analysis on LIBS spectra of (a) Al, (b) Cu, (c) Brass, (d) Au30Ag70, (e) Au50Ag50 (f) Au80Ag20 targets, respectively.

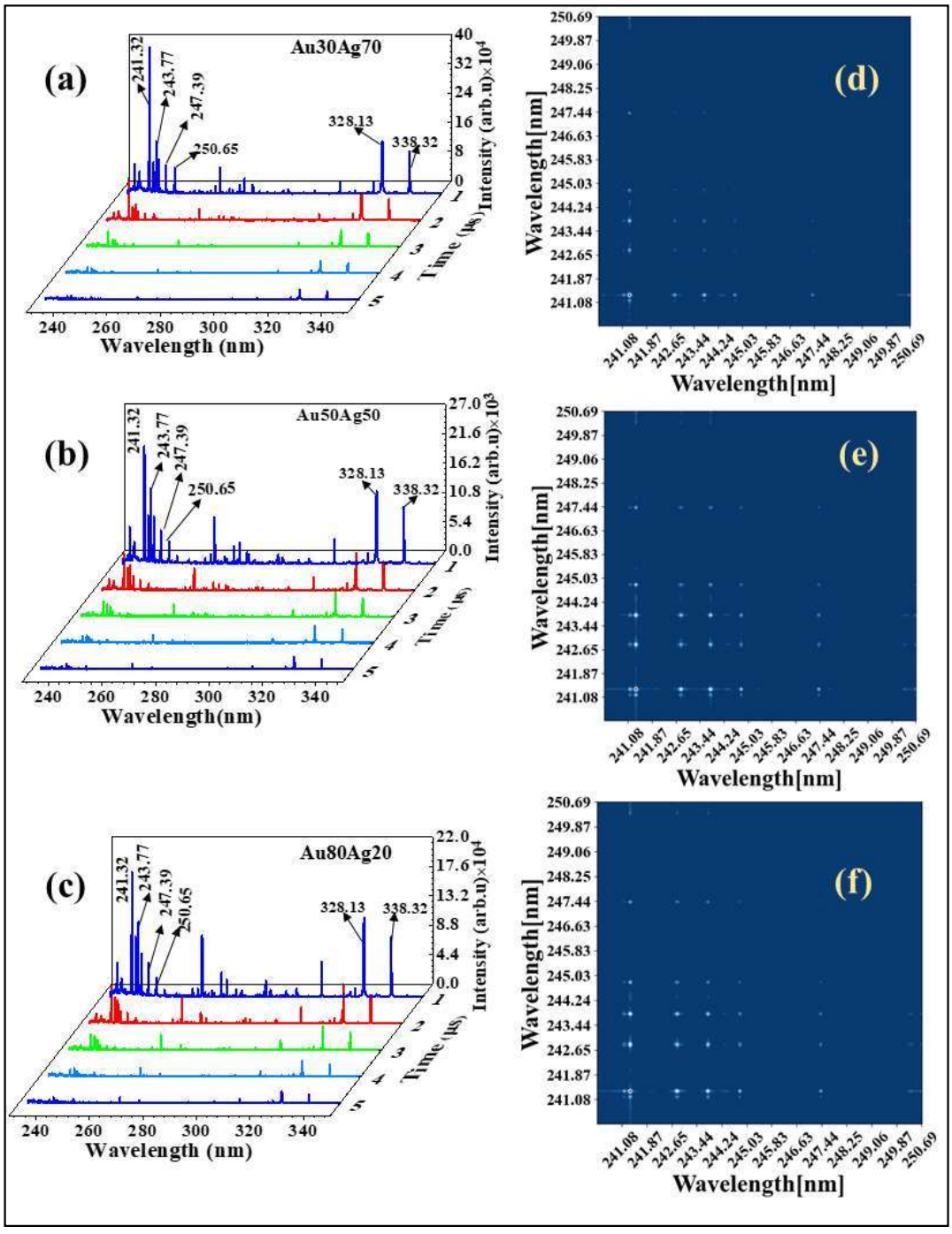

Figure 4.8 Time-resolved LIBS spectra of (a) Au30-Ag70, (b) Au50-Ag50, (c) Au80-Ag20 bimetallic targets at five delays with regular intervals of 1μs with identified peaks. The 2D correlation studies on ns-LIBS spectra of (d) Au30-Ag70, (e) Au50-Ag50, (f) Au80-Ag20 targets.

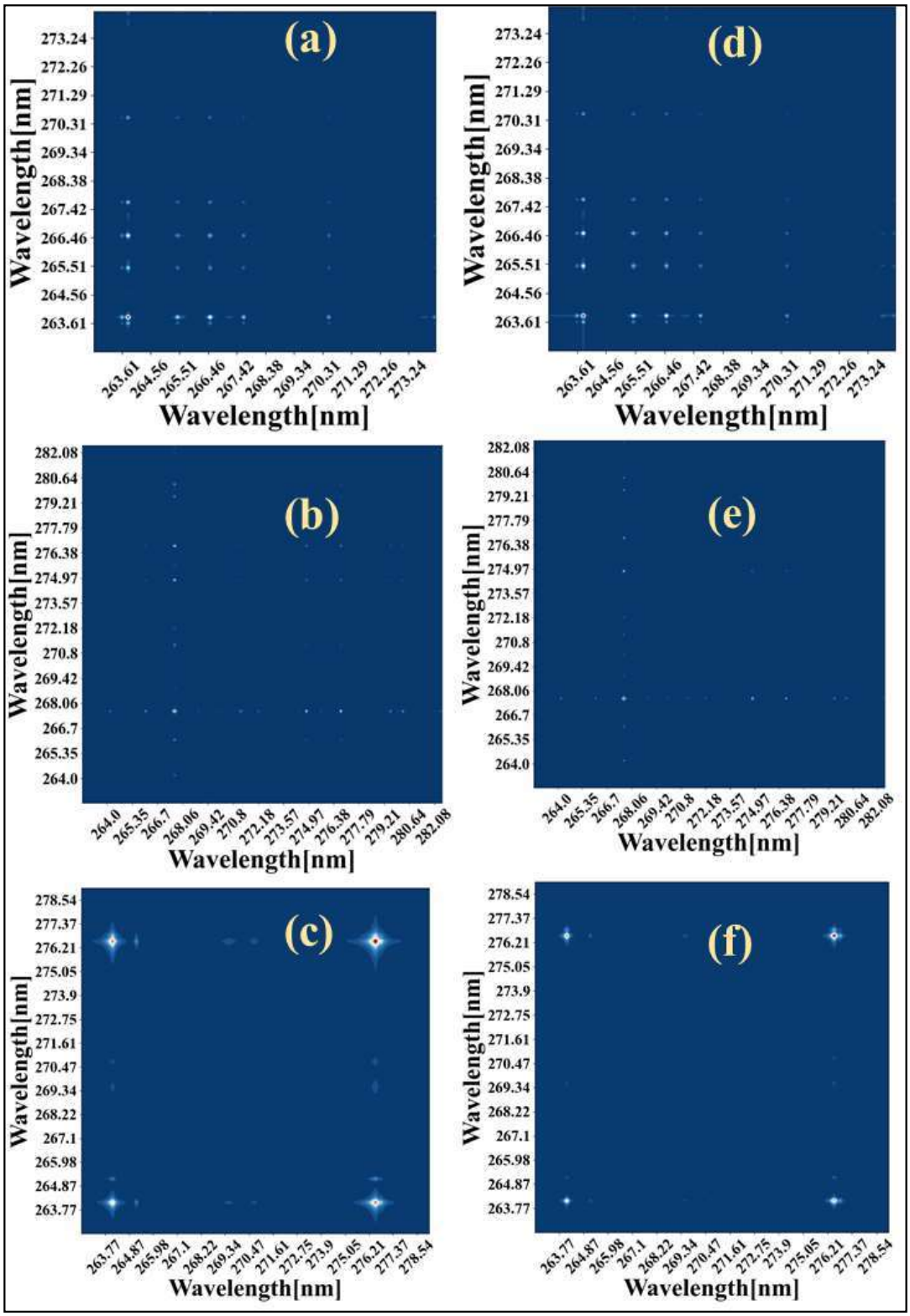

Figure 4.9 2D correlation studies on the ns-LIBS spectra of Au-Ag bimetal with three compositions and at two delays in the range (a) 240-250 nm, (b) 260-280 nm, (c) 520-550 nm at 1 µs and, (d) 240-250 nm, (e) 260-280 nm, (f) 520-550 nm at 2 µs.

Figure 4.9 shows the outcomes after using the variable composition of Ag/Au in the Ag-Au alloy target as a perturbing parameter. The data collected for gate delays of 1 µs and 2 µs were compared in the 2D analysis for three distinct compositions. Analysis on the LIBS spectra in three wavelength range of 240–250 nm, 260–280 nm, and 520–550 nm acquired at 1µs and 240–250 nm, 260–280 nm, and 520–550 nm at 2µs after the laser pulse were compared. The correlations were better in the 240–250 nm range but worse in the 260–280 nm and 520–550 nm ranges. For the 2D correlation experiments, LIBS spectra of Au-Ag bimetal targets at three distinct compositions were utilized. These targets were in the 240–250 nm [figure 4.10(a)], 260–280 nm [figure 4.10(b)], 520–550 nm [figure 4.10(c)], and 240–250 nm [figure 4.10(d)], 260–280 nm [figure 4.10(e)], In the 240–250 nm range, the correlations between various compositions grew with time whereas they shrank in the other two ranges. Table 4.5 provides an overview of the Au and Ag LIBS peaks that were found.

Table 4.5 Identified peaks form the ns-LIBS spectrum of Au-Ag bimetallic target.

Sl. No.	Wavelength Observed (nm)	Element	Ionization State
1	241.32	Ag	II
2	242.7	Au	I
3	243.77	Ag	II
4	247.39	Ag	II
5	267.5	Au	I
6	276.7	Au	I
7	328.13	Ag	I
8	338.32	Ag	I
9	520	Ag	I
10	546	Ag	I
11	768	Ag	I

4.3.3 Classification studies

Figure 4.10 shows the outcomes of PCA on the diagonal of the 2D synchronous analysis and the LIBS spectra. PCA achieves dimensional reduction [33] by maximizing the principal components' variance; with less dimensional information, we may be able to

explain the system. The information contained in the component increases with the variation. The cumulative explained variance tells us how many primary components to include in the data description. Figure 4.10(a) displays the PCA score plot, while figure 4.10(b) displays the variance plot (b). The cumulative explained plot for the typical LIBS spectra is shown in figure 4.10(c). Additionally, the enhanced spectra score plot, variance plot, and cumulative variance plot [figures 4.10(d), 4.10(e), and 4.10(f)] were compared. We achieved 95% variance with just the first three principal components in this case, whereas in regular spectra (with the noise) it took more than 5 components to get 80% variance, which is much lower than the earlier number. This improvement was possible by reducing the noise and increasing the peak intensity using the correlation analysis.

The SNR of the spectra was significantly enhanced in the case of intense peaks and the strongly associated peaks in regular spectra. Figure 4.2 depicts the relationship between the atomic peaks of Al (303 nm–310 nm range), Cu (320 nm–340 nm range), and Brass (320 nm–340 nm range). Brass shows the substantial coupling between the Cu and Zn lines in the 320–340 nm range. Compared to the other compositions in the 240 nm–250 nm range, the cross-peaks for the Au50–Ag50 sample were particularly strong. For various compositions, the Au-Ag correlation peaks were plotted from the time-resolved LIBS spectra, and the observed cross-peaks were found to be strong in the 260 nm-280 nm region, as shown in figure 4.8. By eliminating the components that remain constant, these 2D plots also aid in differentiating samples of various compositions. We can enhance the classification using the diagonal from the 2D analysis data. The classification and understanding of the association between various transitions will significantly benefit the investigation of diverse samples using different perturbation techniques. Additionally, this might be a useful tool for investigating the molecular emissions in fs-LIBS [34, 35] and the analysis of data using machine learning applications.

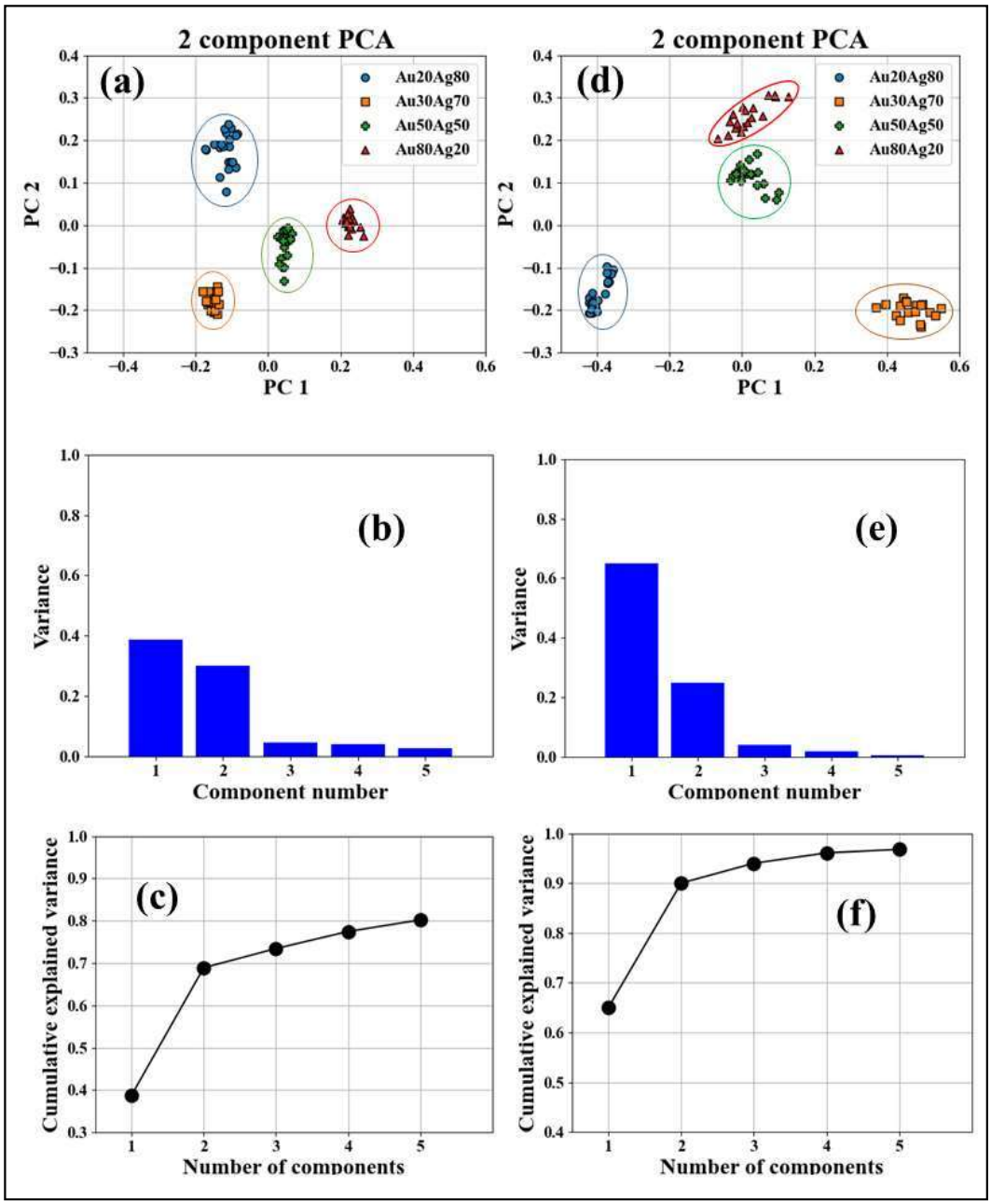

Figure 4.10 PCA on the ns-LIBS spectra of bimetal targets and the diagonal of the 2D correlation analysis (a) PCA score plot (b) variance plot (c) cumulative explained variance on ns-LIBS spectra and (d) PCA score plot (e) variance plot (f) cumulative explained variance on the improved diagonal of the 2D spectra. A solid line is a guide to the eye.

4.3.4 2D correlation analysis of standoff LIBS data

The improvement in the SNR of the femtosecond LIBS spectra is shown in figures 4.11 (a), (b), (c) for Polyvinyl chloride (PVC) and 4.12 (a), (b), (c) for Hydroxypropyl Cellulose (HPC), wherein the spectra were obtained from a standoff distance of 6.5 m. Figures 4.11

(d), (e), (f) and 4.12 (d), (e), (f) illustrate how the SNR is improved using the 2D analysis on PVC and HPC data published in our work [18].

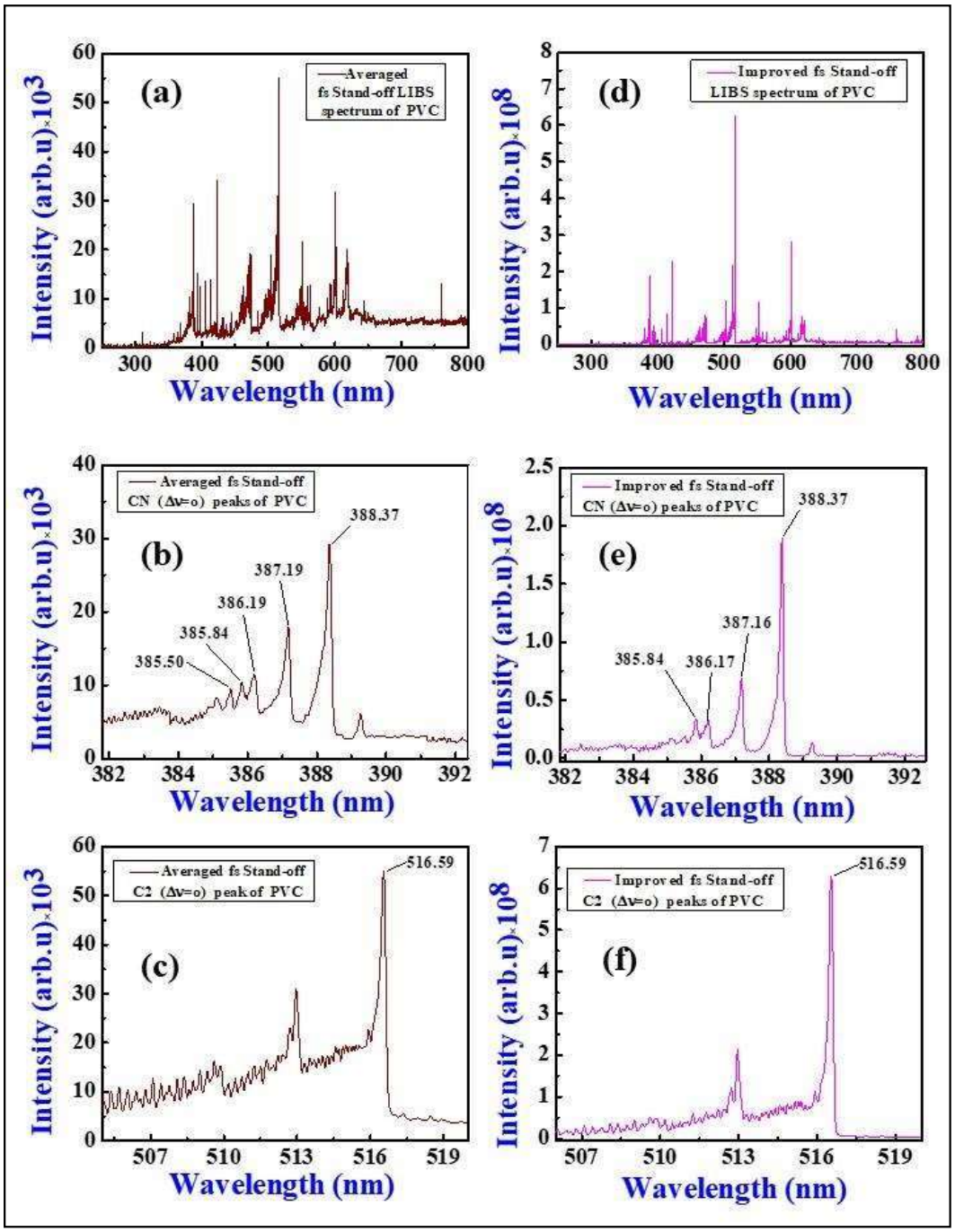

Figure 4.11 The average of fs-standoff LIBS spectra of (a) PVC, (b) CN band, (c) C_2 band compared with the diagonal of the 2D correlation analysis demonstrating the improvement of five orders of magnitude (d) whole spectra (e) the CN band, and (f) C_2 band.

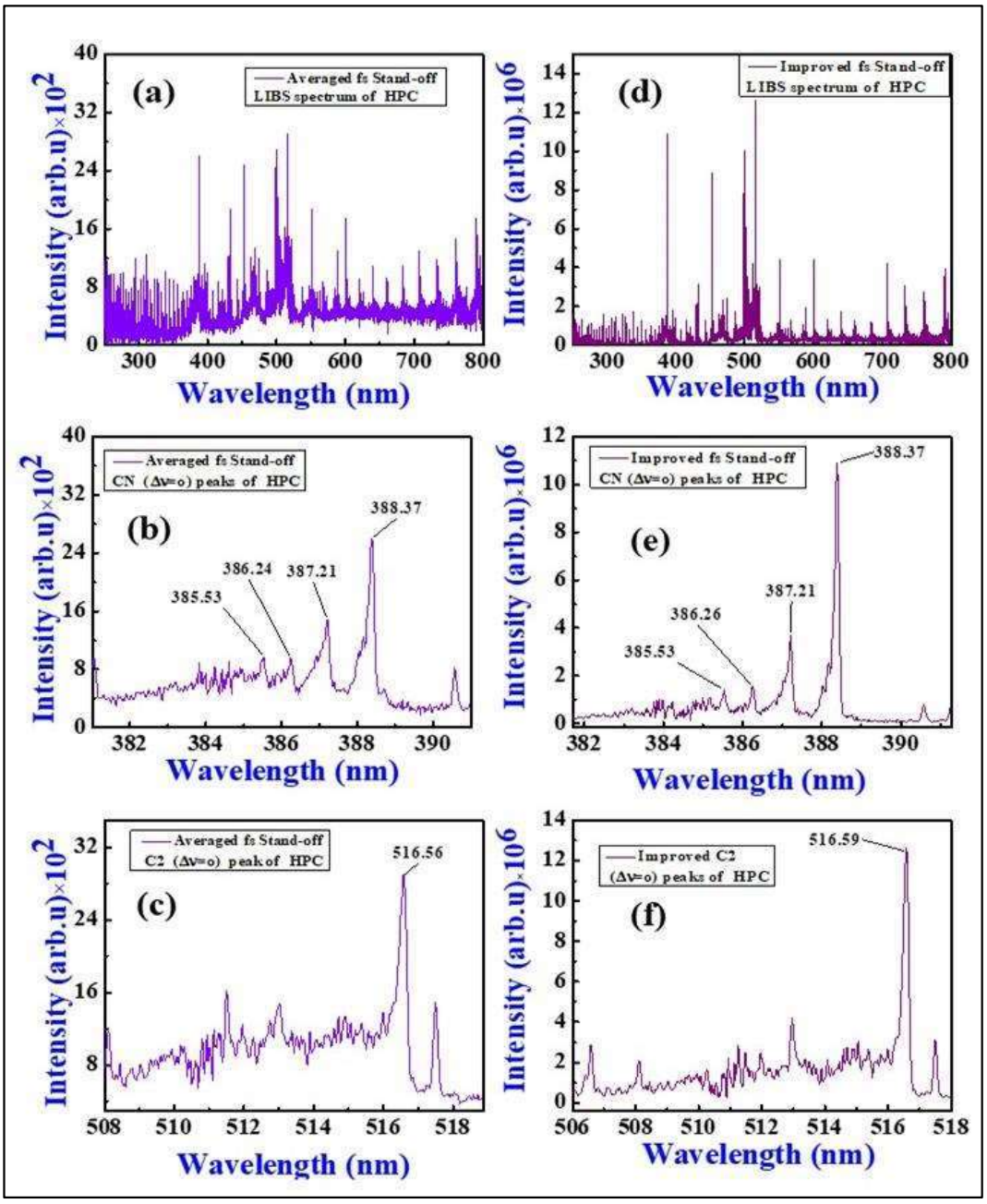

Figure 4.12 The average of fs-standoff LIBS spectra of (a) HPC, (b) CN band, (c) C_2 band compared with the diagonal of the 2D correlation analysis demonstrating the improvement of five orders of magnitude (d) whole spectra, (e) the CN band, and (f) C_2 band.

4.4 Conclusions

The randomly fluctuating noise in LIBS spectra has little correlation in time and the transitions are well correlated resulting in the improvement of SNR when 2D correlation analysis is used. The correlations in the transitions cannot be inferred from the linear spectroscopic data. Furthermore, 2D correlation analysis seems to be an effective method

for resolving the overlap peaks in the spectra. The interpretation of correlations between LIBS transitions is made simpler by 2D correlation analysis, and it helps visualize the wavelength shift and time-dependent decay of various LIBS peaks. We also include recommendations for future research and the key findings from this work. These investigations will improve knowledge of the molecular peaks and their association, particularly in the femtosecond LIBS spectra. For instance, molecular emissions such as CN, C_2, AlO, and TiO in the LIBS spectra may provide further information regarding the sample properties. Due to the spread of peaks in second dimension, improved SNR, and resolution from regular spectrum with overlapped peaks were achieved, which was impossible otherwise. 2D studies in combination with time-resolved LIBS spectra or other perturbation methods result in better resolution with the simple spectrometer. To better understand the transitions, the same experiments can be carried out with other perturbations, such as modifying the input laser energy, gate delays, ICCD gain, the distance at which the emissions are collected, compositions, etc. The SNR weakens in the standoff LIBS, and this method can be utilized to improve it, particularly in the case of explosives detection [36, 37].

Reference

1) S. N. Thakur and J. P. Singh, Fundamentals of laser induced breakdown spectroscopy. In Laser-induced breakdown spectroscopy, Elsevier, 2007, 3-21.
2) S.S. Harilal, J. Yeak, B.E. Brumfield, J.D. Suter, M.C. Phillips, Dynamics of molecular emission features from nanosecond, femtosecond laser and filament ablation plasmas, J. Anal. At. Spectrom. 31 (2016) 1192–1197. doi:10.1039/c6ja00036c.
3) D. Prochazka, M. Mazura, O. Samek, K. Rebrošová, P. Pořízka, J. Klus, P. Prochazková, J. Novotný, K. Novotný and J. Kaiser, Combination of laser-induced breakdown spectroscopy and Raman spectroscopy for multivariate classification of bacteria, Spectrochim. Acta Part B At. Spectrosc. 139 (2018) 6–12. doi:10.1016/j.sab.2017.11.004.
4) SJ Rehse, A review of the use of laser-induced breakdown spectroscopy for bacterial classification, quantification, and identification, Spectrochim. Acta Part B At. Spectrosc. 154 (2019) 50–69. doi:10.1016/j.sab.2019.02.005.
5) Q. Wang, G. Teng, X. Qiao, Y. Zhao, J. Kong, L. Dong, X. Cui, Importance evaluation of spectral lines in Laser-induced breakdown spectroscopy for classification of pathogenic bacteria, Biomed. Opt. Express. 9 (2018) 5837–5850. doi:10.1364/BOE.9.005837.
6) S. Abdul Kalam, S. V. Balaji Manasa Rao, M. Jayananda, S. Venugopal Rao, Standoff femtosecond filament-induced breakdown spectroscopy for classification of geological materials, J. Anal. At. Spectrom. 35 (2020) 3007–3020. doi:10.1039/d0ja00355g.
7) R.S. Harmon, J. Remus, N.J. McMillan, C. McManus, L. Collins, J.L. Gottfried Jr, FC DeLucia, A.W. Miziolek, LIBS analysis of geomaterials: geochemical fingerprinting for the rapid analysis and discrimination of minerals, Appl. Geochemistry. 24 (2009) 1125–1141. doi:10.1016/j.apgeochem.2009.02.009.
8) V. Lazic, F. Colao, R. Fantoni, V. Spizzicchino, Recognition of archeological materials underwater by laser induced breakdown spectroscopy, Spectrochim. Acta Part B At. Spectrosc. 60 (2005) 1014–1024. doi:10.1016/j.sab.2005.06.014.
9) F. Ruan, T. Zhang, H. Li, Laser-induced breakdown spectroscopy in archeological science: a review of its application and future perspectives, Appl. Spectrosc. Rev. 54 (2019) 573–601. doi:10.1080/05704928.2018.1491857.
10) A.K. Myakalwar, N. Spegazzini, C. Zhang, S.K. Anubham, R.R. Dasari, I. Barman, M.K. Gundawar, Less is more: Avoiding the LIBS dimensionality curse through judicious feature selection for explosive detection, Sci. Rep. 5 (2015) 13169. doi:10.1038/srep13169.
11) FC De Lucia, J.L. Gottfried, A.W. Miziolek, Evaluation of femtosecond laser-induced breakdown spectroscopy for explosive residue detection, Opt. Express. 17 (2009) 419–425. doi:10.1364/OE.17.000419.
12) R. González, P. Lucena, L.M. Tobaria, J.J. Laserna, Standoff LIBS detection of explosive residues behind a barrier, J. Anal. At. Spectrom. 24 (2009) 1123–1126. doi:10.1039/B821566A.
13) J. Moros, F.J. Fortes, J.M. Vadillo, J.J. Laserna, LIBS detection of explosives in traces, in: Laser-Induced Break. Spectrosc. J. Moros, F. J. Fortes, J. M. Vadillo J. J. Laserna, Laser-Induced Break. Spectrosc. Springer, 2014, Pp. 349–376 Berlin, Heidelberg. doi:10.1007/978-3-642-45085-3_13
14) L. Burgio, K. Melessanaki, M. Doulgeridis, R.J.H. Clark, D. Anglos, Pigment identification in paintings employing laser induced breakdown spectroscopy and Raman microscopy, Spectrochim. Acta Part B At. Spectrosc. 56 (2001) 905–913. doi:10.1016/S0584-8547(01)00215-4.
15) D.W. Hahn, N. Omenetto, Laser-induced breakdown spectroscopy (LIBS), part I: Review of basic diagnostics and plasmaparticle interactions: Still-challenging issues within the analytical plasma community, Appl. Spectrosc. 64 (2010) 335–366. doi:10.1366/000370210793561691.
16) S.K. Sharma, A.K. Misra, P.G. Lucey, R.C.F. Lentz, A combined remote Raman and LIBS instrument for characterizing minerals with 532 nm laser excitation, Spectrochim. Acta Part A Mol. Biomol. Spectrosc. 73 (2009) 468–476. doi:10.1016/j.saa.2008.08.005.
17) A. Giakoumaki, I. Osticioli, D. Anglos, Spectroscopic analysis using a hybrid LIBS-Raman system, Appl. Phys. A. 83 (2006) 537–541. doi:10.1007/s00339-006-3541-0.
18) NL. Murthy, S. Abdul Salam, S.V. Rao, Stand-off Femtosecond Laser Induced Breakdown Spectroscopy of Metals, Soil, Plastics and Classification Studies, 2019 Work. Recent Adv. Photonics, WRAP 2019. (2019) 16–18. doi:10.1109/WRAP47485.2019.9013674.
19) A. De Giacomo, M. Dell'Aglio, R. Gaudiuso, C. Koral, G. Valenza, Perspective on the use of nanoparticles to improve LIBS analytical performance: nanoparticle enhanced laser induced breakdown spectroscopy (NELIBS), J. Anal. At. Spectrom. 31 (2016) 1566–1573. doi:10.1039/C6JA00189K.

20) C.G. Parigger, Atomic and molecular emissions in laser-induced breakdown spectroscopy, Spectrochim. Acta Part B At. Spectrosc. 79 (2013) 4–16. doi:10.1016/j.sab.2012.11.012
21) C.G. Parigger, J.O. Hornkohl, Computation of AlO B2Σ+→ X2Σ+ emission spectra, Spectrochim. Acta Part A Mol. Biomol. Spectrosc. 81 (2011) 404–411. doi:10.1016/j.saa.2011.06.029
22) SJ Mousavi, M. Hemati Farsani, S.M.R. Darbani, A. Mousaviazar, M. Soltanolkotabi, A. Eslami Majd, CN and C2 vibrational spectra analysis in molecular LIBS of organic materials, Appl. Phys. B Lasers Opt. 122 (2016). doi:10.1007/s00340-016-6371-6.
23) S.A. Kalam, N.L. Murthy, P. Mathi, N. Kommu, A.K. Singh, S.V. Rao, Correlation of molecular, atomic emissions with detonation parameters in femtosecond and nanosecond LIBS plasma of high energy materials, J. Anal. At. Spectrom. 32 (2017) 1535–1546. doi:10.1039/c7ja00136c.
24) E.N. Rao, P. Mathi, S.A. Kalam, S. Sreedhar, A.K. Singh, B.N. Jagatap, S.V. Rao, Femtosecond and nanosecond LIBS studies of nitroimidazoles: correlation between molecular structure and LIBS data, J. Anal. At. Spectrom. 31 (2016) 737–750. doi:10.1039/C5JA00445D.
25) I. Noda, A.E. Dowrey, C. Marcott, Recent developments in two-dimensional infrared (2D IR) correlation spectroscopy, Appl. Spectrosc. 47 (1993) 1317–1323. doi:10.1366/0003702934067513
26) I. Noda, Generalized two-dimensional correlation method applicable to infrared, Raman, and other types of spectroscopy, Appl. Spectrosc. 47 (1993) 1329–1336. doi:10.1366/0003702934067694.
27) Y.M. Jung, I. Noda, New approaches to generalized two-dimensional correlation spectroscopy and its applications, Appl. Spectrosc. Rev. 41 (2006) 515–547. doi:10.1080/05704920600845868.
28) I. Noda, Y. Liu, Y. Ozaki, Two-Dimensional Correlation Spectroscopy Study of Temperature-Dependent Spectral Variations of N-Methylacetamide in the Pure Liquid State. 2. Two-Dimensional Raman and Infrared- Raman Heterospectral Analysis, J. Phys. Chem. 100 (1996) 8674–8680. doi:10.1021/jp9534141.
29) L. Ma, V. Sikirzhytski, Z. Hong, I.K. Lednev, S.A. Asher, Insight into resolution enhancement in generalized two-dimensional correlation spectroscopy, Appl. Spectrosc. 67 (2013) 283–290. doi:10.1366/11-06541.
30) M.A. Czarnecki, Interpretation of two-dimensional correlation spectra: Science or art?, Appl. Spectrosc. 52 (1998) 1583–1590. doi:10.1366/0003702981943086.
31) L. Quaroni, E. Normand, Two-Dimensional Correlation Spectroscopy Analysis for the Recovery of Weak Bands from Time-Resolved Infrared Spectra of Single Cells, in: AIP Conf. Proc., 2010: pp. 66–68. doi:10.1063/1.3326352.
32) P. Pořízka, J. Klus, E. Képeš, D. Prochazka, D.W. Hahn, J. Kaiser, On the utilization of principal component analysis in laser-induced breakdown spectroscopy data analysis, a review, Spectrochim. Acta Part B At. Spectrosc. 148 (2018) 65–82. doi:https://doi.org/10.1016/j.sab.2018.05.030.
33) L.M. Narla, S.V. Rao, Identification of metals and alloys using color CCD images of laser-induced breakdown emissions coupled with machine learning, Appl. Phys. B Lasers Opt. 126 (2020) 1–8. doi:10.1007/s00340-020-07469-6.
34) E.N. Rao, S. Sunku, S.V. Rao, Femtosecond laser-induced breakdown spectroscopy studies of nitropyrazoles: the effect of varying nitro groups, Appl. Spectrosc. 69 (2015) 1342–1354.
35) E.J. Kautz, P.J. Skrodzki, M. Burger, B.E. Bernacki, I. Jovanovic, M.C. Phillips, S.S. Harilal, Time-resolved imaging of atoms and molecules in laser-produced uranium plasmas, J. Anal. At. Spectrom. 34 (2019) 2236–2243. doi: 10.1039/C9JA00228F.
36) AK Shaik, N.R. Epuru, H. Syed, C. Byram, V.R. Soma, Femtosecond laser induced breakdown spectroscopy based standoff detection of explosives and discrimination using principal component analysis, Opt. Express. 26 (2018) 8069-8083. doi:10.1364/oe.26.008069.
37) AK Shaik, V.R. Soma, Standoff discrimination and trace detection of explosive molecules using femtosecond filament induced breakdown spectroscopy combined with silver nanoparticles, OSA Contin. 2 (2019) 554–562. doi:10.1364/osac.2.000554.

5 Nanoparticle-enhanced LIBS

Abstract: The impact of various nanoparticles (NPs) on the laser-induced plasma characteristics and optical emissions of multiple materials are reviewed. There have been many recent investigations on the dependence of enhancement on several laser parameters, including input wavelength, energy, and pressure. The effects of NPs factors such as size, shape, substance, and distribution on the surface are thoroughly studied and reported in this chapter. Gold nanoparticles were used to demonstrate the signal improvement from a liquid sample in the femtosecond laser-induced breakdown spectroscopy (fs-LIBS). The fs laser ablation-produced nanoparticles with average diameters of 10-15 nm were used. The strong peak in the CN violet band at 389.4 nm was compared. Achieved two-time amplification in fs-LIBS of Al sheet coated with polyvinyl alcohol (PVA) nanofibers packed with gold nanoparticles in. The fs laser ablation in liquid approach was used to create gold nanoparticles, which had an average size of 10-15 nm.

5.1 Introduction

LIBS is a rapid elemental analysis method requiring little to no sample preparation. The process depends on recombining the plasma's atomic and molecular emissions [1]. The sample is ablated using powerful laser pulses. The laser-generated plasma is commonly created using focused nanosecond pulses from a Q-switched Nd: YAG laser or femtosecond pulses from a Ti: sapphire laser. The identification and categorization of minerals, forensics, national security, planetary exploration, archaeology, and the arts are only a few of the essential domains where LIBS has applications [2–6]. This method was also used to study samples that were in solid, liquid, and gaseous forms. The LIBS method is quick, sensitive, and effective in quantification investigations when integrated with machine learning algorithms like PCA, SVM, and ANN [7,8]. Numerous techniques, including double pulse LIBS, regulating the environment around the plasma plumes, the spatial constraint approach, the magnetic constraint method, chemical replacement techniques, and nanoparticle-enhanced LIBS (NE-LIBS), can be used to improve the LIBS signal [9]. This method involves pre-treating the material by coating it with NPs, which, when exposed to laser pulses, increases the LIBS signal strength. This paper focuses on many NELIBS applications, with a particular emphasis on sensing.

5.1.1 Earlier reviews

The field enhancement close to NPs and the change in the field with the distance between the NPs and their size were shown in the initial review of the NE-LIBS. Additionally, it addressed the issue of the coffee ring effect and the requirement to improve the size and dispersion of NPs. Based on the Keldysh parameter, which is affected by the laser settings, the work function of the sample, and enhanced field intensity because of the localized surface plasmon, the enhancement mechanism was addressed by Dell'Aglio et al. (LSP). The spatial distribution effect on the optical emission intensity demonstrated that the augmentation was significantly more significant within 1-3 mm of the target. Compared to the traditional LIBS, an improvement of two orders of magnitude was recorded [10]. Metals and liquids were the subjects of an extensive review. In the presence of NPs on the sample, a decrease in the slope of the calibration curve that further lowered the limit of detection (LOD) for metal samples and an improvement in the ablation with the NPs was held accountable for the improvement in the LIBS signal [11,12]. Hashimoto et al. Temperature models speculated that the interaction of pulsed lasers with plasmonic gold nanoparticles was used to thoroughly describe the photoinduced dynamics of the NPS, including shape transformation, size reduction, and heat transfer from the NPS to the surrounding medium. Additionally, the surface on which the NPs are applied has undergone nanofabrication, and outstanding characteristics, including light collection and efficient light-to-heat conversion of NPs have been described in detail [13]. This review captures the critical aspects of the results and applications while also debating the mechanisms involved, making it a source of information for the researchers in their early stages of NELIBS experiments. Earlier reviews discussed the sample preparation and the mechanism(s) responsible for the enhancement to a certain extent.

5.1.2 Enhancement via different conditions

Enhancement was achieved in the femtosecond LIBS spectra of copper using the nanoparticle [14]. With changing input laser fluence, the optical emission spectroscopy of ZnO and different nanomaterials, including Fe_3O_4, Ag_2O, TiO_2, SiO_2, and Al_2O_3, were investigated [15]. A maximum enhancement factor (EF) of roughly 37 was seen with silver oxide nanomaterial. Studies report enhancement factors for Zn I-lines at various laser fluencies. Only the strong peaks from each material were shown for multiple laser fluences. The enhancement was noted to diminish as laser fluence increased, which was due to the NPS—fragmenting as laser fluence increased. According to the authors, fluctuations in the relative plasma temperature and electron density were sporadic and showed no connection to the amplification. According to the author, from the the Boltzmann analysis, the enhancement was caused by a higher ground state population. It was shown how a potential mechanism might promote improvement in nanomaterials instead of bulk materials. Zn I at 468.2 nm was found to have an EF of 5, and the reported enhancements were identified as Fe I, Zn I, Si I, Ti I, Al I, and Ag I in that order, respectively, in atomic spectral lines [15]. Figure 5.1 (a) Ag_2O, (b) ZnO, (c) SiO, (d) Al_2O_3, (e)Fe_3O_4 and (f) TiO_2 depicts the enhncements obtained from various materials.

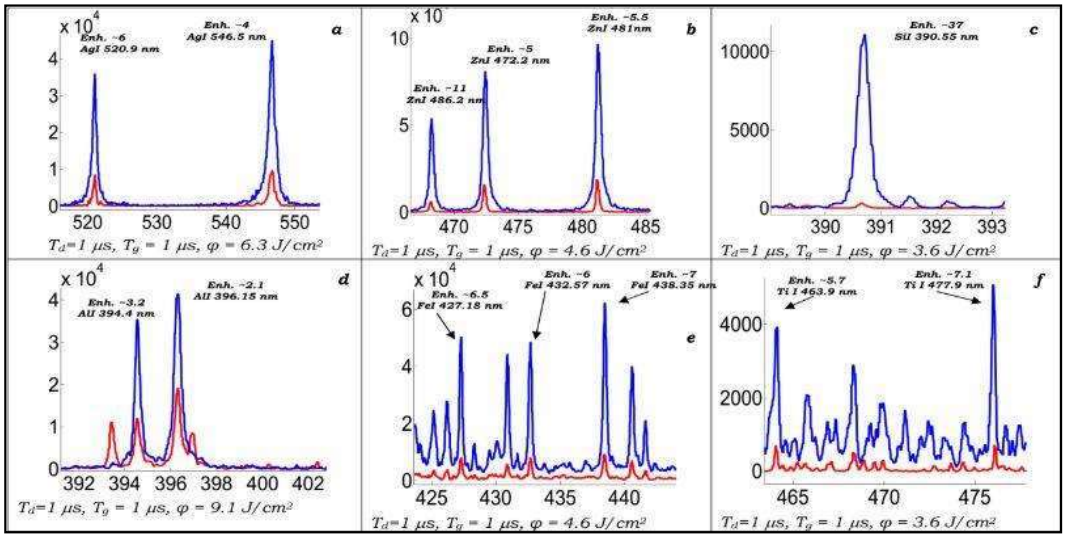

Figure 5.1 Exhibites the enhancement by the nanomaterial (blue colored) as compared to bulk (red colored) spectral lines of (a) Ag_2O, (b) ZnO, (c) SiO, (d) Al_2O_3, (e)Fe_3O_4 and (f) TiO_2. [adopted from IOP publishing, Journal of Physics, Conference series 548 (2014), 012031] [15].

According to experiments using scanning electron microscopes, De Giacomo et al. [16] found that NP explosion on the surface resulted in the creation of several hotspots when

compared to a surface devoid of NPs. According to the intensity ratio of LIBS and NELIBS at various concentrations, the emissions increased exponentially only after reaching the critical concentration and then saturating as the attention was raised further. According to the author, only a small number of ignition points were reportedly damaged by the ablation. The researchers also noted that when the time delays rose, the NELIBS intensity showed a dramatic initial jump before flattening off as the time delays increased. Titanium's atomic and ionic lines were compared, and the results showed amplification of the order of 2 at a delay of 400 ns for ionic peaks and 1 μs for atomic peaks. It was also shown that the enhancement increased logarithmically with a higher energy level [16]. The silver oxide nanomaterial showed the highest EF, which was ~37.

Recently, Cu-Ag and Ni-C composites were ablated using pulsed lasers to create composite NPs, which were then employed in NELIBS investigations [17]. In the instance of Cu-Ag, the Al foil emissions were multiplied by 20. Using LIBS and the NP colloidal solution on the surface, the nutrients in the leaf were studied. Both with and without applying the NPs colloidal solution, the macronutrients calcium, potassium, and molybdenum (Mo I 317.035 nm) were detected, and significant enhancement was noted. It was also documented how the concentration and size of the NPs affected the enhancement. On an indium sheet with varying concentrations of 20 nm and 80 nm silver NPs, an amplification of up to 5 times was recorded. This improvement was caused by localized surface plasmon [18]. Pb was measured in human serum at lower amounts using the NE-LIBS approach. The increase in the calibration curve's slope was used to measure the EF The observed rise in the NELIBS was 25 times the slope of the LIBS calibration curve, which has a one-order lower limit of detection (higher sensitivity compared to the LIBS approach) (LOD). The studies employed one liter of 500 ppb $PbCl_2$ and $Pb(NO_3)_2$ aqueous solutions. While the authors stated the physiologically relevant concentration of Pb in blood was below 50 ppb, NELIBS could measure concentration down to 74 ppb, compared to the 5 ppm lower concentration of lead observed by conventional LIBS in human serum micro droplet [19]. Adjusting the distance from the sample, the total plasma emissions from LIBS were compared to the NELIBS, as shown in figure 5.2. The emission in the NELIBS scenario [figure 5.2(b)] was higher than it was in the LIBS case [figure 5.2(a)].

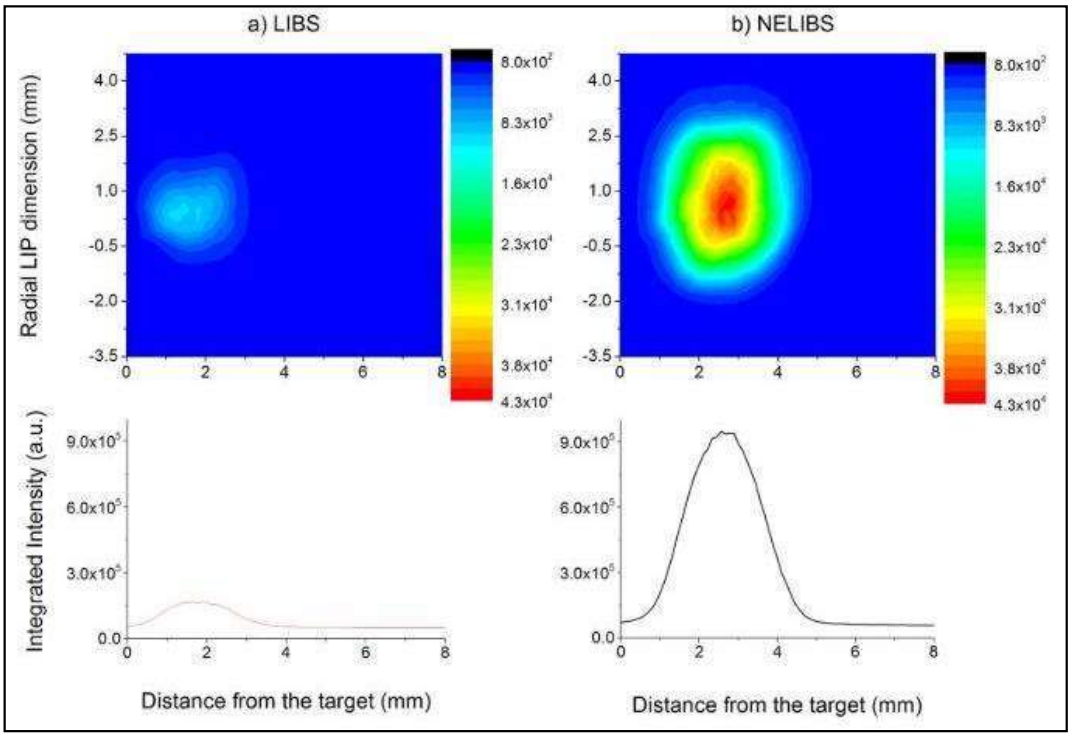

Figure 5.2 Images of (a) LIBS and (b) NELIBS plasma emissions from 1 µl of 1 ppm $PbCl_2$ (Au-NPs solution 0.04 mg ml^{-1}. [Adopted from Analytical Chemistry (2016) 88 (2016), 5251-5257] [19].

When the results from the three ns laser wavelengths of 1064 nm, 532 nm, and 355 nm were examined in the work [20], high enhancement factors (EF) were found at lower wavelengths. The EF was also higher for lower threshold fluence. The stated relative plasma parameters included electron temperature, density, and concentration. The authors suggested that boosted emissions and removed mass from sample could be greater than the experimentally measured values based on the observed self-absorption ratio >1. The scientists attributed the improvement in the NELIBS to altered heat capacity and thermal conductivity, with a modification in conduction. The experts also estimated that a decrease in thermal conduction length to the nanoscale dimension would result in a 15-fold reduction in the laser fluence threshold compared to the bulk material [20]. Figure 5.3 depicts data about the impact of wavelength and fluence on the enhancement.

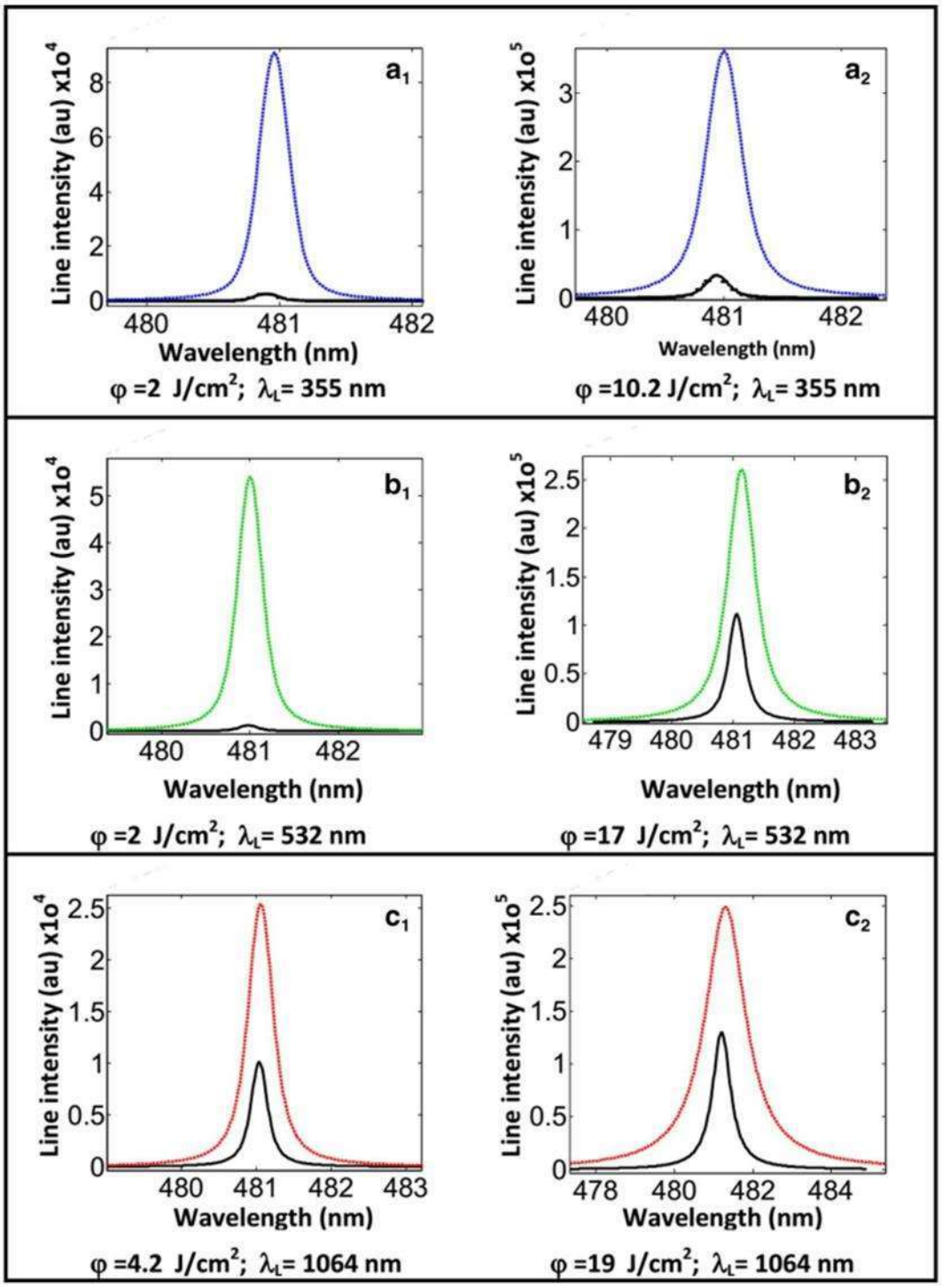

Figure 5.3 The enhancement in the spectral intensities of Zn I peak at 481 nm and the corresponding dotted line with NPs [Adopted from Spectrochimica Acta Part B 116 (2016) 8–15] [20].

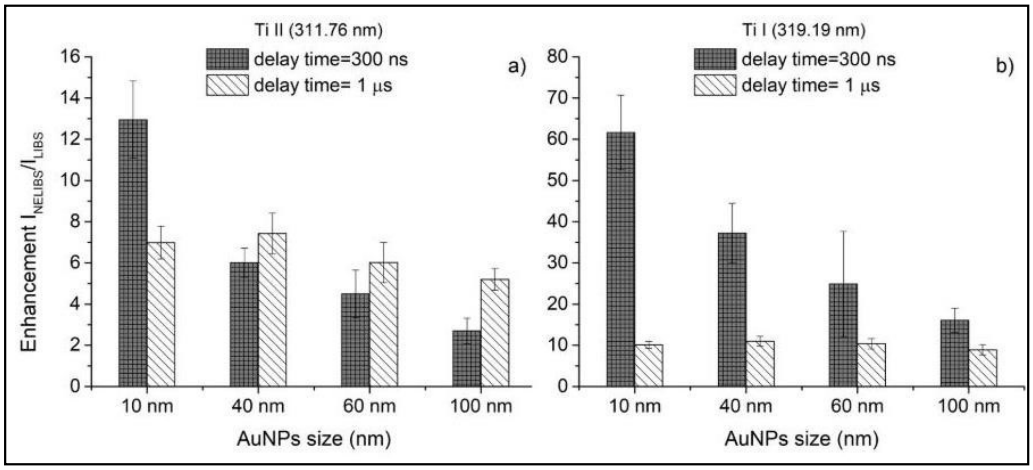

Figure 5.4 the enhancements obtained for a) Ti II 311.76 nm and b) Ti I 319.99 nm at two different delay times [Adopted from Spectrochimica Acta Part B, 179 (2021) 106105, 0584-8547] [21].

Recently, it was observed that altering NP size impacts the intensification of LIBS emissions [21]. The impact of the size of the NPS was investigated together with the effects of surface concentration, fluence, and spot size. The EF for four distinct NP sizes with two different Ti II and Ti I emission peak delays is shown in figure 5.4. The impact on NELIBS was investigated using four different vacuum pressures [975 mbar, 800 mbar, 400 mbar, and 60 mbar]. The NP solution was dropped on a surface with a diameter of about 2 mm, and an average of nine shots were taken from each drop. Using composite Marangoni flow-assisted drop-drying was suggested to ensure that the solution dried evenly. The study examined how changes in NP concentration, laser fluence, and gate delay affected the EF Pb I's emission lines at 368.34 and 405.78 nm were used for the research. The improvement began to rise, peaked at a concentration of 36.3×10^9 particles/cm^2, and then started to fall. It was noted that enhancement factors varied with gate delays and laser energy of 96 mJ, 78 mJ, 61 mJ, and 43 mJ. At 60 mbar for 61 mJ laser pulse intensity and a gate delay of 100 ns, the maximum EF of four was noted. The authors postulated that the larger standard deviation may be due to the non-uniform dispersion of the NP solution and the coffee stain effect of the NPs solution. According to a recent study, this method may also detect minor and trace elements with higher energy transition levels, such as halides [22]. For smaller NPs, it was observed that the plasma emissions were enhanced more. The targets in this investigation include zinc monoxide, NP of sizes 20, 40, 70, and 100 nm, and powder crushed into tablets. It is reported that the threshold fluence and NP sizes have a linear relationship. The authors also reported the simultaneous effects of laser fluence, ranging from 0.05 J/cm^2 to 0.2 J/cm^2, and Zinc NPS size, with the aforementioned diameters [23].

Abdelhamid et al. [24] reported on the EF in the NELIBS by altering the form of the NPs. The impact of the NPs' substance on the enhancement is depicted in Figure 5.5.

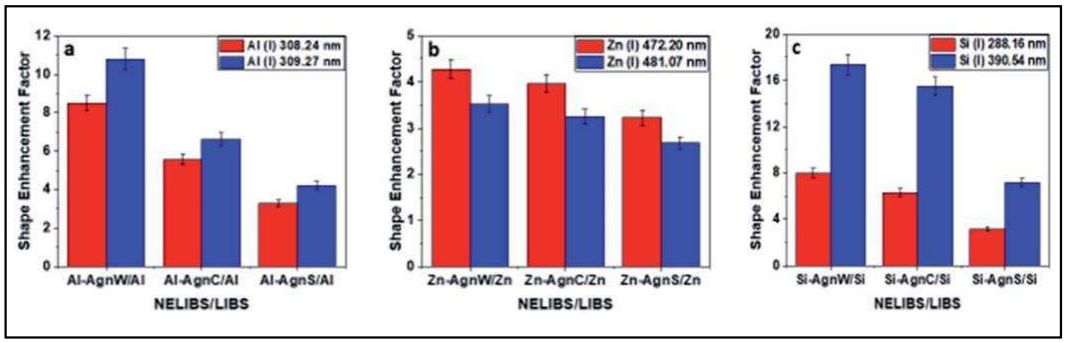

Figure 5.5 Enhancement factors of different shaped NPs on the (a) aluminum, (b) zinc, and (c) silicon after adding silver chloride nanospheres, nanocubes, and nanowires. [Adopted from J. Anal. At. Spectrom., 35 (2020) 2982–2989] [24].

For NELIBS investigations on copper and soda-lime glass, Qayyum et al. [25] employed laser-ablated Au and Ag NPS, and the EF for Au and Ag NPS were compared. The Ag and Au NPs, respectively, contributed factors of 8 and 18 to the improvement. The application of NPs to the sample surface improved the LIBS signal [26]. Liu et al. claimed that the pre-ablated sample would provide superior enhancement to the conventional NELIBS. This study [27] compared four separate situations.

Additionally, the authors have discussed systematic research using RSD and SNR in NELIBS. The NELIBS technique on aqueous solutions was supplemented with solid-phase support [28]. To detect Cr, Pb, and Cu in aqueous solutions, the electrospun fibres loaded with Au NPs were employed. With the addition of the NPs, the LODs were seen to improve. For detecting trace elements in liquid samples, Liu et al. employed the impact of NPs aggregation with metal-chelate [29]. It was observed that the LODs of the trace metals in the aqueous solution had decreased 7–10 times. For the NELIBS-based detection of heavy trace elements, Niu et al. exploited the adsorption of Al_2O_3 NPs [30]. Calibration curves and RSD studies were used to report the LODs of several trace metals. In the NELIBS experiments of commercial tuna fish of various qualities, Ag NPs generated from potato extracts were utilized [31]. The C_2 and CN bands in the molecular emissions were employed for the qualitative and quantitative examination of the protein in the fish when the EF of three times was recorded, as shown in figure 5.6.

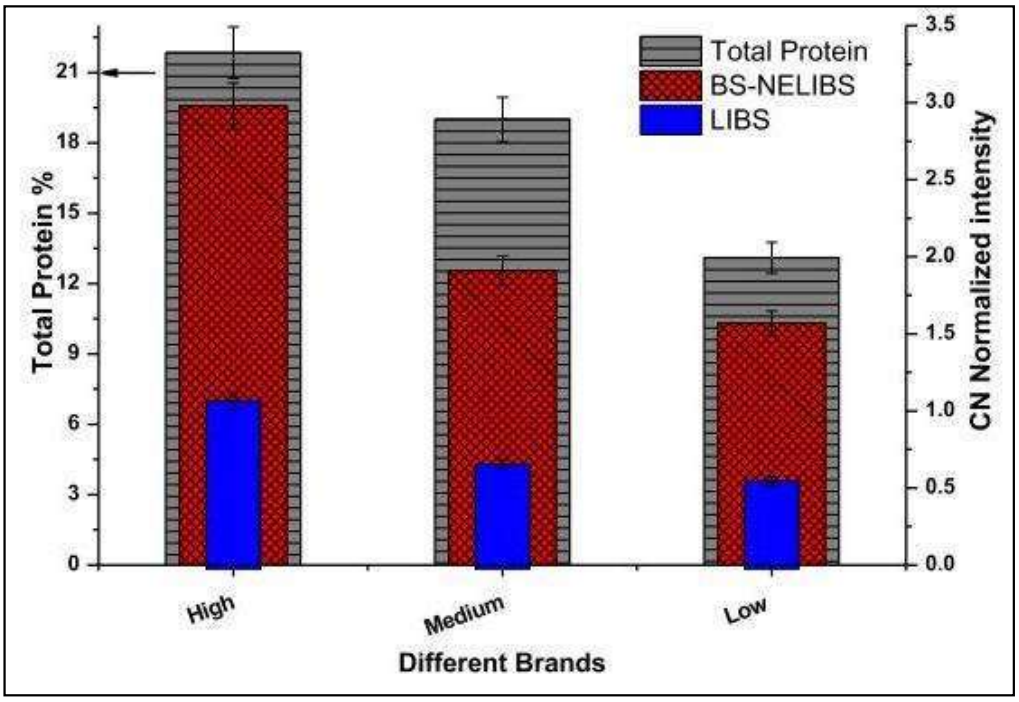

Figure 5.6 The comparison of LIBS and BS-NELIBS of three different quality brands of canned tuna from the normalized intensities of CN molecular bands [Adopted from Spectrochimica Acta Part B 149 (2018) 112–117] [31].

With Au NPs, a spectrum increase of eight times in the trace element Mg in the Al alloy was reported [32]. Researchers looked at how the NPs' inclusion affected the electron density. Farooq et al. [33] went into detail on the plasma characteristics, such as the electron density and temperature, and the temporal evolution studies from nanostructured plasma. The research employed the electron number density (END) conservation model and self-absorption peak adjustments. After analyzing the Sn and Ni lines, an EF of roughly 39 for nanomaterial was reported.

5.2 NELIBS of liquids

LIBS is a flexible, rapid method with a wide range of applications in areas like environmental monitoring and categorization of geological samples and in the anlysis of industrial waste, and space exploration [34] [2]. The multivariate analysis combined with LIBS makes a particularly effective tool for both classification and identification. The molecular and atomic lines in the spectra are produced by plasma recombination emissions from the ablated material in liquid, gaseous and solid states. The signal can be amplified using a variety of techniques, including double pulse and nanoparticle-enhanced LIBS [35]. Nanoparticles were used by De Giacomo et al. [36] to demonstrate strengthening of

the order of two in the LIBS signal. The classification of materials is based on the change in intensity of these bands. Compared to nanosecond lasers, ultrashort laser pulses have advantages such as lower ablation thresholds and less liquid splashing. Figure 5.7 (a) shows the fs-LIBS spectra of water in acetonitrile, figure 5.7 (b) show the TEM image of laser ablated Au NPs in water at 20 nm scale bar, figure 5.7 (c) is an attempt to record the LIBS spectra of water with no visible peaks. Acetonitrile tend to evoperate when dropped on substrate and recording the LIBS spectrum is a challeng to overcome. Here we have mixed acetronitrile in water and dropped on to the substrate for recording the LIBS spectra.

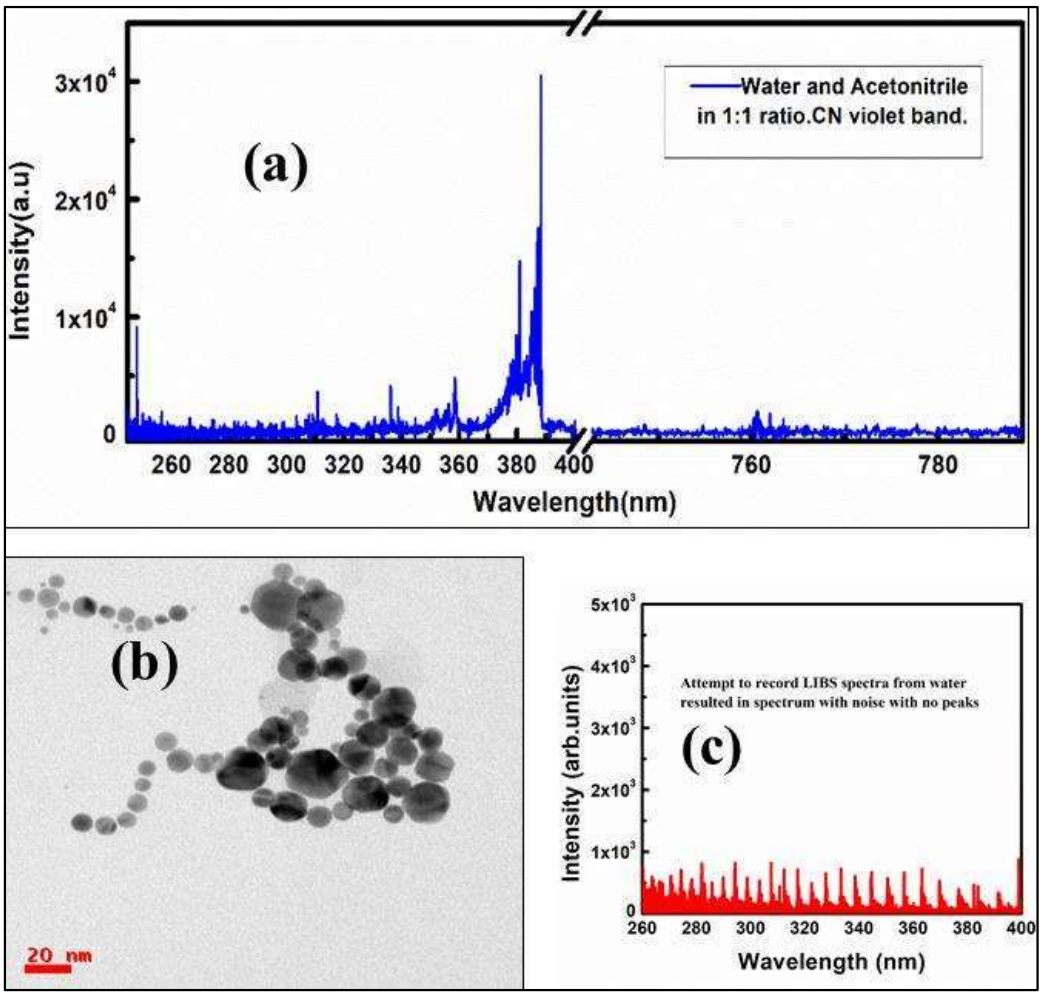

Figure 5.7 (a) Fs-LIBS spectrum of acetonitrile in water with dominant CN violet band around 388 nm, (b) TEM image of fs laser ablated Au nanoparticles in water at 20 nm scale bar, (c) spectrum obtained after attempting the recording of LIBS on water.

5.2.1 Results and discussion

In the present study, acetonitrile at different concentrations and fs laser-ablated Au NPS solution were used. The CN violet band is observed with $\Delta v = 0$ between 384 and 389 nm.

The well reported molecular peaks in LIBS spectrum of organic materials are the CN violet band and C_2 swan band [37]. Figure.5.8 (a) shows the LIBS spectrum of water and acetonitrile in a 1:1 ratio at a wavelength of 384–389 nm (CN band). Figure 5.8 (b) shows the LIBS spectrum of acetonitrile and water in a 2:1 ratio with and without NPS. In figure, an enhanced signal of around two times and a similar enhancement for a 4:1 ratio are shown figure 5.8(c). The improvement in the coupling of the laser pulse energy to the material in the presence of NPS is the cause of the signal's improvement.

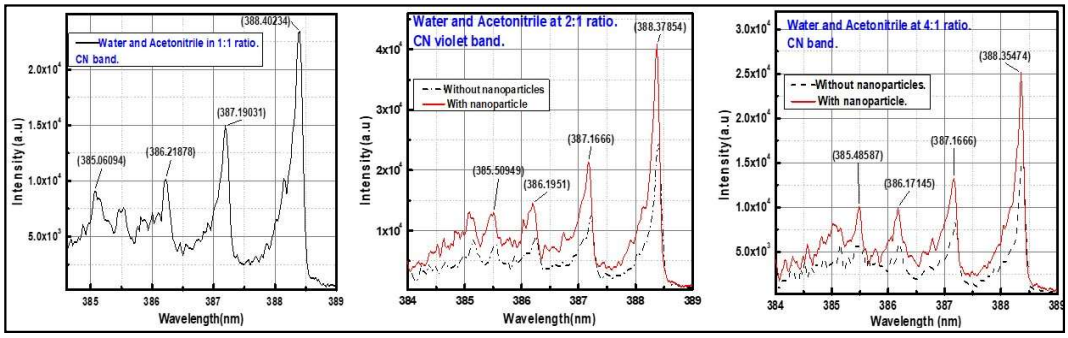

Figure 5.8 The CN violet band in the fs-LIBS spectra of Acetonitrile in water at (a) 1:1 ratio. (b) 1:2 ratios with and without addition of NPs. (c) 1:4 ratios with and without NPs.

5.3 NE-fs-LIBS of aluminum sheet coated with gold nanoparticle-embedded nanofibers

5.3.1 Introduction

LIBS provides a quick and safe means to evaluate any material being studied at a distance, even in hazardous industrial conditions. This method uses the NIST atomic spectral line database to identify the elements present in the sample. This is accomplished by gathering the laser-generated plasma's ion, atom, and molecule recombination emission lines. Explosive detection, mining, planetary exploration, environmental monitoring, archaeology, geological sample analysis, and other fields found uses for LIBS. This method can be combined with Raman spectroscopy and inductively coupled plasma spectroscopy to enhance its performance. Raman spectroscopy and LIBS can be used simultaneously with the same instrumentation to gather both molecular and elemental data. The limit of detection for trace elements can be increased using noble metal nanoparticles in nanoparticle-enhanced LIBS, which can boost the signal by up to two orders of magnitude. The De Giacomo group has published comprehensive reports on the enhancement in the atomic and molecular peaks and elemental analysis of analyte concentration at sub-ppm level [14, 16, 19, 38, and 41]. The additional generation of local

surface plasmons by metal nanoparticles such as gold, silver, and copper lower the ablation threshold locally [38, 39, 40] increases the efficiency of the production of seed electrons, and promotes multipoint ignition [16, 42]. The method's classification, identification, and capabilities are improved by employing machine learning methods for data analysis, such as PCA, SVM, and ANN. The current study focuses on the nanoparticle-enhanced LIBS studies of Al sheet and its applicability as a substrate in detecting liquid traces of organic explosives that have molecular emissions [41] with peaks at 388.3 nm and 516.42 nm, respectively.

5.3.2 Experimental procedure

The sample was positioned on the Newport transnational stage to displace the sample in the horizontal plane. The emissions were routed into a sensitive and time gated ICCD spectrometer combination after being captured by the collection optics. The gate was opened for 500 ns and the pulse incident on the target, the distinctive optical emissions from the plasma appeared after 100 ns (gate delay) (gate width). The electrospinning approach is used to produce the Al sheet coated with PVA nanofibers and implant Au in PVA nanofibers was described in previous research [43]. Figure 5.9 shows the TEM micrograph of nanoparticles embedded in PVA nanofibers (a) at 50 nm scale bar (b) at 20 nm scale bar. The laser beam's input pulse energy was reduced to 500 µJ because the sheet was thin, and stages were operated at a significantly higher speed (2 mm/s) than usual to prevent total burnout of the thin sheet. Then, fs LIBS was recorded from 230 nm to 850 nm for both plain PVA and PVA electro spun nanofibers loaded with nanoparticles. Typically, 25 spectra from each target were recorded.

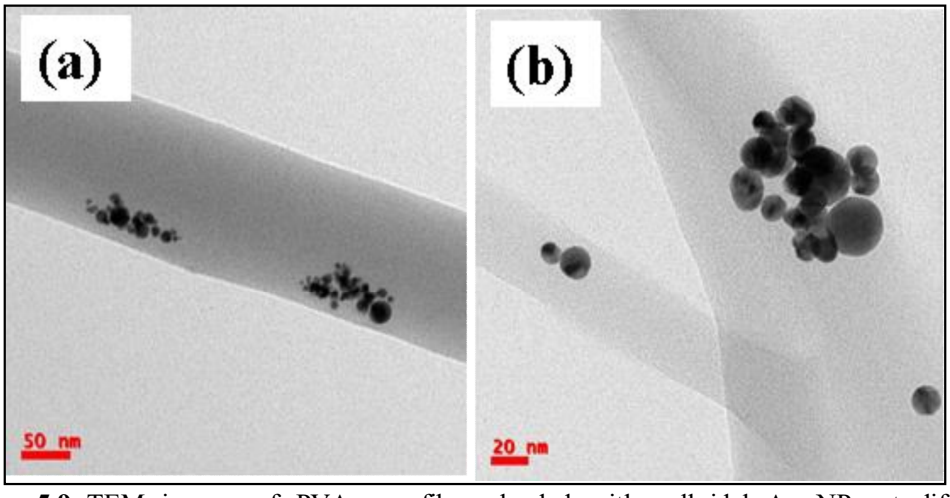

Figure 5.9 TEM images of PVA nanofibers loaded with colloidal Au NPs at different magnifications (a) 50 nm scale bar, (b) 20 nm scale bar.

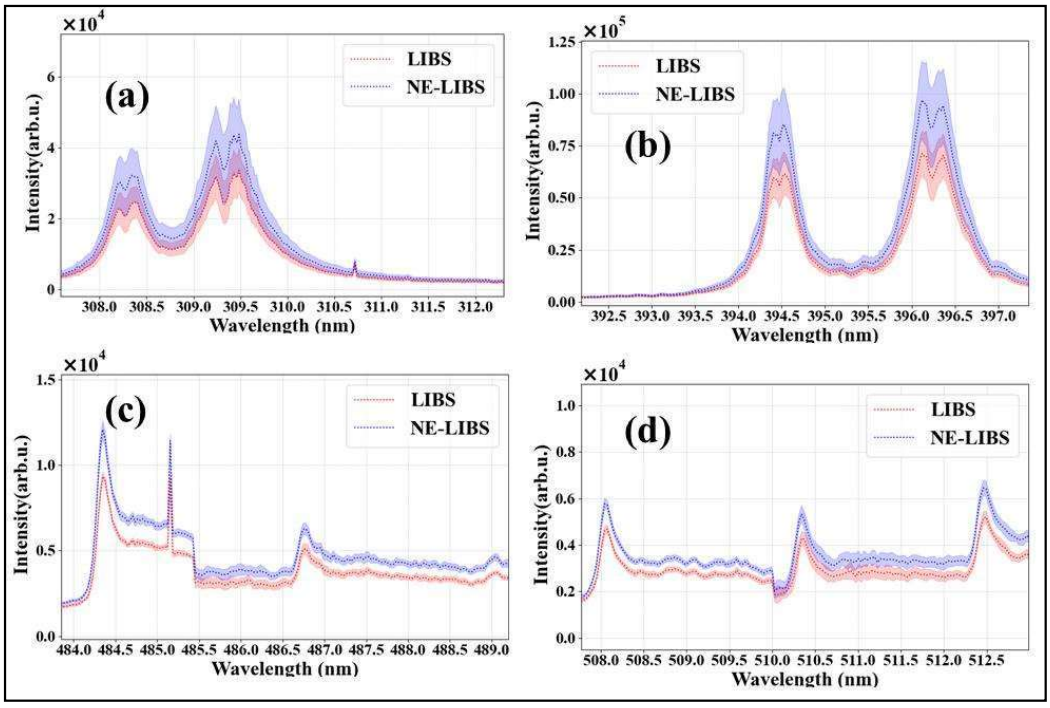

Figure 5.10 Aluminum atomic (a),(b) and molecular peaks (c),(d) from the fs-LIBS with and without NPs. Regular LIBS spectra in red and NE-LIBS spectra in blue with the mean and standard deviation of 25 spectra each.

5.3.3 Results

The intense Al I peaks at 308.4 nm, 309.2 nm, 394.4 nm, and 396.15 nm were amplified by gold nanoparticles embedded in PVA nanofibers. Similar augmentation was seen for AlO molecular emissions caused by $B^2\Sigma^+ \rightarrow X^2\Sigma^+$ transition bands for $\Delta\upsilon$ =-1, 0, 1 seen in the region of 450 nm to 550 nm, 510 nm to 520 nm, 480 nm to 500 nm, and 465 nm to 460 nm, respectively. The mean and standard deviation with and without nanoparticles were shown using the twenty-five spectra of each recorded sample. Figure 5.10 depicts the increased peaks from the Al LIBS and NE-LIBS spectrum with Al atomic (a), (b) and molecular peaks (c), (d) from the fs-LIBS with and without NPs. The molecular peaks formed later during the recombination of plasma were found to be not overlapped, while the atomic peaks formed early during the process were found to be overlapped. More time-resolved investigations of the NE-LIBS are needed to further understand the phenomena because the enhancement of the molecular peaks are modest compared to the atomic peaks.

5.4 Conclusions

The majority of the NELIBS studies used Au or Ag NPs. Additionally, in-depth investigations on the optimization of the time window, laser energy, surface NP distribution and collection distance are carefully assessed for the observation of greater improvements. The detection of NPS peaks proved that NPs catalyzed reactions in NELIBS. This technique is beneficial for the selective ablation of the sample surface in the case of precious stones and the detection of trace elements at remarkably low sample volumes. Insightful attempts are made to comprehend the underlying mechanism using the LSPR, quantum chemistry variation methods, two temperature models, and observations based on the spatial and temporal investigations of the LIBS spectra (s). Three different ratios of acetonitrile in water (1:1, 1:2, and 1:4) were used to acquire the LIBS spectra. Au-nanoparticles effectively lower the excitation threshold and increase spectral intensity in LIBS. We noticed a two-fold increase in the CN band in the region of the nanoparticles, demonstrating the viability of NE-LIBS in improving the liquid sample. The electrospinning method creates the laser-ablated gold nanoparticles embedded in PVA nanofibers on the Al sheet. Additionally, the field between the Al sheet and the nanoparticles may cause several ignition hotspots to appear on the surface where the nanoparticles are. The gold nanoparticles on the surface can effectively increase intensity and lower the excitation threshold. The physical process could be responsible for the LIBS signal's two-fold enhancement.

References

[1] D.A. Cremers, L.J. Radziemski, Handbook of laser-induced breakdown spectroscopy, John Wiley & Sons, 2013.

[2] NK. Rai, A.K. Rai, LIBS—an efficient approach for the determination of Cr in industrial wastewater, J. Hazard. Mater. 150 (2008) 835–838.

[3] D. Anglos, Laser-induced breakdown spectroscopy in art and archaeology, Appl. Spectrosc. 55 (2001) 186A--205A.

[4] T. Delgado, J. Ruiz, L.M. Cabalín, J.J. Laserna, Distinction strategies based on discriminant function analysis for particular steel grades at elevated temperature using stand-off LIBS, J. Anal. At. Spectrom. 31 (2016) 2242–2252. doi:10.1039/c6ja00219f.

[5] A.K. Knight, N.L. Scherbarth, D.A. Cremers, M.J. Ferris, Characterization of laser-induced breakdown spectroscopy (LIBS) for application to space exploration, Appl. Spectrosc. 54 (2000) 331–340.

[6] J.L. Gottfried, F.C. De Lucia, C.A. Munson, A.W. Miziolek, Standoff detection of chemical and biological threats using laser-induced breakdown spectroscopy, Appl. Spectrosc. 62 (2008) 353–363. doi:10.1366/000370208784046759.

[7] P. Pořízka, J. Klus, E. Képeš, D. Prochazka, D.W. Hahn, J. Kaiser, On the utilization of principal component analysis in laser-induced breakdown spectroscopy data analysis, a review, Spectrochim. Acta Part B At. Spectrosc. 148 (2018) 65–82.

[8] M.M. Tripathi, K.E. Eseller, F.Y. Yueh, J.P. Singh, Multivariate calibration of spectra obtained by Laser Induced Breakdown Spectroscopy of plutonium oxide surrogate residues, Spectrochim. Acta - Part B At. Spectrosc. 64 (2009) 1212–1218. doi:10.1016/j.sab.2009.09.003.

[9] X. Fu, G. Li, D. Dong, Improving the Detection Sensitivity for Laser-Induced Breakdown Spectroscopy: A Review, Front. Phys. 8 (2020) 1–11. doi:10.3389/fphy.2020.00068.

[10] M. Dell'Aglio, R. Alrifai, A. De Giacomo, Nanoparticle Enhanced Laser Induced Breakdown Spectroscopy (NELIBS), a first review, Spectrochim. Acta - Part B At. Spectrosc. 148 (2018) 105–112. doi:10.1016/j.sab.2018.06.008.

[11] A. De Giacomo, M. Dell'Aglio, R. Gaudiuso, C. Koral, G. Valenza, Perspective on the use of nanoparticles to improve LIBS analytical performance: nanoparticle enhanced laser induced breakdown spectroscopy (NELIBS), J. Anal. At. Spectrom. 31 (2016) 1566–1573. doi:10.1039/C6JA00189K.

[12] Qingcao Liu, Philipp Rupp, Benjamin Förg, Johannes Schötz, Frederik Süßmann, William Okell, Johannes Passig, Josef Tiggesbäumker, Karl-Heinz Meiwes-Broer, Lennart Seiffert, Thomas Fennel, Eckart Rühl, Michael Förster, Peter Hommelhoff, Sergey Zherebtsov, Nano-Optics: Principles Enabling Basic Research and Applications, Nano-Optics Princ. Enabling Basic Res. Appl. 104302 (2017) 283–299. doi:10.1007/978-94-024-0850-8.

[13] S. Hashimoto, D. Werner, T. Uwada, Studies on the interaction of pulsed lasers with plasmonic gold nanoparticles toward light manipulation, heat management, and nanofabrication, J. Photochem. Photobiol. C Photochem. Rev. 13 (2012) 28–54. doi:10.1016/j.jphotochemrev.2012.01.001.

[14] S.A. Kalam, N.L. Murthy, J.R. Krishna, V. Srikanth, S.V. Rao, Nanoparticle enhanced laser induced breakdown spectroscopy with femtosecond pulses, in: Int. Conf. Fibre Opt. Photonics, 2016: pp. Th3A--89.

[15] A.M. El Sherbini, AA Galil, S.H. Allam, T.M. El Sherbini, Nanomaterials induced plasma spectroscopy, in: J. Phys. Conf. Ser., 2014: p. 12031.

[16] A. De Giacomo, R. Gaudiuso, C. Koral, M. Dell'Aglio, O. De Pascale, Nanoparticle Enhanced Laser Induced Breakdown Spectroscopy: Effect of nanoparticles deposited on sample surface on laser ablation and plasma emission, Spectrochim. Acta Part B At. Spectrosc. 98 (2014) 19–27. doi:10.1016/j.sab.2014.05.010.

[17] V. V. Kiris, A. V. Butsen, E.A. Ershov-Pavlov, M.I. Nedelko, A.A. Nevar, Nanoparticle-Enhanced Laser Induced Breakdown Spectroscopy Using Copper-Silver and Nickel-Carbon Nanocomposites on Aluminium, Int. J. Nanosci. 18 (2019). doi:10.1142/S0219581X19400222.

[18] T. Ohta, M. Ito, T. Kotani, T. Hattori, Emission enhancement of laser-induced breakdown spectroscopy by localized surface plasmon resonance for analyzing plant nutrients, Appl. Spectrosc. 63 (2009) 555–558.

[19] A. De Giacomo, C. Koral, G. Valenza, R. Gaudiuso, M. Dellaglio, Nanoparticle Enhanced Laser-Induced Breakdown Spectroscopy for Microdrop Analysis at subppm Level, Anal. Chem. 88 (2016) 5251–5257. doi:10.1021/acs.analchem.6b00324.

[20] A.M. El Sherbini, C.G. Parigger, Wavelength dependency and threshold measurements for nanoparticle-enhanced laser-induced breakdown spectroscopy, Spectrochim. Acta - Part B At. Spectrosc. 116 (2016). doi:10.1016/j.sab.2015.11.006.
[21] Z. Salajková, V. Gardette, J. Kaiser, M. Dell'Aglio, A. De Giacomo, Effect of spherical gold nanoparticles size on nanoparticle enhanced Laser Induced Breakdown Spectroscopy, Spectrochim. Acta Part B At. Spectrosc. 179 (2021) 106105. doi:10.1016/j.sab.2021.106105.
[22] L. Sládková, D. Prochazka, P. Pořízka, P. Škarková, M. Remešová, A. Hrdlička, K. Novotný, L. Čelko, J. Kaiser, Improvement of the Laser-Induced Breakdown Spectroscopy method sensitivity by the usage of combination of Ag-nanoparticles and vacuum conditions, Spectrochim. Acta - Part B At. Spectrosc. 127 (2017). doi:10.1016/j.sab.2016.11.005.
[23] A.M. EL Sherbini, C.G. Parigger, Nanomaterial size dependent laser-plasma thresholds, Spectrochim. Acta - Part B At. Spectrosc. 124 (2016). doi:10.1016/j.sab.2016.08.015.
[24] M. Abdelhamid, Y.A. Attia, M. Abdel-Harith, The significance of nano-shapes in nanoparticle-enhanced laser-induced breakdown spectroscopy, J. Anal. At. Spectrom. 35 (2020) 2982–2989. doi:10.1039/d0ja00329h.
[25] H. Qayyum, R. Ali, Z.U. Rehman, S. Ullah, B. Shafique, AH Dogar, A. Shah, A. Qayyum, Synthesis of silver and gold nanoparticles by pulsed laser ablation for nanoparticle enhanced laser-induced breakdown spectroscopy, J. Laser Appl. 31 (2019) 022014. doi:10.2351/1.5086838.
[26] V. V. Kiris, N. V. Tarasenko, E.A. Nevar, M.I. Nedelko, E.A. Ershov-Pavlov, M. Kuzmanović, J. Savović, Enhancement of Analytical Signal of Laser Induced Breakdown Spectroscopy by Deposition of Gold Nanoparticles on Analyzed Sample, J. Appl. Spectrosc. 86 (2019) 900–907. doi:10.1007/s10812-019-00913-2.
[27] J. Liu, Z. Hou, T. Li, Y. Fu, Z. Wang, A comparative study of nanoparticle-enhanced laser-induced breakdown spectroscopy, J. Anal. At. Spectrom. 35 (2020) 2274–2281. doi:10.1039/d0ja00257g.
[28] X. Wen, Q. Lin, G. Niu, Q. Shi, Y. Duan, Emission enhancement of laser-induced breakdown spectroscopy for aqueous sample analysis based on Au nanoparticles and solid-phase substrate, Appl. Opt. 55 (2016). doi:10.1364/ao.55.006706.
[29] X. Liu, Q. Lin, Y. Tian, W. Liao, T. Yang, C. Qian, T. Zhang, Y. Duan, Metal-chelate induced nanoparticle aggregation enhanced laser-induced breakdown spectroscopy for ultra-sensitive detection of trace metal ions in liquid samples, J. Anal. At. Spectrom. 35 (2020) 188–197. doi:10.1039/c9ja00324j.
[30] S. Niu, L. Zheng, A. Qayyum Khan, H. Zeng, Laser-Induced Breakdown Spectroscopic (LIBS) Analysis of Trace Heavy Metals Enriched by Al 2 O 3 Nanoparticles, Appl. Spectrosc. 73 (2019) 380–386. doi:10.1177/0003702819829509.
[31] Z. Abdel-Salam, S.M.I. Alexeree, M.A. Harith, Utilizing biosynthesized nano-enhanced laser-induced breakdown spectroscopy for proteins estimation in canned tuna, Spectrochim. Acta - Part B At. Spectrosc. 149 (2018) 112–117. doi:10.1016/j.sab.2018.07.029.
[32] A.A. Khedr, M.A. Sliem, M. Abdel-Harith, Gold Nanoparticle-Enhanced Laser-Induced Breakdown Spectroscopy and Three-Dimensional Contour Imaging of an Aluminum Alloy, Appl. Spectrosc. (2020). doi:10.1177/0003702820973040.
[33] Z. Farooq, R. Ali, A. ul Ahmad, M. Yaseen, M.H.R. Mahmood, M. Fahad, M.N. Hussain, I. Rehan, MZ. Khan, Ramiza, M.U. Farooq, M.A. Qayyum, M. Shafique, Electron number density conservation model combined with a self-absorption correction methodology for analysis of nanostructure plasma using laser-induced breakdown spectroscopy, Appl. Opt. 59 (2020) 2559. doi:10.1364/ao.379641.
[34] H. Suyanto, N.N. Rupiasih, T.B. Winardi, M. Manurung, K.H. Kurniawan, Qualitative analysis of Pb liquid sample using laser-induced breakdown spectroscopy (LIBS), in: AIP Conf. Proc., American Institute of Physics, 2013: pp. 14–16.
[35] C. Gautier, P. Fichet, D. Menut, J. Dubessy, Applications of the double-pulse laser-induced breakdown spectroscopy (LIBS) in the collinear beam geometry to the elemental analysis of different materials, Spectrochim. Acta Part B At. Spectrosc. 61 (2006) 210–219.
[36] A. De Giacomo, J. Hermann, Laser-induced plasma emission: from atomic to molecular spectra, J. Phys. D. Appl. Phys. 50 (2017) 183002.
[37] E.N. Rao, S. Sreedhar, S.P. Tewari, G.M. Kumar, S.V. Rao, CN, C2 molecular emissions from pyrazole studied using femtosecond LIBS, in: Int. Conf. Fibre Opt. Photonics, Optica Publishing Group, 2012: p. TPo-3.
[38] A. De Giacomo, R. Gaudiuso, C. Koral, M. Dell'Aglio, O. De Pascale, M. Dell'Aglio, O. De Pascale, Nanoparticle-enhanced laser-induced breakdown spectroscopy of metallic samples, Anal. Chem. 85 (2013) 10180–10187. doi:10.1021/ac4016165.

[39] C. Koral, A. De Giacomo, X. Mao, V. Zorba, R.E. Russo, Nanoparticle enhanced laser induced breakdown spectroscopy for improving the detection of molecular bands, Spectrochim. Acta Part B At. Spectrosc. 125 (2016) 11–17.

[40] M. Dell'Aglio, Z. Salajková, A. Mallardi, R. Mezzenga, L. van't Hag, N. Cioffi, G. Palazzo, A. De Giacomo, Application of gold nanoparticles embedded in the amyloids fibrils as enhancers in the laser induced breakdown spectroscopy for the metal quantification in microdroplets, Spectrochim. Acta - Part B At. Spectrosc. 155 (2019). doi:10.1016/j.sab.2019.04.002.

[41] N. Linga Murthy, S.V. Rao, Nanoparticle Enhanced Laser Induced Breakdown Spectroscopy of Liquids, Springer Singapore, 2021. doi:10.1007/978-981-15-9259-1_105.

[42] C. Koral, M. Dell'Aglio, R. Gaudiuso, R. Alrifai, M. Torelli, A. De Giacomo, Nanoparticle-Enhanced Laser Induced Breakdown Spectroscopy for the noninvasive analysis of transparent samples and gemstones, Talanta. 182 (2018) 253–258. doi:10.1016/j.talanta.2018.02.001.

[43] MSS Bharathi, C. Byram, D. Banerjee, D. Sarma, B. Barkakaty, V.R. Soma, Gold nanoparticle nanofibres as SERS substrate for detection of methylene blue and a chemical warfare simulant (methyl salicylate), Bull. Mater. Sci. 44 (2021). doi:10.1007/s12034-021-02402-9.

This page is left intentionally blank

6 Standoff LIBS and automation studies

Abstract: To examine materials that are harmful, radioactive, and in inaccessible conditions, the standoff LIBS approach is desirable. An overview of the most recent advancements in standoff LIBS, including fs-filamentation for sample probing and machine learning algorithms for data analysis, as well as instrumentation like the beam expander, telescopes, and multi-collector systems are discussed in the chapter. A brief overview of the benefits of the double pulse, and the variants that stand out due to their distinctiveness, like the standoff LIBS from the structured beams, are included. The femtosecond standoff LIBS setup is optimized to acquire the target's optical emissions at 5 meters. We have used principal component analysis (PCA), in the LIBS spectra of the materials used as a target to improve the identification and classification capabilities. Also, a novel instrumentation procedure in the automation of laser beam steering for raster/spiral scanning of the samples was used in standoff femtosecond LIBS experiments. A readily available and easy-to-handle Arduino-based CNC shield, along with the universal G-code sender (UGS), was used for the automation. The standoff femtosecond filamentation induced breakdown spectroscopy (St-Fs-FIBS) spectra were recorded at a standoff distance of ~5 meters utilizing a simple hand-held spectrometer.

6.1 Literature survey of the standoff LIBS

6.1.1 Introduction

The LIBS technique is based on the emission spectroscopy of the recombination from the ions and atoms in the plasma that results from the interaction of intense pulsed lasers with any targets (samples) [1, 2]. It is helpful when it is necessary to obtain qualitative information on the elemental composition quickly. The elemental mapping of samples, such as plants, geological rocks, archaeological specimens, etc., was reported with this method [3]. Numerous advancements and studies have been made using LIBS-based quantitative elemental composition analysis. It is a simple and rapid method that needs minimal amounts of samples in their liquid, gaseous, and solid states. Different applications have led to the development of LIBS variants, such as the double-pulse LIBS for enhancing the signal-to-noise ratio and the nanoparticle-enhanced LIBS for handling minimal sample volumes. Raman and fluorescence are two spectroscopic methods that can be used with the LIBS methodology for complimentary data acquisition from the sample

[4]. The targets at the far field can also be examined using the LIBS since the plasma emission intensities following the breakdown are high. The basic experimental setup, various analyses were done, enhancements suggested, and different delivering and collecting optics (configurations) used are explained in this chapter. We offer an outlook for the standoff LIBS bottlenecks, solutions to them, and a few applications after this chapter.

6.1.2 Experimental setup

The fs pulses (800 nm, 1 kHz repetition rate, 1.8 mJ per pulse) were focused on the sample at 6 m using the combination of 100 cm convex lenses and -50 cm concave in Galilean configuration. The sample was placed on the translational stage (M/s Newport, USA) to displace it in the X and Y planes. A SCT with 6 inche aperture was placed at five meters from the target for collecting the optical emissions from the cooling plasma. These emissions were sent into an intensified gated spectrograph (Mechelle spectrometer and Andor istar ICCD combination) using a 600 µ optical fiber. The setup is shown in figure 6.1. Pulsed laser systems, such as nanosecond and femtosecond lasers (a few Hz to a few kHz repetition rate), are typically employed for standoff LIBS experiments. Typically, power densities of at least a few GW/cm^2 are required to vaporize the target at a distance and make the emissions observable. For the LIBS studies, either mode-locked femtosecond lasers or Q-switched nanosecond lasers (fundamental at 1064 nm, second harmonic at 532 nm, or third harmonic at 366 nm) were utilized. Ti: Sapphire crystal is typically used as a gain medium in mode-locking and chirped pulse amplification to produce femtosecond pulses. We used a femtosecond laser that coherently delivered 4 W (maximum average power; 4 mJ energy/pulse) at 800 nm wavelength, 1 kHz repetition rate, and 50 femtoseconds (fs) pulse duration.

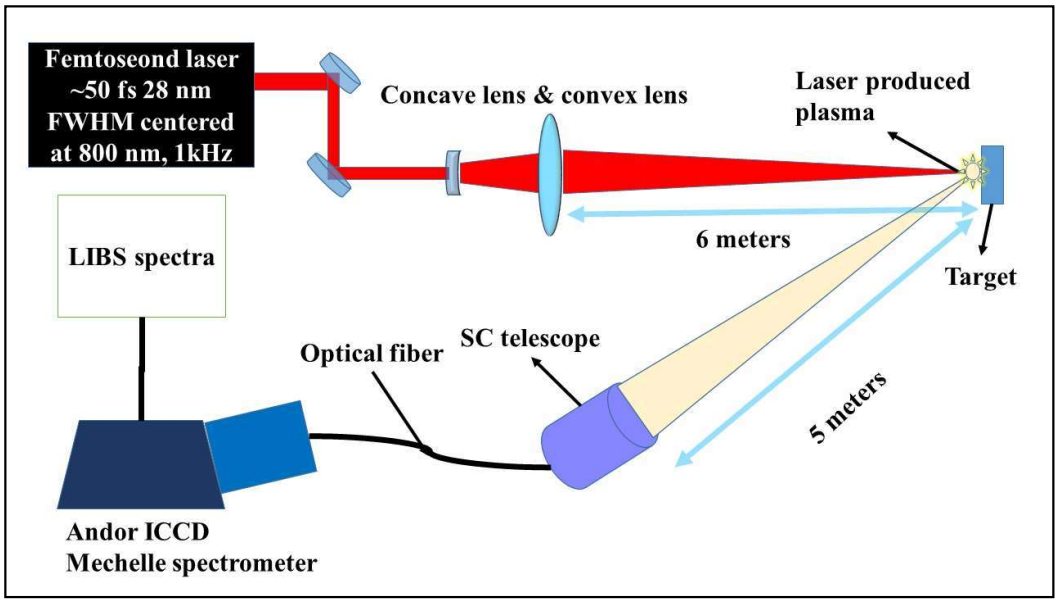

Figure 6.1 The experimental schematic of the fs-ST-LIBS with the target placed at beam 6 m. A combination of convex and concave lenses used for focusing. The emissions are acquired at 5 meters from the sample using SC telescope.

The setup of the optical components detailed, along with the delay generator for starting the acquisitions and oscilloscope to see the delays, are included in the standoff LIBS experiment. Figure 6.1 depicts the optical components in the standoff LIBS. We can continuously change the laser pulses' input power using the half-wave plate and Brewster window. The pulses are focused on the target positioned on the translational stage using a plano-convex lens. After the prior zone has been ablated, the translational stage continuously exposes a new one while preventing pitting-related variations in plasma emissions. When employing high-energy fs laser pulses, it would be ideal to steer clear of all lenses because they cause filaments [5] to develop as they travel through the atmosphere.

6.1.3 Earlier reviews on standoff LIBS

Fortes and Laserna [6] have delved into details of the various applications for LIBS, including in the preservation of cultural heritage, industrial processing, defense, and homeland security. They also detail the instrumentation used in field-capable, portable, at-a-distance, and commercial LIBS systems. The advancements in laser sources, such as microchips and fiber lasers, as well as the LIBS devices created explicitly for in situ field applications, were also discussed [6]. The earlier review on remote LIBS by Wanting Li et al. [7] covered the various configurations of LIBS, signal augmentation methods like

double-pulse LIBS, and remote LIBS applications in multiple fields like geological, archaeological, planetary exploration, and industrial for metallurgy monitoring, among others. Several LIBS configurations, such as Raman-LIBS instrumentation, were presented. Furthermore, the authors reported LIBS's in-situ and real-time measurement capabilities. Additionally, the benefits and challenges to be overcome were discussed [7].

6.1.4 Notable standoff LIBS studies

Rock samples were analyzed quantitatively from standoff distances in the Martian atmosphere. Additionally, the authors note that line intensities decrease exponentially as target distance increases. Fe, Si, Al, Ca, Na, Mg, and K were all detected in basalt BON samples up to 12 m. Earlier works [8] have described changes in the crater volume changes as the target distance increased. The ionic lines of Cl and S were easier to detect in comparison studies between air and Martian environments than atomic transitions seen at atmospheric pressure in the IR region. To examine the Cathedral of M'alaga, a Spanish cultural landmark, mineralogically from 35 meters, standoff LIBS is utilized in the field. Because of the significant Si, Al, Ca, and Mg emissions, it is established that the whole structure is made of sandstone. The tests also showed how the standoff LIBS may be used to identify the source of colored marbles. Other contaminants, including Al, Ba, Si, Ca, Mg, Fe, and Sr, came from natural sources (movement of dust and atmospheric suspensions linked to marine aerosols). Additionally, Ti, Pb, and Mn, three trace elements, were used to study the surface pollutants from the exhaust of gasoline and diesel engines [9].

The geochemical composition of carbonated rocks at a depth of 15 m was also studied using standoff LIBS. The Mg/Ca and Sr/Ca ratios were measured [10]. Correlations were found between fluctuations in the LIBS data and the primary geological information about the ancient environment (such as temperature, salinity, precipitation, and geological events). The 2D mapped data of the Mg/Ca and Sr/Ca ratios of rocks from Yunnan, China further supported their conclusion that the geochemical contents vary spatially. The surfaces of the geological samples were examined at a standoff distance of 1 m in the ultraviolet, visible, near infrared, and longwave infrared spectral areas up to 10 m [11]. At a standoff distance of 1 m, several terrestrial minerals were studied.

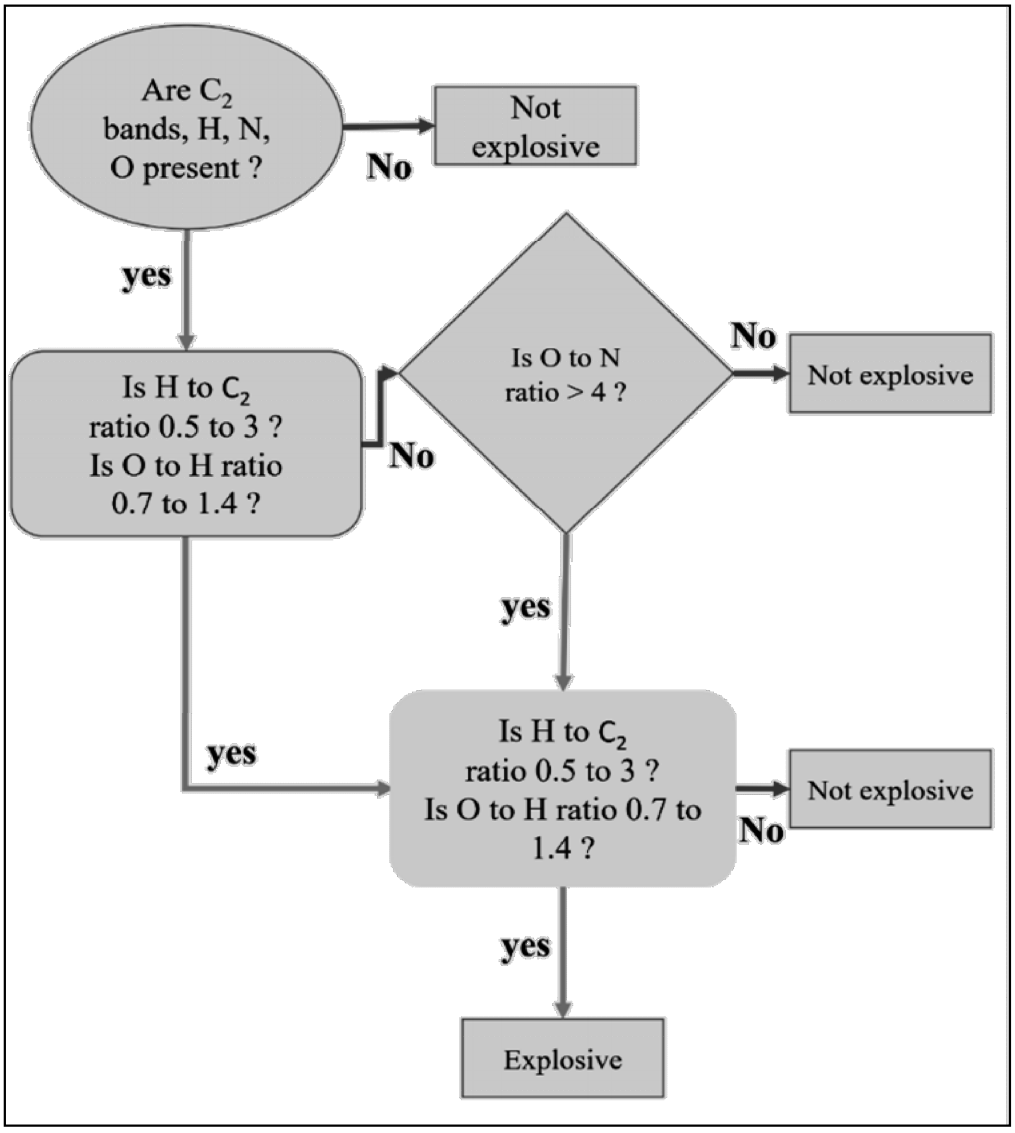

Figure 6.2 Algorithm developed by López-Moreno et al. [13] for the classification of explosive residues in standoff mode from the various elemental and molecular intensity ratios of the LIBS peaks.

Additionally described were time-resolved studies of atomic lines and plasma-generated molecular species. Geological samples were analyzed using a small spectrograph in standoff LIBS under Martian atmospheric conditions [12]. The authors successfully showed that the ICCD-based detection was not required for the LIBS measurements at reduced pressure (7 torr CO_2 for the Mars atmosphere) for elements such as Ba and Li. Additionally, Sr. López-Moreno and coworkers investigated the targets at 45 m in the standoff mode, and the data was used to classify explosive materials. To distinguish between organic explosives, organic non-explosives, and nonorganic samples, the C_2 swan system, O, H, and N emissions intensity ratios were used. It was proposed that the CN

band emissions might result from CN production in the surrounding atmosphere. Thus, it was claimed that the sole measurement that could be relied upon for analysis based on an open atmosphere was the measurement of the C_2 peaks. Figure 6.2 depicts the categorization procedure for explosives and non-explosive using the LIBS peak intensity ratios.

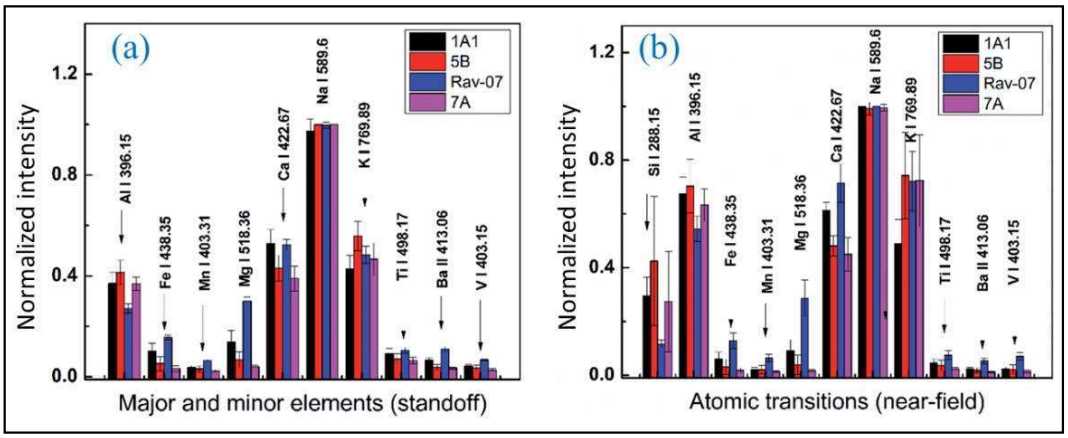

Figure 6.3 Intensities from atomic peaks of significant elements in geological rocks observed in near-field LIBS (a) and standoff configuration (b) [Adopted from Kalam et al. [17]].

The elemental analysis of magnesium alloy was performed using a double-pulse standoff LIBS technique. At 2.5 m, the impact of inter-pulse delay on the LIBS spectra was documented [14]. When DP LIBS were used instead of the single-pulse LIBS of the Y line, the signal strength was increased by approximately 4.7 times at a 6 μs inter-pulse delay (366.4 nm). Analysis was done on the link between the plasma temperature, electron density, and DP LIBS inter-pulse delay. It was reported that even when the input laser pulses were repeatedly focused at the same spot, the ablation depth produced by DP LIBS was less than the SP LIBS. The optical breakdown produced at a distance of 10 m allowed sodium standoff detection in the aerosol [15, 16]. The authors investigated Na's doublet trait (in the 588.6–589.5 nm spectral region). A linear approximation was used to evaluate the limit of detection (LOD), and a value of 55 ppm was obtained. Kalam et al. [17] contrasted the standoff femtosecond filamentation-induced breakdown spectroscopy and the near-field situations. Figure 6.3 displays the line intensities of the significant and trace elements in the near-field and standoff LIBS. It was claimed that while using fs filaments for ablation, the target roughness (1-2 mm) could be disregarded owing to the filament's short (30 cm) length. Compared to the standoff instance (26-52%), the near-field scenario had a more fantastic range of observed variation for a single peak (21-68%). The limited breakup of the surrounding environment was cited as the cause of lacked O and N lines in

their fs LIBS and ST-FIBS spectra. López-Moreno et al. [18] also performed standoff LIBS tests for the quantitative characterization of Mn, Cr, and Ni in stainless steel at 1000^0 C between LIBS at normal temperature and LIBS at high temperatures, the calibration was transferred [18]. The average ablation rate was inversely related to material hardness, thermal conductivity, and elasticity modulus values, proving that the heavy tungsten alloy's hardness was determined using LIBS in standoff mode [19]. The relationship between the heavy tungsten alloy's thermomechanical characteristics and the study of crater size aided in developing the materials detecting application. For the examination of complex matrix at 6 m, Tamboli et al. optimized the standoff LIBS parameters [20]. The ICCD's gate widths and delays, the laser source's input pulse energy and repetition rate, and the choice of emissions lines for the specific sample were all thoroughly reviewed. The optimal settings for Ni, Cr, and Pb were gate width (7 s), gate delay (1.0-1.1 s), and 150 mJ of pulse energy at 100 Hz repetition rate. The analysis was conducted on the lines at 356.6, 428.9, and 405.7 nm (Ni, Cr, and Pb).

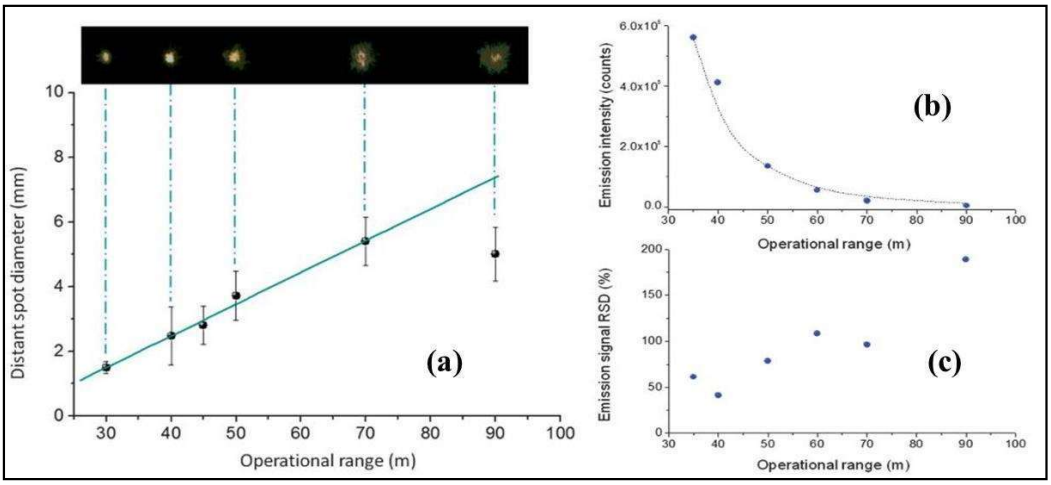

Figure 6.4 (a) Fluctuation in the diameters of focused laser pulses as a function of the distant. Inset shows the prints from laser pulses on heat-sensitive paper at corresponding distances, (b) variation in the intensity with range, (c) relative standard deviation in the emission signal. [Adopted from Gaona et al. [21].

Gaona et al. [21] previously reported detailed investigations on the diameters of focused laser beam as a function of the distant target position. The experimental observations shown in figure 6.4 provide a good description of how the spot size, intensity, and relative standard deviation vary with operating distance. According to the target location, the emission strength for the Al emission line (around 396 nm) changed over time [21]. It was claimed that the transmission-related degradation of beam quality also produces significant

ambiguity. Random flutuations in the laser beam's bright central position on the target had little impact. Regardless of the working distance, parameters like the pulse-to-pulse variation of the input energy remained constant (RSD intra-range of 0.5%). The distribution of the beam was noticeably deformed during transmission in the atmosphere. The spot diameter "d" is a linear function of the distance from the detector to the target "r" after it has been experimentally confirmed that the change in beam diameter over the operational range studied (from 30 to 90 m) was minimal. According to the reports, the irradiance deteriorates more rapidly with the range. These impact the shot-to-shot uncertainty of the emission intensity.

Furthermore, irrespective of the operating range, it was discovered that the propagation of plasma emissions had little to no impact on the total variability (at least in the absence of severe weather events). The samples were detected using standoff LIBS at 30 m using a range of radioactive surrogates (59Co, 130Ba, 88Sr, 133Cs, 193Ir, and 238U) [22]. According to the authors, the laser beam sampled area at a standoff distance was unquestionably greater than in the close-contact LIBS. The standoff spot size (diameter of 1500 μm) was significantly more critical for sampling than the close-contact approach's 450 μm requirement. It was found that the reported standoff LODs of cesium and iridium were better than those calculated in the case of close-contact results. Loosely focused (LF) and free propagation (FP) filament-based ablation was shown to have significant differences in the decay time of the emission. The lowest was for FP filament ablation, with the decay time of 300 ns [23]. In another study less than a 1% false alarm rate, filamentation-induced breakdown spectroscopy was employed to detect uranium (U). It is also suggested that UO should be considered for detecting U, in addition to U atomic transitions because the UO 593.55 nm band is easily visible at 10 m [24]. They compared the signal-to-background ratio for atomic and molecular emissions at three different standoff distances and the results are shown in figure 6.5.

Compared to in-situ measurements, standoff detection was reported to have strong S/N ratio for detecting LIBS signals below pressure of 1 torr [25]. The authors also showed that the univariate analysis produced high correlation coefficients for geological samples. According to the authors, the findings would be helpful in standoff LIBS designed for harsh environments. In certain places, signal-to-noise ratios were higher (order of a few hundred), whereas S/N ratios were just a few tens of orders at high pressures. They consequently observed that a greater focused spot size was caused by the beam divergence

[26]. Since the LIBS emission process was constrained by the fixed peak intensity and filament beam size (~10^{14} W/cm^2, ~100 µm, respectively), authors report the decline in LIBS signal as a function of range for low divergence lasers (M^2 of 1) by $1/R^3$.

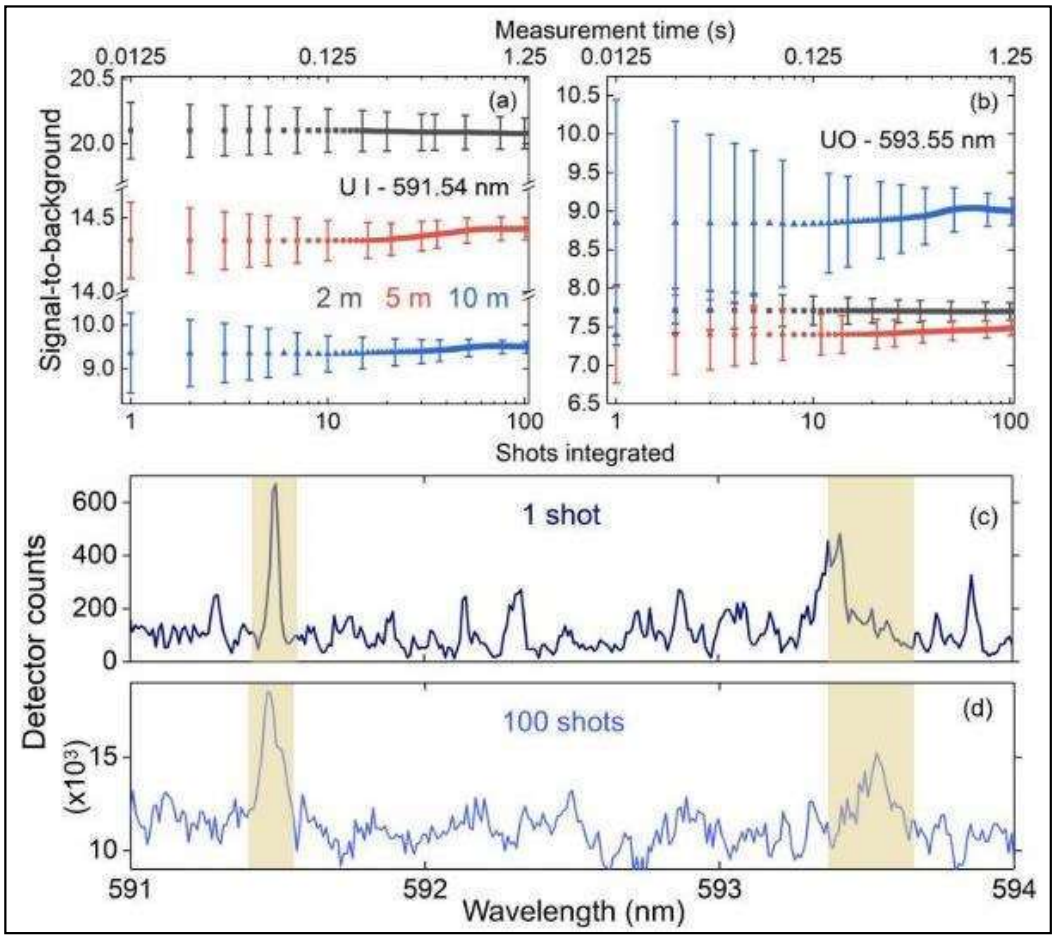

Figure 6.5 Variation in the SBR with the number of shots for (a) atomic U I, (b) molecular UO for the remote collection from 2, 5, and 10 m, (c) for a single shot, (d) for 100 shots at 10 m. [Adopted from Finney et al. [24]].

The burst mode was proposed to compensate for the divergence effects. Toluca (an iron meteorite) and Sahara 98222 (an L6 chondrite) samples were subjected to quantitative analysis utilizing a standoff arrangement at 5 m [27]. Theoretical calculations for wavelength-dependent studies relevant to standoff LIBS transmissions and absorption via the atmosphere were reported [28]. When weighed to the attenuation caused by the inverse square law, it was discovered that the air extinction of the return plasma light was minimal (with target distance).

6.2 Standoff fs LIBS studies of possible interferents

6.2.1 Introduction

Standoff LIBS is a safe technique devised for probing in hazardous industrial environments and a quick way of testing any material at a distance to be investigated. LIBS has applications in diverse fields. Areas that profit from LIBS technique include explosive detection [13], [29], exploration of planets, mining, etc. It is based on the elemental analysis from the plasma's emission spectra of molecules, atoms, and ions. It also has the benefit of simultaneous use of Raman and LIBS spectroscopy with the analogous instrumentation demonstrated in standoff configuration by Moros, Javier, et al. [30]. Both the molecular and elemental information were acquired at the same time. Double-pulse standoff LIBS can improve the signal-to-noise ratio [31] [32]. These methods can be helpul for plastic waste sorting and recycling in real time for environmental benefits. As the SNR decreases with the distance LIBS and multivariate analysis [33] combined can overcome the difficulty in identification and classification of different compounds [34] [35].

6.2.2 Experimental procedure

The femtosecond laser pulses of 1.5 mJ are used the details of the laser source are mentions in the chapter 2. In the acquisition of the LIBS spectrum the gate delay was adjusted for intense signals. The gate width is set for 2 µs, and each target spectrum is the integration of 2000 pulses and 40 accumulations. The acquired LIBS spectrum wavelength range is from 230 nm to 850 nm. Twenty spectra from each target were acquired for classification studies.

6.2.3 Results

Aluminum atomic emissions at 393.2 nm, 393.56 nm were stronger with 3.0 $\times 10^5$ counts compared to the other materials, and CN emission from HPC were the lowest with 2.0×10^3 counts. Major peaks from the copper target were identified are tabulated in table 6.1 (see below). Molybdenum, calcium, sodium, potassium, and iron lines were identified in the soil target and presented in table 6.2. Iron, manganese, chromium lines were recognized in steel target, are tabulated in table 6.3. The spectra of all the six targets used for the studies are shown in figure 6.6 (a) aluminum, (b) Cu, (c) HPC, (d) steel, (e) soil in pellet form, (f) PVC.

Table 6.1 Peaks identified from the standoff LIBS spectrum of copper.

Sl. No.	Observed peaks (nm)	Reference peaks NIST (nm)	Ionized state
1	510.65	510.55	Cu I
2	515.44	515.32	Cu I
3	521.89	521.84	Cu I
4	508.83	508.84	Cu II
5	502.48	502.40	Cu II

Table 6.2 Elemental peaks identified from the standoff LIBS spectrum of soil.

Sl. No.	Observed peaks (nm)	Reference peaks NIST (nm)	Ionization state
1	388.64	388.62	Fe I
2	393.43	393.52	Ca I
3	394.5	394.6	Ca I
4	427.23	427.17	Fe I
5	428.36	428.36	Fe I
6	430.34	430.25	Ca I
7	442.62	442.54	Ca I
8	443.6	443.49	Ca I
9	526.31	526.95	Fe I
10	572.17	572.27	Mo I
11	572.8	572.87	Mo I
12	589.13	588.99	Na I
13	589.71	589.59	Na I
14	616.35	616.21	Ca I
15	649.2	649.37	Ca I
16	649.5	649.96	Ca I
17	714.96	714.81	Ca I
18	766.7	766.48	K I
19	770.09	769.89	K I

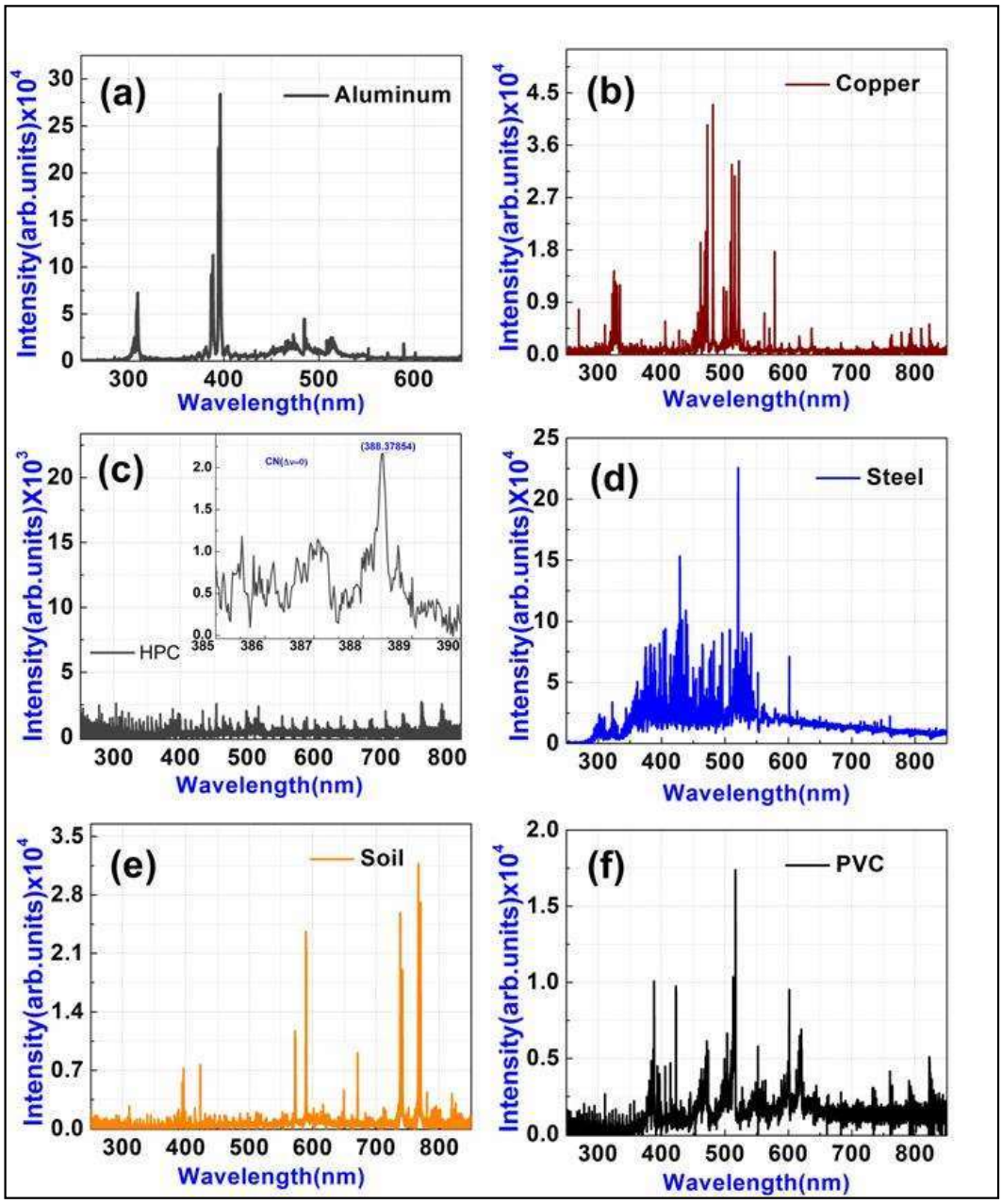

Figure 6.6 The fs-ST-LIBS spectra from (a) aluminum, (b) copper, (c) HPC, (d) steel, (e) soil in pellet form, (f) PVC.

Table 6.3 Peaks identified from the fs-ST-LIBS spectrum of steel

Sl. No.	Observed peaks (nm)	Reference peaks (NIST) (nm)	Ionization state
1	344.13	344.18	Mn II
2	346.64	346.05	Mn II
3	347.64	347.38	Mn II
4	349.15	348.45	Mn II
5	349.83	349.51	Mn II
6	396.46	396.38	Cr I
7	396.68	396.95	Cr I
8	398.46	398.38	Cr I
9	399.05	399.13	Cr I
10	400.2	400.17	Cr I
11	403.16	403.26	Mn I
12	403.48	403.88	Fe I
13	405.64	405.86	Mn I
14	406.44	406	Mn I
15	408.41	408.4	Mn I
16	416.57	416.56	Cr I
17	423.62	423.67	Mn I
18	425.5	425.42	Cr I
19	427.25	427.5	Cr I
20	434.54	434.46	Cr I
21	435.27	435.18	Cr I
22	438.44	438.9	Fe I
23	460.17	460.48	Mn I
24	462.73	462.68	Mn I
25	471.2	471.09	Mn I
26	476.72	476.35	Mn I
27	478.46	478.42	Mn I
28	482.47	482.29	Mn I
29	520.67	520.7	Cr I
30	529.93	529.78	Cr I
31	532.92	532.96	Cr I
32	541.1	541	Cr I

Aluminum oxide (AlO) band corresponds to the transition $B^2\sum^+ \rightarrow X^2\sum^+$ for $\Delta\upsilon$ = -1, 0, 1 are observed in range 510-520 nm, 480-500 nm and 465-460 nm, respectively [36]. The major peak from each transition were identified from the standoff LIBS spectra of Al target and shown in figure 6.7 also the major identified peaks are tabulated in table 6.4.

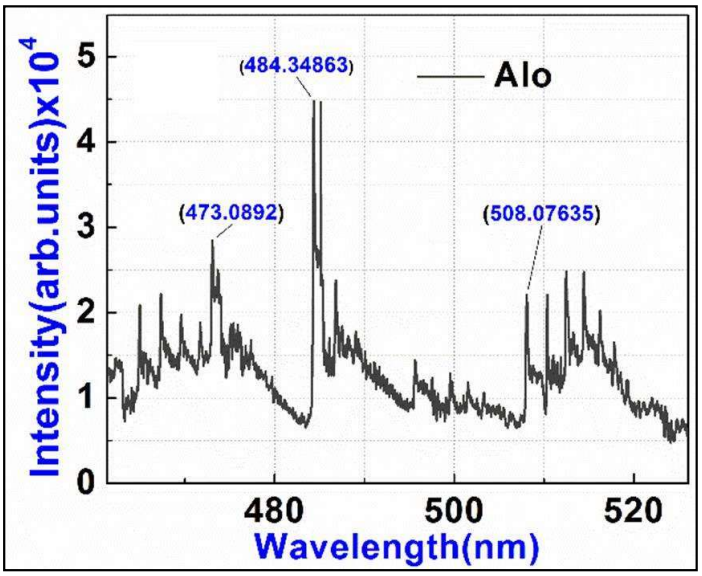

Figure 6.7 The aluminum oxide band from the fs-ST-LIBS spectrum with major peaks identified.

Table 6.4 Peaks identified from the fs-standoff LIBS spectrum of the Al sample.

Sl.no	Observed peaks (nm)	Reference peaks (NIST) (nm)	Ionization state
1	394.4	394.47	Al I
2	396.15	396.21	Al I
3	386.61	386.85	Al I
4	308.16	308.21	Al I
5	308.405	308.70	Al I
6	309.18	308.98	Al I
7	309.52	309.27	Al I

The CN violet band [37] corresponds to the transition $B^2\sum^+ \rightarrow X^2\sum^+$ for $\Delta\upsilon$ = -1, 0, 1 are in the range 357-360 nm, 384-389 nm, and 414-423 nm, respectively, and were detected in the PVC LIBS spectra. $\Delta\upsilon$ = 0 (peak at 388.34 nm) lines with less intensity were observed in HPC. The C_2 swan band corresponds to the molecular transitions $d^3\Pi^g \rightarrow a^3\Pi^u$ (with peaks at 471.5 nm, 516.5 nm, and 563.5 nm) $\Delta\upsilon$ = -1, 0, 1 in the range of 460-475 nm, 510-520 nm, and 550-565 nm were observed in PVC, and its intensity was greater than that of CN band. The C_2 peak was not observed in HPC. The CN and C_2 peaks are presented in table 6.5. The significant peaks of CN and C_2 in the PVC are depicted in figure 6.8.

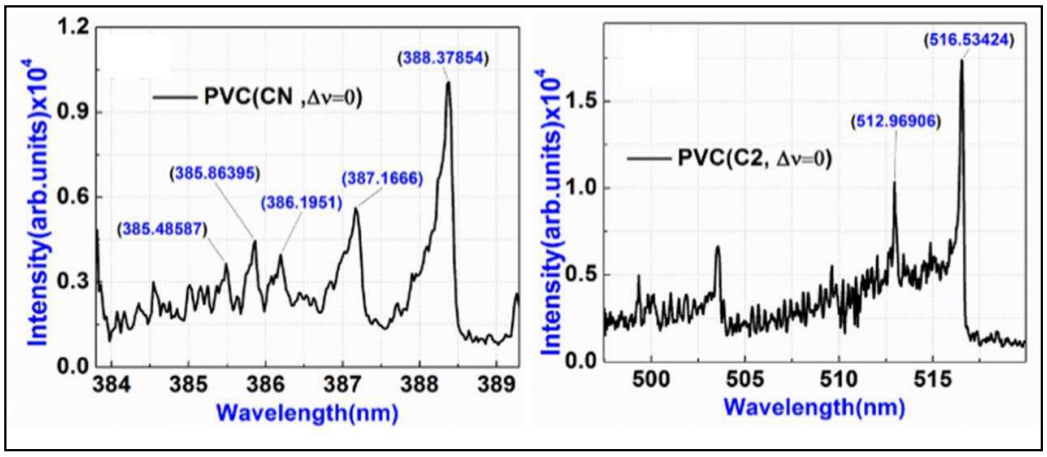

Figure 6.8 The molecular bands from the fs-ST-LIBS spectrum of the PVC (h) CN violet band and, (i) C_2 swan band from the PVC traget.

Table 6.5 Identified peaks from the fs-St-LIBS spectrum of PVC.

Sl. No.	Observed peaks (nm)	Reference Peaks (nm)	Ionization, molecular state
1	378.88	378.78	Fe I
2	379.86	379.95	Fe I
3	385.51	385.03	CN(4,4)
4	385.88	385.44	CN(3,3)
5	386.2	386.14	CN(2,2)
6	387.19	387.08	CN(1,1)
7	512.97	512.80	C2(0,0)
8	516.57	516.42	C2(1,1)
9	589.13	588.99	Na I
10	589.71	589.69	Na I

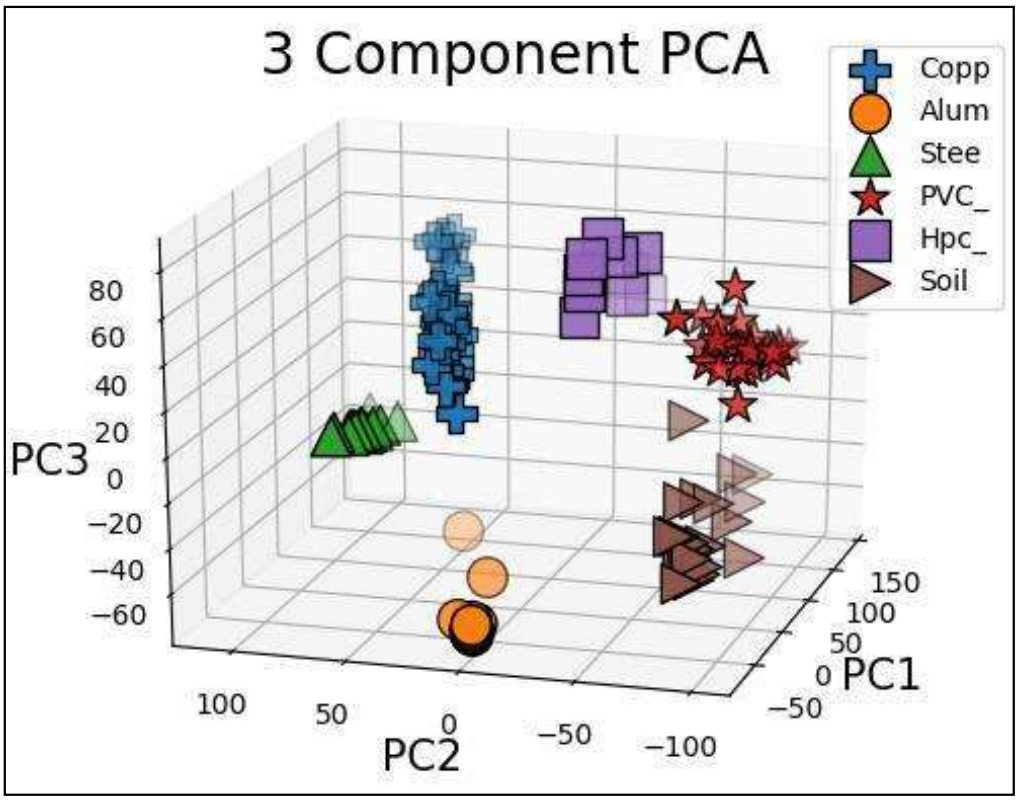

Figure 6.9 Classification of the fs-St-LIBS spectrum of Cu, Al, steel, PVC, HPC and soil using PCA. Each data point in the plot corresponds to a LIBS spectrum and pluse marker is used for copper, circle for Al, triangle for steel, star for PVC, square of HPC, and arrow for soil.

6.2.4 Conslusions

Twenty spectra each from six targets were used for the classification studies. Figure 6.9 shows the 3component PCA with each point in the plot corresponds to a single spectrum PVC and HPC, metals and soil form different groups. Figure 6.9 shows the distinguishable groups formed by six samples. Most of the atomic and molecular peaks were identified and tabulated from the acquired spectra in the standoff configuration for each sample.

6.3 Laser beam steering with arduino-based CNC shield for standoff Fs FIBS studies

LIBS uses the plasma recombination emissions from the atoms and ions formed when the laser beam is focused on the sample (typically nanosecond or femtosecond) for the elemental analysis of the given sample [1, 2]. Further, remote, standoff LIBS combined with chemometrics have found numerous applications in distinct fields because of ability for rapid identification of the samples, classification, and quantification [6, 7, 18, and 27]. Detecting hazardous compounds from standoff distances is important for homeland security and safety related applications. Rapid improvements in LIBS instrumentation

made the techniques portable and compact [38-41]. Recently, the standoff LIBS technique was utilized to detect biological and radiological threats [22, 42], such as uranium [24, 43], from standoff distances. Standoff LIBS can interrogate the target in inaccessible and hostile environments, like probing targets through a shield window [44] and in high-temperature environments in steel factories [18, 45-47]. The standoff LIBS was tested to be helpful in planetary exploration, in studying the elemental composition of rocks in the Martian environment [8, 12, 48, and 49]. Standoff LIBS measurements at variable distances were recently achieved in environmental monitoring (surface pollutants detection) [50]. The standoff detection of heavy metals in complex matrix, like soil, was demonstrated using LIBS [20, 51]. The underwater standoff LIBS was also valuable for environmental monitoring [52]. The aerosols of NaCl or Na_2SO_4 suspended in the air at different compositions and sizes were also reported using standoff LIBS [15, 16]. Other applications in real-life scenarios include the standoff measurement of the hardness of tungsten alloy [19], the characterization of the materials at cultural and heritage sites like Cathedral Málaga [9], and the classification of marbles used. Likewise, it is used in the analysis of geological samples, rocks [10, 17, 25, 53], and trace detection of explosives and plastics [5, 26, 54-56].

The standoff LIBS signal can further be improved using the double pulse technique, as demonstrated by Qi et al. [14]. They attribute the signal enhancement to the higher surface penetration and the effect of inter-pulse delay in standoff double-pulse studies of a magnesium alloy was emphasized. Wiens et al. demonstrated the classification of solids and minerals at standoff distances by combining the standoff LIBS and Raman techniques [57, 58]. López-Moreno et al. developed a decision-making strategy based on the ratiometric analysis to identify and classify explosives and organic non-explosives in traces on a metal surface at 30 m [13]. They also extended the standoff LIBS studies to slowly moving targets [59]. The enhanced capabilities like rapidity and better classification and quantification results with compact spectrometers in standoff LIBS studies for geological samples were achieved using the machine learning algorithms like principal component analysis (PCA). [60-65]. Shaik et al. demonstrated the improvement in the standoff LIBS signal in the vicinity of nanoparticles [66-68]. Gaona et al. have reported an adaptive range algorithm for identifying explosive samples such as DNT, TNT, RDX, or PETN at changing collection distances [69]. The technique was made compact by Barnett et al. using a spatial heterodyne spectrometer with a large field of view and high

spectral resolution at a 20 m distance [54]. Gaona et al. again have studied the potential factors causing the deterioration in standoff LIBS signal strength [21], such as variation in the focus spot size with increasing target distance and its Effect on the LIBS intensity. In another study, Li et al. reported a reduction in the volume of the collection optics without compromising the collection efficiency by using the multi-collector system, where small lenses were arranged like an optical compound eye in place of a telescope [70].

The propagation of intense femtosecond pulses of wavelength λ and in medium with refractive index 'n' and nonlinear refractive index 'n_2' (with power >$P_c = \frac{3.77\lambda_0^2}{8\pi n_2 n_0}$ for a linearly polarized light) results in an intriguing diffraction-free phenomenon called self-focusing. Self-channelized propagation of an intense beam is advantageous in standoff interrogation of target samples and remote detection [71, 72]. For solid transparent media, the critical power P_c is a few MW, whereas, for gases, it is a few GW. Inside the filamentation, the intensity hits a threshold of ~5×10^{13} W/cm^2 [73, 74] and is referred to as intensity clamping. The input laser pulse intensity affects both phenomena. In addition to free propagation, filamentation can also be accomplished using a focusing lens (low energies) (high pulse energies). Due to the challenge in delivering high intensities adequate for ablation and ionization of the remote target. While propagating across great lengths in the surrounding atmosphere, they frequently experience beam distortion conventional ns-LIBS is typically limited to 100 meters. By utilizing the intense fs laser pulses' unique capability to form filamentation in air the laser beam diameter at great distances (even up to 20 km) without the use of focusing lenses can be maintained. Filamentation makes it possible to provide laser pulses with the high-power density required to ablate faraway samples. Furthermore, the surface/substrate contribution in the ns LIBS example will be quite significant due to the longer pulse duration allowing it to interact with the sample for a longer time. This will be important if there are traces on the surface that need to be found, and in the fs scenario, this is reduced significantly.

Harilal et al. studied the parameters of the laser ablation and the plasma plume for three different situations to understand the optical emissions for LIBS applications better. They compared the persistence of the atomic and molecular emissions from plasma plumes by pulses focused at close ranges, and by loose focusing, by free propagation. For isotopic analysis, laser-induced fluorescence of laser-produced plasmas was used [75, 76]. The impact of various structured beams on plasma plume filamentation and filamentation-

induced optical emissions were reported in detail [77, 78], demonstrating the benefits of Airy, Bessel-Gaussian, Laguerre-Gaussian, and Gaussian beams for standoff applications. Shaik et al. employed filamentation-induced breakdown spectroscopy (FIBS) to detect and classify explosives, geological samples, and bimetallic samples. In-depth research was conducted on the impact of the focusing lens's separation from the target in femtosecond FIBS [79]. The laser pulses utilized in the LIBS process concentrate on the target, which removes the surface material (at the focal spot).

With the incidence of more pulses at one point, the LIBS signal is severely reduced. Hence it is necessary to move the sample or steer the input beam/pulses to capture the LIBS signal from a new spot. A few of the earlier standoff LIBS studies were mostly concerned with the study of moving targets, such as salt deposits on rotating wind turbine blades and Steel on conveyor belts, as well as the impact of sample velocities on the LIBS signal. Samples were also put on a motorized translational stage for movement. Here, we provide the instrumentation for automated beam steering with precision and speed in probing the sample at standoff distances, resulting in an enhanced signal advantageous for real-world applications. An Arduino microcontroller was previously employed in laser producing microstructures for plasmonic applications and illustrating physics concepts. [80-82]. Data acquisition for the ultrafast frequency-resolved pump-probe spectroscopy was built using an inexpensive optical chopper based on an Arduino [83]. Here, we've utilized an Arduino-based CNC to control the mirrors that direct the beam and the lens positioned on the manual stage that adjusts the focusing distance. The kinematic mirror mount adjuster, which has a net displacement of 25 m each revolution, and the stepper motor, which makes 200 steps every rotation (1.8° per step), were employed. Here, we show how the two components can be used to probe targets at a standoff distance with higher accuracy and speed.

6.3.1 Experimental setup

Intense femtosecond laser pulses (~50 fs) of ~1.8 mJ energy operating at 1 kHz repetition rate were focused at ~5 m distance using a concave lens and convex lens of 50 cm focal length to achieve the filamentation. When the filamentation interacts with the target placed at 5 m leads to plasma generation. The plasma emissions were fed to a hand-held (MAYA, Ocean Optics) spectrometer using an integration time of 200 ms via an optical fiber of 400 µm core diameter, using a Schmidt-Cassegrain telescope. Figure 6.10 shows the

representation and of the experimental setup used in lab for the standoff femtosecond FIBS studies and the actual experimental design with MAYA CCD spectrometer, Celestron telescope, Arduino Uno, two kinematic mirror mounts by Thorlabs, and target highlighted in the red box in the inset.

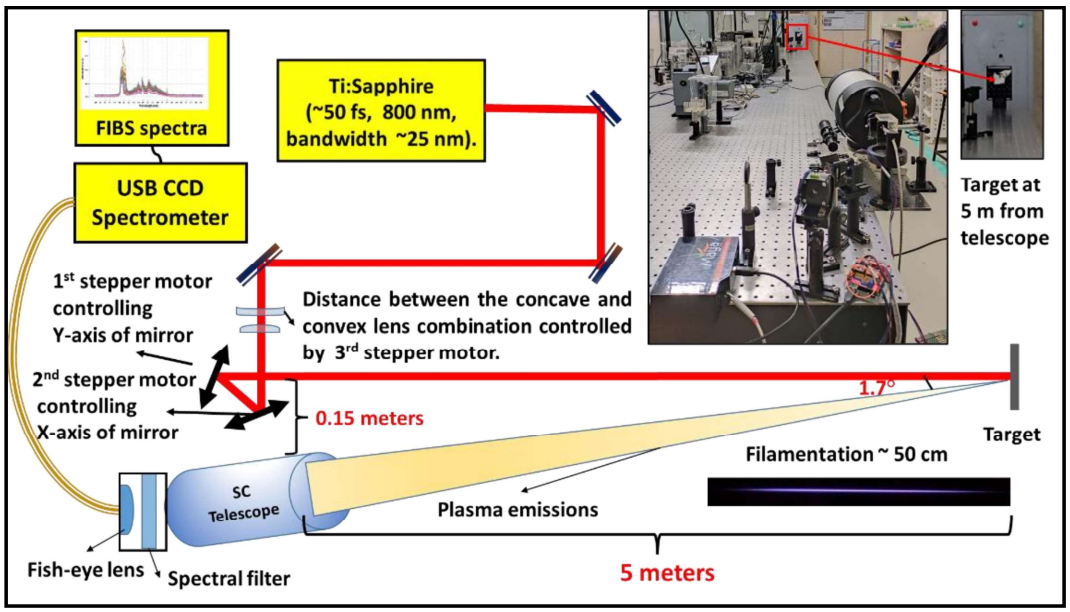

Figure 6.10 Fs-ST-FIBS setup with SCT. Inset: The actual laboratory setup with a telescope, Maya CCD spectrometer, Arduino microcontroller, two kinematic mirror mounts, variable iris, and target highlighted in the red box at 5 m distance, filamentation in the lab. The bigger inset shows the actual experimental setup in the lab whereas the smaller inset depicts the target at 5 m distance.

From the measurements shown in figure 6.10, the length of filamentation in the current investigation was estimated to be around 50 cm. When the crater diameter at the target surface was examined with an optical microscope, it was discovered to be between 260 and 320 nm for various metals. The data in figure 6.11 shows that the crater diameter on copper was approximately 320 µm, that on Brass was around 280 µm, and that on Al was around 260 µm. This was obtained following a one-second exposure of each target to fs pulses (1000 pulses). The fs pulses (~ 50 fs) with energy per pulse of 1.8 mJ, and 36 GW peak power were used. An average crater size of about 300 µm yields irradiance at the sample surface of about 51 TW/cm^2. The laser source centered at 800 nm reflecting from the target was removed using a BG18 visible-IR bandpass filter (which blocks light in the NIR), allowing the collection of plasma emission in the visible region exclusively. The image of the plasma created at the telescope's focal plane was moving since the beam was scanning the target at 5 m. The best spectra filtered using the intensity of the highest peak from each target for the analysis. A fish-eye lens with a 5 mm aperture was used to collect

the moving image of emissions formed by the telescope. The emissions are fed into the spectrometer via optical fiber and fish-eye lens.

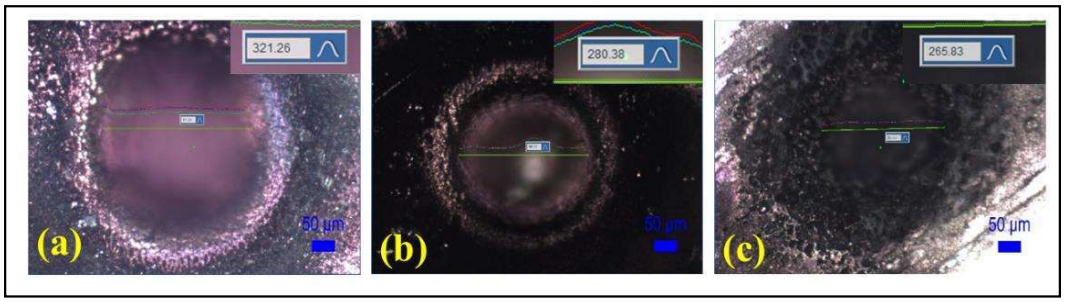

Figure 6.11 Optical microscope images of craters formed from the fs-filamentation interaction with (a) Cu (diameter of ~320 µm), (b) Brass (diameter of ~280 µm), (c) Al (diameter of ~260 µm) for one second (i.e., 1000 number of pulses).

6.3.2 Automation

An economic Arduino (an open-source prototyping platform), readily accessible kinetic mirror mounts, and free software are used for automation. The stepper motor is connected to the differential adjuster of the kinematic mirror mount using a coupler (5 mm one side and 6.3 mm on another side). Figure 6.12 (b) shows, the first mirror was at 67.5° with the incoming beam, and the second is at 67.5° with the outgoing beam. Stepper motors were used to control the high precision (25 m/rev) adjustable differential screw of two separate kinematic mirror mounts from M/s Thorlabs (one for X-direction steering and another for Y-direction steering). Figure 6.12 (b) shows the two kinematic mirror mounts in the figure "4" configuration were then coupled to the NIMA 17 stepper motor mounted on the optical bench in the laboratory setup. A coupler connects the Z-axis of the stepper motor to the micrometer on the manual translation stage. This was used to optimize the FIBS intensity by changing the focus for the best interaction. The stepper motor was mounted on a spring-loaded slider, which is essential for correcting for jerks and the backward and forward movement of the adjuster screw as it passes through the nut. The mirror mount and stepper motor on the slider were connected and fastened to the optical table. With the aid of beam guiding, the sample scanning over 1 cm^2 region at 5 m was accomplished. As indicated in figures 6.12(a) the CNC shield V3 board was combined with A4988 drivers in the automation process.

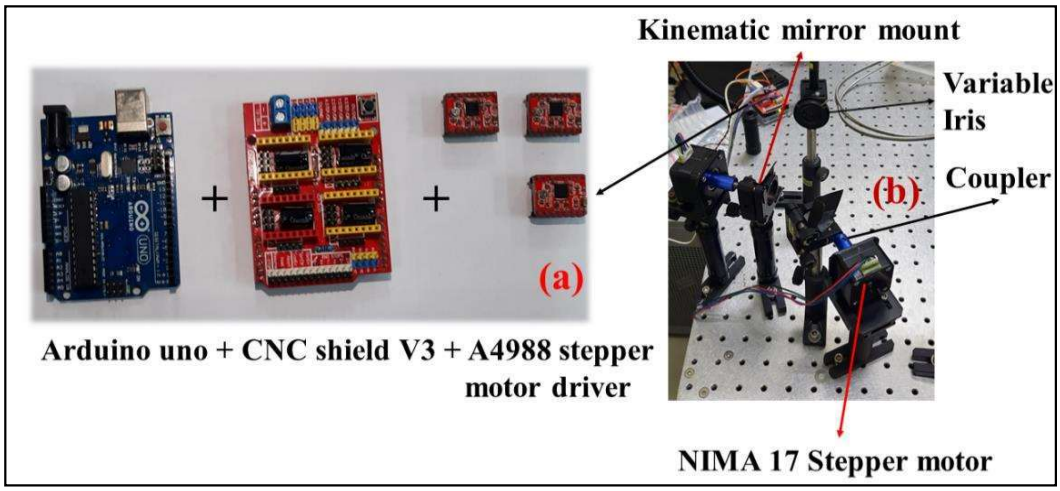

Figure 6.12 The components used for the automation (a) Arduino Uno microcontroller, CNC shield V3, and the A4988 stepper motor drivers (b) the two kinematic mirrors coupled to the stepper motors fixed to the optical table.

The CNC shield V3 is a PCB board with male and female headers compatible with the Arduino Uno and the A4988 driver. It has jumpers for adjusting the stepper motor's micro-stepping and the fourth axis for cloning, as well as built-in 10 k resistors and 100 µF capacitors. Power supply up to 36V is supported. The A4988 is an easy-to-use micro-stepping motor driver with an integrated translator. It supports the five-step modes of the whole, half, quarter, eighth, and sixteenth for bipolar stepper motors such as the NIMA 17. To prevent overheating and thermal shutdown during continuous operation, the limiting current (I_{MAX}) in the driver is regulated to 0.9 A by adjusting the tiny potentiometer on the device to obtain 0.49 V of VREF using equation 6.1. Using jumpers on the CNC shield board attached to the drivers' micro-step pins, the stepper motors configured to the sixteenth step's micro-step resolution. Because the driver's limiting current is smaller than the motor's rated current of 1.2 A, the stepper motor's torque is slightly reduced.

$$V_{REF} = I_{MAX} \times 8 \times R_s \ (R_s \text{is taken as } 0.068 \text{ ohms}) \qquad (6.1)$$

The stepper motors were not connected to the CNC shield until the Arduino flashed with the GRBL and uploaded. UGS software, a user-friendly GUI and documentation with step-by-step operating instructions, was used to control the stepper motors. The G-code uploaded to the UGS was used to control the speed and direction of the three stepper motors' combined motion for raster and spiral scans. Since plastic samples have a low

density, the plastic samples were scanned at high feed rate (40% for plastics and 20% for metals). The filamentation took less pulses than the metals to melt and drill through the polymers.

6.3.3 Results and discussions

After concentrating on the sample, the laser beam was precisely guided within the 1 cm^2 area at a standoff distance of 5 meters. The universal gcode sender (UGS) software's feed rate option regulates the laser scanning speed. Low-density targets like plastics were scanned at an average speed of 12 mm/s because filamentation drills a hole through the material with fewer pulses than it did for metals and metal alloys, which had an average rate of 6 mm/s and rapid decline in the plastics FIBS signal was observed. Superior LIBS signal was acquired even with the non-gated CCD spectrometer as compared to earlier results obtained utilizing a gated ICCD spectrometer from our lab [67]. The better signal achieved was primarily due to the rapid scanning and because of near-coaxial geometry. Only the Ag-Au FIBS spectra with the intensity of the Ag 546.54 nm peaks higher than 20000 counts were taken into consideration for the classification investigations, with the remaining spectra being eliminated. These spectra were collected for three distinct compositions. The femtosecond FIBS spectra of (a) Al with peaks at 394.4 and 396.15 nmi n figure 6.13 are shown (a) AlO $B^2\Sigma^+ \rightarrow X^2\Sigma^+$ transition bands in the range of 450-550 nm (b) CU with Cu I peaks identified at 510.55 nm, 515.32 nm, and 521.82 nm (c) Brass with Cu I peaks determined at 510.55 nm, 515.32 nm, and 521.82 nm and Zn I peaks at 468.01 nm, 472.21 nm, 481.05 nm, respectively.

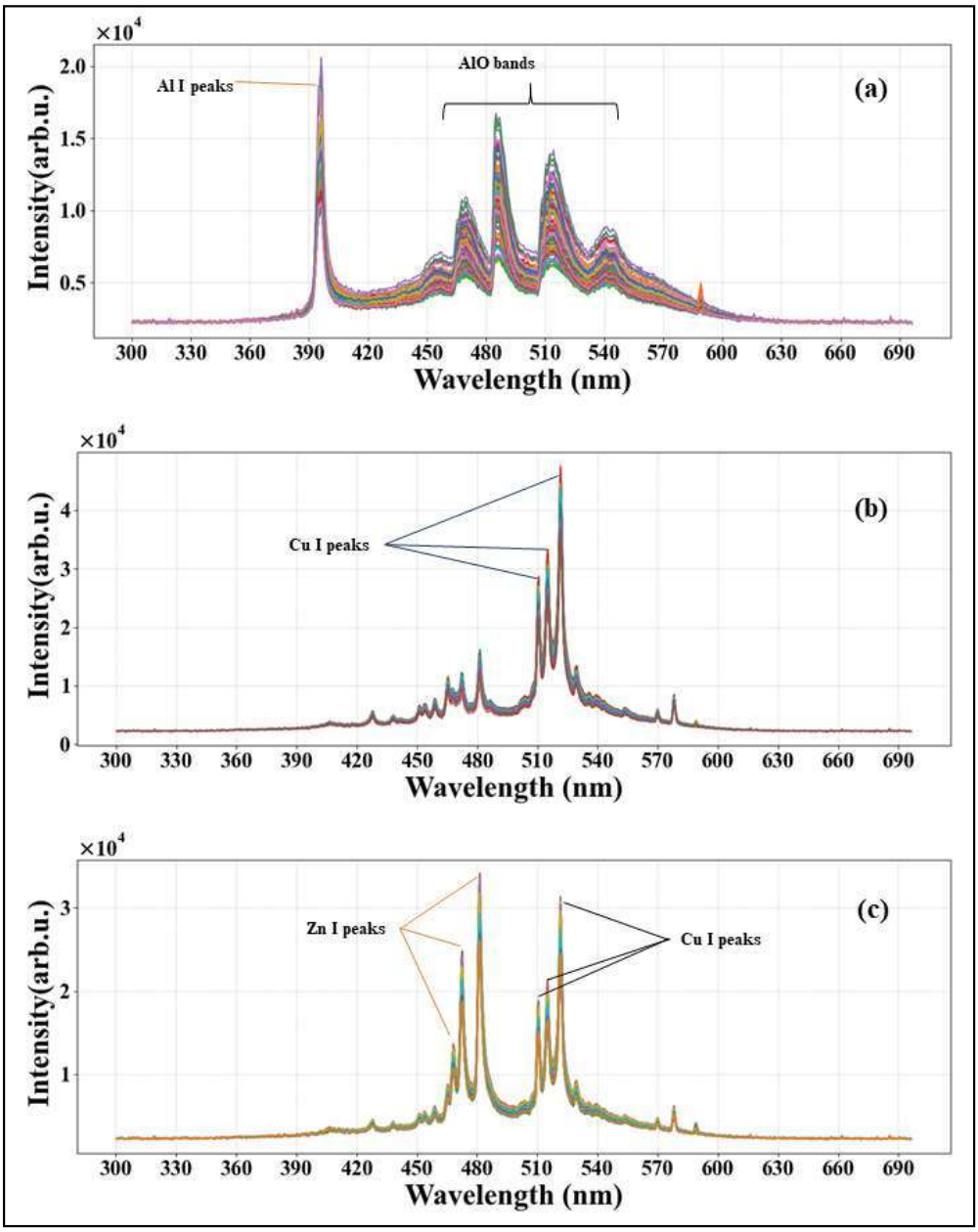

Figure 6.13 Fs-ST-FIBS spectra of (a) aluminum wherein Al atomic and AlO molecular bands were identified, (b) copper (c) Brass. Fifty spectra from each target filtered out using the highest intensity.

Figure 6.14 shows the FIBS spectra of three low-density plastic materials a) PVC, (b) CPVC with background noise, (c) UPVC. The swan band from transitions between the C_2 molecule's $d^3\Pi_g \rightarrow a^3\Pi_u$ electronic states. The swan band is composed of the sequences ($\Delta v = 0$) with a peak at 516.5 nm, ($\Delta v = 1$) with a peak at 563.5 nm, and ($\Delta v = -1$) with a peak at 437.7 nm. With Ca I peaks at 422.65 nm, 445.2 nm, 526.62 nm, 559.24 nm, 616.1 nm, and 617.58 nm and Ca II peaks at 393.5 nm, 396.77 nm, and 593.16 nm, calcium was also

found in UPVC. The spectra of three distinct compositions of Ag-Au bimetallic alloys with identifiable Ag I peaks at 520.9 nm, 546.55 nm, Au I peaks at 479.2 nm, and 606.9 nm, respectively, were confirmed from the NIST database.

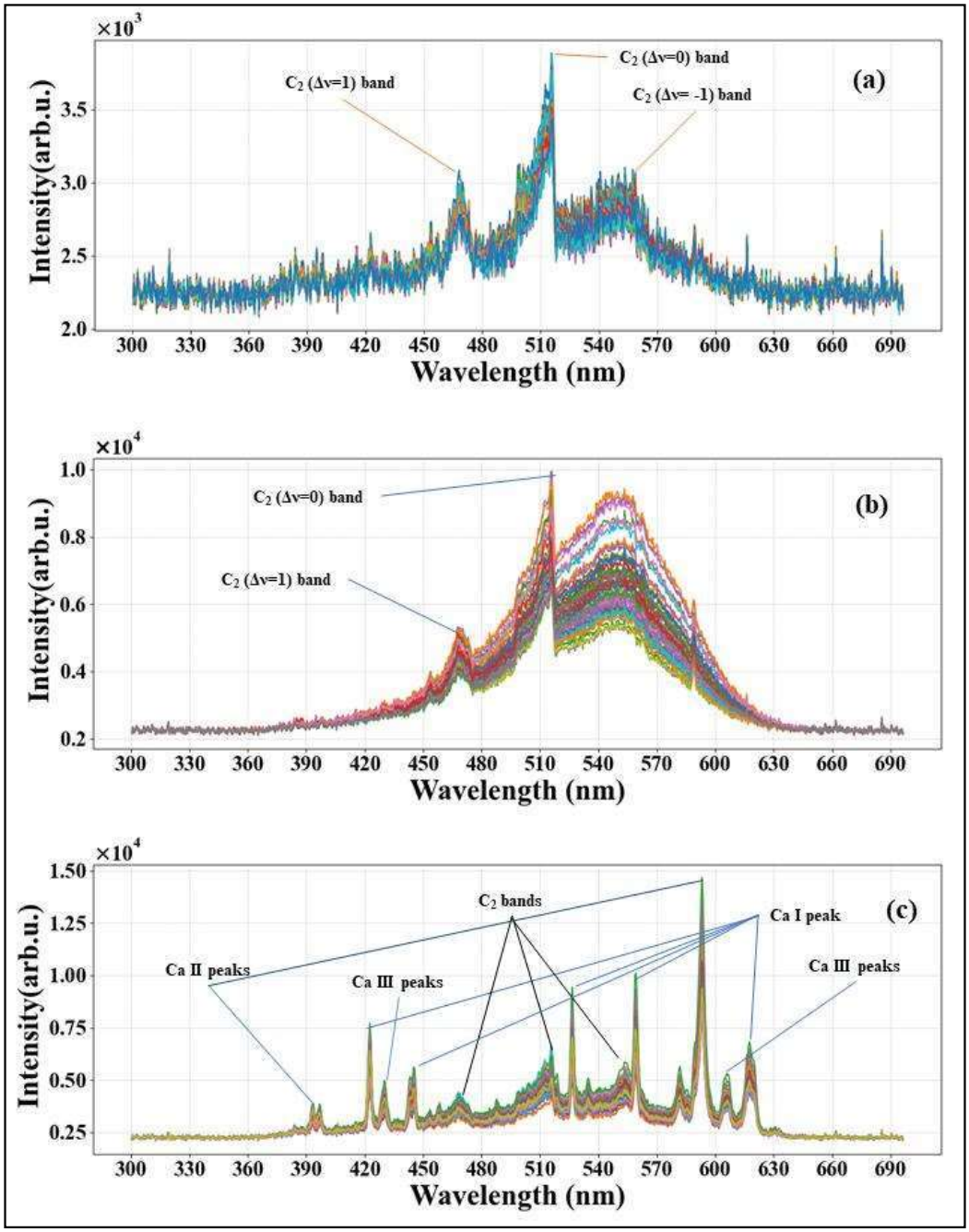

Figure 6.14 The fs-ST-FIBS spectra of three plastic samples (a) PVC, (b) CPVC with background noise, (c) UPVC. All the spectra contain the C_2 swan bands, calcium lines are identified in UPVC spectra.

Figure 6.15 illustrates the FIBS spectra of Ag-Au alloy [three different compositions of (a) Ag30-Au70, (b) Ag50-Au50, (c) Ag70-Au30 were investigated] collected for three different compositions, and ~50 spectra of highest intensities were used for the PCA studies/analyses.

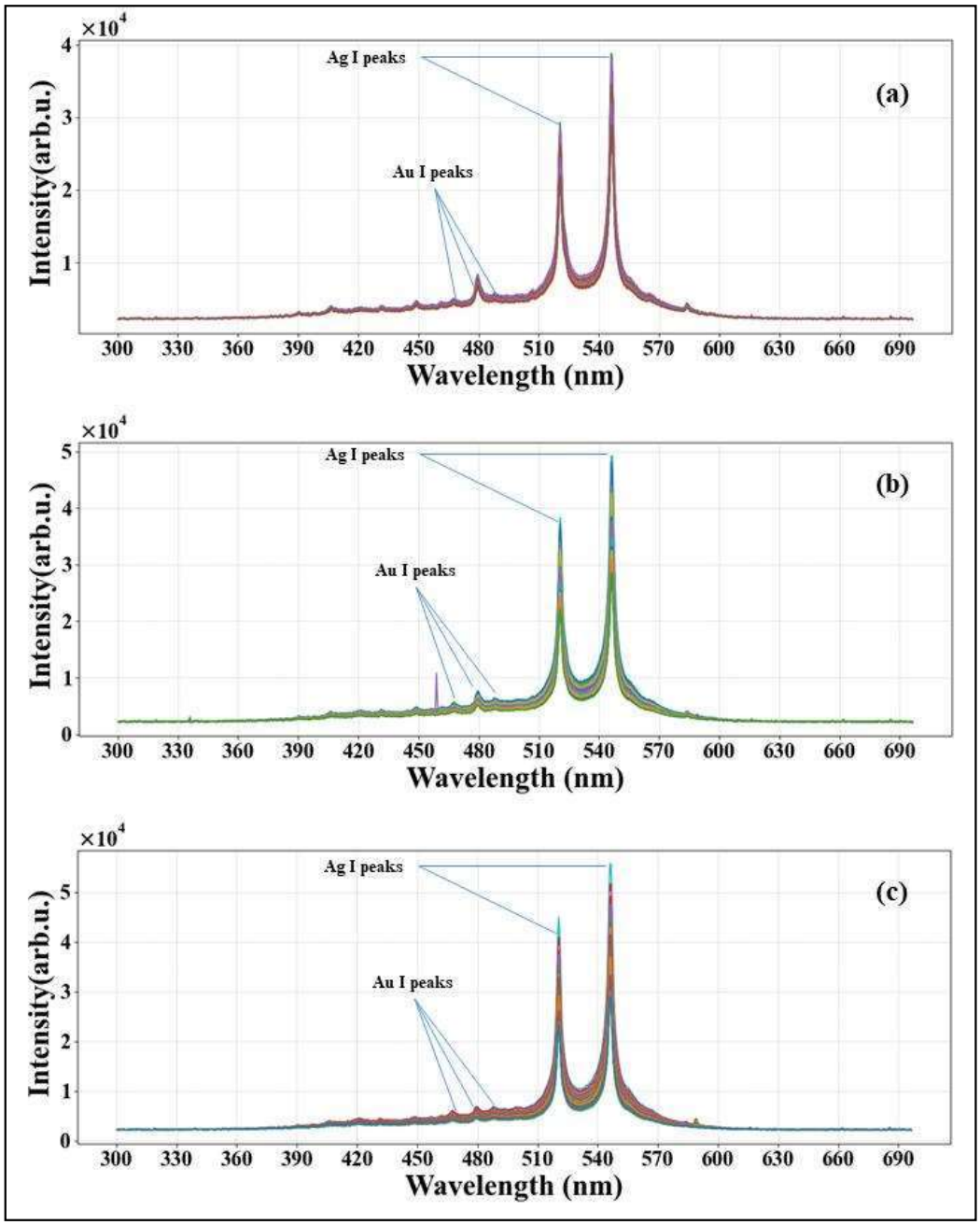

Figure 6.15 The fs-ST-FIBS spectra of Au-Ag bimetal alloy of three compositions (a) Ag30-Au70, (b) Ag50-Au50, (b) Ag70-Au30. Fifty spectra for three compositions were filtered out using the intensity of Ag I peak at 546.55 nm.

Figure 6.16(a) shows the probe areas of the samples (<1×1cm^2 for square/spiral patterns) at 5 m standoff distance. Figure 6.16(b) shows the classification of the three different compositions of Au-Ag bimetallic alloy targets in which the signal seems to be slightly fluctuating and, as a result, the clusters are distributed in two dimensions but well apart. In the current instance, we used 1 kHz pulses (1000 pulses/sec), but one can use a single pulse and gather as many spectra as feasible in practical situations. In addition to minimizing sample destruction, this will help reduce the substrate/surface contribution on which the sample is placed (for instance, trace levels of any dangerous chemical). The experimental setup will be automated as part of this study. We have shown several strategies in enhancing the SNR and classification of alloys and other materials in the near-field and standoff LIBS investigations. This work will be used to incorporate machine learning techniques and LIBS data analysis. [10, 34, 38, 51, 52, 67, 73, 74].

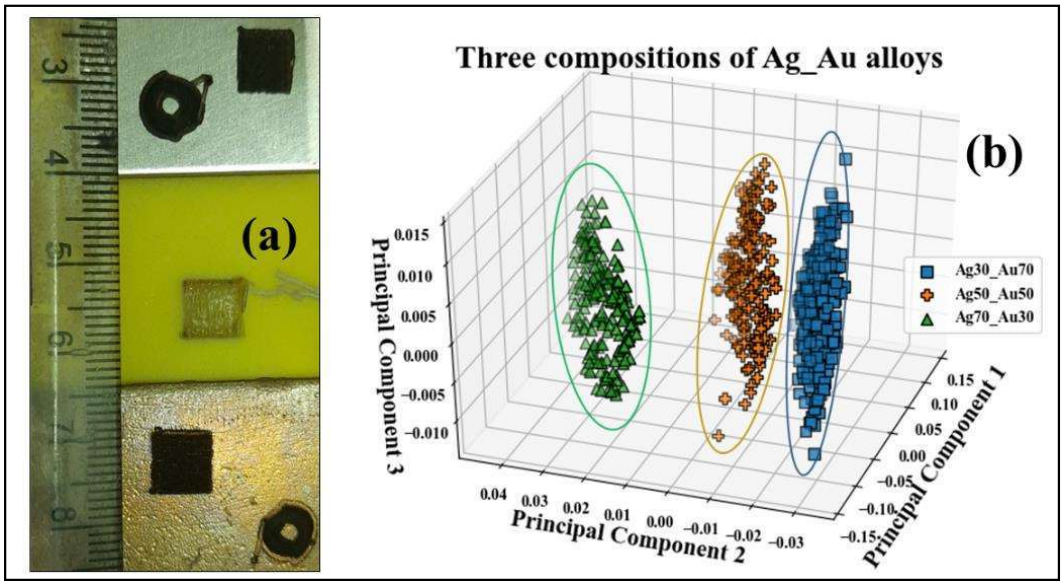

Figure 6.16 Precision of the automated standoff beam steering is demonstrated from the (a) raster scan (box shape) on steel, plastic, and Brass plates and a spiral scan (circle shape) on steel and Brass with in 1cm × 1cm area on the target placed at 5 meters standoff distance, (b) Classification of three compositions of Au-Ag alloy from the fs-ST-FIBS spectra using PCA.

6.4 Conclusions

Even under challenging circumstances, the standoff LIBS has enormous promise for quick material identification and detection. With several advancements in techniques for detection through clear windows and moving objects, underwater applications, and samples with uneven surfaces, the area is continuously growing. Combining Raman-LIBS with other systems, helps to increase the information about the sample under examination

and the SNR. Modern machine learning techniques combined with ST-LIBS data increase the speed and precision of detection. These methods adjust the technique range and enable higher detection capabilities even with a small spectrometer. When the SNR in the collected standoff LIBS data is low, newly discovered algorithms/machine-learning approaches and their judicious application are vitally important. To increase the SNR, we have been developing 2D correlation approaches [84]. As the number of lenses and mirrors is higher than the near field, there is substantial radiation loss on each reflection and refaction. As a result, the power densities at the target are compromised. We have optimized the technique for collecting emissions from the target at 5 meters, and most of the peaks are identified. PCA was implemented on all the acquired spectra and shows that it gives better classification and could be used when signal-to-noise ratios are small. By separately managing the horizontal and vertical movement of two kinematic mirror mounts with differential adjusters for beam steering and the spacing between concave and convex lenses for adjusting the focus, we successfully automate the St-Fs-FIBS arrangement. Classification analysis was conducted on the spectra of three different Au-Ag alloy compositions. The results show that a CCD spectrometer may be utilized for bulk targets, such as metals and metal alloys, at standoff distances and that this capability can be expanded to include in-depth analyses of geological targets. Translating the filament along the Z-axis will help adjust the filament's contact with the target and investigate targets with various densities and surface traces without adjusting the input laser pulse energy. The standoff LIBS data can be combined with advanced machine learning and deep learning methods to quantify the targets [65] further. The variations in the spectra can be reduced by lens combination for image stabilization.

References

[1] J.P. Singh, S.N. Thakur, Laser-induced breakdown spectroscopy, Elsevier, 2020.

[2] D.A. Cremers, L.J. Radziemski, Handbook of laser-induced breakdown spectroscopy, John Wiley & Sons, 2013.

[3] J. Novotný, K. Novotný, D. Prochazka, A. Hrdlička, J. Kaiser, Two dimensional elemental mapping by laser-induced breakdown spectroscopy, Spectroscopy. 26 (2014) 6–10.

[4] J. Moros, J.A. Lorenzo, P. Lucena, L.M. Tobaria, J.J. Laserna, Simultaneous Raman-LIBS for the standoff analysis of explosive materials Raman-LIBS hybrid sensor system Laser power, 22 (2013) 2–5.

[5] AK Shaik, N.R. Epuru, H. Syed, C. Byram, V.R. Soma, Femtosecond laser induced breakdown spectroscopy based standoff detection of explosives and discrimination using principal component analysis, Opt. Express. 26 (2018) 8069. doi:10.1364/oe.26.008069.

[6] F.J. Fortes, J.J. Laserna, The development of fieldable laser-induced breakdown spectrometer: No limits on the horizon, Spectrochim. Acta - Part B At. Spectrosc. 65 (2010) 975–990. doi:10.1016/j.sab.2010.11.009.

[7] W. Li, X. Li, X. Li, Z. Hao, Y. Lu, X. Zeng, A review of remote laser-induced breakdown spectroscopy, Appl. Spectrosc. Rev. 55 (2020) 1–25. doi:10.1080/05704928.2018.1472102.

[8] B. Sallé, J.L. Lacour, E. Vors, P. Fichet, S. Maurice, D.A. Cremers, R.C. Wiens, Laser-induced breakdown spectroscopy for Mars surface analysis: Capabilities at standoff distances and detection of chlorine and sulfur elements, Spectrochim. Acta - Part B At. Spectrosc. 59 (2004) 1413–1422. doi:10.1016/j.sab.2004.06.006.

[9] I. Gaona, P. Lucena, J. Moros, F.J. Fortes, S. Guirado, J. Serrano, J.J. Laserna, Evaluating the use of standoff LIBS in architectural heritage: Surveying the Cathedral of Málaga, J. Anal. At. Spectrom. 28 (2013) 810–820. doi:10.1039/c3ja50069a.

[10] M. Wang, Q. Wang, M. Zhu, L. Sun, X. Peng, L. Liu, J. Qu, Applying standoff LIBS to paleoclimatic research: A case study on geochemical content of carbonate rocks, 2015 Optoelectron. Glob. Conf. OGC 2015. (2015) 2–4. doi:10.1109/OGC.2015.7336854.

[11] C.S.C. Yang, F. Jin, S. Trivedi, E. Brown, U. Hömmerich, L. Nemes, A.C. Samuels, In situ chemical analysis of geology samples by a rapid simultaneous ultraviolet/visible/near-infrared (UVN) + longwave-infrared laser induced breakdown spectroscopy detection system at standoff distance, Opt. Express. 27 (2019) 19596. doi:10.1364/oe.27.019596.

[12] B. Sallé, D.A. Cremers, S. Maurice, R.C. Wiens, P. Fichet, Evaluation of a compact spectrograph for in-situ and standoff Laser-Induced Breakdown Spectroscopy analyses of geological samples on Mars missions, Spectrochim. Acta - Part B At. Spectrosc. 60 (2005) 805–815. doi:10.1016/j.sab.2005.05.007.

[13] C. López-Moreno, S. Palanco, J.J. Laserna, F. DeLucia, A.W. Miziolek, J. Rose, R.A. Walters, A.I. Whitehouse, Test of a standoff laser-induced breakdown spectroscopy sensor for the detection of explosive residues on solid surfaces, J. Anal. At. Spectrom. 21 (2006) 55–60. doi:10.1039/b508055j.

[14] L. Qi, L. Sun, Y. Xin, Z. Cong, Y. Li, H. Yu, Application of standoff double-pulse laser-induced breakdown spectroscopy in elemental analysis of magnesium alloy, Plasma Sci. Technol. 17 (2015) 676–681. doi:10.1088/1009-0630/17/8/11.

[15] L.A. Álvarez-Trujillo, V. Lazic, J. Moros, J. Javier Laserna, Standoff monitoring of aqueous aerosols using nanosecond laser-induced breakdown spectroscopy: droplet size and matrix effects, Appl. Opt. 56 (2017) 3773. doi:10.1364/ao.56.003773.

[16] L.A. Álvarez-Trujillo, A. Ferrero, J. Javier Laserna, Preliminary studies on standoff laser induced breakdown spectroscopy detection of aerosols, J. Anal. At. Spectrom. 23 (2008) 885–888. doi:10.1039/b716762h.

[17] S. Abdul Kalam, S. V. Balaji Manasa Rao, M. Jayananda, S. Venugopal Rao, Standoff femtosecond filament-induced breakdown spectroscopy for classification of geological materials, J. Anal. At. Spectrom. 35 (2020) 3007–3020. doi:10.1039/d0ja00355g.

[18] C. López-Moreno, S. Palanco, J.J. Laserna, Calibration transfer method for the quantitative analysis of high-temperature materials with standoff laser-induced breakdown spectroscopy, J. Anal. At. Spectrom. 20 (2005) 1275–1279. doi:10.1039/b508528d.

[19] H. Sattar, H. Ran, W. Ding, M. Imran, M. Amir, H. Ding, An approach of standoff measuring hardness of tungsten heavy alloys using LIBS, Appl. Phys. B Lasers Opt. 126 (2020) 1–11. doi:10.1007/s00340-019-7355-0.

[20] M.M. Tamboli, V.K. Unnikrishnan, R. Nayak, P. Devangad, K.M. Muhammed Shameem, V.B. Kartha, C. Santhosh, Development of a standoff laser induced breakdown spectroscopy (ST-LIBS) system for the analysis of complex matrices, J. Instrum. 11 (2016). doi:10.1088/1748-0221/11/08/P08021.

[21] I. Gaona, J. Moros, J.J. Laserna, New insights into the potential factors affecting the emission spectra variability in standoff LIBS, J. Anal. At. Spectrom. 28 (2013) 1750–1759. doi:10.1039/c3ja50181g.

[22] I. Gaona, J. Serrano, J. Moros, J.J. Laserna, Evaluation of laser-induced breakdown spectroscopy analysis potential for addressing radiological threats from a distance, Spectrochim. Acta - Part B At. Spectrosc. 96 (2014) 12–20. doi:10.1016/j.sab.2014.04.003.

[23] S.S. Harilal, J. Yeak, B.E. Brumfield, M.C. Phillips, Consequences of femtosecond laser filament generation conditions in standoff laser induced breakdown spectroscopy, Opt. Express. 24 (2016) 17941. doi:10.1364/oe.24.017941.

[24] L.A. Finney, P.J. Skrodzki, M. Burger, J. Nees, S.S. Harilal, I. Jovanovic, Single-shot, multi-signature remote detection of uranium by filament-induced breakdown spectroscopy, Opt. Lett. 44 (2019) 2783. doi:10.1364/ol.44.002783.

[25] J.J. Choi, S.J. Choi, J.J. Yoh, Standoff Detection of Geological Samples of Metal, Rock, and Soil at Low Pressures Using Laser-Induced Breakdown Spectroscopy, Appl. Spectrosc. 70 (2016) 1411–1419. doi:10.1177/0003702816664858.

[26] C.G. Brown, R. Bernath, M. Fisher, M.C. Richardson, M. Sigman, R.A. Walters, A. Miziolek, H. Bereket, L.E. Johnson, Remote femtosecond laser induced breakdown spectroscopy (LIBS) in a standoff detection regime, Enabling Technol. Des. Nonlethal Weapons. 6219 (2006) 62190B. doi:10.1117/12.663821.

[27] M. Dell'Aglio, M. López-Claros, J.J. Laserna, S. Longo, A. De Giacomo, Stand-off laser induced breakdown spectroscopy on meteorites: calibration-free approach, Spectrochim. Acta - Part B At. Spectrosc. 147 (2018) 87–92. doi:10.1016/j.sab.2018.05.024.

[28] A. Ferrero, J.J. Laserna, A theoretical study of atmospheric propagation of laser and return light for standoff laser induced breakdown spectroscopy purposes, Spectrochim. Acta - Part B At. Spectrosc. 63 (2008) 305–311. doi:10.1016/j.sab.2007.11.020.

[29] S.A. Kalam, S. V Rao, S.V. Rao, Standoff LIBS for explosives detection-challenges and status, Laser Focaus World April. (2017) 24–28.

[30] J. Moros, J.A. Lorenzo, P. Lucena, L.M. Tobaria, J.J. Laserna, Simultaneous Raman spectroscopy-laser-induced breakdown spectroscopy for instant standoff analysis of explosives using a mobile integrated sensor platform, Anal. Chem. 82 (2010) 1389–1400. doi:10.1021/ac902470v.

[31] J.L. Gottfried, F.C. De Lucia, C.A. Munson, A.W. Miziolek, Double-pulse standoff laser-induced breakdown spectroscopy for versatile hazardous materials detection, Spectrochim. Acta - Part B At. Spectrosc. 62 (2007) 1405–1411. doi:10.1016/j.sab.2007.10.039.

[32] Y. Xin, L.X. Sun, Z.J. Yang, P. Zeng, Z.B. Cong, L.F. Qi, In situ analysis of magnesium alloy using a standoff and double-pulse laser-induced breakdown spectroscopy system, Front. Phys. 11 (2016) 1–10. doi:10.1007/s11467-016-0619-9.

[33] V. Gabriela, et al. "Fast identification of biominerals by means of standoff laser-induced breakdown spectroscopy using linear discriminant analysis and artificial neural networks." *Spectrochimica Acta Part B: Atomic Spectroscopy* 73 (2012): 1-6.

[34] K.-Q. Yu, Y.-R. Zhao, F. Liu, Y. He, Laser-induced breakdown spectroscopy coupled with multivariate chemometrics for variety discrimination of soil, Sci. Rep. 6 (2016) 27574.

[35] VK Unnikrishnan, K.S. Choudhari, SD. Kulkarni, R. Nayak, V.B. Kartha, C. Santhosh, Analytical predictive capabilities of Laser Induced Breakdown Spectroscopy (LIBS) with Principal Component Analysis (PCA) for plastic classification, RSC Adv. 3 (2013) 25872–25880. doi:10.1039/c3ra44946g.

[36] C.G. Parigger, Atomic and molecular emissions in laser-induced breakdown spectroscopy, Spectrochim. Acta Part B At. Spectrosc. 79 (2013) 4–16. doi:https://doi.org/10.1016/j.sab.2012.11.012.

[37] SJ Mousavi, M.H. Farsani, S.M.R. Darbani, A. Mousaviazar, M. Soltanolkotabi, A.E. Majd, CN and C 2 vibrational spectra analysis in molecular LIBS of organic materials, Appl. Phys. B. 122 (2016) 106.

[38] G. Guo, G. Niu, Q. Lin, S. Wang, D. Tian, Y. Duan, Compact instrumentation and (analytical) performance evaluation for laser-induced breakdown spectroscopy, Instrum. Sci. Technol. 47 (2019) 70–89. doi:10.1080/10739149.2018.1469146.

[39] Y. Ding, D. Tian, C. Li, Y. Duan, G. Yang, Design and development of a miniature digital delay generator for laser-induced breakdown spectroscopy, Instrum. Sci. Technol. 43 (2015) 115–124. doi:10.1080/10739149.2014.940534.

[40] S. Wang, M. Xu, Q. Lin, G. Guo, Z. Zhang, D. Tian, Y. Duan, A multifunctional sampling chamber for laser-induced breakdown spectroscopy for on-site elemental analysis, Instrum. Sci. Technol. 43 (2015) 485–495. doi:10.1080/10739149.2015.1010091.

[41] L.M. Narla, S.V. Rao, Identification of metals and alloys using color CCD images of laser-induced breakdown emissions coupled with machine learning, Appl. Phys. B Lasers Opt.126 (2020) 1–8. doi:10.1007/s00340-020-07469-6.

[42] J.L. Gottfried, F.C. De Lucia, C.A. Munson, A.W. Miziolek, Standoff detection of chemical and biological threats using laser-induced breakdown spectroscopy, Appl. Spectrosc. 62 (2008) 353–363. doi:10.1366/000370208784046759.

[43] M. Burger, P.J. Skrodzki, L.A. Finney, J. Nees, I. Jovanovic, Remote detection of uranium using self-focusing intense femtosecond laser pulses, Remote Sens. 12 (2020) 1–12. doi:10.3390/RS12081281.

[44] Y. Gong, D. Choi, B.Y. Han, J. Yoo, S.H. Han, Y. Lee, Remote quantitative analysis of cerium through a shielding window by standoff laser-induced breakdown spectroscopy, J. Nucl. Mater. 453 (2014) 8–15. doi:10.1016/j.jnucmat.2014.06.022.

[45] L.M. Cabalín, T. Delgado, J. Ruiz, D. Mier, J.J. Laserna, Stand-off laser-induced breakdown spectroscopy for steel-grade intermix detection in sequence casting operations. At-line monitoring of temporal evolution versus predicted mathematical model, Spectrochim. Acta - Part B At. Spectrosc. 146 (2018) 93–100. doi:10.1016/j.sab.2018.05.001.

[46] T. Delgado, J. Ruiz, L.M. Cabalín, J.J. Laserna, Distinction strategies based on discriminant function analysis for particular steel grades at elevated temperature using standoff LIBS, J. Anal. At. Spectrom. 31 (2016) 2242–2252. doi:10.1039/c6ja00219f.

[47] D. Girón, T. Delgado, J. Ruiz, L.M. Cabalín, J.J. Laserna, In-situ monitoring and characterization of airborne solid particles in the hostile environment of a steel industry using standoff LIBS, Meas. J. Int. Meas. Confed. 115 (2018) 1–10. doi:10.1016/j.measurement.2017.09.046.

[48] P.J. Gasda, T.E. Acosta-Maeda, P.G. Lucey, A.K. Misra, S.K. Sharma, G.J. Taylor, Next generation laser-based standoff spectroscopy techniques for Mars exploration, Appl. Spectrosc. 69 (2015) 173–192. doi:10.1366/14-07483.

[49] C. Liu, A Stand-Off Laser-Induced Breakdown Spectroscopy (LIBS) System Applicable for Martian Rocks Studies, (2021).

[50] V. Sathiesh Kumar, N.J. Vasa, R. Sarathi, Remote surface pollutant measurement by adopting a variable standoff distance based laser induced spectroscopy technique, J. Phys. D. Appl. Phys. 48 (2015) 435504. doi:10.1088/0022-3727/48/43/435504.

[51] M.M. Tamboli, U. V. K., P. Devangad, MS K. M., S. C., ST-LIBS for heavy element detection in complex matrices, Fifth Int. Conf. Opt. Photonics Eng. 10449 (2017) 104492T. doi:10.1117/12.2270895.

[52] F.J. Fortes, S. Guirado, A. Metzinger, J.J. Laserna, A study of underwater standoff laser-induced breakdown spectroscopy for chemical analysis of objects in the deep ocean, J. Anal. At. Spectrom. 30 (2015) 1050–1056. doi:10.1039/C4JA00489B.

[53] WT Li, Y.N. Zhu, X. Li, ZQ. Hao, L.B. Guo, X.Y. Li, X.Y. Zeng, Y.F. Lu, In situ classification of rocks using standoff laser-induced breakdown spectroscopy with a compact spectrometer, J. Anal. At. Spectrom. 33 (2018) 461–467. doi:10.1039/c8ja00001h.

[54] P.D. Barnett, N. Lamsal, S.M. Angel, Standoff Laser-Induced Breakdown Spectroscopy (LIBS) Using a Miniature Wide Field of View Spatial Heterodyne Spectrometer with Sub-Microsteradian Collection Optics, Appl. Spectrosc. 71 (2017) 583–590. doi:10.1177/0003702816687569.

[55] QQ. Wang, K. Liu, H. Zhao, C.H. Ge, Z.W. Huang, Detection of explosives with laser-induced breakdown spectroscopy, Front. Phys. 7 (2012) 701–707. doi:10.1007/s11467-012-0272-x.

[56] J. Laserna, P. Lucena, A. Ferrero, A. Doña, R. González, Standoff LIBS Sensor Technology . Fieldable , Remotely Operated Platforms for Detection of Explosive Residues, (2007) 1–18.

[57] R.C. Wiens, S.K. Sharma, J. Thompson, A. Misra, P.G. Lucey, Joint analyses by laser-induced breakdown spectroscopy (LIBS) and Raman spectroscopy at standoff distances, Spectrochim. Acta - Part A Mol. Biomol. Spectrosc. 61 (2005) 2324–2334. doi:10.1016/j.saa.2005.02.031.

[58] Q. Lin, S. Wang, G. Guo, Y. Tian, Y. Duan, Novel laser induced breakdown spectroscopy–Raman instrumentation using a single pulsed laser and an echelle spectrometer, Instrum. Sci. Technol. 46 (2018) 163–174. doi:10.1080/10739149.2017.1344702.

[59] C. López-Moreno, S. Palanco, J.J. Laserna, Stand-off analysis of moving targets using laser-induced breakdown spectroscopy, J. Anal. At. Spectrom. 22 (2007) 84–87. doi:10.1039/b609705g

[60] NL. Murthy, S. Abdul Salam, S.V. Rao, Stand-off Femtosecond Laser Induced Breakdown Spectroscopy of Metals, Soil, Plastics and Classification Studies, 2019 Work. Recent Adv. Photonics, WRAP 2019. (2019) 16–18. doi:10.1109/WRAP47485.2019.9013674.

[61] G. Vítková, K. Novotný, L. Prokeš, A. Hrdlička, J. Kaiser, J. Novotný, R. Malina, D. Prochazka, Fast identification of biominerals by means of standoff laser-induced breakdown spectroscopy using linear discriminant analysis and artificial neural networks, Spectrochim. Acta - Part B At. Spectrosc. 73 (2012) 1–6. doi:10.1016/j.sab.2012.05.010.

[62] R. Junjuri, A. Prakash Gummadi, M. Kumar Gundawar, Single-shot compact spectrometer based standoff LIBS configuration for explosive detection using artificial neural networks, Optik (Stuttg). 204 (2020) 163946. doi:10.1016/j.ijleo.2019.163946.

[63] FC De Lucia, J.L. Gottfried, C.A. Munson, A.W. Miziolek, Multivariate analysis of standoff laser-induced breakdown spectroscopy spectra for classification of explosive-containing residues, Appl. Opt. 47 (2008). doi:10.1364/AO.47.00G112.

[64] R. Nouir, I. Cherni, H. Ghalila, S. Hamzaoui, Early diagnosis of dental pathologies by front face fluorescence (FFF) and laser-induced breakdown spectroscopy (LIBS) with principal component analysis (PCA), Instrum. Sci. Technol. 0 (2022) 1–16. doi:10.1080/10739149.2021.2024845.

[65] L. Narlagiri, V.R. Soma, Simultaneous quantification of Au and Ag composition from Au–Ag bi-metallic LIBS spectra combined with shallow neural network model for multi-output regression, Appl. Phys. B Lasers Opt. 127 (2021) 1–11. doi:10.1007/s00340-021-07681-y.

[66] AK Shaik, V.R. Soma, Standoff discrimination and trace detection of explosive molecules using femtosecond filament induced breakdown spectroscopy combined with silver nanoparticles, OSA Contin. 2 (2019) 554. doi:10.1364/osac.2.000554.

[67] N. Linga Murthy, S.V. Rao, Nanoparticle Enhanced Laser Induced Breakdown Spectroscopy of Liquids, Springer Singapore, 2021. doi:10.1007/978-981-15-9259-1_105.

[68] S. Abdul Kalam, N. Linga Murthy, J. Rama Krishna, VVSS Srikanth, S. Venugopal Rao, Nanoparticle enhanced laser induced breakdown spectroscopy with femtosecond pulses, in: Opt. InfoBase Conf. Pap., 2014. doi:10.1364/PHOTONICS.2016.Th3A.89.

[69] I. Gaona, J. Serrano, J. Moros, J.J. Laserna, Range-adaptive standoff recognition of explosive fingerprints on solid surfaces using a supervised learning method and laser-induced breakdown spectroscopy, Anal. Chem. 86 (2014) 5045–5052. doi:10.1021/ac500694j

[70] W.T. Li, X.Y. Yang, X. Li, S.S. Tang, J.M. Li, R.X. Yi, P. Yang, Z.Q. Hao, L.B. Guo, X.Y. Li, X.Y. Zeng, Y.F. Lu, A portable multi-collector system based on an artificial optical compound eye for standoff laser-induced breakdown spectroscopy, J. Anal. At. Spectrom. 32 (2017) 1975–1979. doi:10.1039/c7ja00173h.

[71] H.L. Xu, S.L. Chin, Femtosecond laser filamentation for atmospheric sensing, Sensors. 11 (2011) 32–53. doi:10.3390/s110100032.

[72] W. Liu, H.L. Xu, G. Méjean, Y. Kamali, J.F. Daigle, A. Azarm, P.T. Simard, P. Mathieu, G. Roy, S.L. Chin, Efficient non-gated remote filament-induced breakdown spectroscopy of metallic sample, Spectrochim. Acta - Part B At. Spectrosc. 62 (2007) 76–81. doi:10.1016/j.sab.2007.01.001.

[73] J. Kasparian, R. Sauerbrey, S.L. Chin, The critical laser intensity of self-guided light filaments in air, Appl. Phys. B Lasers Opt. 71 (2000) 877–879. doi:10.1007/s003400000463.

[74] S.L. Chin, W. Liu, F. Théberge, Q. Luo, S.A. Hosseini, V.P. Kandidov, O.G. Kosareva, N. Aközbek, A. Becker, H. Schroeder, Some fundamental concepts of femtosecond laser filamentation, Springer Ser. Chem. Phys. 89 (2008) 243–264. doi:10.1007/978-3-540-73794-0_12.

[75] S.S. Harilal, B.E. Brumfield, N.L. Lahaye, K.C. Hartig, M.C. Phillips, Optical spectroscopy of laser-produced plasmas for standoff isotopic analysis, Appl. Phys. Rev. 5 (2018). doi:10.1063/1.5016053.

[76] S.S. Harilal, B.E. Brumfield, M.C. Phillips, Standoff detection of bulk and trace elements using laser-induced fluorescence of laser ablation plumes, 2018 Conf. Lasers Electro-Optics, CLEO 2018 - Proc. 1 (2018) 6–7.

[77] M. Burger, P. Polynkin, I. Jovanovic, Filament-induced breakdown spectroscopy with structured beams, Opt. Express. 28 (2020) 36812. doi:10.1364/oe.412480.

[78] M. Burger, P. Polynkin, I. Jovanovic, Femtosecond beam shaping for filament-induced breakdown spectroscopy, Opt. InfoBase Conf. Pap. Part F183- (2020) 8–9. doi:10.1364/CLEO_SI.2020.STh3H.5.

[79] X.-T. Lu, S.-Y. Zhao, X. Gao, K.-M. Guo, J.-Q. Lin, Effect of the distance between focusing lens and target surface on quantitative analysis of Mn element in aluminum alloys by using filament-induced breakdown spectroscopy, Chinese Phys. B. 29 (2020) 124209. doi:10.1088/1674-1056/abb3ef.

[80] L.R. Mucciaroni, M.G. Vivas, Efficient Yet Accessible Arduino-based Control System for Laser Microfabrication of Photonic Platforms, Lasers Manuf. Mater. Process. 8 (2021) 395–408. doi:10.1007/s40516-021-00153-3.

[81] A.M. Chaudry, Using Arduino Uno Microcontroller to Create Interest in Physics, Phys. Teach. 58 (2020) 418–421. doi:10.1119/10.0001841.

[82] N.B. Tomazio, A.L.S. Romero, C.R. Mendonca, Desenvolvimento de um obturador de feixe óptico utilizando um disco rígido de computador, Rev. Bras. Ensino Fis. 40 (2018) e1307. doi:10.1590/1806-9126-RBEF-2017-0200.

[83] L. Guo, D.M. Monahan, G. Fleming, Rapid and economical data acquisition in ultrafast frequency-resolved spectroscopy using choppers and a microcontroller, Opt. Express. 24 (2016) 18126. doi:10.1364/oe.24.018126.

[84] L. M. Narlagiri and V. R. Soma, "Improving the signal-to-noise ratio of atomic transitions in LIBS using two-dimensional correlation analysis," OSA Continuum 4, (2021)2423-2441. doi:10.1364/OSAC.426995

7 Conclusions and future scope

7.1 Conclusions

LIBS is a versatile technique that can interrogate a broad range of samples in different phases, standoff distances, and even objects behind transparent materials. The highly versatile technique offers enormous scope for development in analysing the data, instrumentation, and probing samples in small quantities. Ns-LIBS is well studies as compared to fs-LIBS. The plasma temperature and electron densities are well reported with diverse samples. The ns laser-induced plasma reaches local thermodynamical equilibrium (LTE) land is reliable in the quantification studies. The molecular bands are prominent in the fs-LIBS and are useful in the classification studies of the organic molecules based on CN and C_2 bands in the LIBS spectra. Fs-filamentation offers a divergence-free beam propagation useful in depositing the desired laser power on the target at standoff distances. The analysis of ns and fs-LIBS data was present in this thesis. The concluding points from the thesis are

- The spectrometers use dispersive optical components like gratings and prism, which split the incoming light with a predefined wavelength-dependent resolution. A better resolution will be useful in the classification and quantification of target samples from the LIBS spectra.

- Further machine learning algorithms applied to the LIBS data improve the classification capabilities of the LIBS spectra from lower-resolution spectrometers. Colour CCD uses Bayer's filter with three colour filters with varying sensitivities and behaves like a very low-resolution colour-separating spectrometer. A new method was demonstrated for classifying metals and alloys from the colour CCD images of the fs laser-produced plasma emissions coupled with machine learning.

- The atomic and ionic emissions from the laser-produced plasma decay with the increasing delay between the incident pulse and ICCD gate delay. The correlation between the time-resolved LIBS spectra could help improve the SNR and resolution of the LIBS spectra. For the first time, two-dimensional correlation analysis is proposed for enhancing the quality of noisy standoff LIBS data.

- Deep learning algorithms perform well with data size, unlike machine learning algorithms. The performance of the deep learning algorithms was demonstrated to improve with data augmentation. These two ideas were explored for the first time by employing the time-resolved LIBS spectra in the generalization. The model improves the multi-output regression's prediction accuracy in estimating the composition of the Au & Ag.

- The fs laser source delivered the pulses at a 1 kHz repetition rate, and the sample portion was rapidly ablated when pulses were focussed on it. The SNR of the LIBS reduces with the number of pulses incident at the same spot, and the sample needs to be displaced continuously to ablate the fresh spot to get better SNR. Translation stages are used for the displacement of the samples. Using the translation stages for standoff studies is impractical. This problem is addressed by rapid beam steering with the motorized kinetic mirrors indigenously developed using the simple Arduino and stepper motors in the standoff studies. Better SNR was also achieved.

- The pre-processing of the data, before applying the machine learning algorithms, is necessary and mean-centering of similar LIBS spectra resulted in a successful discrimination of the high-energy materials. This improved the capability of the fs-LIBS on the cellulose-based filter paper with similar CN, C_2 molecular bands, and C peaks, like other organic compounds.

- The enhancement in the LIBS signal is confirmed with the addition of nanoparticles to the target sample. But, the enhancement ~2 times was observed in the Al, AlO peaks in the fs-LIBS spectra with the nanoparticle embedded PVC nano fibers coating. The enhancement and the standard deviation in the atomic and molecular peaks were observed to differ.

- Most of the reports in the LIBS are of the bulk sample like metal plates or the sample pressed to a pellet, and the substrate spectra are unavoidable when working with traces. A new experimental configuration with grazing incidence filamentation was proposed to address the concern for analyzing sparse fine powder samples like graphite.

7.2 Femtosecond LIBS for trace detection

Using principal component analysis, we studied the classification of DNT, picric acid, and ammonium nitrate dispersed and dried on filter paper using femtosecond laser-induced breakdown (LIBS) spectra.

7.2.1 Introduction

Laser-induced breakdown spectroscopy (LIBS) is optical emission spectroscopy capable of simultaneous multi-elemental analysis [1]. It uses the atomic and molecular emissions from the cooling plasma formed during the interaction of an intense pulse laser and the sample. The molecular emissions in the femtosecond LIBS technique are substantial when compared to the nanosecond, picosecond LIBS. The atomic and molecular emissions combined with the chemometric analysis help identify and classify explosives [2]. LIBS technique was employed to detect explosive traces on substrates such as aluminum in the near field case and at standoff distances [3, 4]. A further enhancement is achieved in the signal by adding nanoparticles to the sample, which improves the capacity for detecting traces with the other process [5-7]. Earlier works performed LIBS studies to determine calcium ions in water using the solution with filter paper [8]. In the present study, the femtosecond LIBS spectra are used to analyze traces of liquid explosive samples drop cast on the filter paper. Significant variation in the intensities of CN and C_2 bands and the spectra were classified using principal component analysis.

7.2.2 Experimental details

Employed femtosecond amplifier delivering ~ 50 fs pulses at 800 nm and 500 Hz repetition for the present experiments. The experiments were conducted at one mJ laser energy. The laser was focused vertically down using a 100 mm focal length lens onto the sample. The emissions were collected with the Andor collection optics and fed to a Michelle spectrometer coupled with Andor iStar ICCD using a 400 μm fiber. The solutions of ammonium nitrate, picric acid, and DNT were prepared and drop cast on filter paper with an adjustable-volume micro-pipette. Each spectrum is the accumulation of 10 spectra with 2 seconds exposure time. The LIBS studies of traces in filter paper are quite challenging as the thickness of the paper was ~180 μm shown in the inset of figure 7.1 and the need to

be ablated rapidly and collected the spectra in the wavelength range of 200- 900 nm. 15-20 spectra of each sample.

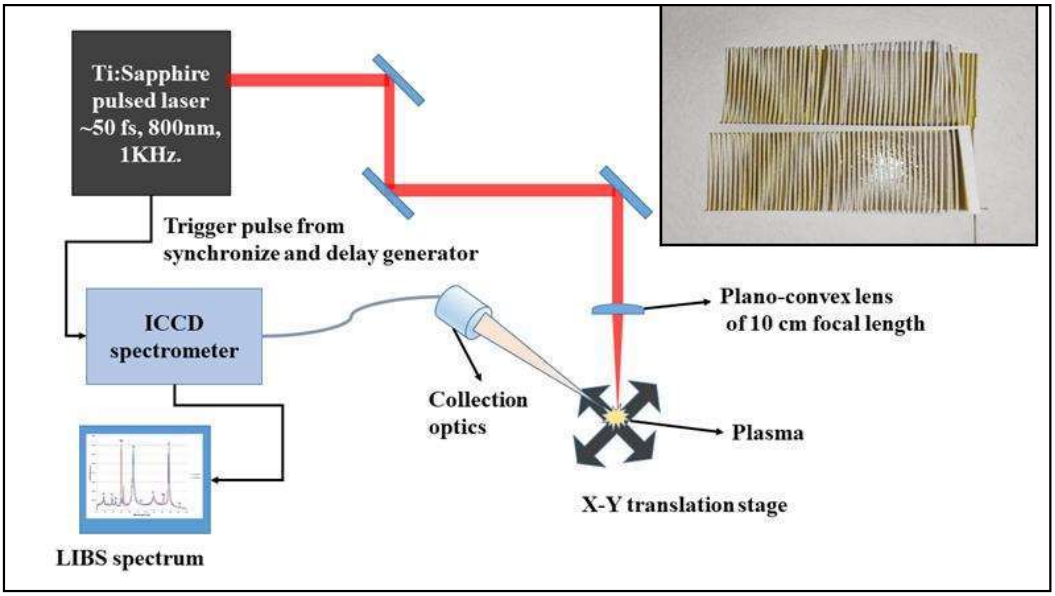

Figure 7.1 Experimental setup used for recording the femtosecond LIBS of traces on filter paper. The filter paper ablated with femtosecond laser pulses in the inset during the raster scan.

Commercially available cellulose $(C6H10O5)_n$ filter paper (Whatman grade 1) with 90 mm diameter and thickness of ~180 µm, the weight of ~ 87 g/m^2 was fixed to the circular frame for ablation after drop cast with a solution. The DNT (2,4- Dinitrotoluene, $C_7H_6N_2O_4$), Picric acid ($C_6H_3N_3O_7$), Ammonium nitrate NH_4NO_3 solutions were drop cast on the filter paper. The filter paper after ablation with a rapid raster scan (2 mm/s) with a long step size along the horizontal direction is shown in figure 1 inset. The spectra were collected for two secondary explosives, picric acid and DNT, and an oxidizer (ammonium nitrate) of 5 milli molar concentration. The solutions were drop-casted, allowed to spread, and dried on the filter paper. The filter paper had similar CN, and C_2 bands in the LIBS spectra, except that the sodium and calcium peaks in the spectra when compared to the energetic materials as shown in figure 7.2 (a) CN band and (b) C_2 band for the filter paper, picric acid (PA) on filter paper, DNT on filter paper, and AN on a filter paper. The classification studies on the spectra of three different samples were performed. These initial studies are promising for further trace detection studies.

7.2.3 Results

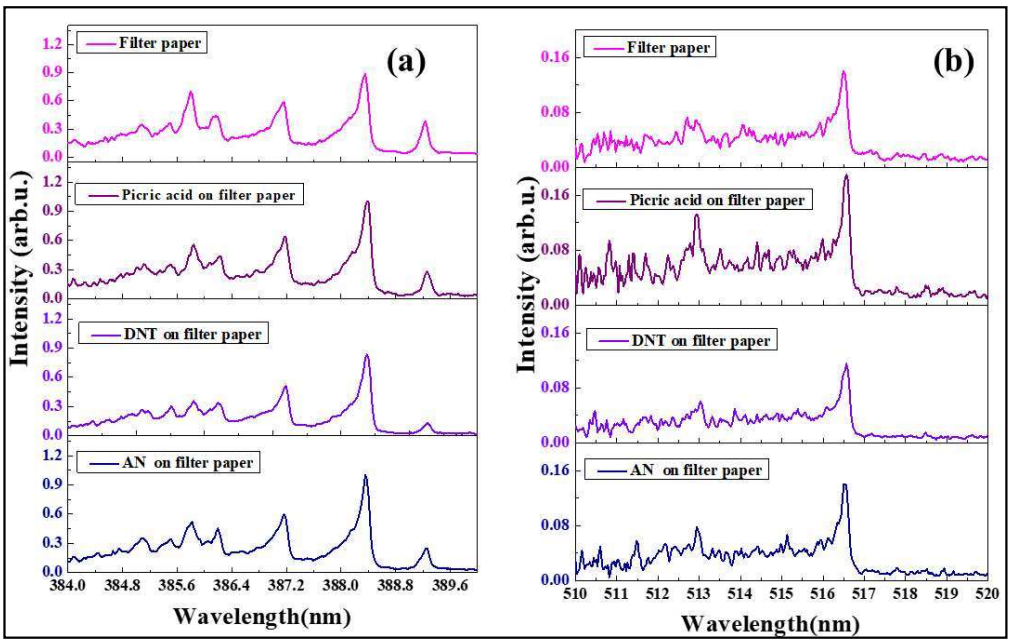

Figure 7.2 (a) CN band and (b) C_2 band for the filter paper, picric acid (PA) on filter paper, DNT on filter paper, and AN on a filter paper.

The CN, C_2 molecular band, and the normalized spectra of the three samples demonstrated a variation in the CN and C_2 band with the major peaks at 388.4 nm and 516.5 nm, and a significant variation in the intensities was observed. The spectral data were standardized by subtracting the mean and was divided by the standard deviation before performing the PCA. The blue square symbols in figure 7.3 correspond to ammonium nitrate, the orange plus symbol to picric acid, the green triangle symbol to DNT, and the red diamond symbol to filter paper. The ellipses are just a guide to the eye in discriminating the clusters.

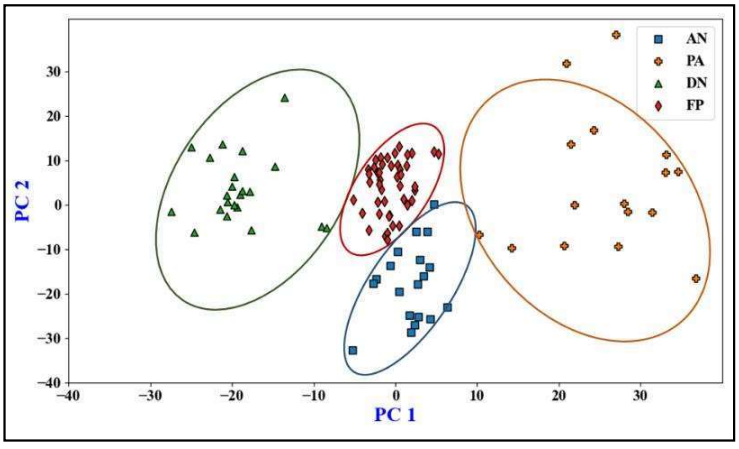

Figure 7.3 The principal component analysis on the Fs-LIBS spectra of picric acid (PA) on filter paper in blue plus symbols, plane filter paper (FP) in green triangles, DNT on filter paper (DN) in orange circles, and ammonium nitrate on filter paper (AN) in red stars.

7.2.4 Conclusions

The three molecules of ammonium nitrate, DNT, and picric acid in traces were successfully classified from the fs-LIBS spectra. The spread in the clusters could be due to the varying interaction between the laser pulse and deformed filter paper surface after the solution is drop cast. The similarities between the spectra of the filter paper to that of the molecules are challenging, and the study can be extended with the glass fabrics loaded with nanoparticles for superior identification and classification of the explosive molecules in traces.

7.3 Future scope

7.1.1 Image stabilization in standoff LIBS

Even though beam steering in the standoff studies resulted in a good SNR, the image formation by the telescope was moving as the image was from the scanning beam. This moving image leads to the fluctuation in the LIBS signal. A fisheye lens was used to focus the image into the optical fiber to reduce the fluctuations. Synchronizing the detector with the moving image could be a better option to evade the LIBS spectra fluctuations completely. The clone slot in the CNC shield V3 could be particularly useful in addressing this problem. Image stabilization in this setup can be especially useful in improving the reliability of the LIBS spectra in standoff classification and quantification of the target samples.

7.1.2 Standoff double pulse LIBS

Further, the SNR in the standoff LIBS could be improved with the double pulse configuration. The configuration with two polarizers proven more efficient could be beneficial compared to other cases and, when combined with the automated beam steering instrumentation and better machine learning algorithms, lead to a real-time standoff LIBS setup. The effect of the delay between the two pulses could be a fascinating investigation.

7.1.3 Glass fiber filter paper and nanoparticle LIBS

The CN and C_2 were observed from the fs-LIBS studies of the cellulose-made filter paper, and PCA was used to classify the LIBS spectra of filter paper drop cast with explosive traces. CN and C_2 bands are avoided by using the substrate glass fiber filter instead of cellulose. This simple adaptation could make the classification more reliable. In the case

of NE-LIBS of the aluminum sheet, time-resolved studies could lead to a better understanding of the difference in the enhancement factor for Al atomic and AlO molecular peaks.

7.1.4 Grazing incidence

The experimental configuration can be improved with a cylindrical lens to collect the plasma emissions along the longitudinal direction. This could enable us to extend the studies to compounds other than graphene. Further, the use of nanoparticles for better interaction and signal enhancement could be productive.

7.1.5 Single deep learning model for the quantification from LIBS spectra

A single model can be trained with the LIBS data of well-calibrated all possible compositions of metal alloys to estimate the elemental composition of any metal alloy from corresponding LIBS spectra. A deep learning model can be trained with massive data for predicting compositions from the LIBS spectra.

7.1.6 Extension of the classification of the compounds based on the color CCD images to the standoff configuration

The images of plasma emissions from the standoff distances can be used to classify simple targets like metal and alloys. Other multispectral images of plasma emissions combined with machine learning algorithms could improve classification studies. This method, with high potential in reducing the instrumentation, can be deployed in monitoring simple compounds in real time.

References

[1] J.L. Gottfried, F.C. De Lucia, C.A. Munson, A.W. Miziolek, Strategies for residue explosives detection using laser-induced breakdown spectroscopy, J. Anal. At. Spectrom. 23 (2008) 205–216. doi:10.1039/b703891g.

[2] F.C. De Lucia, J.L. Gottfried, C.A. Munson, A.W. Miziolek, Multivariate analysis of standoff laser-induced breakdown spectroscopy spectra for classification of explosive-containing residues, Appl. Opt. 47 (2008). doi:10.1364/AO.47.00G112.

[3] A.K. Shaik, N.R. Epuru, H. Syed, C. Byram, V.R. Soma, Femtosecond laser induced breakdown spectroscopy based standoff detection of explosives and discrimination using principal component analysis, Opt. Express. 26 (2018) 8069. doi:10.1364/oe.26.008069.

[4] C. López-Moreno, S. Palanco, J.J. Laserna, F. DeLucia, A.W. Miziolek, J. Rose, R.A. Walters, A.I. Whitehouse, Test of a stand-off laser-induced breakdown spectroscopy sensor for the detection of explosive residues on solid surfaces, J. Anal. At. Spectrom. 21 (2006) 55–60. doi:10.1039/b508055j.

[5] A. De Giacomo, C. Koral, G. Valenza, R. Gaudiuso, M. Dellaglio, Nanoparticle Enhanced Laser-Induced Breakdown Spectroscopy for Microdrop Analysis at subppm Level, Anal. Chem. 88 (2016) 5251–5257. doi:10.1021/acs.analchem.6b00324.

[6] N. Linga Murthy, S.V. Rao, Nanoparticle Enhanced Laser Induced Breakdown Spectroscopy of Liquids, Springer Singapore, 2021. doi:10.1007/978-981-15-9259-1_105.

[7] S. Abdul Kalam, N. Linga Murthy, J. Rama Krishna, V.V.S.S. Srikanth, S. Venugopal Rao, Nanoparticle enhanced laser induced breakdown spectroscopy with femtosecond pulses, in: Opt. InfoBase Conf. Pap., 2014. doi:10.1364/PHOTONICS.2016.Th3A.89.

[8] Choi D, Gong Y, Nam SH, Han SH, Yoo J, Lee Y. Laser-induced breakdown spectroscopy (LIBS) analysis of calcium ions dissolved in water using filter paper substrates: an ideal internal standard for precision improvement. Appl Spectrosc. 2014;68(2):198-212. doi: 10.1366/13-07163. PMID: 24480276.

Code used for the pca of the images of plasma emissions.

```
from sklearn import svm
from time import time
import os
from sklearn.decomposition import PCA
import numpy as np
import matplotlib.image as impg


path= path to the images from plasma emissions
pics=os.chdir(path)
piclist=os.listdir(pics)
targets=[]
for i in range(len(piclist)):
#    if piclist[i][:4]=='BRON':
       targets.append((piclist[i][:4]))
t0=time()

from scipy import signal
Cxy=[]
for i in range(0,len(piclist)):
   img =impg.imread(piclist[i])
   x=(img[0:200,150:400,2])
   y=(img[200:400,400:650,2])
   x=np.array(x).ravel()
   y=np.array(y).ravel()
   Cxy.append(signal.coherence(x,y)[1])
print("done hist in %0.5fs" % (time() - t0))
Cxy=np.nan_to_num(Cxy)
t0=time()
pca=PCA(3)
clfp=pca.fit_transform(Cxy)

from sklearn.model_selection import train_test_split
X_train, X_test, y_train, y_test = train_test_split(
  clfp,targets , test_size=0.4, random_state=0)
#targets=np.array(targets)
clf=svm.SVC(gamma=0.0001,C=100)
#x,y=clfp[:-1,:],targets[:-1]
clf.fit(X_train,y_train)
clf.score(X_test, y_test)
```

Code used for the two-dimensional correalation analysis

```
import numpy as np
import matplotlib.pyplot as plt
import os

plt.rcParams["font.family"] = "Times New Roman"

path= path to the folder containing data
pics=os.chdir(path)
piclist=sorted(os.listdir(pics))
#%%
import scipy.signal
import time
dataall=[]
wavelength=np.genfromtxt(piclist[2],skip_header=10,skip_footer=19000,usecols=0)
#np.savetxt("wavelength.csv",wavelength,delimiter=',')
#%%
plt.rcParams["font.family"] = "Times New Roman"
plt.rcParams["font.size"]=10
plt.rcParams["font.weight"]="bold"
csfont = {'fontname':'Times New Roman','weight':'bold'}
import seaborn as sns
start_time=time.time()
#from scipy.signal import savgol_filter
#from scipy import signal
#b, a = signal.butter(8, 0.325)
for k in range (0,1):
   file=np.genfromtxt(piclist[k],skip_header=10,skip_footer=19000)
   A=[]
#    A.append(file)

   for i in range(1,6):
      A.append(file[:,i])
   A=np.array(A)
np.round(wavelength[::40],2),fontsize=15,rotation=45,fontweight='bold')
#
plt.yticks(range(0,len(wavelength),40),np.round(wavelength[::40],2),fontsize=15,fontweight='bold')
#     plt.imshow(asy, cmap="RdBu_r",origin="lower")
#     plt.xlabel("Wavelength[nm]",csfont,fontsize=20,fontweight='bold')
#     plt.ylabel("Wavelength[nm]",csfont,fontsize=20,fontweight='bold')
# #    plt.title("2D-correlation of time varying Copper peaks")
#     plt.savefig("/home/linga009/Documents/bim/{}.{}".format("asyn"+str(k),"png"),
bbox_inches='tight')
# #           plt.show()
#     plt.close()
#     print(k)
   # X,Y=np.meshgrid(wavelength,wavelength)
   # fig = plt.figure()
   # ax = fig.gca(projection='3d')
```

```
   # surf = ax.plot_surface(X, Y, asy, rstride=1, cstride=1, cmap="RdBu_r", linewidth=0,
antialiased=False)
   # ax.w_xaxis.set_pane_color((1.0,1.0,1.0,0.1))
   # ax.w_yaxis.set_pane_color((1.0,0.0,1.0,0.1))
   # ax.set_xlabel\
   Ar=np.average(A,axis=0)
# import pandas as pd
# df=pd.DataFrame(A)
#df.index=wavelength

   matrix=A.sum(axis=0).reshape(A.shape[1],1)
   Ad=A
    #np.transpose((1/A.shape[0])*matrix*np.ones(A.shape[0]))
   syn=(1/A.shape[0])*np.dot(np.transpose(Ad),Ad)
   #np.savetxt("syn_Au20_Ag80.csv", syn, delimiter=",")
    #dataall.append(syn.diagonal())
    #plt.plot(wavelength,diag)
 # scipy.signal.medfilt2d(syn,kernel_size=31)

#plotting in surface_plot 3D

   # X,Y=np.meshgrid(wavelength,wavelength)
   # fig = plt.figure()
   # ax = fig.gca(projection='3d')
   # surf = ax.plot_surface(X, Y, syn, rstride=1, cstride=1, cmap="RdBu_r", linewidth=0,
antialiased=False)
   # ax.w_xaxis.set_pane_color((1.0,1.0,1.0,0.1))
   # ax.w_yaxis.set_pane_color((1.0,0.0,1.0,0.1))
   # ax.set_xlabel('Wavelength [nm]',csfont, fontsize=15)
   # ax.set_ylabel('Wavelength [nm]',csfont, fontsize=15)
   # ax.set_zlabel('Intensity (arb.u)',csfont, fontsize=15)
   # plt.show()
##%%
# np.savetxt('bim.asc',syn,delimiter='')

# ax=sns.kdeplot(data=sy)
# #square=True, xticklabels="auto",yticklabels="auto",cmap="Spectral",cbar=False)
# ax.invert_yaxis()
# ax.figure.savefig('output_figure4.png',figsize=(50,50),dpi=2000,bbox_inches='tight')
#    plt.figure()
#    syn=sni.zoom(syn,3)

   dpi = 100 # Arbitrary. The number of pixels in the image will always be identical

   # height, width = np.array(syn.shape, dtype=float) / dpi
   # plt.ioff()
   # fig = plt.figure(figsize=(width, height),dpi=dpi)
   plt.xticks(range(0,len(wavelength),160),
np.round(wavelength[::160],2),fontsize=15,rotation=45,fontweight='bold')

plt.yticks(range(0,len(wavelength),160),np.round(wavelength[::160],2),fontsize=15,fontweight='bol
d')
```

```
    plt.xlabel("Wavelength[nm]",csfont,fontsize=20,fontweight='bold')
    plt.ylabel("Wavelength[nm]",csfont,fontsize=20,fontweight='bold')
#    plt.axis("off")
#    sns.heatmap(data=syn,cmap="magma",cbar=False)
    plt.contourf(syn,30,cmap="RdBu_r",origin="lower")
    plt.show()
#     #plt.colorbar()
#   #  "RdBu_r"
 #   plt.title("2D-correlation of time varying Copper peaks")
#plt.grid(True)
    #
plt.savefig("/home/linga009/Documents/bim/final/{}.{}".format("rbr520_50"+piclist[k][:4]+str(k),"
png"), bbox_inches='tight',dpi=dpi)
    # plt.close()
    # time.sleep(1)
#%%
#    plt.show()
# ax.set_xticks(wavelength
# ax.set_yticks(wavelength)
# ax.set_xticklabels(wavelength,rotation=90)
# ax.set_yticklabels(wavelength)
    print(time.time()-start_time)

    N= np.zeros((A.shape[0],A.shape[0]))
    for i in range(1,(A.shape[0])):
        for j in range(i):
            N[j][i]=1/(np.pi*(j-i))
            N[i][j]=-N[j][i]
    asy=(1/A.shape[0])*np.dot(np.dot(np.transpose(Ad),N),Ad)
    np.savetxt("asyn_Au20_Ag80.csv", asy, delimiter=",")
            # ax=sns.heatmap(asy,square=True,
xticklabels="auto",yticklabels="auto",cmap="Spectral",cbar=False)
            # ax.invert_yaxis()
#     fig= plt.figure(figsize=(width, height),dpi=dpi)
#     plt.xticks(range(0,len(wavelength),40),
np.round(wavelength[::40],2),fontsize=15,rotation=45,fontweight='bold')
#
plt.yticks(range(0,len(wavelength),40),np.round(wavelength[::40],2),fontsize=15,fontweight='bold')
```

Code used for the diagonal extraction in the two-dimensional correlation analysis

```
import numpy as np
import matplotlib.pyplot as plt
import os


path="path to the folder containing data"
pics=os.chdir(path)
piclist=sorted(os.listdir(pics))
#%%
```

```
import time
wavelength=np.genfromtxt(piclist[0],skip_header=1000,skip_footer=1500,usecols=0)
#%%
from sklearn.preprocessing import RobustScaler,MinMaxScaler,Normalizer,StandardScaler
from scipy.signal import savgol_filter
norm1=StandardScaler()
norm=MinMaxScaler(feature_range=(0, 100))
A=[]
for k in range (0,5):

   A.append(np.genfromtxt(piclist[k],skip_header=1000,skip_footer=1500,usecols=(1)))
A=np.array(A)

matrix=A.sum(axis=0).reshape(A.shape[1],1)
Ad=np.transpose((1/A.shape[0])*matrix*np.ones(A.shape[0]))
with open('/home/linga009/Documents/ssecond paper/PVC.txt', 'a+') as data:
np.asarray([np.concatenate((np.diagonal((1/A.shape[0])*np.dot(np.transpose(Ad),Ad)),
np.diagonal((1/A.shape[0])*np.dot(np.transpose(Ad),Ad),offset=100)))]),delimiter=',',newline='\n')

np.savetxt(data,list(zip(wavelength,(np.diagonal((1/A.shape[0])*np.dot(np.transpose(Ad),Ad))))))
print(k)
```

Code used for PCA on the diagonal of the two-dimensional correlation analysis

```
from sklearn.preprocessing import StandardScaler,RobustScaler
from sklearn.preprocessing import Normalizer
import numpy as np
import matplotlib.pyplot as plt
from mpl_toolkits.mplot3d import axes3d
import os
from sklearn.decomposition import PCA

plt.rcParams["font.family"] = "Times New Roman"
plt.rcParams["font.size"] = 15
plt.rcParams["font.weight"]="bold"
diag1= path to the folder containing diagonal data
path1= path to the folder containing LIBS spectra
pics=os.chdir(path1)
piclist=sorted(os.listdir(pics))
#%%
import scipy.signal
import time
from sklearn.preprocessing import MinMaxScaler
A=[]
for i in range(0,len(piclist)):
   A.append(np.genfromtxt(piclist[i],skip_header=2000,skip_footer=3500,usecols=1))
#data1=np.genfromtxt(piclist[1],skip_header=1000,skip_footer=500,usecols=1)
#%%
import pandas
```

```
df0 = pandas.read_csv(diag1,header=None)
#df1=pandas.read_csv(diag2,header=None)
#df2=pandas.concat([df0,df1],axis=1)
#%%
green=df0.drop([77])
#.drop([77])
#.iloc[:,1000:6000].drop([77])

#%%
norm=Normalizer()
green=norm.fit_transform(green)
pca=PCA(5)

clf=pca.fit_transform(np.array(green))
#loadings=np.cumsum(clf.explained_variance_ratio_)
plt.figure(1)
plt.plot([1,2,3,4,5],np.cumsum(pca.explained_variance_ratio_), '-o', markersize=12,color='black')
plt.xlim(0.5, 6.0)
plt.ylim(0.3, 1.0)
plt.xlabel('Number of components',fontsize=20,fontweight="bold")
plt.xticks([1,2,3,4,5],weight="bold")
plt.ylabel('Cumulative explained variance',fontsize=20,fontweight="bold")
plt.yticks(weight="bold")
plt.grid(axis='both')
plt.figure(2)
features = range(5)
plt.bar(features, pca.explained_variance_ratio_, color='blue')
plt.xlim(-1.0, 5.0)
plt.ylim(0.0, 1.0)
plt.xlabel('Component number',fontsize=20,fontweight="bold")
plt.ylabel('Variance',fontsize=20,fontweight="bold")
plt.yticks(weight="bold")
plt.xticks([0,1,2,3,4],[1,2,3,4,5],weight = 'bold')
plt.xticks(features)
```

Code used for the shallow neural network model

```
from numpy import asarray
from sklearn.datasets import make_multilabel_classification
from keras.models import Sequential
from keras.layers import Dense,Dropout
from keras.optimizers import SGD
from sklearn.preprocessing import QuantileTransformer
from keras.utils import to_categorical
from sklearn.model_selection import train_test_split
#%%
import os
import pandas as pd
import numpy as np
path= path to the folder containing the time resolved LIBS data
data_tmp=os.chdir(path)
```

```
data=sorted(os.listdir(data_tmp))

train = pd.read_csv(path to the training data)

############################################################
header=1000
footer=3000

X=[]
y=[]
from tqdm import tqdm
for i in tqdm(range(0,len(data))):

    X.append(np.genfromtxt(data[i],skip_header=header,skip_footer=footer,usecols=(1)))
    y.append(np.array(train.drop([ 'Composition'],axis=1).iloc[i]))
    X.append(np.genfromtxt(data[i],skip_header=header,skip_footer=footer,usecols=(2)))
    y.append(np.array(train.drop([ 'Composition'],axis=1).iloc[i]))
    X.append(np.genfromtxt(data[i],skip_header=header,skip_footer=footer,usecols=(3)))
    y.append(np.array(train.drop([ 'Composition'],axis=1).iloc[i]))
    # X.append(np.genfromtxt(data[i],skip_header=1500,skip_footer=4000,usecols=(4)))
    # y.append(np.array(train.drop(['Id', 'Composition'],axis=1).iloc[i]))
    # X.append(np.genfromtxt(data[i],skip_header=1500,skip_footer=4000,usecols=(5)))
    # y.append(np.array(train.drop(['Id', 'Composition'],axis=1).iloc[i]))
    # # # X.append(np.genfromtxt(data[i],skip_header=1500,skip_footer=4000,usecols=(6)))
    # y.append(np.array(train.drop(['Id', 'Composition'],axis=1).iloc[i]))
    # X.append(np.genfromtxt(data[i],skip_header=1500,skip_footer=4000,usecols=(7)))
    # y.append(np.array(train.drop(['Id', 'Composition'],axis=1).iloc[i]))
    # X.append(np.genfromtxt(data[i],skip_header=1500,skip_footer=4000,usecols=(8)))
    # y.append(np.array(train.drop(['Id', 'Composition'],axis=1).iloc[i]))
    # X.append(np.genfromtxt(data[i],skip_header=1500,skip_footer=4000,usecols=(9)))
    # y.append(np.array(train.drop(['Id', 'Composition'],axis=1).iloc[i]))
    # X.append(np.genfromtxt(data[i],skip_header=1500,skip_footer=4000,usecols=(10)))
    # y.append(np.array(train.drop(['Id', 'Composition'],axis=1).iloc[i]))


#%%
from sklearn.preprocessing import MinMaxScaler,StandardScaler,Normalizer,MaxAbsScaler
X1=np.array(X)
y1=np.array(y)

#norm1=MaxAbsScaler().fit(np.float64(X1))
norm=Normalizer().fit(np.float64(X1))
from sklearn.decomposition import PCA
clf1=norm.transform(X1)
pca=PCA(len(X1))
pc=pca.fit(clf1)
clf=pc.transform(clf1)
#print(np.cumsum(pca.explained_variance_ratio_)[-1])

#####################################################################
import random as rn
import tensorflow as tf
```

```
tf.random.set_seed(43)
np.random.seed(37)
rn.seed(1254)
import keras
initializer = tf.keras.initializers.Ones()
from keras.regularizers import l1_l2
from keras.regularizers import l1
from keras.regularizers import l2
from keras.callbacks import EarlyStopping
callback = tf.keras.callbacks.EarlyStopping(monitor='val_loss',
patience=8,mode="min",restore_best_weights=True)
X_train, X_test, y_train, y_test = train_test_split(clf, y1,random_state=41,test_size=0.1)
def create_model():
    # initial_learning_rate =0.001
    # lr_schedule = keras.optimizers.schedules.ExponentialDecay(initial_learning_rate,
    # decay_steps=1000,decay_rate=0.96,  staircase=False)
    opt1 = keras.optimizers.RMSprop(learning_rate=0.005,momentum=0.9,epsilon=1e-
9,centered=False)
    # sgd = SGD(learning_rate=lr_schedule, momentum=0.9, nesterov=True)
    # opt1 = keras.optimizers.RMSprop(learning_rate=0.0045,momentum=0.9,epsilon=1e-
8,centered=False)
    opt2=keras.optimizers.Adamax(learning_rate=0.005, beta_1=0.6, beta_2=0.4, epsilon=1e-09,
name="Adamax")
    # # create model

    model = Sequential()
    model.add(Dense(1200,input_dim=X_train.shape[1], activation='relu',
                    kernel_regularizer=l2(0.0001),
                    kernel_initializer=initializer))
    model.add(Dropout(0.5))
    # model.add(Dense(900,activation='relu',kernel_regularizer=l2(0.001)))
    # model.add(Dropout(0.5))
   # model.add(Dense(80,activation='relu'))
    #                #,kernel_regularizer=l2(0.01)))
    # model.add(Dropout(0.3))
#    model.add(Dense(10,activation='relu',kernel_regularizer=l2(0.01)))
    # model.add(Dropout(0.3))
    # model.add(Dense(2000,activation='relu',kernel_regularizer=l2(0.001)))
    # model.add(Dropout(0.1))

    model.add(Dense(2,activation='linear'))
    model.compile( optimizer=opt1,loss
=('mean_absolute_error','mean_absolute_error'),loss_weights=(1,1),metrics
=["mean_absolute_error"])
    return model
model = create_model()
model.summary()
#%%
from sklearn.metrics import mean_absolute_error,make_scorer
from sklearn.metrics import mean_absolute_error as MAE
#from sklearn.metrics import mean_absolute_percentage_error as MAPE
from sklearn.metrics import r2_score
```

```
from sklearn.metrics import mean_squared_error as MSE
from sklearn.model_selection import cross_val_score
from sklearn.model_selection import RepeatedStratifiedKFold
# cv = RepeatedStratifiedKFold(n_splits=6, n_repeats=3, random_state=1)
# # evaluate model
# scoring_function=make_scorer(mean_absolute_error,greater_is_better=False)
# scores = cross_val_score(model, X_train, y_train[:,0], scoring=scoring_function, cv=cv,
n_jobs=2)
# report result
# print('Mean Accuracy: %.3f (%.3f)' % (np.mean(scores), np.std(scores)))
history=model.fit(X_train, y_train,
validation_split=0.1,shuffle=False,epochs=500,batch_size=40,callbacks=[callback])
res=model.evaluate(X_test, y_test, verbose=0)
print('error in Au= %.3f' % res[0],'error in Ag=%.3f' % res[1])
#model.save(args["model"], save_format="h5")
#%%
from matplotlib import pyplot as plt
pathout="/home/linga009/Documents/ssecond paper/bimna/Au3g"
outlist=sorted(os.listdir(os.chdir(pathout)))

out1=[]

for j in range(0,len(outlist)):
   out1.append(np.genfromtxt(outlist[j],skip_header=header,skip_footer=footer,usecols=1))

out2=norm.transform(out1)
#out3=norm2.transform(out1)
out4=pc.transform(out2)
seven_three=model.predict(out4)
print(seven_three)

#print(model.predict(X_test))
true=list(zip([30]*19,[70]*19))
y_pred = model.predict(X_test)
print(y_pred-y_test)
print("R^2",r2_score(y_test, y_pred,multioutput='raw_values'))
print("RMSE",np.sqrt(MSE(y_test, y_pred,multioutput='raw_values')))
print("mean_absolute_error",MAE(y_test,y_pred,multioutput='raw_values'))
print("RMSE",np.sqrt(MSE(true,seven_three,multioutput='raw_values')))
print("mean_absolute_error",MAE(true,seven_three,multioutput='raw_values'))

#%%
print("STD of Au error",np.std(y_pred[:,0]-y_test[:,0]))
print("STD of Ag error",np.std(y_pred[:,1]-y_test[:,1]))
print(abs(np.mean(seven_three[:,0]-30)/30)*100,abs(np.mean(seven_three[:,1]-70)/70)*100)
print(np.mean(seven_three[:,0]),np.mean(seven_three[:,1]))
print(np.std(seven_three[:,0]),np.std(seven_three[:,1]))
# # for i in range(len(y_test)):
#     print((abs(y_pred[i]-y_test[i])/y_test[i])*100)
plt.rcParams["font.family"] = "Times New Roman"
plt.rcParams["font.size"]=25
plt.rcParams["font.weight"]="bold"
```

```
fig=plt.figure(figsize=(8,6),constrained_layout=True)
ax = fig.gca()
for axis in ['top','bottom','left','right']:
   ax.spines[axis].set_linewidth(2)
error1 = abs(y_pred[:,0]-y_test[:,0])
error2 = abs(y_pred[:,1]-y_test[:,1])
plt.hist(error1,bins=100, alpha=0.7, label="Au",color="red")
plt.hist(error2,bins=100,alpha=0.7, label="Ag",color='green')
plt.xlabel(' % Error in prediction',fontsize=30,fontweight="bold")
plt.ylabel('Count',fontsize=30,fontweight="bold")
plt.legend(loc='best')
plt.title("% Error in predicion on test set",fontsize=35,fontweight="bold")
fig=plt.figure(figsize=(8,6),constrained_layout=True)
ax = fig.gca()
for axis in ['top','bottom','left','right']:
   ax.spines[axis].set_linewidth(2)
################
plt.hist(abs((seven_three[:,0]-30)/30)*100,bins=100, alpha=0.7, label="Au",color='red')
plt.hist(abs((seven_three[:,1]-70)/70)*100, bins=100, alpha=0.7, label="Ag",color='green')
plt.xlabel('% Error in prediction ',fontsize=30,fontweight="bold")
plt.ylabel('Count',fontsize=30,fontweight="bold")
plt.legend(loc='best')
plt.title("% Error in Prediction on Au30-Ag70",fontsize=35,fontweight="bold")
fig=plt.figure(figsize=(8,6),constrained_layout=True)

plt.axes(aspect='equal',alpha=0.8)
ax = fig.gca()
for axis in ['top','bottom','left','right']:
   ax.spines[axis].set_linewidth(2)
plt.scatter(y_test[:,0], y_pred[:,0], s=50,alpha=0.7, label="Au",color='red')
plt.scatter(y_test[:,1],y_pred[:,1], s=50,alpha=0.7, label="Ag",color='green')
plt.xlabel('True Values [% weight]',fontsize=25,fontweight="bold")
plt.ylabel('Predicted Values [% weight]',fontsize=25,fontweight="bold")
plt.title('True Vs Predicted values',fontsize=30,fontweight="bold")
plt.xticks(np.arange(0, 100, step=10))
plt.yticks(np.arange(0, 100, step=10))
lims = [-10, 100]
plt.xlim(lims)
plt.ylim(lims)
plt.plot(lims, lims)
plt.grid(True, color = "grey", linewidth = "0.5", linestyle = "-.")
plt.legend()


#%%
from matplotlib import pyplot as plt
plt.rcParams["font.family"] = "Times New Roman"
plt.rcParams["font.size"]=25
plt.rcParams["font.weight"]="bold"
fig=plt.figure(figsize=(8,6),constrained_layout=True)
ax = fig.gca()
for axis in ['top','bottom','left','right']:
```

```
    ax.spines[axis].set_linewidth(2)
plt.plot(history.history['mean_absolute_error'],linewidth=3)
plt.plot(history.history['val_mean_absolute_error'],linewidth=3)
plt.title('Training and Validation error',fontsize=35,fontweight="bold")
plt.ylabel('MAE',fontsize=30,fontweight="bold")
plt.xlabel('Epoch',fontsize=30,fontweight="bold")
plt.xticks(np.arange(0, 35, step=5))
plt.legend(['Training error', 'Validation error'], loc='upper right')
plt.grid(True, color = "grey", linewidth = "1", linestyle = "-.")
plt.show()
fig=plt.figure(figsize=(8,6),constrained_layout=True)
ax = fig.gca()
for axis in ['top','bottom','left','right']:
    ax.spines[axis].set_linewidth(2)
plt.plot(history.history['loss'],linewidth=3)
plt.plot(history.history['val_loss'],linewidth=3)
plt.title('Training and validation loss',fontsize=35,fontweight="bold")
plt.ylabel('Loss',fontsize=30,fontweight="bold")
plt.xlabel('Epoch',fontsize=30,fontweight="bold")
plt.xticks(np.arange(0, 35, step=5))
plt.legend(['Training loss', 'Validation loss'],loc="upper right")
plt.grid(True, color = "grey", linewidth = "1", linestyle = "-.")
plt.show()
```

Appendix

Publications related to the thesis

1. **Narlagiri, L. M**. & Rao, S. V. (2020). Identification of metals and alloys using color CCD images of laser-induced breakdown emissions coupled with machine learning. ***Appl. Phys. B***, *126*, article # 113. DOI: https://doi.org/10.1007/s00340-020-07469-6
2. **Narlagiri, Linga Murthy**, and Venugopal Rao Soma. "Improving the signal-to-noise ratio of atomic transitions in LIBS using two-dimensional correlation analysis**."** ***OSA Continuum*** 4.9 (2021): 2423-2441. https://doi.org/10.1364/OSAC.426995
3. **Narlagiri, Lingamurthy**, and Venugopal Rao Soma. "Simultaneous quantification of Au and Ag composition from Au–Ag bi-metallic LIBS spectra combined with shallow neural network model for multi-output regression." ***Appl. Phys. B*** 127.9 (2021): 1-11. https://doi.org/10.1007/s00340-021-07681-y
4. **L.M. Narlagiri**, C. Byram, S.K. Satani, V.R. Soma, Laser beam steering automation with an Arduino-based C.N.C. shield for standoff femtosecond filament-induced breakdown spectroscopic studies, ***Appl. Opt.*** 61 (2022) 4947–4955. doi:10.1364/AO.453824.
5. **L.M. Narlagiri,** M.S.S. Bharati, R. Beeram, D. Banerjee, V.R. Soma, Recent trends in laser-based standoff detection of hazardous molecules, ***TrAC - Trends Anal. Chem.*** 153 (2022) 116645. doi:10.1016/j.trac.2022.116645.
6. Kalam, S. A., **Murthy, N. L.,** Mathi, P., Kommu, N., Singh, A. K., & Rao, S. V. (2017). Correlation of molecular, atomic emissions with detonation parameters in femtosecond and nanosecond LIBS plasma of high energy materials. ***J. Anal. Atom. Spectrom.***, *32*(8), 1535-1546. https://doi.org/10.1039/C7JA00136C.

Conference proceedings

1. **Murthy, N. L.,** Kalam, S. A., & Rao, S. V. (2019, December). Stand-off Femtosecond Laser Induced Breakdown Spectroscopy of Metals, Soil, Plastics and Classification Studies. In *2019 Workshop on Recent Advances in Photonics* ***(WRAP)*** **(pp. 1-3). IEEE.** D.O.I:10.1109/WRAP47485.2019.9013674
2. **Linga Murthy N.,** Rao S.V. (2021) Nanoparticle Enhanced Laser Induced Breakdown Spectroscopy of Liquids. In: Singh K., Gupta A.K., Khare S., Dixit N., Pant K. (eds) ICOL-2019. Springer Proceedings in Physics, vol 258. Springer, Singapore. https://doi.org/10.1007/978-981-15-9259-1_105
3. **L. M. Narlagiri** and V. R. Soma, "Plasma Temperature Evolution with Varying Compositions in an Alloy Using Laser Induced Breakdown Spectroscopy," in *Frontiers in Optics + Laser Science 2021*, C. Mazzali, T. (T.-C.) Poon, R. Averitt, and R. Kaindl, eds., Technical Digest Series (Optical Society of America, 2021), paper JW7A.29.
4. Kalam, S. A., **Murthy, N. L**., Krishna, J. R., Srikanth, V. V. S. S., & Rao, S. V. (2016, December). Nanoparticle enhanced laser induced breakdown spectroscopy with femtosecond pulses. In *International Conference on Fibre Optics and Photonics* (pp. Th3A-89). Optical Society of America. DOI:10.1364/PHOTONICS.2016.Th3A.89
5. **L. M. Narlagiri** and V. R. Soma, "Plasma Temperature Evolution with Varying Compositions in an Alloy Using Laser Induced Breakdown Spectroscopy," in *Frontiers in Optics + Laser Science 2021*, C. Mazzali, T. (T.-C.) Poon, R. Averitt, and R. Kaindl, eds., Technical Digest Series (Optica Publishing Group, 2021), paper JW7A.29.

Book chapters

1. **Linga Murthy Narlagiri,** Venugopal Rao Soma,* "Nanoparticle Enhanced LIBS for Sensing Applications," Laser-Induced Breakdown Spectroscopy (LIBS): Concepts, Instrumentation, Data Analysis and Applications, Eds: Dr. Vivek K. Singh, Prof. Y. Deguchi, Dr. Zhenzhen Wang, and Dr. Durgesh K. Tripathi, John Wiley & Sons, **In Press, 2022.**
2. **Linga Murthy Narlagiri,** Venugopal Rao Soma,* "Recent developments in standoff laser induced breakdown spectroscopy," Laser-Induced Breakdown Spectroscopy (LIBS): Concepts, Instrumentation, Data Analysis and Applications, Eds: Dr. Vivek K. Singh, Prof. Y. Deguchi, Dr. Zhenzhen Wang, and Dr. Durgesh K. Tripathi, John Wiley & Sons, **In Press, 2022.**

Achievements

1. Received **Best Poster Award** for the poster titled" **Identification of Metals and Metal Alloys from the Femtosecond Laser Induced Plasma Emissions using Machine Learning"** in DAE-BRNS National Laser Symposium **(NLS-28)** 2020 held at Vellore Institute of Technology (VIT), Chennai from 08-11 January, 2020.
2. **Seventh place in Euro-Mediterranean LIBS** conference competition results published in "J. Vrábel, E. Képeš, L. Duponchel, V. Motto-Ros, C. Fabre, S. Connemann, F. Schreckenberg, P. Prasse, D. Riebe, R. Junjuri, M. K. Gundawar, X. Tan, P. Pořízka, and J. Kaiser, "Classification of challenging Laser-Induced Breakdown Spectroscopy soil sample data - EMSLIBS contest," Spectrochim. Acta - Part B At. Spectrosc. 169, 105872 (2020)."

Workshops Attended

1. Attended the **DST-SERB School on Ultrahigh Intensity Laser Produced Plasmas: Physics and Application**s (Jan 7-25 2019) Laser Plasma Division RRCAT, Indore -452013 MP India.
2. Attended the GIAN **course on Attosecond Photonics**, from 07 - 11 Nov.2016 at IIT – Madras.
3. Attended "**International conference on python for education and scientific computing**" Annual SciPy conference India 2019, held on 29 and 30 November 2019 at I.I.T. Bombay.
4. Attended the GIAN one-week short term course on "**Vibrational Spectroscopy and the Molecular Vibrations**" (Sponsored by Ministry of Human Resource Development (MHRD), Under the Scheme ' GIAN') (15 January 2018 to 19 January 2018)

Prof. SOMA VENUGOPAL RAO
F.N.A.Sc., F.Inst.P, FRSC
ACRHEM
DRDO Industry Academic-Centre of Excellence
(DIA-COE)
University of Hyderabad
Hyderabad-500046. Telangana, INDIA.

Machine Learning and Improved Experimental Techniques for Near-field, Standoff LIBS Studies of Hazardous Materials

by Linga Murthy Narlagiri

Submission date: 01-Dec-2022 03:19PM (UTC+0530)
Submission ID: 1968149987
File name: for_Near-field,_Standoff_LIBS_Studies_of_Hazardous_Materials.pdf (7.85M)
Word count: 31284
Character count: 164936

Machine Learning and Improved Experimental Techniques for Near-field, Standoff LIBS Studies of Hazardous Materials

ORIGINALITY REPORT

16%	8%	14%	1%
SIMILARITY INDEX	INTERNET SOURCES	PUBLICATIONS	STUDENT PAPERS

PRIMARY SOURCES

1	Lingamurthy Narlagiri, Venugopal Rao Soma. "Simultaneous quantification of Au and Ag composition from Au–Ag bi-metallic LIBS spectra combined with shallow neural network model for multi-output regression", Applied Physics B, 2021 Publication	3%
2	arxiv.org Internet Source	3%
3	Linga Murthy Narla, S. Venugopal Rao. "Identification of metals and alloys using color CCD images of laser-induced breakdown emissions coupled with machine learning", Applied Physics B, 2020 Publication	2%
4	www.acrhem.org Internet Source	1%
5	N Linga Murthy, M S S Bharathi, S Venugopal Rao. "Nanoparticle enhanced femtosecond laser induced breakdown spectroscopy of	1%

S Venugopal Rao 16/12/2021
Prof. SOMA VENUGOPAL RAO
F.N.A.Sc., F.Inst.P, FRSC
ACRHEM
DRDO Industry Academic-Centre of Excellence
(DIA-COE)
University of Hyderabad
Hyderabad-500046. Telangana, INDIA.

1-8 publications are 8 students own work. After removing them the similarity is <10%. S Venugopal Rao 16/12/2021

aluminum sheet coated with gold nanoparticle embedded nanofibers", Journal of Physics: Conference Series, 2022
Publication

6	dspace.uohyd.ac.in Internet Source	1%
7	Linga Murthy Narlagiri, Venugopal Rao Soma. "Improving the signal-to-noise ratio of atomic transitions in LIBS using two-dimensional correlation analysis", OSA Continuum, 2021 Publication	1%
8	Linga Murthy Narlagiri, Venugopal Rao Soma. "Plasma Temperature Evolution with Varying Compositions in an Alloy Using Laser Induced Breakdown Spectroscopy", Frontiers in Optics + Laser Science 2021, 2021 Publication	1%
9	"ICOL-2019", Springer Science and Business Media LLC, 2021 Publication	<1%
10	www.newport.com Internet Source	<1%
11	S THAKUR. "Atomic Emission Spectroscopy", Laser-Induced Breakdown Spectroscopy, 2007 Publication	<1%
12	hdl.handle.net Internet Source	<1%

Prof. SOMA VENUGOPAL RAO
F.N.A.Sc., F.Inst.P, FRSC
ACRHEM
DRDO Industry Academic-Centre of Excellence
(DIA-COE)
University of Hyderabad
Hyderabad-500046. Telangana, INDIA.

13	"Solid-State Laser Engineering", Springer Science and Business Media LLC, 2006 Publication	<1 %
14	Francisco J. Fortes, Javier Moros, Patricia Lucena, Luisa M. Cabalín, J. Javier Laserna. "Laser-Induced Breakdown Spectroscopy", Analytical Chemistry, 2012 Publication	<1 %
15	www.azom.com Internet Source	<1 %
16	www.frontiersinoptics.com Internet Source	<1 %
17	facss.org Internet Source	<1 %
18	Abdul Kalam S, Balaji Manasa Rao S.V., Jayananda M., Venugopal Rao Soma. "Standoff Femtosecond Filament-Induced Breakdown Spectroscopy for Classification of Geological Materials", Journal of Analytical Atomic Spectrometry, 2020 Publication	<1 %
19	Alessandro De Giacomo, Can Koral, Gabriele Valenza, Rosalba Gaudiuso, Marcella Dell'Aglio. "Nanoparticle Enhanced Laser-Induced Breakdown Spectroscopy for Microdrop Analysis at subppm Level", Analytical Chemistry, 2016 Publication	<1 %

S Venugopal Rao 14/1/20

Prof. SOMA VENUGOPAL RAO
F.N.A.Sc., F.Inst.P, FRSC
ACRHEM
DRDO Industry Academic-Centre of Excellence
(DIA-COE)
University of Hyderabad
Hyderabad-500046. Telangana, INDIA.